COLLECTED PAPERS

ON

NANO/ATOM PHOTONICS

Volume 17

August 2001 – July 2002

Professor

Motoichi OHTSU

TOKYO INSTITUTE OF TECHNOLOGY

Interdisciplinary Graduate School of Science and Engineering
4259 Nagatsuta-cho, Midori-ku, Yokohama, Kanagawa 226-8502, JAPAN
TEL : +81 – 45 – 924 – 5455
FAX : +81 – 45 – 924 – 5599
E-mail : ohtsu @ ae. titech. ac. jp

PREFACE

In order to realize the ultimate status of light and matter, M. Ohtsu tries to control the spatial properties of light. The approach he has used is through the research of near-field optics and its application to nano-structure fabrication and atom manipulation(Fig.1). This will open up a new era of nano/atom photonics. It should be pointed out that the nano/atom photonics is closely related to quantum optics, atom optics, high density optical storage, nano-structure fabrication technology, and so on. And for this relationship of near-field optics with a variety of fields, nano/atom photonics exhibits rapid progress. Further researches are done to realize novel nanometric materials ,devices, and their integration(Fig.2).

Ohtsu-Saiki group, which is executed in Kanagawa Academy of Science and Technology(KAST) and directed by Ohtsu and Saiki, has started from April, 2001 in order to transfer the results of the research of the previous "PHOTON CONTROL" project to industry so as to produce commercial near field optical spectrometers, optical memories, fiber probes, and so on(*). The "LOCALIZED PHOTON" project, which is supported as ERATO (Exploratory Research for Advanced Technology) by Japan Science and Technology Corporation and directed by Ohtsu, studies a novel theory of optical near-field, nano-photonics, and atom-photonics.(+) Further, a national project on "Ultrahigh capacity optical storage", which is supported by METI(Ministry of Economy, Trade and Industry) and directed by Ohtsu, has started from the fiscal year 2002 to develop a prototype of an optical storage system of 1Tb/in^2 storage density. Results of the recent research carried out by Ohtsu are reviewed in this issue of the COLLECTED PAPERS.

August 2002

Motoichi OHTSU

大津 元一

(*) **Address:** Ohtsu-Saiki group,
　　　　　　　 Kanagawa Academy of Science and Technology
　　　　　　　 KSP East, Rm. 408, 3-2-1 Sakado, Takatsu-ku,

Kawasaki-shi, Kanagawa 213-0012, JAPAN

Phone: +81-44-819-2075

Fax: +81-44-819-2072

〒213-0012　神奈川県川崎市高津区坂戸３－２－１

ＫＳＰ東棟４０８号室

（財）神奈川科学技術アカデミー，光科学重点研究室

大津・斎木グループ

(+) Address: Localized photon project,

Japan Science and Technology

4th.-floor, Tenko Building #17

687-1 Tsuruma, Machida-shi, Tokyo 194-0004

Phone: +81-42-788-6030

Fax: +81-42-788-6031

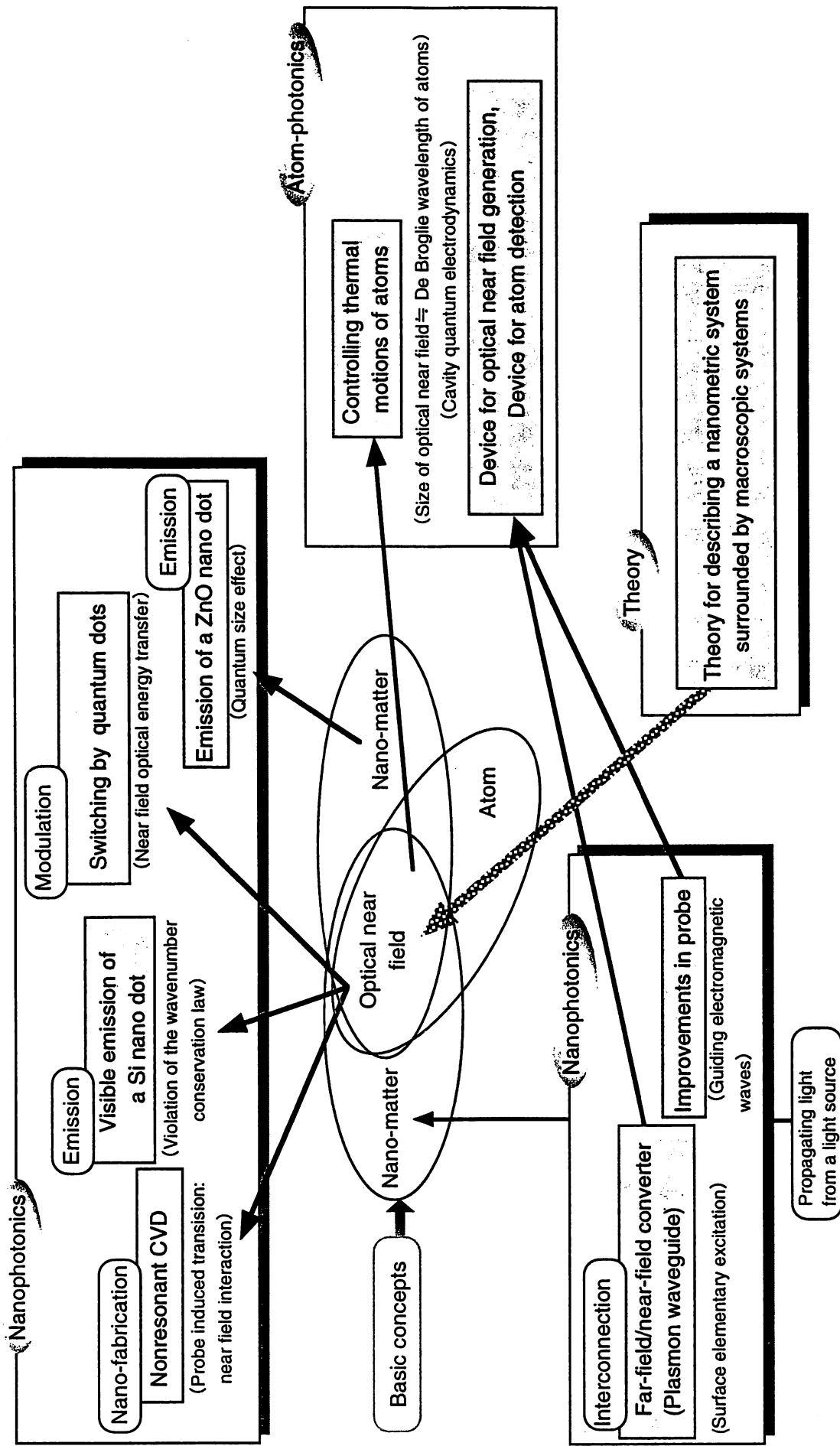〒194-0004　東京都町田市鶴間 687-1

第１７天幸ビル４階

科学技術振興事業団　「局在フォトン」プロジェクト

Nanophotonics

Nano-fabrication

Nonresonant CVD

(Probe induced transision:
near field interaction)

Emission

**Visible emission of
a Si nano dot**

(Violation of the wavenumber
conservation law)

Modulation

Switching by quantum dots

(Near field optical energy transfer)

Emission

Emission of a ZnO nano dot

(Quantum size effect)

Atom-photonics

**Controlling thermal
motions of atoms**

(Size of optical near field≒ De Broglie wavelength of atoms)
(Cavity quantum electrodynamics)

**Device for optical near field generation,
Device for atom detection**

Theory

**Theory for describing a nanometric system
surrounded by macroscopic systems**

Nano-matter

Atom

Optical near
field

Nano-matter

Nanophotonics

Improvements in probe

(Guiding electromagnetic
waves)

Basic concepts

Interconnection

**Far-field/near-field converter
(Plasmon waveguide)**

(Surface elementary excitation)

**Propagating light
from a light source**

Fig.1 Concepts of nanophotonics, atom-photonics, and theory of optical near field.

Conventional photonic devices

Nanophotonic devices and an integrated circuit

Cavity

Lightwave

Diode laser

300 μm

Optical fiber

Equivalent size

Quantum dot laser
Photonic crystal
Optical micromachine

Diffraction limit

Optical fiber

Frequency multiplex

Electric/optical near field conversion

Nanophotonic integrated circuit

Frequency demultiplex

Electric output terminal

Photo-detector

Optical amplifier

Optical switch

Light emitter

Optical output terminal

Optical amplifier

Optical input terminal

Optical input terminal

Optical near field

Fig.2 Concepts and structures of nanophotonic devices and their integration.

MEMBERS

(From April 1, 2002)

[I] TOKYO INSTITUTE OF TECHNOLOGY

Professor

     Motoichi OHTSU[a-c]   (Dr. Eng.)

Associate Professor

     Haruhiko ITO[d]   (Dr. Sci.)

Research Associate

     Motonobu KOUROGI[d-f]   (Dr. Eng.)

Graduate Students (Doctor Candidates)

     Akifumi TAKAMIZAWA

Graduate Students (Master Course)

     Kazutaka ITSUMI
     Satoru TAKUBO
     Jung-Shik LIM
     Yuji ECHIGO
     Shungo YAMADA
     Kazuhiro YAMAMOTO
     Wataru NOMURA
     Shinya MARUYAMA
     Shunsuke YAMAZAKI
     Kiichi SUZUKI
     Yoshihiko MATUURA

Undergraduate Students

     Kazunori KOBAYASHI
     Takashi NAGIRA
     Takumi IMAI

Research Students

Yun-Jin CHOI

Visiting Scientists

Bambang WIDIYATMOKO   (Dr. Eng.)
Osamu NAKAMOTO
Takashi YATSUI [g]   (Dr. Eng.)

Secretaries

Chikako ISHIDA
Kaoru OGURA

a) Also with Kanagawa Academy of Science and Technology
   (Director, Ohtsu-Saiki group)
b) Also with ERATO, Japan Science and Technology Corporation
   (Director, "Localized photon" project)
c) Also a director, "Ultrahigh capacity optical storage",
   Ministry of Economy, Trade and Industry
d) Also with "Localized photon" project, ERATO,
   Japan Science and Technology Corporation
e) Also with Kanagawa Academy of Science and Technology
   (Part-time researcher, Ohtsu-Saiki group)
f) Also a director,   Optical Comb Laboratories, Inc.
g) Permanent affiliation: "Localized photon" project, ERATO,
   Japan Science and Technology Corporation

[II] "LOCALIZED PHOTON" PROJECT, ERATO, JAPAN SCIENCE AND TECHNOLOGY CORPORATION

Researchers

Theory Group

Kiyoshi KOBAYASHI[h]	(Dr. Sci.)	(Group Leader)
Suguru SANGU	(Dr. Eng.)	
Akira SHOJIGUCHI	(Mr. Sci.)	

Nano-photonics Group

Tadashi KAWAZOE	(Dr. Sci.)
Takashi YATSUI	(Dr. Eng.)
T.-W. KIM	(Dr.Eng.)

Atom-photonics Group

Kouki TOTSUKA	(Dr. Sci.)
S. M. IFTIQUAR	(Ph.D.)

Managers

Akiyoshi ORIDE[i]

Takaaki MORIYAMA

Secretaries

Tomoko TOTAKE

h) Permanent affiliation: Japan IBM Co. Ltd.

i) Permanent affiliation: RICOH Co.Ltd.

[III] KANAGAWA ACADEMY OF SCIENCE AND TECHNOLOGY

Full-Time Researchers

Shuji MONONOBE (Dr. Eng.)

Part-Time Researchers

Motonobu KOUROGI[j] (Dr. Eng.)

Secretary

Tomoko NAKAMURA

j) Permanent affiliation: Tokyo Institute of Technology

LIST OF PAPERS

[(pp.XX-XX); pages in this issue of the COLLECTED PAPERS]

[I] PAPERS IN NANO/ATOM PHOTONICS

[I-1] PAPERS IN ATOM PHOTONICS

(a) Journal Papers

[1] K. Totsuka, H. Ito, T. Kawamura, and M. Ohtsu, "High Spatial Resolution Atom Detector with Two-Color Optical Near Fields", Jpn J. Appl. Phys., Vol.41, Part 1, No.3A, March 2002, pp.1566-1571

(pp.1-6)

(b) International Conferences

[1] K. Totsuka, K. Yamada, H. Ito, and M. Ohtsu, "Atom Deflector with Optical Near Fields", Technical Digest of Quantum Electronics and Laser Science Conference, May 19-24, 2002, Long Beach, LA, pp. 66-67, (paper number QTuE1)

(pp.7-8)

[2] S.M. Iftiquar, H. Ito, A. Takamizawa, and M. Ohtsu, "Excitation of a funnel-shape optical near field by the Laguarre-Gaussian Doughnut beam", Abstract of te 3rd Asia Pacific Workshop on Near Field Optics, Nov.28-Dec.1, 2001, Melbourne, Australia, p.36

(p.9)

[3] A. Takamizawa, S.M. Iftiquar, H. Ito, and M. Ohtsu, "Observation of cold atoms reflection in a near-field optical funnel", Abstract of te 3rd Asia Pacific Workshop on Near Field Optics, Nov.28-Dec.1, 2001, Melbourne, Australia, p.37

(p.10)

[I-2] PAPERS IN NANO PHOTONICS

(a) Journal Papers

[1] T. Yatsui, K. Itsumi, M. Kourogi, and M. Ohtsu, "Metallized pyramidal silicon probe with extremely high throughput and resolution capability for optical near-field technology", Appl. Phys. Lett., Vol.80, No.13, April 2002, pp.2257-2259

[Also published in Virtual Journal of Nanoscale Science and Technology, April 8, 2002, Vol.5, Iss.4, Optical Properties and Quantum Optics,http://ojps.aip.org/journal_cgi/dbt?KEY=VIRT01&Volume=5&Issue=14]

(pp.11-13)

[2] T. Yatsui, T. Kawazoe, T. Shimizu, Y. Yamamoto, M. Ueda, M. Kourogi, M. Ohtsu, and G.H. Lee, "Observation of size-dependent features in the photoluminescence of zinc oxide nanocrystallites by near-field ultraviolet spectroscopy", Appl. Phys. Lett., Vol.80, No.8, February 2002, pp.1444-1446

[Also published in Virtual Journal of Nanoscale Science and Technology, March 4, 2002, Vol.5, Iss.9, Imaging Science and Technology, http://ojps.aip.org/journal_cgi/dbt?KEY=VIRT01&Volume=5&Issue=9]

(pp.14-16)

[3] T. Kawazoe, K. Kobayashi, J. Lim, Y. Narita, and M. Ohtsu", Direct Observation of Optically Forbidden Energy Transfer between CuCl Quantum Cubes via Near-Field Optical Spectroscopy", Phys. Rev. Lett., Vol.88, No.6, February 2002, pp.067404-1—067404-4

(pp.17-20)

[4] T. Yatsui, M. Kourogi, and M. Ohtsu, "Plasmon waveguide for optical far/near-field conversion", Appl. Phys. Lett., Vol.79, No.27, December 2001, pp.4583-4585

(pp.21-23)

[5] H.N. Aiyer, T. Kawazoe, J. Lim, Y. Echigo, and M. Ohtsu, "Mercury treatment of optical near-field fibre probes for smoother tips with reduced light leakage", Nanotechnology, Vol.12, 2001, pp.368-371

(pp.24-27)

[6] T. Kawazoe, T. Shimizu, and M. Ohtsu, "Second-harmonic generation in a near-field optical-fiber probe", Opt. Lett., Vol.26, No.21, November 2001, pp.1687-1689

(pp.28-30)

[7] T. Yatsui, T. Shimizu, Y. Yamamoto, M. Kourogi, M. Ohtsu, and G.H. Lee, "Near-field ultraviolet photoluminescence spectroscopy for evaluating the crystallinity of polycrystalline zinc oxide", Appl. Phys. Lett., Vol.79, No.15, October 2001, pp.2369-2371

(pp.31-33)

[8] S. Mononobe and M. Ohtsu, "Characterization of Silica Optical Fibers Based on Chemical Etching", Trans. Inst. Electron., Information, and Commun. Eng. C, Vol.J84-C, No.9, September 2001, pp.894-895
【物部秀二、大津元一、「化学エッチングに基づく石英系光ファイバの評価法」、電子情報通信学会論文誌、第Ｊ８４－Ｃ巻、第９号、２００１年９月、pp.894-895】

(pp.34-35)

[9] T. Kawazoe, Y. Yamamoto, and M. Ohtsu, "Fabrication of a nanometric Zn dot by nonresonant near-field optical chemical-vapor deposition", Appl. Phys. Lett., Vol.79, No.8, August 2001, pp.1184-1186

(pp.36-38)

[10] H. Fukuda, T. Saiki, and M. Ohtsu, "Diagnostics of Semiconductor Devices beyond the Diffraction Limit of Light", Sensors and Materials, Vol.13, No.8, August 2001, pp.445-460

(pp.39-54)

(b) International Conferences

[1] K. Kobayashi, A. Shojiguchi, S. Sangu, K. Kitahara, and M. Ohtsu, "Coherent dipole oscillation induced by localized photons", Abstract of the 5th International Conference on Exciton Process in Condensed Matter, July 22-26, 2002, Darwin, Australia, (paper number 7C60)

(pp.55-56)

[2] M. Ohtsu, "Nano- and atom-photonics: Beyond the fundamental limit of light", Abstract of the 7th "Science in Japan" Forum, - Nanoscale Science and Technology -, June 14, 2002, Washington, D.C. p.18
[Invited presentation]

(p.57)

[3] S. Sangu, K. Kobayashi, A. Shojiguchi, and M. Ohtsu, "Characteristics of Relaxation Process in an Optically Coupled Quantum-Dots System", Technical Digest of Quantum Electronics and Laser Science Conference, May 19-24, 2002, Long Beach, LA, pp. 9-10 (paper number QMC3)

(pp.58-59)

[4] K. Kobayashi, A.Shojiguchi, S. Sangu, K. Kitahara, and M. Ohtsu, "Coherent Excitation Dynamics Controlled by Localized Photons", Technical Digest of Quantum Electronics and Laser Science Conference, May 19-24, 2002, Long Beach, LA, pp. 104-105 (paper number QTuI1)

(pp.60-61)

[5] T. Kawazoe, K. Kobayashi, J. Lim, Y. Narita, and M. Ohtsu, "Dipole-forbidden Energy Transfer between CuCl Quantum Cubes via Optical Near-field", Technical Digest of Quantum Electronics and Laser Science Conference, May 19-24, 2002, Long Beach, LA, pp. 181-182 (paper number QThB6)

(pp.62-63)

[6] T. Yatsui, T. Abe, M. Kourogi, and M. Ohtsu, "A Plasmon Waveguide for Optical Far/Near-Field Conversion", Technical Digest of Conference on Lasers and Electro-Optics, May 19-24, 2002, Long Beach, LA, pp.76-77 (paper number CMP5)

(pp.64-65)

[7] T. Yatsui, T. Kawazoe, and M. Ohtsu, "Near-field Components and Evaluation of the Photoluminescence in Si Nano-structure", Technical Digest of Conference on Lasers and Electro-Optics, May 19-24, 2002, Long Beach, LA, pp.242-243 (paper number CTuK67)

(pp.66-67)

[8] T. Yatsui, T. Kawazoe, M. Ueda, M. Kourogi, M. Ohtsu, and G.H. Lee, "Observation of Size-dependent Features in the Photoluminescence of ZnO Nanocrystallites by Near-field UV Spectroscopy", Technical Digest of Conference on Lasers and Electro-Optics, May 19-24, 2002, Long Beach, LA, pp.651-652 (paper number CFF7)

(pp.68-69)

[9] K. Kobayashi, S. Sangu, T. Kawazoe, A. Shojiguchi, K. Kitahara, and M. Ohtsu, "Coherent excitation dynamics of quantum dots systems controlled by optical near fields", Abstract of the 19th General Conference of the EPS Consensed Matter Division held jointly with CMMP 2002-Condensed Matter and Maerials Physics, April 7-11, 2002, Brighton, UK, p.195 (paper number S10.P.2.21)

(p.70)

[10] T. Kawazoe and M. Ohtsu, "Near-Field Optical Microscopy and Application to Nano-Photonics", Abstract of the 14th International Conference on Confocal Microscopy and the 15th International Conference on 3D Image Processing in Microscopy, April 7-10, 2002, Kaohsiung, Taiwan, p.32 (paper number MpB1)
[Invited presentation]

(p.71)

[11] T. Yatsui and M. Ohtsu, "Development of nano-photonic devices and their integration by optical near field", Abstract of the MRS 2002 Spring Meeting, April 1-5, 2002, San Francisco, CA, p.126 (paper number S7.1)
[Invited presentation]

(p.72)

[12] T. Kawazoe, T. Yatsui, and M. Ohtsu, "Nano Photonic Device and Nano Optical Process using Optical Near-Field", Technigal Digests of SEMI Technology Symposium 2001, December 5-7, 2001, Makuhari, Chiba, pp.4-27 –4-32
[Invited presentation]

(pp.73-78)

[13] M. Ohtsu, "Design, fabrication, and operation of nano-photonic devices by optical near-field", Proceedings of the Australasian Conference on Optics,

Lasers and Spectroscopy 2001, December 3-6 2001, Brisbane, Australia, p.27
(paper number Plenary 3)
[Plenary presentation]

(p.79)

[14] M. Ohtsu, "Developing nano-photonic devices and their integration by optical near-field", Abstract of the 3rd Asia Pacific Workshop on Near Field Optics, November 28-December 1, 2001, Melbourne, Australia, p.29
[Invited presentation]

(p.80)

[15] H.N. Aiyer, T. Kawazoe, and M. Ohtsu, "New methods for improved optical near field fiber probes", Abstract of the 3rd Asia Pacific Workshop on Near Field Optics, November 28-December 1, 2001, Melbourne, Australia, p.51

(p.81)

[16] T. Yatsui, T. Abe, M. Kourogi, and M. Ohtsu, "A plasmon waveguide for optical far/near-field conversion", Abstract of the 3rd Asia Pacific Workshop on Near Field Optics, November 28-December 1, 2001, Melbourne, Australia, p.63

(p.82)

[17] T. Yatsui, T. Kawazoe, and M. Ohtsu, "Near-field components of the photoluminescence in silicon nano-structure and its evaluation", Abstract of the 3rd Asia Pacific Workshop on Near Field Optics, November 28-December 1, 2001, Melbourne, Australia, p.64

(p.83)

[18] K. Kobayashi, S. Sangu, T. Kawazoe, A. Shojiguchi, and M. Ohtsu, "Optical near-field interaction and its application to a nano-device", Abstract of the 3rd Asia Pacific Workshop on Near Field Optics, November 28-December 1, 2001, Melbourne, Australia, p.80

(p.84)

[19] S. Sangu, K. Kobayashi, T. Kawazoe, and M. Ohtsu, "Inter-quantum dot energy transfer via optical near-field interaction", Abstract of the 3rd Asia Pacific Workshop on Near Field Optics, November 28-December 1, 2001, Melbourne, Australia, p.81

(p.85)

[20] A. Shojiguchi, K. Kobayashi, K. Kitahara, S. Sangu, and M. Ohtsu, "Excitation transfer by optical near-field interaction: localized photon picture", Abstract of the 3rd Asia Pacific Workshop on Near Field Optics, November 28-December 1, 2001, Melbourne, Australia, p.82

(p.86)

[21] T. Kawazoe, K. Kobayashi, S. Sangu, J. Lim, Y. Narita, and M. Ohtsu, "Dipole forbidden energy transfer via optical near-field interaction between cuprous chloride quantum cubes", Abstract of the 3rd Asia Pacific Workshop on Near Field Optics, November 28-December 1, 2001, Melbourne, Australia, p.84

(p.87)

[I-3] REVIEW PAPERS

[1] M. Ohtsu, "Nanophotonics", Journal of Japanese Society of Mechanical Engineering, Vol.105, No.1004, July 2002, pp.11-15
【大津元一、「ナノフォトニクス」、日本機会学会誌、第１０５巻、第１００４号、２００２年７月、pp.11-15】

(pp.89-93)

[2] M. Ohtsu and K. Sawada, "High-Resolution and High-Throughput Probes", Chapter 3 in *Nano-Optics*, ed. by S. Kawata, M. Ohtsu, and M. Irie, Springer-Verlag, Berlin, 2002, pp.61-74

(pp.94-107)

[3] M. Ohtsu, "Nanophotonics System using Optical Near Fields", Chapter 5, *Frontier of Nano-materials*, ed. by K. Hirao, Kagaku-dojin, Kyoto, June 2002, pp.52-57

(pp.108-113)

[4] M. Ohtsu, "Materials and Devices of", Chapter 14 of Frontier of Nano-materials, ed. by K. Hirao, Kagaku-dojin, Kyoto, June 2002, pp.110-114

(pp.114-118)

[5] M. Ohtsu, "Optical Recording by Optical Near Field", OITDA Newsletter, No.17, March 2002, by Optoelectronic Industry and Technology Development Association, Tokyo, pp.1-8

(pp.119-126)

[6] M. Ohtsu, "Introduction to Near-field Optics for Nano-Photonics", J. Optical Society of Japan, Vol.31, No.2, February 2002, pp.120-127

【大津元一、「ナノフォトニクスのための近接場光学入門」、光学、第３１巻、第２号、２００２年２月、pp.120-127】

(pp.127-134)

[7] M. Ohtsu, "Nanophotonics and nanophotonic integrated devices", O plus E, Vol.24, No.1, January 2002, pp.28-33

【大津元一、「ナノフォトニクスとナノ光集積デバイス」、OplusE、第２４巻、第１号、２００２年１月，pp.28-33】

(pp.135-140)

[II] PAPERS IN OTHER FIELDS

(a) Journal Papers

[1] S.J. Lee, B. Widiyatmoko, M. Kourogi, and M. Ohtsu, "Ultrahigh Scanning Speed Optical Coherence Tomography Using Optical Frequency Comb Generators", Jpn. J. Appl. Phys., Vol.40, Part 2, No.8B, August 2001, pp.L878-L880

(pp.141-143)

[III] PUBLISHED BOOKS

[1] S. Kawata, M. Ohtsu, and M. Irie (eds.), *Nano-Optics*, Springer-Verlag, Berlin, 2002 (321 pages)

[2] M. Ohtsu, *Small Particle of Light*, Popular Science, No.239, Shokabo Publishers, Tokyo, 2001 (139 pages)

【大津元一、「光の小さな粒」、ポピュラーサイエンス２３９，裳華房、東京、２００１年１１月、（１３９ページ）】

(pp.145-150)

[IV] PRESENTED PH.D THESIS

[1] N. Saito, "Study on composition-modulated films and lateral p-n junctions

for light sources of a magneto-optical storage system", January 2002
【斉藤信雄、「光磁気記録のための媒体用組成変調膜および光源用横型 p-n 接合の開発に関する研究」、2002 年 1 月】

[V] AWARDS

[1] T. Kobayashi, J. Ishibashi, H. Inaba, S. Mononobe, M. Ohtsu and H. Homma, The best paper award from the Surface Technology Association(February 27, 2002), for the paper entitled, "Electroless Nickel Plating to a Minute Area" (published in Surface Technology, Vol.51, No.2, February 2000, pp.193-198)
【小林健、石橋純一、稲葉裕之、物部秀二、大津元一、本間英夫、平成 14 年度表面技術協会論文賞（平成 14 年 2 月 27 日）、論文名「微小領域への無電解ニッケルめっき」（表面技術、第 51 巻、第 2 号、2000 年 2 月）】

[2] A. Shojiguchi, The best student paper award, the 3rd Asia Pacific Workshop on Near Field Optics (December 1, 2001), for the paper entitled, "Excitation transfer by optical near-field interaction: localized photon picture", Abstract of the 3rd Asia Pacific Workshop on Near Field Optics, November 28-December 1, 2001, Melbourne, Australia, p.82

[I] PAPERS IN
NANO/ATOM PHOTONICS
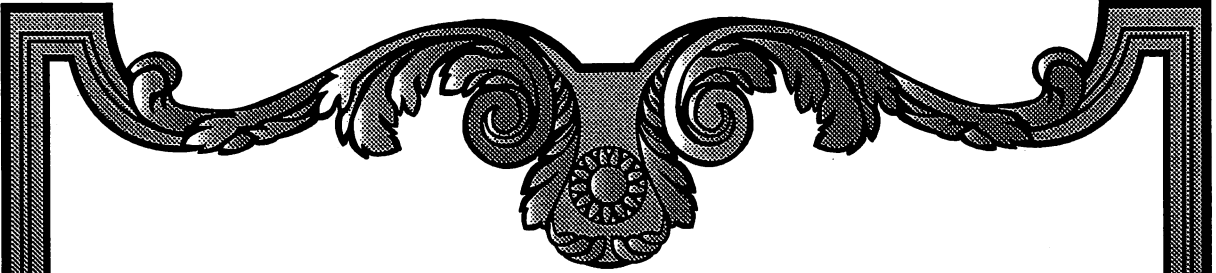
[I-1] PAPERS IN ATOM PHOTONICS
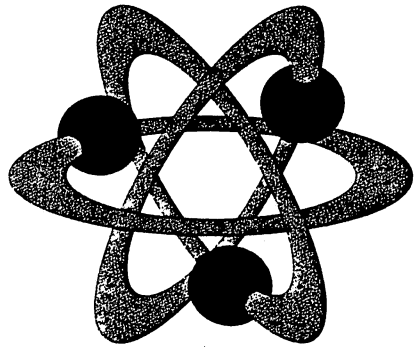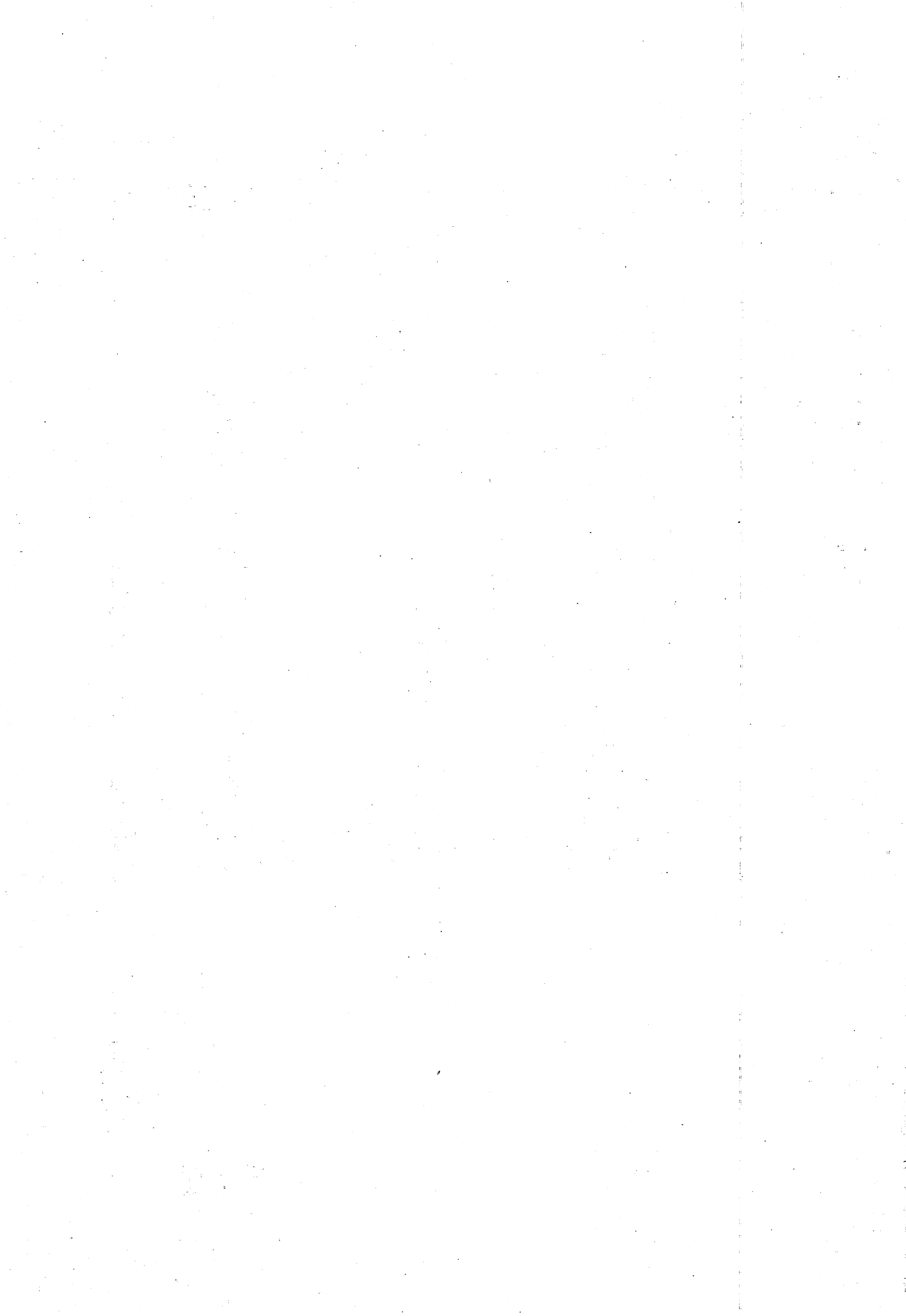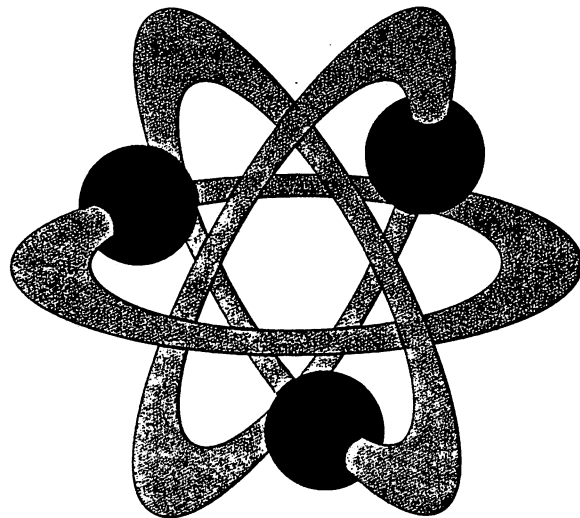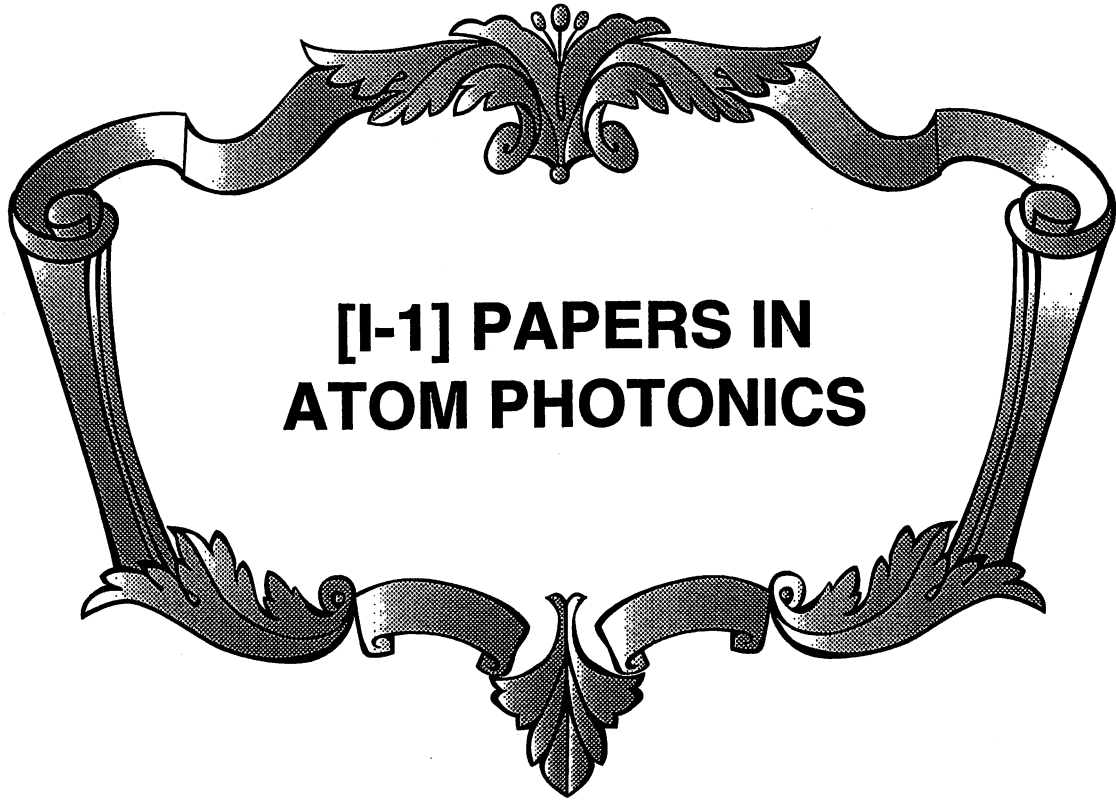
High Spatial Resolution Atom Detector with Two-Color Optical Near Fields

Kouki TOTSUKA[1], Haruhiko ITO[2], Tomoto KAWAMURA[2] and Motoichi OHTSU[1,2]

[1]ERATO Localized Photon Project, Japan Science and Technology Corporation, 687-1 Tsuruma, Machida, Tokyo 194-0004, Japan
[2]Interdisciplinary Graduate School of Science and Engineering, Tokyo Institute of Technology,
4259 Nagatsuta-cho, Midori-ku, Yokohama 226-8502, Japan

We describe a slit-type detector for ground-state atoms with nanometer optical near fields. The detector with a slit width of 70 nm and a slit length of 100 μm is fabricated by processing a silicon-on-insulator wafer with photolithography and anisotropic etching. Measurement with a fiber probe of the intensity distribution on the slit reveals that the spatial resolution is 96 nm. Rubidium atoms can be selectively detected by means of two-step photoionization. The detection efficiency is estimated at 25% for Rb atoms with a mean velocity of 10 m/s. The atom detector can be used for atom deflection experiments with a fiber probe. [DOI: 10.1143/JJAP.41.1566]

KEYWORDS: optical near field, atom detector, spatial resolution, intensity distribution, fiber probe, photoionization, detection efficiency, Rb atom, atom deflection

1. Introduction

Some atom-optical methods using the resonant interaction between atoms and laser light have been applied to the fabrication of nanometer structures. For example, line and array patterns with an individual width of several 10 nm have been made with vapor atoms.[1–5] Basically, in these experiments, an atomic beam is focused on a substrate at every half wavelength by standing light waves that work as a sort of lens. The fabrication of arbitrary patterns, in particular, a dot-shape nanostructure, is now expected with atom-optical methods. However, the conventional ones with far-field light cannot precisely control atoms with a spatial accuracy of more than about half-wavelength, due to the diffraction effect. This makes it difficult to produce a nanoscale structure with the atom-optical methods.

In order to manipulate atoms with high spatial accuracy beyond the diffraction limit, we consider the use of optical near fields localized in the nanometer region. As the beginning, we are developing atom deflection with a nanometer fiber probe.[6] In this case, atoms entering the near-field region near the aperture of the fiber probe are deflected by the dipole force. It should be noted that cold atoms with low kinetic energy are required for efficient interaction with the nanometric optical near field. As our first demonstration, we shall use a cold Rb atomic beam. As is well known, cold atoms with a mean temperature below 1 mK are easily produced by laser-cooling techniques.[7] In the case of Rb atoms with a velocity of 10 m/s, which is at the high-speed end of the velocity distribution, the deflection angle is estimated to be 0.1°.[6,8] This indicates that the atom deviates from the incidence axis by approximately 10 μm at 1 cm downstream of the fiber probe. Consequently, in order to determine the position of the deflected atoms almost over the velocity distribution with a high accuracy of 1%, we need an atom detector with a spatial resolution of 100 nm. Moreover, it should be noted that the number of atoms interacting with the nanometric optical near field is very small. Therefore, a high detection efficiency is also required for the atom detector.

It is not easy to detect a small number of neutral atoms. The most popular method is to use a microchannel plate (MCP). Unfortunately, the highest resolution of commercial MCPs is only 5 μm. Although an elaborate detection system including secondary electron multipliyer with a resolution of 1 μm has been reported,[9] it is effective for metastable atoms but not the ground-state atoms we manipulate. These detectors use surface ionization: the ionization efficiency for the ground-state atoms is estimated to be at most 0.1% per second at room temperature from the Saha-Langmuir equation and the adsorption time.[10,11] Thus, the conventional atom detectors have low detection efficiency as well as low spatial resolution, so that they are insufficient for the atom-deflection experiment with the nanometric optical near field.

In this paper, we present a new scheme of detecting ground-state atoms with two-step near-field light ionization. In this scheme, a slit-type silicon detector with a slit width of 70 nm is illuminated with two-wavelength laser light beams and two-color optical near fields are excited on the slit. When atoms go through the near-field region, they are selectively ionized by the two-color optical near fields. From this, it follows that the spatial resolution is principally determined by the size of the optical near fields, i.e., the slit width. Besides, in order to increase the photoionization efficiency, we make the slit length 100 μm. As a result, the detection efficiency is expected to be 25% for slow Rb atoms.

After the introduction of the atom-detection system in the next section, the fabrication process of the slit-type detector is shown in §3. Then, we describe our measurement of intensity distribution of the optical near field generated on the slit. From the results, the spatial resolution is discussed. In §5, we estimate the detection efficiency of the slit-type detector, based on a two-step photoionization experiment of an Rb atomic beam with evanescent light excited on a prism. Finally, we discuss the high-temperature stability of the slit-type detector when using the high-power Ar-ion laser beam.

2. Slit-Type Detector with Two-Step Near-Field Light Ionization

For high-density and high-speed recording/reading with optical near fields, a pyramidal silicon probe was produced by Yatsui et al.[12] The pyramidal probe with a small aperture at the peak generates the nanometric optical near field with high throughput, which is defined as the conversion ratio
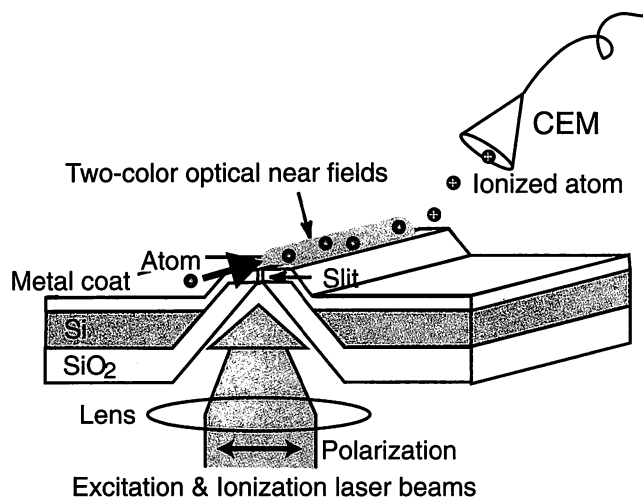
1

Fig. 1. Atom detection with a slit-type detector fabricated from a silicon-on-insulator wafer. Two-color optical near fields are excited on the nanometric-width slit by illumination of the V-groove with two-wavelength light beams. Atoms entering the near-field region are ionized with two steps and detected by a CEM. The light polarization is chosen in the direction perpendicular to the slit-length direction such that the throughput is high.

Fig. 2. Fabrication process of the slit-type detector. (a) A V-groove is made by photolithography and anisotropic etching. (b) The top SiO_2 layer is first removed and then a new SiO_2 layer covering the V-groove is remade on the Si surface. (c) The SiO_2 layer is coated with Cr and then the part outside the V-groove is eliminated. Next, a Pyrex glass plate is bonded. (d) After removal of the extra SiO_2 and Si layers, the residual Si layer is etched until the peak of the V-groove appears. Then, the slit is made at the peak and the underside of the Si layer is coated with Al.

from far-field light to near-field one. Considering its advantages, by developing the pyramidal probe, we fabricate a slit-type silicon probe shown in Fig. 1 as an atom detector. The probe consists of a Si layer and a SiO_2 layer. Contrary to the Si layer, the SiO_2 layer hardly absorbs excitation light beams because the absorption coefficient is very small for the wavelengths used here. The metal (Al) coating is made to block far-field light and generate near-field light only on the slit.

In order to detect ground-state atoms efficiently and selectively, we use two-step photoionization. When two-wavelength laser light beams are coupled to the slit from the back with a V-groove, two-color optical near fields are excited on the nanometric slit. Thanks to the V-groove, if the polarization is choosen in the direction perpendicular to the slit such that no cutoff exists, the excitation efficiency of the optical near fields greatly increases.[13] Atoms going through the near-field region are ionized by the optical near fields in two steps and counted by a channel electron multiplier (CEM). In this case, the nanometric slit width ensures the high spatial resolution. On the other hand, the slit length is taken to be large as shown in the next section. This is for increasing the interaction time and opportunity between atoms and optical near fields.

Let us consider the case of Rb atoms with a resonant wavelength of 780 nm. First, the optical near field generated by a diode laser with a wavelength of 780 nm excites the Rb atoms from the $5S_{1/2}$ ground state to the $5P_{3/2}$ state. Then, the second optical near field generated by a high-power Ar-ion laser with a wavelength of 476.5 nm excites them to the ionization level at 4.18 eV above the ground state. The positive Rb ions are measured with the CEM negatively biased. Owing to the resonant excitation, one can detect only Rb atoms state-selectively.
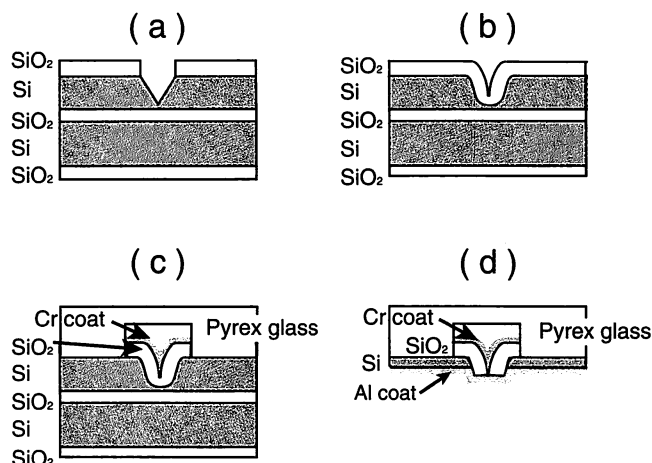
3. Fabrication of Slit-Type Detector

The slit-type detector is made out of a (100)-oriented silicon-on-insulator wafer by means of photolithography and anisotropic etching.[14] The silicon-on-insulator wafer has two Si layers and three SiO_2 ones. Figure 2 shows the fabrication process. At the first stage, the V-groove is made by anisotropic etching with a 34% KOH solution at 80°C [Fig. 2(a)]. At the second stage, the top SiO_2 layer is first cleared by selective etching with a buffered hydrofluoric (BHF) acid. Then, the naked Si-layer surface is thermally oxidized with wet oxygen at 1150°C, so that a new SiO_2 layer covering the V-groove is remade on the Si layer [Fig. 2(b)]. At the third stage, after Cr deposition on the SiO_2 layer by vacuum evaporation, a part of the SiO_2 layer located outside of the V-groove is eliminated and then a Pyrex glass plate is bonded to the open part of the Si layer by anodic bonding with 300 V at 350°C [Fig. 2(c)]. Note that the Cr coat protects the SiO_2 layer on the V-groove from percolation of the BHF acid which is used at the next stage for perforating the slit, while the Pyrex glass plate protects the fragile thin slit structure. At the last stage, after removal of the extra SiO_2 and Si layers used as support, the residual Si layer is etched with tetramethyl ammonium hydroxide until the peak of the V-groove appears and then the slit is made at the peak through slight etching with the BHF acid. Finally, the underside of the Si layer is coated with Al of 50 nm thickness [Fig. 2(d)]

Figure 3 shows the SEM images of the slit-type detector we made. The slit width is 70 nm and the slit length is taken to be 100 μm for enhancement of the detection efficiency, which is discussed in §5. One can control the slit length between 100 nm and 100 μm within the dispersion of about $\pm$30 nm by changing the length of the mask used in the photolithography process. The height of the V-groove is 10 μm and the foot width is 14 μm.
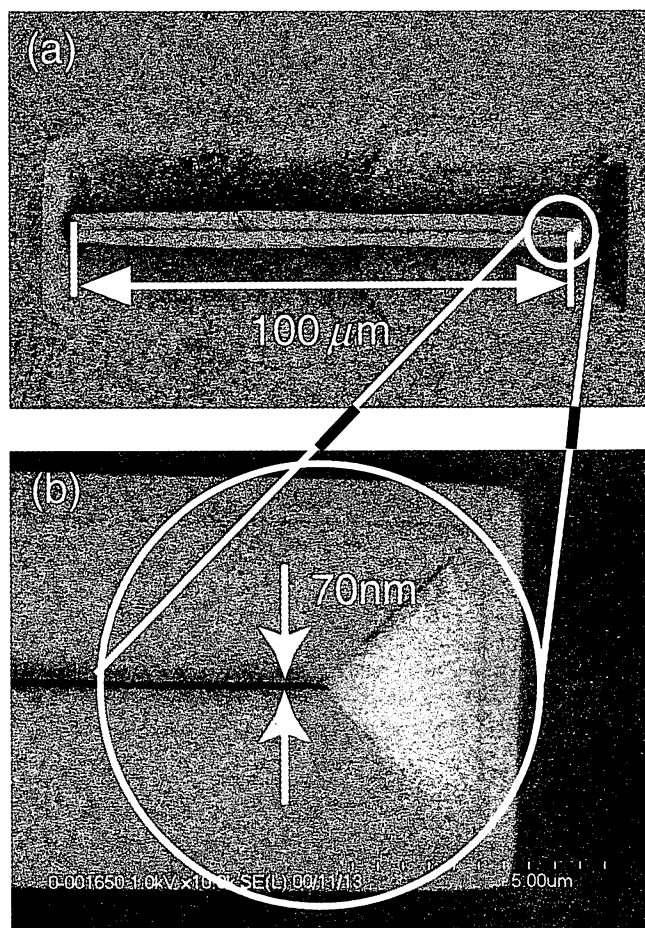
Fig. 3. SEM images of a slit-type detector. The upper picture (a) shows the entire slit with a length of 100 μm, while the lower picture (b) shows the slit with a width of 70 nm.
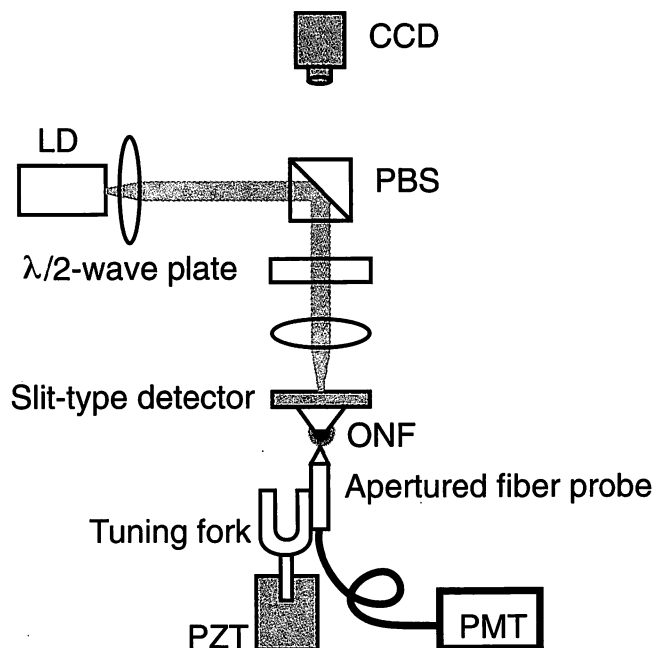

Fig. 4. Experimental setup for measurement of the near-field light intensity distribution. A fiber probe with a nanometric aperture, which is position-controlled by the shear-force technique with a tuning fork and a PZT, collects scattered photons from the ONF generated on the slit. The linear polarization of the LD beam is adjusted to the direction perpendicular to the slit-length direction with a $\lambda/2$ wave plate. A CCD camera is used for alignment of the light beam.

4. Estimation of Spatial Resolution

The intensity distribution of the optical near field generated in the vicinity of the slit is measured with a nanometric fiber probe. Figure 4 shows the experimental configuration. A diode laser (LD) beam with a wavelength of 780 nm is coupled to the slit-type detector and the optical near field is excited at the peak of the slit. A fiber probe with a small aperture of 70 nm is mounted on a tuning fork. When the fiber probe, which is controlled with a piezoelectric transducer (PZT), goes into the near-field region, far-field photons are scattered and collected by the fiber probe. The output signal is sent to a photomultiplier tube (PMT) connected to the fiber probe. Here, the shear-force control, which monitors the resonant frequency of the fiber-probe dithering, is used for measurement of the distance d between the probe tip and the slit. Figure 5(a) shows the image of the optical near field obtained from a 300-nm $\times$ 1.6-μm-size raster scanning at $d = 5$ nm, in which the scanning area is indicated in the upper SEM image of the slit-type detector. The dotted curve in Fig. 5(b) shows the intensity-distribution profile in the direction designated by the white solid line. The FWHM of the profile is estimated to be 96 nm.

The intensity distribution of the optical near field can be approximately expressed with a Yukawa-type function given by[15]

$$\Psi(r) \propto \int_A \frac{\exp(-|r - r'|/\Lambda)}{|r - r'|} dS, \tag{1}$$

where the decay length Λ is taken to be the half-width of the slit. The integration is carried out over the slit area $A = a \times L$, where a and L are the width and the length of the slit, respectively. The coordinate vectors r and r' are the measurement point and the source point on the slit, respectively, where the origin is taken at the center of the area. The intensity distribution $I_{\mathrm{onf}}(r)$ is written as[15]

$$I_{\mathrm{onf}}(r) = I_0 \frac{H(r)}{H(0)}, \tag{2}$$

where I_0 is the light intensity on the slit, and $H(r)$ is given by

$$H(r) = |\nabla\Psi(r)|^2 + \frac{1}{\Lambda^2} |\Psi(r)|^2. \tag{3}$$

The intensity distribution calculated at $d = 5$ nm in the case of $\Lambda = a/2 = 35$ nm and $L = 100$ μm is shown by the solid curve in Fig. 5(b). The numerical result is in good agreement with the experimental result on the left-hand side, but there is a deviation on the right-hand side. It results from leakage of the light passing through the slit from the back, due to the imperfect Al coating. The FWHM of the calculated profile is 65 nm, which is almost equal to the slit width and gives the theoretical spatial resolution.

5. Estimation of Detection Efficiency

In order to examine the detection efficiency, we conduct a two-step photoionization experiment of an Rb atomic beam using a prism. Figure 6 schematically shows the experimental setup. A planar optical near field (evanescent wave)
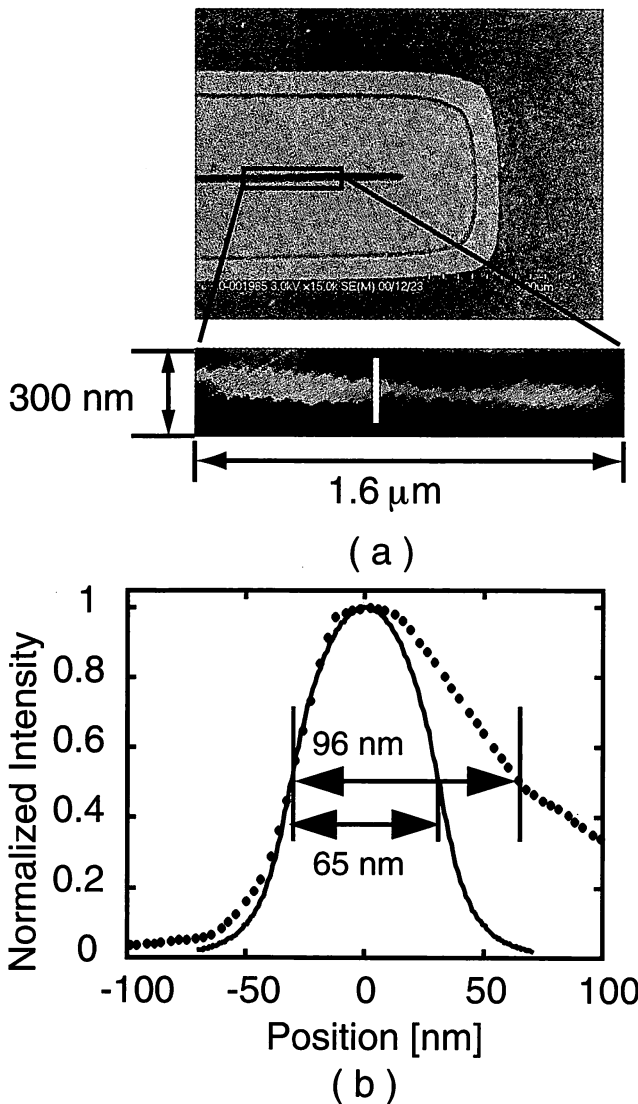
300 nm

1.6 μm

(a)

(b)

Fig. 5. (a) Image of the optical near field excited on the 70-nm-wide slit, where the area of 300 nm × 1.6 μm is scanned. (b) Intensity-distribution profile along the white solid line drawn in (a), where the intensity is normalized to the peak value. The dotted curve with an FWHM of 96 nm shows the experimental result, while the solid curve with an FWHM of 65 nm shows the theoretical profile.

is produced on a prism surface via the total internal reflection of an Ar-ion laser with a wavelength of 476.5 nm and a peak intensity of 2.5 kW/cm^2 in a vacuum pressure of 10^{-9} Torr. Here, the linear light polarization is chosen in the direction parallel to the plane of incidence. From the incidence angle $\theta = 46°$ and the refractive index $n = 1.52$ of the prism, we obtain the penetration depth $L_{pd} = \lambda/2\pi\sqrt{n^2 \sin^2 \theta - 1} = 193$ nm for $\lambda = 476.5$ nm. An LD beam with a wavelength of 780 nm, a peak intensity of 9 W/cm^2 and a beam spot of $w_{LD} = 100$ μm is incident in the direction perpendicular to the prism surface. An Rb atomic beam, which has a flux of 7.4 × 10^{14}/m^2·s and a diameter of 300 μm, goes out of an oven with a temperature of 120°C. When the atoms enter the near-field region in the vicinity of the prism surface, they are ionized through the two-step photoionization and gathered by a CEM biased at −3 kV. In this case, the quantum efficiency of the CEM is 0.9. Figure 7 shows the photoionization spectrum for the
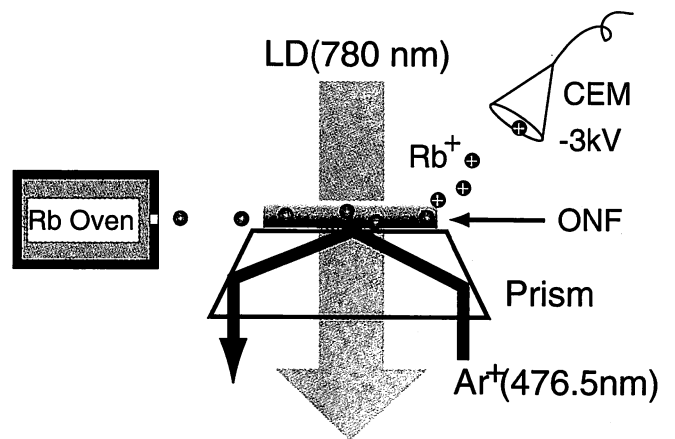
Fig. 6. Experimental setup for measurement of the two-step photoionization efficiency of Rb atoms. A planar optical near field (evanescent wave) is generated on a prism surface via total internal reflection of an Ar-ion laser beam with a wavelength of 476.5 nm at a vacuum pressure of 10^{-9} Torr. When an Rb atomic beam from an oven with a temperature of 120°C passes through the near-field region illuminated with a LD beam tuned to the resonant wavelength of 780 nm, the Rb atoms are ionized and detected by a CEM with a negative bias of −3 kV. The linear polarization of the Ar-ion laser beam is chosen in the direction parallel to the plane of incidence.
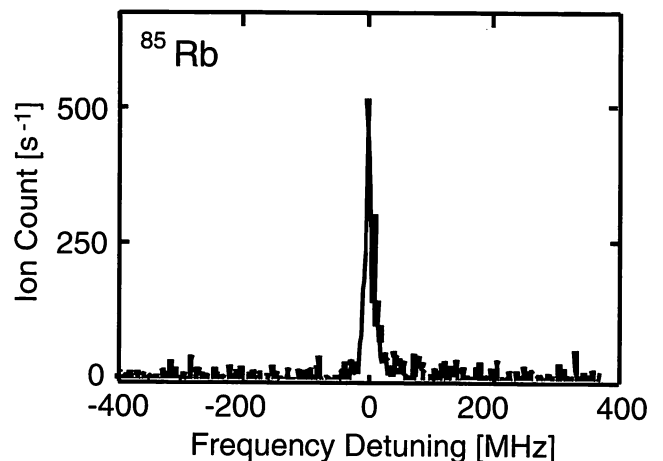

Fig. 7. Two-step photoionization spectrum for ^{85}Rb in the $5S_{1/2}$, $F = 3$ ground state. The ion number counted per second is plotted as a function of the LD frequency detuning, which is measured with respect to the $5S_{1/2}$, $F = 3 \rightarrow 5P_{3/2}$, $F = 4$ transition.

^{85}Rb atoms in the $5S_{1/2}$, $F = 3$ ground state. The peak value of the ion count is about 500 per second on resonance. From this value, considering that the number of atoms that pass through the interaction area of $L_{pd} \times w_{LD}$ is 1.5 × 10^4 per second, we obtain a detection efficiency of 3%.

Let us estimate the detection efficiency of the slit-type detector, based on the above experimental result. To this end, we first evaluate the cross section σ_{ion} of the near-field light ionization from the $5P_{3/2}$ excited state. Since the LD intensity is sufficiently high that the transition from the $5S_{1/2}$ ground state to the $5P_{3/2}$ excited state is saturated, we can detect half of the Rb atoms in the $5P_{3/2}$ state on average. As a result, the number N_{ion} of the atoms ionized per second is given by

$$N_{ion} = \int_{-\infty}^{\infty} dx \int_{-\infty}^{\infty} dy \int_{0}^{\infty} dz \int_{0}^{\infty} dv \frac{N(y,z)}{2} \sigma_{ion} \phi(x,y,z) \frac{f(v)}{v},$$

$$(4)$$

where $N(y,z)$ is the atom flux, $\phi(x,y,z)$ is regarded as the virtual photon flux of the optical near field, and $f(v)$ is the velocity distribution of the atomic beam. Here, the xy-plane is on the prism surface. The x-axis is in accordance with the incident direction of the atomic beam, while the z-axis is perpendicular to the prism surface. The origin of this coordinate system is at the center of the near-field region on the prism surface.

Since the penetration depth $L_{pd} = 193$ nm is sufficiently small compared to the atomic beam diameter $l_a = 300\,\mu$m, $N(y,z)$ is independent of z and expressed with a Gaussian function as

$$N(y,z) = N_0 \exp\left(-\frac{y^2}{l_a^2}\right),$$

$$(5)$$

where $N_0 = 7.4 \times 10^{14}/\text{m}^2\cdot\text{s}$. On the other hand, $\phi(x,y,z)$ is given by

$$\phi(x,y,z) = \phi_0 \exp\left(-\frac{2x^2}{w_x^2} - \frac{2y^2}{w_y^2} - \frac{2z}{L_{pd}}\right),$$

$$(6)$$

where ϕ_0 is the value at the origin, and $w_x = 300\,\mu$m and $w_y = 200\,\mu$m are the major and minor axes of the elliptical Ar-ion laser beam, respectively. From the Fresnel laws on transmission, the conversion equation from far-field light to near-field one is derived as[16]

$$I_0 = \frac{4n\cos^2\theta}{(n^2-1)\left[(n^2+1)\sin^2\theta - 1\right]^p} I_i,$$

$$(7)$$

where I_i is the intensity of the Ar-ion laser light, and $p = 0$ and 1 for the TE and TM polarizations, respectively. From eq. (7), if the light polarization is parallel to the plane of incidence ($p = 1$), it follows that $\phi_0 = 3.1\phi_i$, where $\phi_i = 2.4 \times 10^{26}/\text{m}^2\cdot\text{s}$ is the photon flux of the Ar-ion laser light. The velocity distribution $f(v)$ is given by

$$f(v) = 2\left(\frac{m}{2k_BT}\right)^2 \exp\left(-\frac{mv^2}{2k_BT}\right)v^3,$$

$$(8)$$

where v is the atomic velocity, m is the atomic mass, T is the oven temperature, and k_B is the Boltzmann constant. Substituting the experimental value of $N_{ion} \simeq 500$/s and eqs. (5), (6) and (7) into eq. (4), we obtain $\sigma_i = 2.4 \times 10^{-18}$ cm^2.

Now, let us consider the case of detecting slow [85]Rb atoms with the slit-type detector. If the intensity of the optical near field excited by the LD beam is sufficiently strong to saturate the transition from the $5S_{1/2}$ ground state to the $5P_{3/2}$ state, the ionization efficiency $\eta(v)$ is given by

$$\eta(v) = 1 - \exp\left(-\frac{\sigma_{ion}\phi_{onf}L}{2v}\right),$$

$$(9)$$

where ϕ_{onf} is the virtual photon flux of the optical near field excited by the Ar-ion laser beam. Figure 8 shows the detection efficiency $\eta(v)$ plotted as a function of the atomic velocity, where $\phi_{onf} \simeq 2.4 \times 10^{26}/\text{m}^2\cdot\text{s}$ is used. For exam-
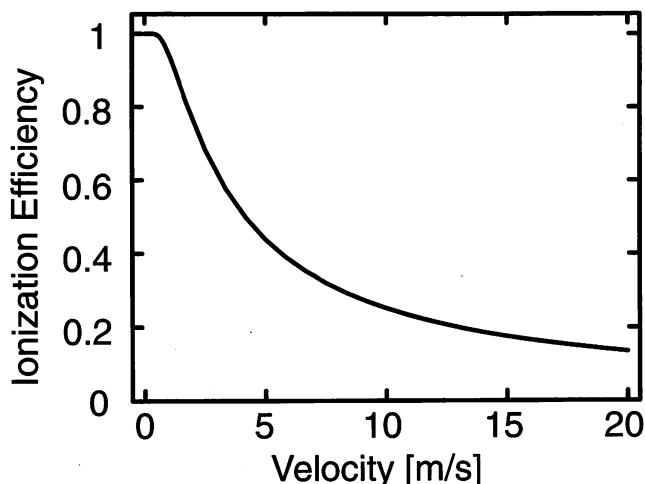

Fig. 8. Ionization efficiency of the slit-type detector for slow Rb atoms plotted as a function of the atomic velocity. Here, the virtual photon flux of the optical near field excited by the Ar-ion laser beam is assumed to be $2.4 \times 10^{26}/\text{m}^2\cdot\text{s}$ and the LD intensity is sufficiently high that the $5S_{1/2}$, $F = 3 \rightarrow 5P_{3/2}$, $F = 4$ transition is saturated.

ple, the detection efficiency at $v = 10$ m/s is estimated to be 0.25.

6. High-Temperature Stability of Slit-Type Detector

Since the ionization cross section σ_i of the Rb atom in the $5P_{3/2}$ state is small, a high-power Ar-ion laser beam with more than 1 W power is used for the slit-type detector. By making the beam waist of the Ar-ion laser smaller, one can increase the detection efficiency. However, the high-intensity light leads to damage of the slit-type detector due to heating.

Let us estimate the critical intensity at which the Al coat is damaged (melting). The Ar-ion laser beam is reflected by the Al coat with a reflectance $R = 0.9$ at the V-groove. The loss is transformed into thermal energy. Comparing the thermal conduction κt of each layer at the V-groove, where κ and t are the thermal conductivity and the layer's thickness, respectively, we find that $(\kappa t)_{Si}$ is 46 times as large as $(\kappa t)_{Al}$ and $(\kappa t)_{Al}$ is 12 times as large as $(\kappa t)_{SiO_2}$: $\kappa = 138$ W/cm·K and $t = 4\,\mu$m for the Si layer, $\kappa = 1$ W/cm·K and $t = 1\,\mu$m for the SiO$_2$ layer, and $\kappa = 240$ W/cm·K and $t = 50$ nm for the Al coat. Therefore, we consider transmission of the thermal energy from the Al coat to the Si layer, neglecting that to the SiO$_2$ layer.

The thermal energy flux j between two points with the distance Δs and the temperature difference ΔT is given by

$$j = \kappa \frac{\Delta T}{\Delta s}.$$

$$(10)$$

For simplicity, we assume that the thermal energy inflows from the window $L \times s$, where s is the slope length of the Al coat contacting the SiO$_2$ layer at the V-groove. Then, from eq. (10), we get

$$I_i(1-R)Ls = \kappa \frac{\Delta T}{\Delta s}Lt.$$

$$(11)$$

Now, let us consider the case where the temperature of the Al coat reaches the melting point of 660°C. If the Si layer contacts the body of a vacuum chamber with a room

temperature of 30°C, the temperature difference ΔT is 630 K for $s = \Delta s = 7\,\mu$m. Consequently, from eq. (11), the critical intensity I_i^c is estimated to be 150 kW/cm^2. This leads to the detection efficiency at $v = 10$ m/s of 0.98.

7. Conclusion

We fabricated a slit-type detector with a slit width of 70 nm by photolithography and anisotropic etching. Ground-state atoms can be detected with spatial accuracy determined by the slit width. In addition, taking the slit length of 100 μm, one can detect more than 10% of the incident cold Rb atoms by means of two-step near-field light ionization.

The slit-type detector is used for atom deflection experiment. Using this detector, one can resolve the position of the deflected Rb atoms with an accuracy of more than 1%. We are currently developing an atom deflector with a similar structure.

1) G. Timp, R. E. Behringer, D. M. Tennant, J. E. Cunningham, M. Prentiss and K. K. Berggren: Phys. Rev. Lett. **69** (1992) 1636.
2) M. Prentiss, G. Timp, N. Bigelow, R. E. Behringer and J. E. Cunningham: Appl. Phys. Lett. **60** (1992) 1027.
3) J. J. McClelland, R. E. Scholten, E. C. Palm and R. J. Celotta: Science **262** (1993) 877.
4) R. Gupta, J. J. McClelland, Z. J. Jabbour and R. J. Celotta: Appl. Phys. Lett. **67** (1995) 1378.
5) W. R. Anderson, C. C. Bradley, J. J. McClelland and R. J. Celotta: Phys. Rev. A **59** (1999) 2476.
6) *Near-Field Nano/Atom Optics and Technology*, ed. M. Ohtsu (Springer, Tokyo, 1998) Chap. 11.
7) H. J. Metcalf and P. van der Straten: *Laser Cooling and Trapping* (Springer, New York, 1999).
8) K. Kobayashi, S. Sangu, H. Ito and M. Ohtsu: Phys. Rev. A **63** (2000) 13806.
9) Ch. Kurtsiefer and J. Mlynek: Appl. Phys. B **64** (1997) 85.
10) M. D. Scheer and J. Fine: J. Chem. Phys. **39** (1963) 1752.
11) S. Datz and E. H. Taylor: J. Chem. Phys. **25** (1956) 389.
12) T. Yatsui, M. Kourogi, K. Tsutsui, M. Ohtsu and J. Takahashi: Opt. Lett. **25** (2000) 1279.
13) H. U. Danzebrink, Th. Dziomba, T. Sulzbach, O. Ohlsson, C. Lehrer and L. Frey: J. Microsc. **194** (1999) 335.
14) P. N. Minh, T. Ono and M. Esashi: Rev. Sci. Instrum. **71** (2000) 3111.
15) M. Ohtsu and H. Hori: *Near-field Nano-Optics* (Kluwer/Plenum, New York, 1999) Chap. 8.
16) R. Kaiser, Y. Levy, N. Vansteenkiste, A. Aspect, W. Seifert, D. Leipold and J. Mlynek: Opt. Commun. **104** (1994) 234.
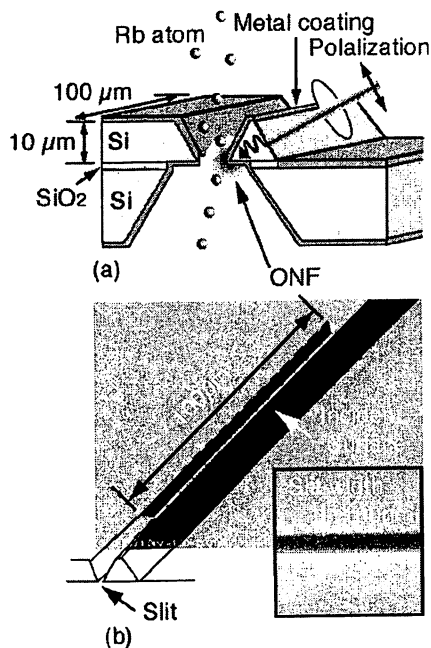
QTuE1 **Fig. 1.** (a) Sketch of a slit-type atom deflector. A repulsive optical near field (ONF) is generated on a slit-edge of the triangular-pillar part by a blue-detuned light beam. (b) SEM images of the slit-type deflector. The slit length is 100 μm, while the slit width is 100 nm as shown in the inset.

QTuE1   **10:15 am**

Atom Deflector with Optical Near Fields

Kouki Totsuka,* Kazuhiko Yamada,**
Haruhiko Ito,*** Motoichi Ohtsu,*** *ERATO
Localized Photon Project, Japan Science and
Technology Corporation, 684-1 Tsuruma,
Machida, Tokyo 194-0004, Japan, Email:
ktotsu@ohtsu.jst.go.jp; **Interdisciplinary
Graduate School of Science and Engineering,
Tokyo Institute of Technology, 4259 Nagatsuta-
cho, Midori-ku, Yokohama, Kanagaw 226-8502,
Japan

Atom-manipulation techniques, deflection and trap, with optical near fields are under development in order to perform atom-by-atom deposition with high spatial accuracy beyond the diffraction limit of light waves.[1,2] For atom-deflection experiments, we have previously fabricated a slit-type atom detector with a spatial resolution of 96 nm and a detection efficiency of more than 10% for slow Rb atoms.[3,4] We are planning to use the detector. In this paper, we report a slit-type atom deflector for Rb atoms. The deflec-

tor has a structure suitable for the use in combination with the slit-type detector.

Figure 1(a) is a sketch of the slit-type atom deflector. It is produced from a silicon-on-insulator substrate through photolithography and anisotropic etching.[5] Figure 1(b) shows a SEM image of the deflector: the slit length is taken to be 100 μm, which is the same as that of the slit-type detector. As shown in the magnified SEM image, the slit width is 100 nm. We can fabricate a variety of slit lengths and widths. In the deflector, a repulsive optical near field deflecting atoms is excited on a slit edge by coupling of a blue-detuned light beam from a slope of the triangular-pillar part. Thanks to the slit structure, atoms not entering the near-field region are blocked, so that it reduces background signals in observation of the
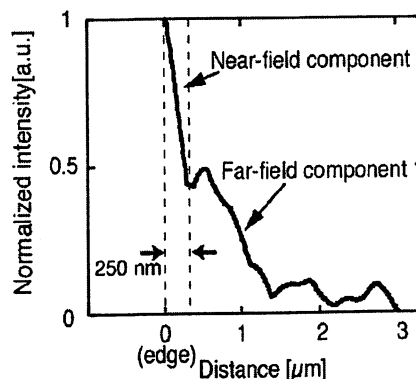
QTuE1 **Fig. 2.** Intensity profile of the optical near field generated near the edge, where the intensity is normalized to the value at the edge. The distance at the half maximum is 250 nm.

deflected atoms with the slit-type detector put behind the deflector. In addition, the linear polarization of the incident light beam is chosen to be perpendicular to the slit-length direction such that there is no cut-off and the intense optical near field can be excited.

We measure the intensity change of the optical near field generated on the slit edge by scanning with a nanometric fiber probe. Figure 2 shows the intensity profile plotted as a function of the distance from the edge. In Fig. 2, the near field component is observed in a region within 250 nm near the edge, while the far-field component appears in the outside region. The large decay length is due to the insufficient metal coating. Since the size of the optical near field determines the atom-manipulation accuracy and the slit width is 100 nm, the decay length should be decreased below 100 nm. It is shown from numerical simulations that the optical near field localized within 100 nm can be generated by increase of the alminum-coating thickness to 20 nm. The fabrication is now in progress.

Based on the result of the intensity-distribution measurement, we estimate the deflection angle θ of a Rb atom with a slow velocity of 10 m/s from the Rutherford-scattering formula.[1] Figure 3 shows the result obtained in the case where the peak intensity of the optical near field and the frequency detuning are 10 W/cm2 and +1.5 GHz, respectively. Here, we assume that the deflection potential is composed of the repulsive dipole-force potential and the attractive van der Waals potential, and that these potentials are cylindrically distributed around the edge. As shown by Fig. 3, the Rb atom can be deflected with an angle of 0.75° from the incident axis, when passing through the repulsive-potential region. On the other hand, the Rb atom is attracted toward the deflector in the case where it goes through the attractive-potential region in the right vicinity of the edge.

1. *Near-Field Nano/Atom Optics and Technology,* M. Ohtsu, ed. (Springer, Tokyo, 1998), Chap. 11.
2. K. Totsuka *et al.,* "Evaluation of near-field optical potential on a nanometric sharpened fiber probe for atom trapping," Technical Digest of QELS 2000, 18 (San Francisco, CA, USA).
3. K. Totsuka *et al.,* "A slit-type near-field optical detector for neutral atoms with high sensitivity and nanometric resolution," Technical Digest of QELS 2001, 110 (Baltimore, MA, USA).

QTuE1 **Fig. 3.** Deflection angle of a Rb atom with a velocity of 10 m/s plotted as a function of the distance from the slit edge.

4. K. Totsuka *et al.*, "High spatial resolution aton detector with two color optical near field," Jpn. J. Appl. Phys. (to be published).
5. T. Yatsui *et al.*, "High-density-speed optical near-field recording-reading with a pyramidal silicon probe on a contact slider," Opt. Lett. 25, 1279 (2000).

Tuesday, May 21

EXCITATION OF A FUNNEL-SHAPE OPTICAL NEAR FIELD BY THE LAGUARRE-GAUSSIAN DOUGHNUT BEAM

S. M. Iftiquar[A], Haruhiko Ito[A,B], Akifumi Takamizawa[B] and Motoichi Ohtsu[A,B]

[A] ERATO Localized Photon Project, Japan Science and Technology Corporation, 687-1-17/4F Tsuruma, Tokyo 194-0004, Japan. E-mail: iftiquar@ohtsu.jst.go.jp

[B] Interdisciplinary Graduate School of Science and Engineering, Tokyo Institute of Technology, 4259 Nagatsuta, Kanagawa 226-8502, Japan

For the precise control of atoms beyond the diffraction limit, we consider the use of optical near fields localized in a nanometer region [1]. In this case, high-density cold atoms are required for effective interaction with the nanometric optical near fields. To this end, we are developing an atom funnel, which makes a cold atomic beam from laser-cooled atoms [2]. The atom funnel is composed of an inverse triangular-pyramidal hollow prism with a 200-microns exit hole. The optical near field produced on the inner-wall surface by a doughnut-shaped light beam reflects and cools atoms falling from a magneto-optical trap and collects them at the bottom under a blue-detuning condition. The doughnut beam with a power of more than 500 mW and a diameter of more than 4 mm are required for efficient funneling of Rb atoms. In addition, the dark centre of 200 microns is needed for avoidance of the spontaneous-emission heating [3]. In this paper, we report the generation of the optical near field using the Laguarre-Gaussian beam with a doughnut mode [4]. Figure 1 shows a cross-sectional image of a doughnut beam with a power of 0.5 W produced from a Gaussian one by means of interference [4] of spherical waves. The beam diameter is 5 mm, while the hollow diameter is about 250 microns. The method of Gouy phase difference used here has several advantages, compared to the conventional ones such as holography. First, the conversion efficiency is up to 50 %. Second, the diameter of the dark centre is variable and can be made below 100 microns. Thanks to these advantages, we can make the special doughnut beam with a large bright ring and a small dark centre. Moreover, it is possible to keep the hollow region over a long distance of more than 200 cm. Since the doughnut beam has an angular moment to the propagation direction, the atoms see the radiation pressure toward the same direction. Consequently, the atoms coming out of the exit hole can be confined by the transverse dipole force and guided by the longitudinal spontaneous force through the doughnut beam to an arbitrary point. Figure 2 shows the intensity profile of the optical near field (evanescent field) produced on a surface by the doughnut beam shown in Fig. 1. The peak intensity is estimated to be more than 5 W/cm^2. Assuming this optical near field, we can show that laser-cooled Rb atom of more than 50 % are converted to an atomic beam with a mean kinetic energy of about 100 microkelvin in terms of temperature. In this case, the atomic flux is estimated to be 10^{13} atom/s cm^2, which satisfies our conditions [3].
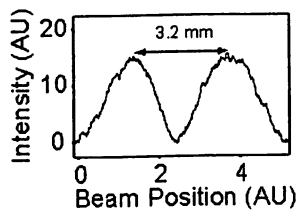
References
[1] Near-Field Nano/Atom Optics and Technology, edited by M. Ohtsu, Chap. 11(Springer, Tokyo,1998)
[2] H. Ito, et al. Phys. Rev. A56 (1997) pp. 712
[3] A. Takamizawa, et al. CLEO/PR2001 pp. I-512
[4] S. M. Iftiquar, et al. Postdeadline paper, CLEO/ Pacific Rim 2001, WJPD1-5, pp. 34.
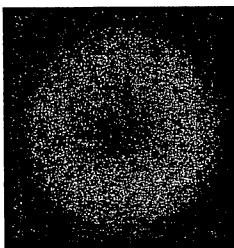
Figure 1
CCD image of a doughnut beam converted from a Gaussuan beam by the interference method.

Figure 2
Cross-sectional intensity profile of an optical near field produced by the doughnut beam

OBSERVATION OF COLD-ATOM REFLECTION IN A NEAR-FIELD OPTICAL FUNNEL

OBSERVATION OF COLD-ATOM REFLECTION IN A NEAR-FIELD OPTICAL FUNNEL

A. Takamizawa[a], S. M. Iftiquer[b], H. Ito[a], M. Ohtsu[a,b]

[a]*Interdisciplinary Graduate School of Science and Engineering, Tokyo Institute of Technology, 4259 Nagatsuta, Midori-ku, Yokohama 226-8502, Japan,*

[b]*ERATO, Japan Science and Technology Corporation, Tenko building 17-4, 687-1 Tsuruma, Machida 194-0004, Japan,*

takami@ae.titech.ac.jp

The use of nanometric optical near fields enables us to manipulate atoms with high spatial accuracy far beyond the diffraction limit [1]. To this end, we need a cold atomic beam with a high flux, which supplies us slow atoms that will efficiently interact with the nanometric optical near field. Here, we report the experimental progress of generating a cold Rb atomic beam by means of a near-field optical funnel composed of a hollow prism [2].

Figure 1 shows the cross section of the near-field optical funnel. A dense cold Rb atom cloud with a density of 10^8 cm^{-3} and a mean temperature of 10 μK is produced by the magneto-optical trap and the polarization-gradient cooling inside the hollow prism with a small exit hole at the bottom. The released cold atoms divergently falling into the prism are repeatedly reflected by the repulsive optical near field excited on the inner-wall surface by a blue-detuned doughnut laser beam shone upward. Moreover, in the process of reflection, they lose their kinetic energy through the Sisyphus cooling mechanism with the help of a repumping laser beam shone downward. Consequently, they are collected at the bottom and go out of the exit hole as a cold atomic beam.

Figure 2 shows the atomic density inside the prism in three cases (Δ: frequency detuning), plotted as a function of the time from after release of cold Rb atoms produced at 5 mm above the exit hole. The atomic density is estimated from monitoring absorption of a weak probe beam introduced along the slope of the inner wall in the vicinity of the surface. Note that we use a Gaussian laser beam with a diameter of 4 mm and a power of 590 mW in order to excite the repulsive optical near field. As shown in Fig. 2, owing to reflection, the number of atoms after 30 ms under blue-detuning conditions increases compared to the case without the optical near field. From the results for various beam diameters and detuning, we find that the optimal beam diameter and detuning for funneling of Rb atoms are 4 mm +0.7 GHz, respectively.

[1] Near-Field Nano/Atom Optics and Technology, edited by M. Ohtsu, Chap. 11 (Springer, Tokyo, 1998)

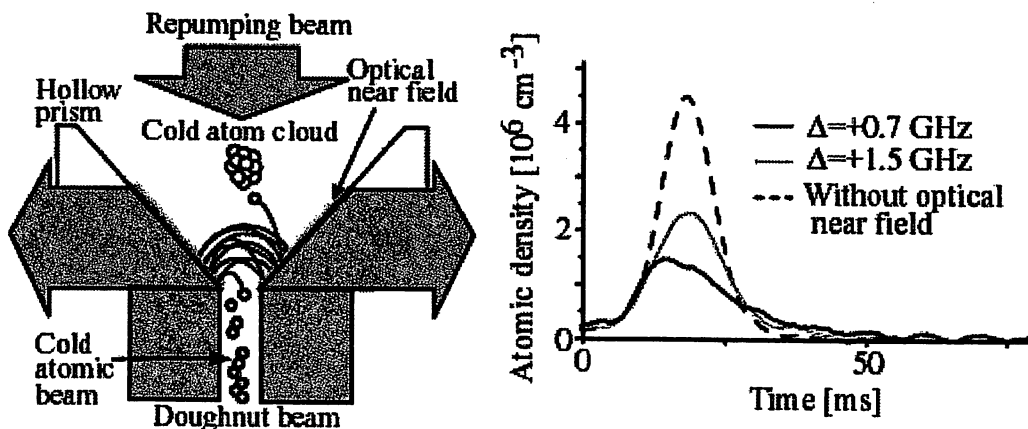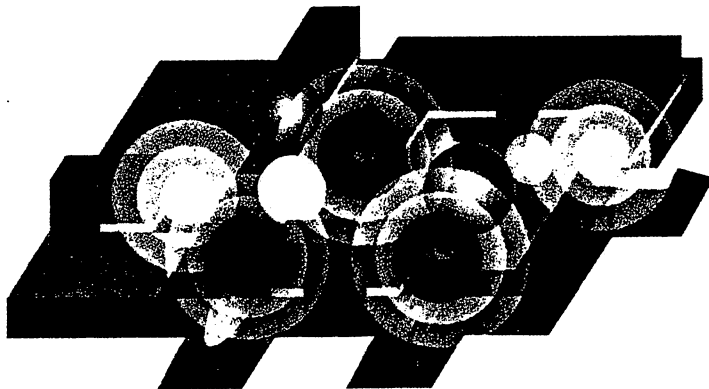[2] H. Ito, K. Sakaki, W. Jhe, M. Ohtsu, Phys. Rev. A 56 712-718 (1997

Fig. 1. Near-field optical funnel.   Fig. 2. Time change of Rb density inside funnel.

10

[I-2] PAPRES IN
NANO PHOTONICS

Metallized pyramidal silicon probe with extremely high throughput and resolution capability for optical near-field technology

T. Yatsui[a)]
Japan Science and Technology Corporation, 687-1 Tsuruma, Machida, Tokyo 194-0004, Japan

K. Itsumi, M. Kourogi,[b)] and M. Ohtsu[b)]
Interdisciplinary Graduate School of Science and Engineering, Tokyo Institute of Technology, 4259 Nagatsuta, Midori-ku, Yokohama 226-8502, Japan

An optical near-field probe with extremely high throughput and resolution capability was fabricated with a metallized pyramidal silicon structure. Using a finite-difference time-domain method, we found the tip parameters that are required for localized surface plasmon resonance at the probe tip. The optical near-field energy distribution on the metallized pyramidal silicon probe was observed by scanning a fiber probe that had an aperture diameter of 50 nm. The spatial distribution profile observed was in good agreement with the numerical results. The throughput and spot size were determined to be 2.3% and 85 nm, respectively. © *2002 American Institute of Physics.*
[DOI: 10.1063/1.1465520]

Near-field optical techniques that involve scanning a metallized fiber probe with a subwavelength aperture have made a remarkable contribution to subwavelength-resolution imaging, spectroscopy, fabrication, memory, and atom manipulation.[1] To improve the spatially resolved spectroscopy, we achieved a tenfold increase in throughput using an edged probe[2] [see Fig. 1(a)]. Since the edged probe has a sharp edge at its foot, the highly efficient excitation of HE-plasmon mode, which is the lowest mode inside the metallized glass core and is localized along the glass core and metal cladding interface,[1] is realized due to scatter coupling. It has been reported that interference of guided modes in the metallic tapered fiber probe results in the maximum electric field intensity and minimum spot size at the cutoff diameter of the modes.[3] By optimizing the interference characteristics and scatter coupling by introducing a triple-tapered structure [see Fig. 1(b)] we achieved a 1000-fold increase in throughput.

Recently, several groups have reported cantilevered near-field optical probes based on micromachining.[4–7] Since cantilevered probes consist of a core with a high refractive index, higher throughput and smaller spot size are realized compared to in conventional fiber probes. However, since they also consist of a dielectric core surrounded by metal, the smallest diameter of the optical beam should be of the order of the skin depth of the metal cladding. In order to realize a narrower beam diameter, a more promising candidate is a metallic probe, through which the surface plasmon mode propagates. Since a metallic core waveguide does not have a cutoff, the beam width decreases with the core diameter.[8]

This is the basis for our optical near-field probe with high throughput and resolution. However, plasmon mode is not easily excited by the mode propagating inside the dielectric core, due to mode mismatching. To overcome this difficulty, we employed a pyramidal silicon probe that is entirely coated with a thin metal film [see Fig. 1(c)]. Due to the high refractive index of the core and the thin metal film, light propagates inside the silicon core and is converted into surface plasmon mode at the metallic tip.

In this letter we report the fabrication of an optical near-field probe with extremely high throughput and small spot size, produced by introducing a pyramidal silicon structure and localized surface plasmon resonance at the metallized probe tip. To confirm the increase in optical near-field energy at the probe's tip, the spatial distribution of the optical near-field energy on the metallized pyramidal silicon probe was observed by scanning a fiber probe that had an aperture. The spatial distribution profile observed indicated that the metallized pyramidal silicon structure had both extremely high throughput and small spot size.

To determine the tip parameters required to increase the optical near-field energy at the probe tip, numerical calculations were carried out using the finite-difference time-domain (FDTD) method.[9] Figure 2(a) shows a schematic diagram of the probe-to-probe method used to measure the spatial distribution of the optical near-field energy of the py-
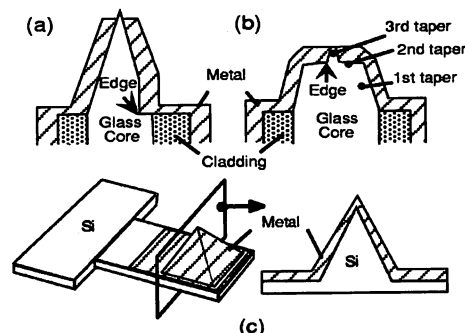

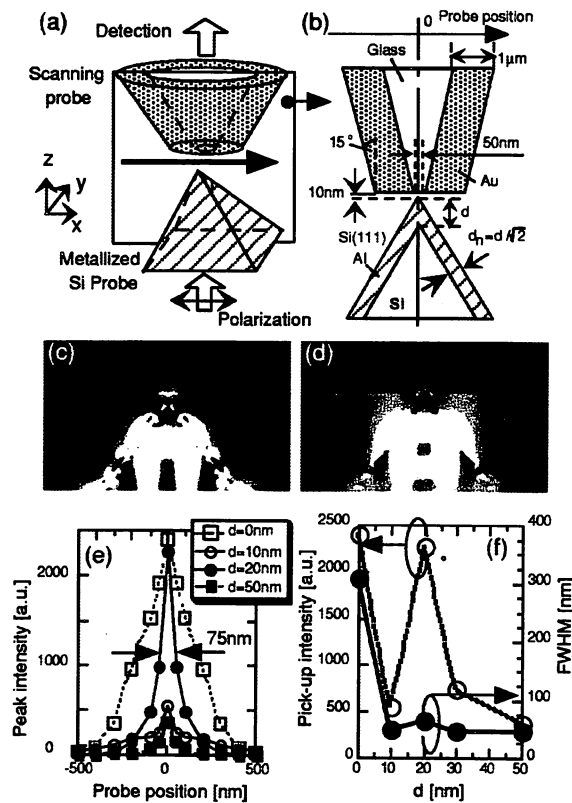FIG. 1. (a) Edged probe. (b) Triple-tapered probe. (c) Proposed metallized pyramidal silicon probe.

FIG. 2. (a) FDTD geometry of the probe-to-probe method. (b) Cross section along the xz plane in (a). d=aluminum thickness. (c), (d) Calculated electric-field energy distributions along the xz plane for d=20 and 0 nm, respectively, when the scanning fiber probe position is 0 nm. Images are 500×800 nm². (e) Thickness dependence of the calculated distributions. (f) Thickness dependence of peak intensity and FWHM in (e).
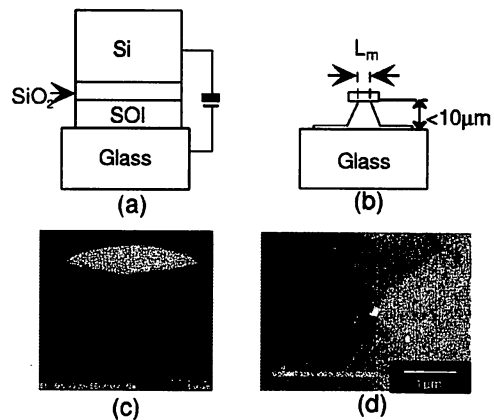

FIG. 3. (a), (b) Schematic of the process used to fabricate the pyramidal silicon probe. SEM images of a pyramidal silicon probe. (c) Bird's-eye view of the probe at step (4). (d) Magnified image of (c).

ramidal silicon probe.[2] Each cell was 10×10×10 nm², and the model consisted of 180×180×150 cells. As shown in Fig. 2(b), the pyramidal silicon probe (refractive index n =3.67 at λ=830 nm) was coated with aluminum film (n =2.74−i8.3),[10] and the four sidewalls were a result of (111) silicon crystal planes. A scanning probe with a glass core (n=1.53) was used to detect the optical near-field energy of the pyramidal silicon probe. The scanning probe had a cone-shaped profile, and was tapered at an angle of 30°. The probe was coated with a 1-μm-thick gold (n=0.19−i5.4) layer, and had an aperture with a diameter D of 50 nm. The separation between the probes was 10 nm. The pyramidal silicon probe was illuminated with linearly polarized light (λ=830 nm).

Figures 2(c) and 2(d) show the calculated distributions along the xz plane of the electric field energy for the metallized pyramidal silicon probe (d=20 nm) and the bare pyramidal silicon probe (d=0 nm), respectively, when the scanning fiber probe position is 0 nm. It can be seen that fields for the metallized probe are strongly enhanced along the sidewalls. Figure 2(e) shows the thickness dependence of the calculated cross-sectional profiles of the detected optical near-field energy. The thickness dependence of the peak energy and full width at half maximum (FWHM) are illustrated in Fig. 2(f). This indicates that the metallized silicon struc-

ture produced a spot size as small as 50 nm ($<\lambda$/10). Furthermore, the peak of the metallized silicon probe (metal thickness d=20 nm) was as great as that of the bare silicon tip (d=0 nm), and the FWHM was 75 nm. Since efficient excitation of the surface plasmon is obtained with a 15-nm-thick aluminum coating ($\approx d/\sqrt{2}$) on silicon in the Kretschmann configuration,[11] this size-dependent feature is attributed to localized surface plasmon resonance.[12,13]

The pyramidal silicon probe was fabricated in four steps

(1) A (100)-oriented silicon-on-insulator (SOI) wafer was bonded to a glass substrate by anodic bonding (300 V, 350 °C, 10 min) [Fig. 3(a)].[14]

(2) After removing the silicon substrate from the SOI wafer by wet etching, the SiO_2 layer was patterned using photolithography.

(3) The probe was fabricated by anisotropic etching (40 g KOH+60 g H_2O+40 g isopropyl alcohol, 80 °C) [Fig. 3(b)]. Maintaining the silicon probe height at less than 10 μm also kept its propagation loss sufficiently low. The mesa length L_m was accurately controlled by the etching time.

(4) After removing the SiO_2 layer, the probe was coated with a 20-nm-thick aluminum layer.

Figures 3(c) and 3(d) show scanning electron microscopic (SEM) images of our sharpened (L_m<10 nm) pyramidal silicon probe with d=20 nm.

The spatial distribution of the optical near-field energy on the pyramidal silicon probe (P_A in Fig. 4) was measured using a scanning probe, i.e., it was scanned with an apertured probe (P_C in Fig. 4) with D=50 nm. The separation between the probes was kept within 10 nm using the shear-force feedback technique. The apertured probe was first sharpened using the selective chemical etching technique.[15] Next, the sharpened core was coated with a 500-nm-thick gold film. Finally, the probe tip was removed by a focused ion beam to form an aperture.[2] For comparison, we also measured the optical near-field energy of a triple-tapered fiber probe with D=60 nm (P_B in Fig. 4), and its throughput was calibrated to be 1.5×10⁻³.[3] As described above, among the fiber probes the triple-tapered fiber probe has the highest

Appl. Phys. Lett., Vol. 80, No. 13, 1 April 2002
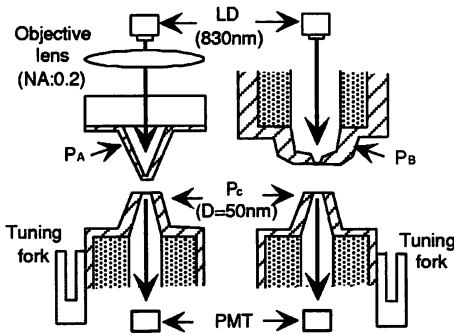
Yatsui *et al.*   2259

FIG. 4. Schematic of the probe-to-probe method. P_A : pyramidal silicon probe, P_B : triple-tapered fiber probe with $D = 60$ nm, P_C : apertured fiber probe with $D = 50$ nm.

throughput, due to interference characteristics of the guided modes and scatter coupling.

Figures 5(a)–5(c) show spatial distributions of the optical near-field energy observed for the metallized pyramidal silicon probe ($d = 20$ nm), the bare pyramidal silicon probe ($d = 0$ nm), and the triple-tapered fiber probe with $D = 60$ nm, respectively. Curves A, B, and C in Fig. 5(d) are cross-sectional profiles along the dashed white lines in Figs. 5(a)–5(c), respectively. Note that the FWHM of the metallized pyramidal silicon probe is 85 nm ($\sim \lambda/10$), which is in good agreement with the value in Fig. 2(e). Furthermore, the
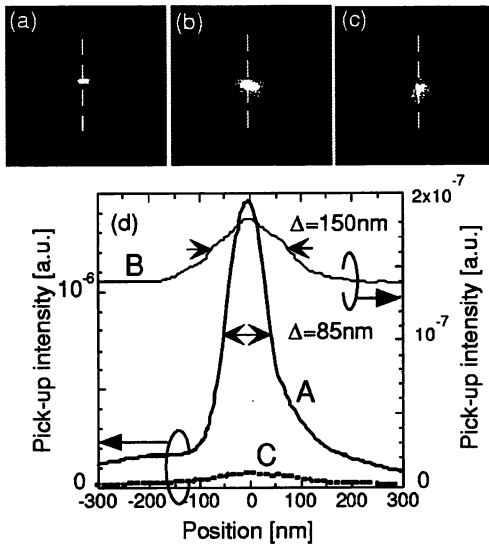
FIG. 5. Observed spatial distributions of the optical near-field energy of the (a) metallized pyramidal silicon probe ($d = 20$ nm), (b) bare pyramidal silicon probe ($d = 0$ nm), and (c) triple-tapered probe with $D = 60$ nm. Images are $1.5 \times 1.5 \ \mu m^2$. (d) Curves A, B, and C are the cross-sectional profiles along the dashed white lines in (a)–(c), respectively.

peak intensity of the metallized pyramidal silicon probe is 5 and 15 times larger than those of the bare pyramidal silicon and the triple-tapered probes, respectively. Such effective excitation of the optical near field by the metallized silicon probe is attributed to localized surface plasmon resonance. These results indicate that the metallized pyramidal silicon structure resulted in high throughput (2.3%) and high resolution (85 nm) simultaneously. Considering the aperture diameter ($D = 50$ nm) of the fiber probe used for detection, the metallized pyramidal silicon probe ($d = 20$ nm) should have the capability of higher resolution; 50 nm or better should be possible.

In conclusion, we have devised and fabricated an optical near-field probe with extremely high throughput and resolution capability by introducing a pyramidal silicon structure and localized surface plasmon resonance at the metallized probe tip. Using the probe-to-probe method, it was confirmed that high throughput and small spot size were achieved simultaneously with the metallized pyramidal silicon probe. Since our near-field optical storage/read-out system realized the shortest mark length of 110 nm and a carrier-to-noise ratio of 10 dB, corresponding to a data transmission rate of 2.0 MHz, using the metallized pyramidal silicon probe with $L_m = 150$ nm ($\lambda = 830$ nm),[16] our results indicate that shortening the mark length to sub-100 nm should improve the performance of near-field optical data storage systems.

[1] *Near-field Nano/Atom Optics and Technology*, edited by M. Ohtsu (Springer, Tokyo, 1999).
[2] T. Yatsui, M. Kourogi, and M. Ohtsu, Appl. Phys. Lett. 71, 1756 (1997).
[3] T. Yatsui, M. Kourogi, and M. Ohtsu, Appl. Phys. Lett. 73, 2090 (1998).
[4] W. Noell, M. Abraham, K. Mayr, A. Ruf, J. Barenz, O. Hollricher, O. Marti, and P. Güthner, Appl. Phys. Lett. 70, 1236 (1997).
[5] S. Heisig, H.-U. Danzebrink, A. Leyk, W. Mertin, S. Münster, and E. Oesterschulze, Ultramicroscopy 71, 99 (1998).
[6] H.-U. Danzebrink, A. Castiaux, C. Girard, X. Bouju, and G. Wilkening, Ultramicroscopy 71, 371 (1998).
[7] R. Eckert, J. M. Freyland, H. Gersen, H. Heinzelmann, G. Schürmann, W. Noell, U. Staufer, and N. F. de Rooij, Appl. Phys. Lett. 77, 3695 (2000).
[8] J. Takahara, S. Yamagishi, H. Taki, A. Morimoto, and T. Kobayashi, Opt. Lett. 22, 475 (1997).
[9] S. Mitsugi, Y. J. Kim, and K. Goto, Opt. Rev. 8, 120 (2001).
[10] *Handbook of Optical Constants of Solids*, edited by E. D. Palik (Academic, New York, 1985).
[11] *Surface Plasmons*, edited by H. Raether (Springer, Berlin, 1988).
[12] G. T. Boyd, T. Rasing, J. R. R. Leite, and Y. R. Shen, Phys. Rev. B 30, 519 (1984).
[13] U. C. Fischer, J. Koglin, and H. Fuchs, J. Microsc. (Paris) 176, 231 (1994).
[14] T. R. Anthony, J. Appl. Phys. 58, 1240 (1985).
[15] T. Pangaribun, K. Yamada, S. Jiang, H. Ohsawa, and M. Ohtsu, Jpn. J. Appl. Phys., Part 2 31, L1302 (1992).
[16] T. Yatsui, M. Kourogi, K. Tsutsui, J. Takahashi, and M. Ohtsu, Opt. Lett. 25, 1279 (2000).

13

Observation of size-dependent features in the photoluminescence of zinc oxide nanocrystallites by near-field ultraviolet spectroscopy

T. Yatsui[a] and T. Kawazoe
Japan Science and Technology Corporation, 687-1 Tsuruma, Machida, Tokyo, Japan 194-0004

T. Shimizu, Y. Yamamoto, M. Ueda, M. Kourogi,[b] and M. Ohtsu[b]
Interdisciplinary Graduate School of Science and Engineering, Tokyo Institute of Technology, 4259 Nagatsuta, Midori-ku, Yokohama, Kanagawa, Japan 226-8502

G. H. Lee
Department of Advanced Materials Engineering, Dong-Eui University, Gaya-Dong 24, Pusanjin-Ku, Pusan, Korea, 614-714

The optical properties of single zinc oxide (ZnO) nanocrystallites were investigated at room temperature by extending the optical near-field technique to the UV region. Using a UV fiber probe with a subwavelength aperture, we performed spatially- and spectrally-resolved photoluminescence (PL) imaging of individual ZnO nanocrystallites with a spatial resolution of 55 nm. Furthermore, decreasing the spot size increased the intensities of higher-energy components of the PL spectrum due to the quantum size effect. © *2002 American Institute of Physics.* [DOI: 10.1063/1.1453487]

ZnO is a promising candidate for future optical applications of UV-light-emitting devices. It has a wide band gap of 3.37 eV and a larger exciton binding energy (60 meV) than those of GaN (28 meV) or ZnSe (19 meV). Recently, several groups have reported room-temperature UV lasing.[1-3] Furthermore, quantum-confinement-induced energy gap enhancement has been reported using ZnO nanocrystallites with 20–60 nm grain sizes.[3]

The application of single ZnO nanocrystallites to these devices requires lateral integration with nanometer-scale resolution. This requirement can be met by near-field optical chemical vapor deposition (NFO-CVD), because the size and positioning is controlled by scanning a fiber probe.[4] Recently, high-quality ZnO nanocrystallites were fabricated by conventional optical CVD,[5] in which UV light irradiation accelerated the oxidation of gas-phase diethylzinc (DEZ).[6] To obtain high-quality ZnO, however, the substrate must be heated to 150 °C,[5] which results in thermal drift of the substrate and probe. To deposit a smaller ZnO dot, this drift must be reduced sufficiently. Furthermore, the substrate temperature should be kept lower than 200 °C, to avoid thermal dissociation of a source gas such as a gas-phase DEZ.[7] This thermal dissociation must be reduced sufficiently in order to deposit isolated ZnO nanocrystallites.

To evaluate the optical properties and crystallinity of ZnO nanocrystallites, the optical properties of nanometer-scale ZnO structures must be measured with nanoscale resolution. Recently, we undertook individual ZnO nanocrystallite spectroscopy using an optical near-field technique.[8] Using a UV fiber probe with a subwavelength aperture, we found that emission intensity depended on topography and crystal orientation. Since the grain sizes were 100 times larger than the exciton Bohr radius of ZnO, we did not ob-

serve a shift in the peak energy in the photoluminescence (PL) spectrum due to the quantum size effect.

Using an optical near-field technique, we present size-dependent features of individual ZnO nanocrystallites. With decreasing spot size, an increase in the intensities of higher-energy components of the PL spectrum was observed. This is considered evidence of an increase in the energy gap due to the quantum confinement effect.

Figure 1 shows the experimental setup used for conventional far-field PL spectroscopy [Fig. 1(a)] and spatially and spectrally resolved near-field PL spectroscopy [Fig. 1(b)]. He–Cd laser light ($\lambda = 325$ nm) was used to excite the ZnO nanocrystallites. The PL signal was detected by a cooled charge coupled device through a monochromator. A fiber probe with an 80 nm aperture diameter was used for near-field PL spectroscopy. As the fiber probe, we used a UV fiber
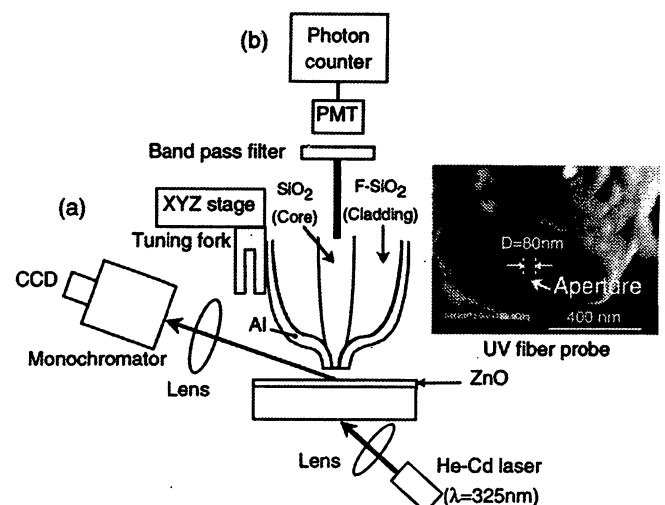

FIG. 1. Experimental setup used for far-field PL spectroscopy (a) and spatially and spectrally resolved near-field PL spectroscopy (b). Inset: UV fiber probe with $D = 80$ nm.

Appl. Phys. Lett., Vol. 80, No. 8, 25 February 2002

Yatsui et al.   1445

FIG. 2. Topographical image of polycrystalline ZnO.

FIG. 3. Far-field PL spectra of polycrystalline ZnO at room temperature [see Fig. 1(a)].
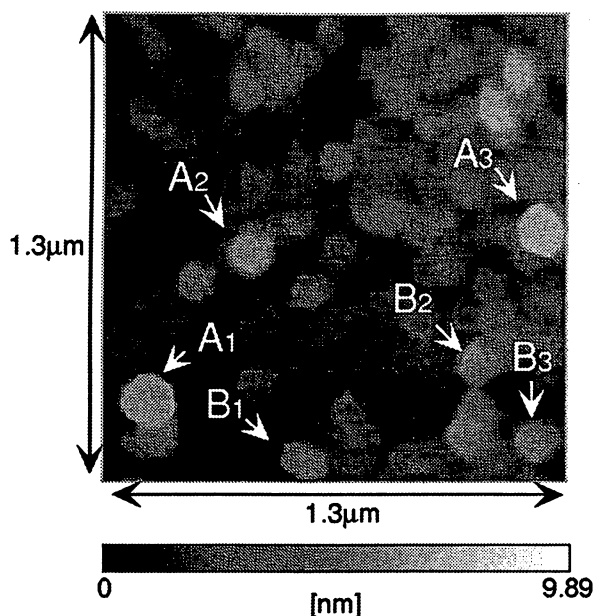
probe with a pure silica core and fluorine-doped cladding. To fabricate this probe, the fiber was first sharpened, using a pulling/etching technique, to realize a cone angle of 60° and an apex diameter of less than 10 nm.[9] Next, the sharpened core was coated with a 500 nm-thick aluminum film. Finally, the top of the core was removed with a focused ion beam to form an aperture. For spatially and spectrally resolved imaging, the signal collected through the fiber probe and band pass filter was focused on a photomultiplier tube to count the number of photons [Fig. 1(b)]. The fiber probe was kept near the sample surface ($\sim$ 10 nm) using the shear-force feedback technique.

ZnO nanocrystallites were prepared by oxidizing zinc (Zn) deposited by optical CVD. First, 200 nm-thick Zn nanocrystallites were grown on a sapphire (0001) substrate at room temperature by optical CVD. Gas-phase DEZ was used as a gas source, where the partial pressure of DEZ was 10 mTorr, in order to deposit sub-100 nm scale grains. Since DEZ gas has a strong absorption at $\lambda < 270$ nm, the second harmonic (SH) light of an Ar^+ laser ($\lambda = 244$ nm) was used as the light source for the photodissociation of DEZ.[10] The power and spot size of the SH light were 10 mW and 600 μm, respectively. Since the Zn is deposited at room temperature, this method is applicable to NFO-CVD, as it avoids thermal drift of the substrate and the probe and also avoids the thermal dissociation of gas-phase DEZ. Second, the deposited Zn nuclei were thermally oxidized in ambient oxygen at 1 atm and 750 °C for 30 min.[3]

Figure 2 shows a shear-force image of oxidized Zn, obtained using a sharpened-fiber probe with an apex diameter of 100 nm. Hexagonal (A_1, A_2, and A_3) and square (B_1, B_2, and B_3) nanocrystallites can be seen. This proves that oxidized Zn is composed of many nanocrystallites with various orientations. The grain sizes were in the range of 30–160 nm.

Figure 3 shows a far-field PL spectrum obtained by focused light with spot of 10 μm at room temperature [see Fig. 1(a)]. The emission peak energy was close to the reported value of 3.26 eV ($\lambda = 380$ nm), which corresponds to spon-
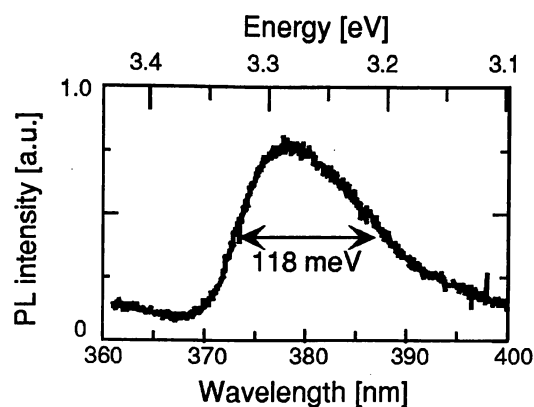
taneous emission from the free exciton in high-quality ZnO nanocrystallites.[2] The full width at half maximum (FWHM) of the PL spectra was about 118 meV, which is comparable with the 117 meV of molecular-beam epitaxy grown ZnO nanocrystallites at room temperature.[11] These results imply that the oxidized Zn was composed of high-quality ZnO nanocrystallites. Furthermore, since ZnO has a wurtzite structure, the hexagonal and square nanocrystallites shown in Fig. 2 represent nanocrystallites oriented along the c axis[1] and in other directions, respectively. These results imply that fabricated ZnO nanocrystallites are polycrystalline.

To examine the optical properties of a single ZnO nanocrystallite, we performed spatially and spectrally resolved PL spectroscopy [see Fig. 1(b)]. Figures 4(a) and 4(b) show monochromatic PL images, in which the respective detection wavelengths were 370 ± 2.5 nm and 380 ± 2.5 nm. The closed and open circles in Fig. 4(c) represent cross sectional profiles along the broken lines through spots s_{1a} and s_{1b} in Figs. 4(a) and 4(b), respectively. Those in Fig. 4(d) are for spots s_{2a} and s_{2b} in Figs. 4(a) and 4(b), respectively. Note that the FWHM of spots s_{1a} and s_{2a} with a detection wavelength of 370 nm was 155 and 55 nm, respectively, which is comparable to the grain sizes of ZnO nanocrystallites (see Fig. 2). This indicates that each emission spot originated from an individual ZnO nanocrystallite.

Furthermore, the PL intensity (I_{PL}) of spot s_{1b} for a detection wavelength of 380 nm was twice that of s_{1a} at 370 nm, whereas that of spot s_{2b} for a detection wavelength of 380 nm was comparable to that of s_{2a} at 370 nm. To examine such size-dependent features in PL of individual ZnO nanocrystallites more quantitatively, we compared the I_{PL} value for several spots. Figure 5 shows the respective relative PL intensity I_{PLR} [$= (I_{PL}$ at a detection wavelength of 370 ± 2.5 nm)/(I_{PL} at a detection wavelength of 380 ± 2.5 nm)] of ZnO nanocrystallites, where the spot sizes were estimated from the FWHM in Fig. 4(a). Although the spatial resolution of the shear-force image may not be sufficiently high for accurately determining the grain size of ZnO nanocrystallites, it should be noted that several spot sizes in Fig. 5 are much smaller than the aperture diameter (80 nm) of the fiber probe. Furthermore, an outstanding feature of Fig. 5 is that the I_{PLR} is larger for a smaller spot size. This originates from nanocrystallites with a higher PL peak energy due to the quantum size effect in ZnO nanocrystallites. Although this
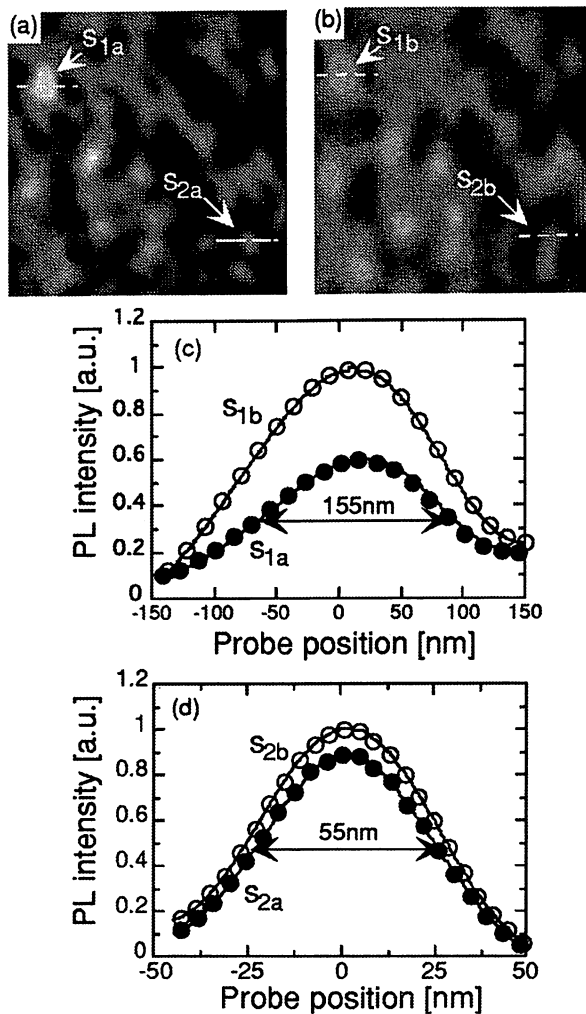
FIG. 4. Monochromatic PL images of polycrystalline ZnO obtained at wavelengths of (a) 370 and (b) 380 nm. The images are 1.25×1.25 μm. (c) Closed and open circles represent cross-sectional profiles along the dashed lines through spots s_{1a} and s_{1b}. (d) Closed and open circles represent cross sectional profiles along the dashed lines through spots s_{2a} and s_{2b}.

FIG. 5. Relative PL intensity (I_{PLR}) [$=(I_{PL}$ at 370±2.5 nm)/(I_{PL} at 380 ±2.5 nm)] of ZnO nanocrystallites as a function of spot size.

with a subwavelength aperture, we performed spatially and spectrally resolved PL imaging of individual ZnO nanocrystallites with a spatial resolution as high as 55 nm. We found that as the spot size decreased, the intensities of higher energy components of the PL spectrum increased, due to the quantum size effect in ZnO nanocrystallites. By applying the ZnO deposition technique reported here to NFO-CVD, the fabrication and integration of nanometer-scale photonic devices are expected.

size-dependent feature of the PL intensity has been evaluated for an ensemble of nanocrystallites using a conventional diffraction-limited optical method,[3] our results are the first to evaluate individual nanocrystallites using an optical near-field method.

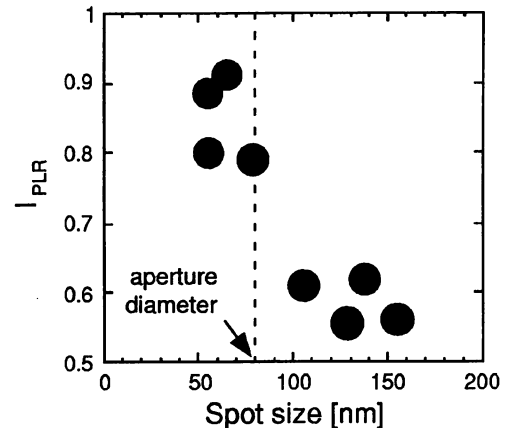In summary, we investigated the size-dependent features of individual ZnO nanocrystallites. Using a UV fiber probe

[1] Z. K. Tang, G. K. L. Wong, P. Yu, M. Kawasaki, A. Ohtomo, H. Koinuma, and Y. Segawa, Appl. Phys. Lett. 72, 3270 (1998).

[2] D. M. Bagnall, Y. F. Chen, Z. Zhu, T. Yao, M. Y. Shen, and T. Goto, Appl. Phys. Lett. 73, 1038 (1998).

[3] S. Cho, J. Ma, Y. Kim, Y. Sun, G. Wong, and J. B. Ketterson, Appl. Phys. Lett. 75, 2761 (1999).

[4] Y. Yamamoto, M. Kourogi, M. Ohtsu, V. Polonski, and G. H. Lee, Appl. Phys. Lett. 76, 2173 (2000).

[5] G. H. Lee, Y. Yamamoto, M. Kourogi, and M. Ohtsu, Thin Solid Films 386, 117 (2001).

[6] M. Shimizu, H. Kamei, M. Tanizawa, T. Shiosaki, and A. Kawabata, J. Cryst. Growth 89, 365 (1988).

[7] Y. Kunita, Y. Deguchim, and M. Ichida, Appl. Organomet. Chem. 5, 337 (1991).

[8] T. Yatsui, T. Shimizu, Y. Yamamoto, M. Kourogi, M. Ohtsu, and G. H. Lee, Appl. Phys. Lett. 79, 2369 (2001).

[9] Near-Field Nano/Atom Optics and Technology, edited by M. Ohtsu, (Springer, Tokyo, 1999), Chap. 3.

[10] R. R. Krchnavek, H. H. Gilgenm, J. C. Chenm, P. S. Shaw, T. J. Licata, and R. M. Osgood, J. Vac. Sci. Technol. B 5, 20 (1987).

[11] Y. Chen, D. M. Bagnall, H. J. Ko, K. T. Park, H. Hiraga, Z. Zhu, and T. Yao, J. Appl. Phys. 87, 3912 (1998).

Direct Observation of Optically Forbidden Energy Transfer between CuCl Quantum Cubes via Near-Field Optical Spectroscopy

Tadashi Kawazoe,[1] Kiyoshi Kobayashi,[1] Jungshik Lim,[2] Yoshihito Narita,[3] and Motoichi Ohtsu[1,2]

[1]*Exploratory Research for Advanced Technology, Japan Science and Technology Corporation,
687-1 Tsuruma, Machida, Tokyo 194-0004, Japan*

[2]*Interdisciplinary Graduate School of Science and Engineering, Tokyo Institute of Technology,
4259 Nagatsuta, Midori-ku, Yokohama 226-8502, Japan*

[3]*JASCO Corporation, 2967-5, Ishikawa-cho, Hachioji, Tokyo, 192-8537, Japan*

We report, for the first time, evidence of near-field energy transfer among CuCl quantum cubes using an ultrahigh-resolution near-field optical microscopy and spectroscopy in the near UV region at 15 K. The sample was high-density CuCl quantum cubes embedded in a NaCl matrix. Measured spatial distributions of the luminescence intensities from 4.6-nm and 6.3-nm quantum cubes clearly established anticorrelation features. This is thought to be a manifestation of the energy transfer from the lowest state of exciton in 4.6-nm quantum cubes to the first dipole-forbidden excited state of exciton in 6.3-nm quantum cubes, which is attributed to the resonant optical near-field interaction.

Observations of a single quantum dot have recently become possible using near-field optical spectroscopy [1,2] and microluminescence spectroscopy [3,4]. Spectroscopy of individual quantum dots is one of the most important topics of nanostructure physics, and several extraordinary phenomena have been reported, such as intermittent luminescence [5] and long coherent time [6]. The coupled quantum-dots system exhibits more unique properties (e.g., the Kondo effect [7,8], Coulomb blockade [9,10], and breaking the Kohn theorem [11]) in contrast with the single quantum-dot system. The quantum dots system reveals a variety of interactions such as carrier tunneling [7–10], Coulomb coupling [11], spin interaction [12], and so on. Investigation of interactions among quantum dots is important not only for deep understanding of the various physical phenomena but also for developing novel functional devices [7–12]. The optical near-field interaction [1] is of particular interest, as it can govern the coupling strength among quantum dots.

Recently, Mukai *et al.* reported ultrafast "optically forbidden" energy transfer from an outer ring of loosely packed bacteriochlorophyll molecules, called B800, to an inner ring of closely packed bacteriochlorophyll molecules, called B850, in the light-harvesting antenna complex of photosynthetic purple bacteria [13]. They theoretically showed that this transfer is possible when the point transition dipole approximation is violated due to the size effect of B800 and B850. From our viewpoint, this energy transfer is due to the optical near-field interaction between B800 and B850. Similarly, the energy can be transferred from one dot to another by the optical near-field interaction for the quantum dots system, even if it is a dipole-forbidden transfer.

CuCl quantum cubes (QCs) embedded in NaCl have the potential to be an optical near-field coupling system

that exhibits this optically forbidden energy transfer. This is because, for this system, another possibility of energy transfer, such as carrier tunneling, Coulomb coupling, and so on, can be neglected, because carrier wave function is localized in QCs due to a deep potential depth of more than 4 eV and the Coulomb interaction is weak due to small exciton Bohr radius of 0.68 nm. Conventional optical energy transfer is also negligible, since the energy levels of nearly perfect cubic CuCl QCs are optically forbidden, and are confined to the energy levels of exciton with an even principal quantum number [14]. However, Sakakura *et al.* observed the optically forbidden transition in a hole-burning experiment using CuCl QCs [15]. Although they attributed the transition to an imperfect cubic shape, the experimental and simulation results did not show such imperfection. We believe that the transition was due to the energy transfer between the CuCl QCs, via the optical near-field interaction similar to the optically forbidden energy transfer between B800 and B850 in the above-mentioned photosynthetic system. Thus far, this type of energy transfer has not been directly observed. This Letter reports the direct observation of energy transfer from the exciton state in a CuCl QC to the optically forbidden exciton state in another CuCl QC by optical near-field spectroscopy.

It is well known that translational motion of the exciton center of mass is quantized due to the small exciton Bohr radius for CuCl quantum dots, and that CuCl quantum dots become cubic in a NaCl matrix [15–17]. The potential barrier of CuCl QCs in a NaCl crystal can be regarded as infinitely high, and the energy eigenvalues for the quantized Z_3 exciton energy level (n_x, n_y, n_z) in a CuCl QC with the side length of L are given by

$$E_{n_x,n_y,n_z} = E_B + \frac{\hbar^2 \pi^2}{2M(L - a_B)^2} (n_x^2 + n_y^2 + n_z^2), \quad (1)$$

where E_B is the bulk Z_3 exciton energy, M is the translational mass of exciton, a_B is its Bohr radius, n_x, n_y, and n_z are quantum numbers ($n_x, n_y, n_z = 1, 2, 3, \ldots$), and $d = (L - a_B)$ corresponds to an effective side length found through consideration of the dead layer correction [15]. The exciton energy levels with even quantum numbers are dipole-forbidden states, that is, optically forbidden [14]. However, the optical near-field interaction is finite for such energy levels [18].

According to Eq. (1), there exists a resonance between the quantized exciton energy level of quantum number (1, 1, 1) for the QCs with effective side length d and the quantized exciton energy level of quantum number (2, 1, 1) for the QCs with effective side length $\sqrt{2}\,d$. For this type of resonant condition, the coupling energy of the optical near-field interaction is given by the following Yukawa function [1,18]:

$$V(r) = A\,\frac{\exp(-\mu r)}{r}. \tag{2}$$

Here r is the separation between two QCs, A is the coupling coefficient, and the effective mass of the Yukawa function μ is given by

$$\mu = \frac{\sqrt{2E_{n_x,n_y,n_z}(E_{\mathrm{NaCl}} + E_{n_x,n_y,n_z})}}{\hbar c}, \tag{3}$$

where E_{NaCl} is the exciton energy of a NaCl matrix. The value of the coupling coefficient A depends on each experimental condition; however, we estimate it from the result of the previous work on the interaction between a Rb atom and the optical near-field probe tip [18]. The value for A for 5-nm CuCl QCs is found to be more than 10 times larger than that for the Rb-atom case, since the coupling coefficient A is proportional to the oscillator strength and square of the photon energy [18,19]. Assuming that the separation r between two QCs is equal to 10 nm, the coupling energy $V(r)$ is the order of 10^{-4} eV. This corresponds to a transition time of 40 ps, which is much shorter than the exciton lifetime of a few ns. In addition, intersublevel transition τ_{sub}, from higher exciton energy levels to the lowest one, is generally less than a few ps and is much shorter than the transition time due to optical near-field coupling [20]. Therefore, most of the energy of the exciton in a CuCl quantum cube with the side length of d transfer to the lowest exciton energy level in the neighboring quantum cubes with a side length of $\sqrt{2}\,d$ and recombine radiatively in the lowest level.

We fabricated CuCl QCs embedded in a NaCl matrix by the Bridgman method and successive annealing, and found the average size of the QCs to be 4.3 nm. The sample was cleaved just before the near-field optical spectroscopy experiment in order to keep the sample surface clean. The cleaved surface of the sample with 100-μm-thick sample was sufficiently flat for the experiment; i.e., its roughness

was less than 50 nm, at least within a few μm squares. A 325-nm He-Cd laser was used as a light source. A double-tapered fiber probe was fabricated by chemical etching and a 150-nm gold coating was applied [21]. A 50-nm aperture was fabricated by the pounding method [22].

The curve in Fig. 1(a) shows a far-field luminescence spectrum of the sample that was recorded with a probe-sample separation of 3 μm in the collection-mode operation [1] of the cryogenic near-field optical microscope at 15 K. It represents the collective luminescence intensity from several CuCl QCs, and is inhomogeneously broadened owing to the size distribution of the QCs. Figure 1(b) represents the differential spectrum, which is the intensity difference between luminescence measured with probe-sample separations of 3 μm and of less than 10 nm. This curve consists of many fine structures. These appear as the contribution of the QCs near the apex of the probe because of the drastic increase in the measured luminescence intensity for a probe-sample separation less than 10 nm. The average density of the QCs is 10^{17} cm^{-3}. Thus, the average separation between the QCs is less than 30 nm, estimated from the concentration of CuCl. Therefore, the spectral peaks in Fig. 1(b), obtained by near-field measurement using the 50-nm aperture fiber probe, originate from several QCs of different size. Among these, the peaks X and Y correspond to the confined Z_3-exciton energy levels of quantum number (1, 1, 1) for the QCs with side lengths (L) of 4.6 and 6.3 nm, respectively. Their effective side lengths d are 3.9 and 5.6 nm, whose size
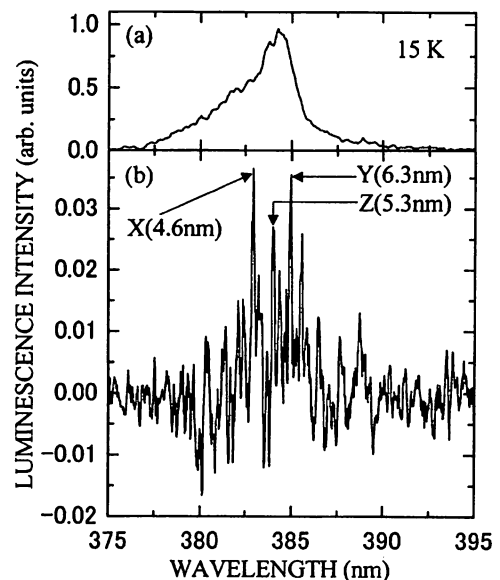

FIG. 1. (a) Far-field luminescence spectrum of a sample recorded with probe-sample separation of 3 μm for the collection-mode operation at 15 K. (b) The differential luminescence spectrum, which is the intensity difference between luminescence measured with the probe-sample separations of 3 μm and of less than 10 nm. X, Y, and Z correspond to the wavelengths of lowest exciton state in quantum cubes with the side lengths of 4.6, 6.3, and 5.3 nm, respectively.

ratio is close to $1:\sqrt{2}$, and thus the $(1,1,1)$ and $(2,1,1)$ quantized exciton levels are resonant with each other to be responsible for energy transfer between the QCs.

Figures 2(a) and 2(b) show the spatial distributions of the luminescence intensity, i.e., near-field optical microscope images, for peaks X and Y in Fig. 1(b), respectively. The spatial resolution, which depends on the aperture diameter of the near-field probe, was smaller than 50 nm. These images clearly establish anticorrelation features in their intensity distributions, as manifested by the dark and bright regions surrounded by white broken curves. In order to confirm the anticorrelation feature more quantitatively, Fig. 3 shows the values of the cross-correlation coefficient C between the spatial distribution of the intensity of the luminescence emitted from the (n_x, n_y, n_z) level of exciton in a QC with 6.3-nm side length and that from the $(1,1,1)$ level in a QC with a different side length L. They have been normalized to that of the autocorrelation coefficient of the luminescence intensity from the $(1,1,1)$ level in a

6.3-nm QC, which is identified by an arrow (1) in Fig. 3. To calculate the values of C, spatial Fourier transform was performed on the series of luminescence intensity values in the chain of pixels inside the region surrounded by the broken white curves in Fig. 2. The large negative value of C identified by an arrow (2) clearly shows the anticorrelation feature between Figs. 2(a) and 2(b), i.e., between the $(2,1,1)$ level in a 6.3-nm QC and the $(1,1,1)$ level in a 4.6-nm QC.

This anticorrelation feature can be understood by noting that these spatial distributions in luminescence intensity represent not only the spatial distributions of the QCs, but also some kind of resonant interaction between the QCs. This interaction induces energy transfer from X cubes ($L = 4.6$ nm) to Y cubes ($L = 6.3$ nm). Interpreting this, most of the 4.6-nm QCs "accidentally" located close to 6.3-nm QCs cannot emit light, but instead transfer the energy to the 6.3-nm QCs. As a result, in the region containing embedded 6.3-nm QCs, the luminescence intensity in Fig. 2(a) from 4.6-nm QCs is low, while the corresponding position in Fig. 2(b) is high. As we mentioned above, it is reasonable to attribute the origin of the
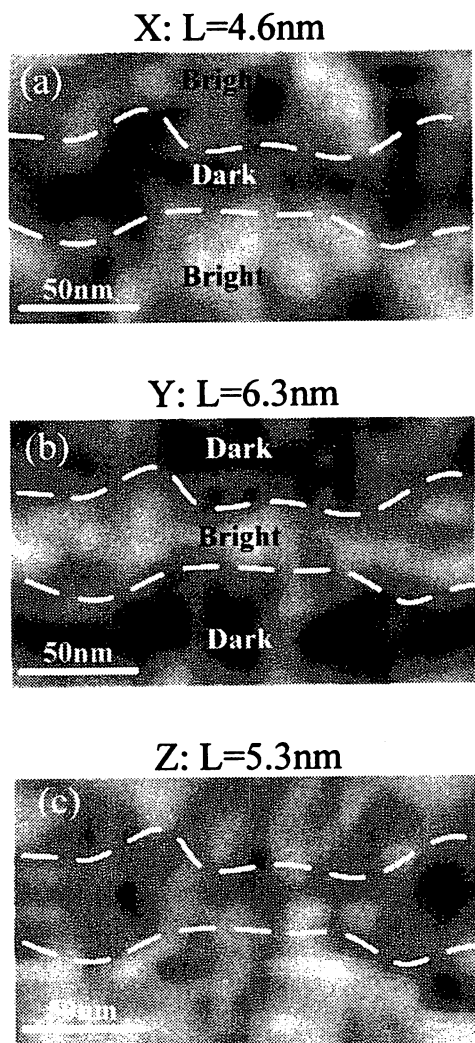
X: L=4.6nm

Y: L=6.3nm

Z: L=5.3nm

FIG. 2. Spatial distributions of the near-field luminescence intensity for peaks marked as X, Y, and Z in Fig. 1(b), respectively.
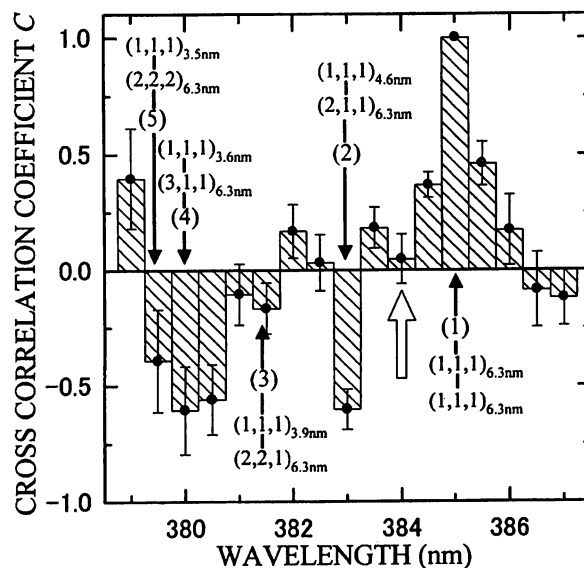

FIG. 3. Values of the cross-correlation coefficient C between the spatial distribution of the intensity of the luminescence emitted from the (n_x, n_y, n_z) level of exciton in a QC with 6.3-nm side length and that from the $(1,1,1)$ level in a QC with the different side length L. They have been normalized to that of the autocorrelation coefficient of the luminescence intensity from the $(1,1,1)$ level in a 6.3-nm QC, which is identified by an arrow (1). The other four arrows (2)–(5) represent the cross-correlation coefficient C between higher levels in a 6.3-nm QC and other sized QCs. They are between (2) the $(2,1,1)$ level in a 6.3-nm QC and the $(1,1,1)$ level in a 3.9-nm QC, (3) the $(2,2,1)$ level in a 6.3-nm QC and the $(1,1,1)$ level in a 3.9-nm QC, (4) the $(3,1,1)$ level in a 6.3-nm QC and the $(1,1,1)$ level in a 3.6-nm QC, and (5) the $(2,2,2)$ level in a 6.3-nm QC and the $(1,1,1)$ level in a 3.5-nm QC. For reference, a white arrow represents the value of C between the $(2,1,1)$ level in a 6.3-nm QC and the nonresonant $(1,1,1)$ level in a 5.3-nm QC.

interaction to the near-field energy transfer. Besides, anti-correlation features appear for every couple of QCs with different sizes satisfying the resonant conditions of the confinement exciton energy levels. Therefore, we claim the first observation of energy transfer between QCs via the optical near field.

For reference, we note the dark area outside the broken curves in Fig. 2(b). This occurs because there are very few 6.3-nm QCs. From the absorption spectrum of the sample, it is estimated that the population of 6.3-nm QCs is one-tenth the population of 4.6-nm QCs. As a result, the corresponding area in Fig. 2(a) is bright due to absence of the energy transfer.

On the other hand, the spatial distributions of the luminescence intensities from other QCs whose sizes do not satisfy the resonant condition given by Eq. (1) did not show any anticorrelation features. This is confirmed by comparing Figs. 2(a), 2(b), and 2(c). Here Fig. 2(c) shows the spatial distribution of the luminescence intensity of peak Z in Fig. 1(b), which corresponds to QCs with a side length of 5.3 nm. The white arrow in Fig. 3 indicates the relationship between Figs. 2(b) and 2(c). The negligibly small value of C identified by this arrow proves the absence of the anticorrelation feature between the exciton energy levels in a 6.3-nm QC and the $(1,1,1)$ level in a 5.3-nm QC due to their nonresonant condition.

Furthermore, arrows (3)–(5) also represent clearly large negative values of C, which means the existence of the anticorrelation feature between higher levels in 6.3-nm QC and other sized QCs. They are (3) the $(2,2,1)$ level in a 6.3-nm QC and the $(1,1,1)$ level in a 3.9-nm QC, (4) the $(3,1,1)$ level in a 6.3-nm QC and the $(1,1,1)$ level in a 3.6-nm QC, and (5) the $(2,2,2)$ level in a 6.3-nm QC and the $(1,1,1)$ level in a 3.5-nm QC. These anticorrelation features can also be explained by the resonant optical near-field energy transfer. The features represented by this figure support our interpretation of the experimental results. The large anticorrelation coefficients C identified by arrows (4) and (5) in Fig. 3 are the evidence of multiple energy transfer: Since the $(1,1,1)$ levels in 3.5-nm and 3.6-nm QCs resonate or nearly resonate to the $(2,1,1)$ level in a 4.6-nm QC, there is another route of energy transfer in addition to direct transfer from the 3.5-nm and 3.6-nm QCs to 6.3-nm QCs, i.e., the transfer via the 4.6-nm QCs. We consider that such multiple energy transfers increase the value of C identified by arrows (4) and (5) in Fig. 3.

In conclusion, CuCl QCs embedded in a NaCl matrix form a system that emphasizes the optical near-field interaction due to its high potential barrier, small radius of exciton, and high density of QCs. Using near-field optical spectroscopic microscopy with a spatial resolution smaller than 50 nm in the near UV region at 15 K, we observed, for the first time, resonant energy transfer occurring from the lowest state of excitons in 4.6-nm QCs to the first dipole-forbidden excited state of excitons in 6.3-nm size QCs. This is attributed to the optical near-field in-teraction between the QCs. In addition, this phenomenon can provide a variety of applications, such as an all-optical near-field switch.

[1] *Near-Field Nano/Atom Optics and Technology*, edited by M. Ohtsu (Springer, Tokyo, Berlin, Heidelberg, New York, 1998).

[2] T. Saiki, K. Nishi, and M. Ohtsu, Jpn. J. Appl. Phys. **37**, 1638 (1998).

[3] J. C. Kim, H. Rho, L. M. Smith, H. E. Jackson, S. Lee, M. Dobrowolska, J. M. Merz, and J. K. Furdyna, Appl. Phys. Lett. **73**, 3399 (1998).

[4] E. Deckel, D. Gershoni, E. Ehrenfreund, D. Spector, J. M. Garcia, and P. M. Petroff, Phys. Rev. Lett. **80**, 4991 (1998).

[5] M. Nirmal, B. O. Dabbousi, M. G. Bawendi, J. J. Macklin, J. K. Trautman, T. D. Harris, and L. E. Brus, Nature (London) **383**, 802 (1996).

[6] N. H. Bonadeo, J. Erland, D. Gammon, D. Park, D. S. Katzer, and D. G. Steel, Science **282**, 1473 (1998).

[7] D. Goldhaber-Gordon, H. Shtrikman, D. Mahalu, D. Abusch-Magder, U. Meirav, and M. A. Kastner, Nature (London) **391**, 156 (1998); D. Goldhaber-Gordon, J. Göres, M. A. Kastner, H. Shtrikman, D. Mahalu, and U. Meirav, Phys. Rev. Lett. **81**, 5225 (1998).

[8] F. Simmel, R. H. Blick, J. P. Kotthaus, W. Wegscheider, and M. Bichler, Phys. Rev. Lett. **83**, 804 (1999).

[9] F. R. Waugh, M. J. Berry, D. J. Mar, R. M. Westervelt, K. L. Campman, and A. C. Gossard, Phys. Rev. Lett. **75**, 705 (1995).

[10] L. W. Molenkamp, K. Flensberg, and M. Kemerink, Phys. Rev. Lett. **75**, 4282 (1995).

[11] M. Taut, Phys. Rev. B **62**, 8126 (2000).

[12] G. Burkard, G. Seelig, and D. Loss, Phys. Rev. B **62**, 2581 (2000).

[13] K. Mukai, S. Abe, and H. Sumi, J. Phys. Chem. B **103**, 6096 (1999).

[14] Z. K. Tang, A. Yanase, T. Yasui, Y. Segawa, and K. Cho, Phys. Rev. Lett. **71**, 1431 (1993).

[15] N. Sakakura and Y. Masumoto, Phys. Rev. B **56**, 4051 (1997).

[16] A. I. Ekimov, Al. L. Eflos, and A. A. Onushchenko, Solid State Commun. **56**, 921 (1985).

[17] T. Itoh, S. Yano, N. Katagiri, Y. Iwabuchi, C. Gourdon, and A. I. Ekimov, J. Lumin. **60&61**, 396 (1994).

[18] K. Kobayashi, S. Sangu, H. Ito, and M. Ohtsu, Phys. Rev. A **63**, 013806 (2001).

[19] T. Kataoka, T. Tokizaki, and A. Nakamura, Phys. Rev. B **48**, 2815 (1993).

[20] T. Suzuki, T. Mitsuyu, K. Nishi, H. Ohyama, T. Tomimasu, S. Noda, T. Asano, and A. Sasaki, Appl. Phys. Lett. **69**, 4136 (1996).

[21] T. Saiki, S. Mononobe, M. Ohtsu, N. Saito, and J. Kusano, Appl. Phys. Lett. **68**, 2612 (1996).

[22] T. Saiki and K. Matsuda, Appl. Phys. Lett. **74**, 2773 (1999).

Plasmon waveguide for optical far/near-field conversion

T. Yatsui[a)]

Japan Science and Technology Corporation, 687-1 Tsuruma, Machida, Tokyo, Japan 194-0004

M. Kourogi and M. Ohtsu

Interdisciplinary Graduate School of Science and Engineering, Tokyo Institute of Technology, 4259 Nagatsuta, Midori-ku, Yokohama, Kanagawa, Japan 226-8502 and Japan Science and Technology Corporation, 687-1 Tsuruma, Machida, Tokyo, Japan 194-0004

A plasmon waveguide was designed and fabricated using a metal-coated silicon wedge structure that converts propagating far-field light to the near field. Illumination ($\lambda = 830$ nm) of the waveguide (plateau width 150 nm) caused transverse magnetic plasmon-mode excitation. Use of a near-field microscope allowed us to determine its beam width and propagation length as 150 nm and 2.5 μm, respectively. © *2001 American Institute of Physics.* [DOI: 10.1063/1.1428405]

Future optical transmission systems will require advanced photonic switching device arrays and advanced photonic integrated circuits (ICs) in order to increase data transmission rates and capacity. Consequently, the size of these devices will need to be significantly decreased as compared to conventional diffraction-limited photonic devices. To fulfill this requirement, we propose a nanometer-scale photonic IC that is composed of sub-100-nm-scale dots and lines. One essential feature of the device is the use of the optical near field as a carrier for signal transmission.[1,2]

We developed a near-field optical chemical-vapor deposition technique for the fabrication of patterns using Zn, Al, and UV-emitting ZnO, which have nanometer-scale resolution and accuracy in size, position, and separation.[3–5] Furthermore, we previously reported the near-field nonlinear absorption spectroscopy of InGaAs single quantum dots[6] and the near-field optical energy transfer among CuCl quantum dots,[7] both of which are utilized in the operation of nanometer-scale photonic switches. However, coupling these photonic devices and ICs with external conventional diffraction-limited photonic devices requires a nanometer-scale optical waveguide for far/near-field conversion and vise versa [see Fig. 1(a)]. It is possible for a tapered fiber probe to act as a converter for conventional near-field optical microscopy.[8] The performance required for this type of waveguide includes:

(A) High conversion efficiency.

(B) The guide beam width should be less than 100 nm for efficient coupling of the converted optical near-field to sub-100 nm dots.

(C) The guide propagation length (the length after which the intensity decreases to the factor of e^{-2}) should be on the order of the optical wavelength to avoid direct coupling of the propagating far-field light to the nanometer-scale dots.

One candidate that meets these requirements is a tetrahedral tip, in which the one-dimensional (1D) mode has been excited efficiently by transverse magnetic (TM) -polarized incident light.[9] Setting the incoming beam at an oblique

angle to the metal slit at the edge of a tetrahedral tip converts far-field light to the 1D internal edge mode. However, the guided mode profile in a tetrahedral tip has not been observed directly. Furthermore, since it consists of a dielectric core surrounded by metal, the smallest diameter of the optical beam is estimated to be 100 nm. This is the theoretical value of the TM mode in a cylindrical glass core (refractive index $n = 1.53$) surrounded by gold ($n = 0.17 + i5.2$) (Ref. 10) at a wavelength of 830 nm.[11] This limitation does not meet requirement (B). In order to realize a narrower beam diameter, a more promising candidate is a cylindrical metal core waveguide, through which the TM plasmon-mode propagates.[12]

This is the basis for our proposed plasmon waveguide for optical far/near-field conversion. However, the TM plasmon mode is not easily excited by far-field light, due to mode mismatching. To overcome this difficulty, we employed a metal-coated silicon wedge structure. Using a near-field optical microscope, we were able to directly observe the TM plasmon mode propagating along the plateau of the silicon wedge.
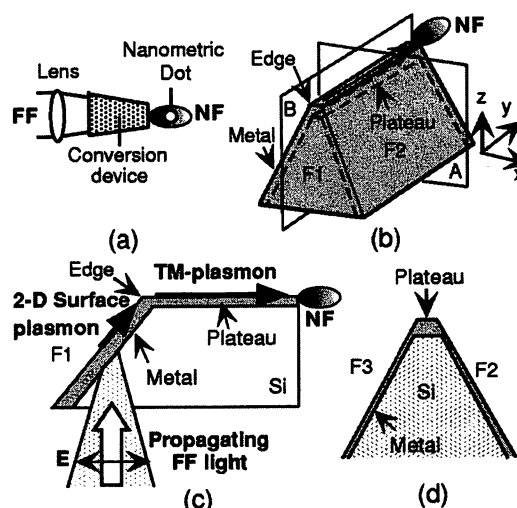

FIG. 1. (a) Optical far/near-field conversion concept. FFs=far field; NFs=near field. (b) Bird's-eye view of a plasmon waveguide. The x and y axes are perpendicular and parallel to the plateau axis, respectively. (c) Cross section along plane B (yz) in (b). (d) Cross section along plane A (xz) in (b).

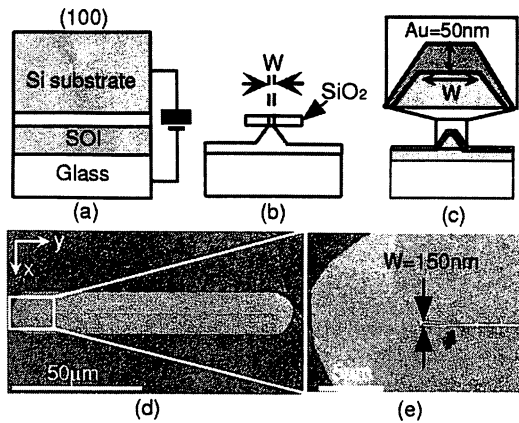[a)]Electronic mail: yatsui@ohtsu.jst.go.jp

FIG. 2. Fabrication steps for a plasmon waveguide: (a) anodic bonding [step (i)]; (b) anisotropic etching for fabrication of the silicon wedge [step (ii)]. W: plateau width; (c) metal coating; (d) and (e) scanning electron microscopic images of the metal-coated silicon wedge, $W = 150$ nm.
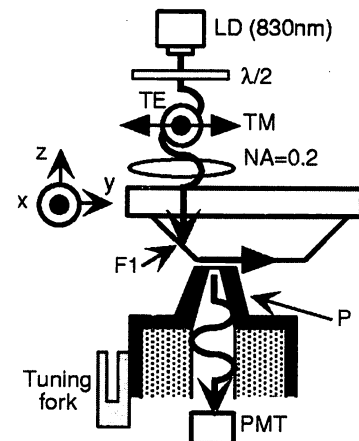

FIG. 3. Experimental setup. TM polarization: incident beam parallel to the plateau (y axis): TE polarization: incident beam perpendicular to the plateau (x axis).

Figure 1(b) shows our plasmon waveguide scheme. The main part consists of a silicon dielectric wedge, coated with a thin metal film. Incoming far-field light, which is polarized parallel to the y axis, is first transformed into the two-dimensional (2D) surface plasmon mode on the F1 side [see Fig. 1(c)]. Next, the 2D surface plasmon mode is converted into the 1D TM plasmon mode at the edge between F1 and the plateau. This conversion occurs because of the scattering coupling at the edge.[13] Third, the TM plasmon mode propagates along the plateau in a manner similar to surface plasmon modes using metal stripes[14] or edge modes using metal wedges.[15] This propagation occurs because the metal film deposited on the plateau is thicker than on the other faces (F1, F2, and F3) due to the normal evaporation process [see Fig. 1(d)].[16] Consequently, the plateau acts as a metal core waveguide. Finally, the TM plasmon mode at the waveguide outlet is converted to the optical near field so that it couples to the nanometer-scale dots, which are located in close proximity to the outlet.

Advantages of our waveguide are:

(1) High conversion efficiency from the 2D surface plasmon mode to the 1D TM plasmon mode, due to the scattering coupling at the edge [see Fig. 1(c)].[8,13]

(2) The beam width decreases (as narrow as 1 nm) with the core diameter, since this waveguide does not have a cutoff.[12] This decrease satisfies requirement (B).

(3) The propagation length of the TM plasmon mode is sufficiently long as to meet requirement (C). For example, the propagation length is 2.5 μm (at $\lambda = 830$ nm) for a TM plasmon with a gold core (diameter $D = 40$ nm) insulated by air.[12]

The plasmon waveguide was fabricated in four steps:

(i) A (100)-oriented silicon-on-insulator (SOI) wafer was bonded to the glass substrate by anodic bonding [Fig. 2(a)].[17]

(ii) After removing the silicon substrate from the SOI wafer by wet etching, the SiO$_2$ layer was patterned using photolithography. In order to create specific shapes for the plateau, F1 face, and edge, the rectangular mask was tilted 30° with respect to the $\langle 110 \rangle$ crystal orientation of silicon. This avoids any deformation of the convex corners.[18]

(iii) The silicon wedge was fabricated by anisotropic etching (40 g KOH + 60 g H$_2$O + 40 g isopropyl alcohol, 80 °C) [Fig. 2(b)]. Maintaining the silicon wedge height at less than 10 μm also kept its propagation loss sufficiently low. The plateau width was accurately controlled using the etching time.

(iv) After removing the SiO$_2$ layer, the silicon wedge was coated with a 50-nm-thick gold layer. Here, the gold vapor was sprayed at the normal incidence angle to the plateau surface so that the metal film deposited on the plateau is sufficiently thicker than on the other faces (F1, F2, and F3) [Fig. 2(c)].

Figures 2(d) and 2(e) show scanning electron microscopic images of our metal-coated silicon wedge. Plateau width W was 150 nm and its length L was 80 μm.

Figure 3 shows the experimental setup for measuring the spatial distribution of the electric-field intensity throughout the plateau of the metal-coated silicon wedge. Linearly polarized light from a laser diode ($\lambda = 830$ nm, 0.1 mW) was focused onto the F1 face. The incident light polarization was varied up to a half-wave plate in order to examine the dependence of the mode propagation characteristics. TE and TM polarizations indicate that the incident light polarization is parallel to the x or y axis, respectively. For this measurement, a fiber probe, P, with aperture diameter D_a of 60 nm was used, and its throughput was calibrated to be 1.0×10^{-6}.[19] The fiber probe was kept in close proximity to the silicon wedge (~ 10 nm) using the shear-force feedback technique.

Figures 4(a) and 4(b) show the observed electric-field intensity distributions on the wedges with $W = 1$ μm and 150 nm for TM polarization. Figures 4(c) and 4(d) are for TE polarization. Figures 4(e) and 4(f) show the cross-sectional profiles along the dashed white lines in Fig. 4(a) ($A - A'$ and $a - a'$), Fig. 4(b) ($B_1 - B_1'$ and $b_1 - b_1'$), and Fig. 4(d) ($B_2 - B_2'$ and $b_2 - b_2'$). Here, transmission was defined as the ratio of the light power detected by the fiber probe to the input light power. Comparing Figs. 4(a) and 4(c) [or Figs. 4(b) and 4(d)] shows that the propagating mode was excited efficiently only by TM-polarized incident light. Note that the transmission with TM-polarized light is five times higher than that with TE-polarized light for the wedge with $W = 150$ nm. From the
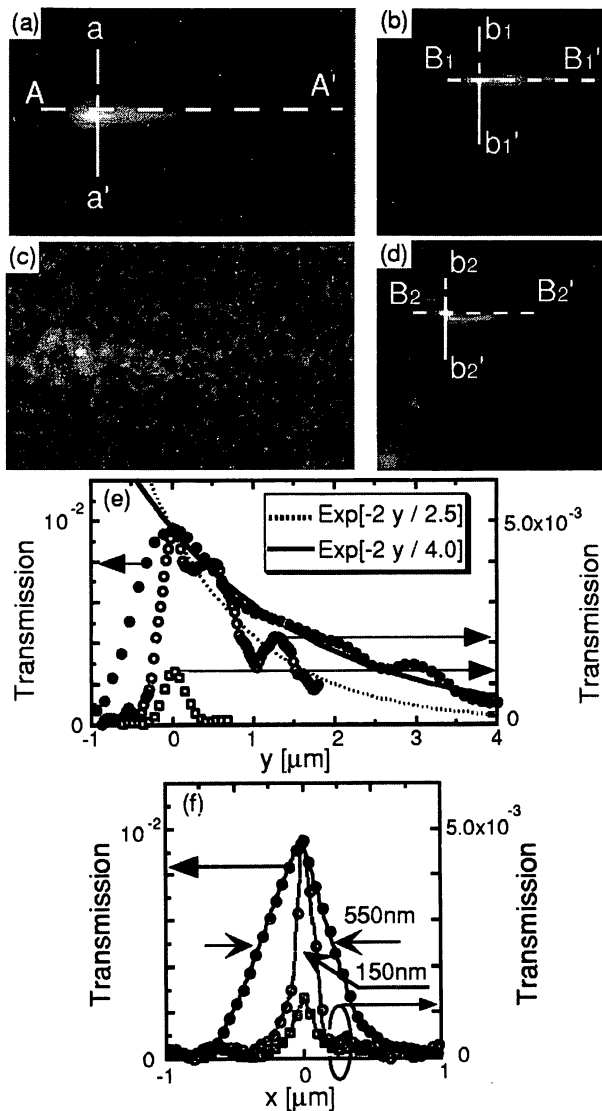
22

Appl. Phys. Lett., Vol. 79, No. 27, 31 December 2001

Yatsui, Kourogi, and Ohtsu   4585

FIG. 4. Electric-field distribution ($\lambda = 830$ nm) on the silicon wedge plateau. (a) TM polarization: $W = 1$ μm. (b) TM polarization: $W = 150$ nm. (c) TE polarization: $W = 1$ μm. (d) TE polarization: $W' = 150$ nm. The images are 7.0 μm×5.0 μm [(a) and (c)] and 5.0 μm×5.0 μm [(b) and (d)]. (e) Cross-sectional profiles along $A-A'$ (closed circles), B_1-B_1' (open circles), and B_2-B_2' (open squares) in (a), (b), and (d), respectively. Solid and dotted curves represent the exponential curves fitted to the experimental values. (f) Cross-sectional profiles along $a-a'$ (closed circles), b_1-b_1' (open circles), and b_2-b_2' (open squares) in (a), (b), and (d), respectively.

dotted exponential curve in Fig. 4(e) fitted to the open circles, the propagation length was estimated as 2.5 μm for the 150 nm wedge. This value is comparable to the theoretical value for TM plasmon mode in a cylindrical metal core waveguide with $D = 40$ nm and consisting of a gold core and air cladding at a wavelength of 830 nm.[12] From fitting the solid exponential curve in Fig. 4(e) to the closed circles, the propagation length for $W = 1.0$ μm was estimated as 4.0 μm, which is longer than that for $W = 150$ nm. This is because, as W increases, the effective refractive index approaches that of surface plasmon at the planar boundary between gold and air.[12] These experimental results confirm that the observed excitation along the plateau was the TM plasmon mode.

Figure 4(f) shows that the full width at half maxima (FWHM) of the cross-sectional profiles were 550 and 150 nm for $W = 1.0$ μm and 150 nm, respectively. With minor improvements to the waveguide, this FWHM value of 150

nm for $W = 150$ nm should meet requirement (B). Furthermore, note that the transmission was 5.0×10^{-3} for $W = 150$ nm, which is ten times higher than that of a fiber probe with $D_a = 150$ nm.[19] This efficient excitation of the TM plasmon mode can be attributed to the scattering coupling at the edge between F1 and the plateau in Fig. 1(b).[8,13] In other words, the 2D surface plasmon mode is scattered at this edge and converted to the TM plasmon mode. Furthermore, the electric charge induced by the surface plasmon also increases the scattering efficiency.[20] Even higher excitation efficiency is expected for $W < 100$ nm, since the induced electric charge can be concentrated on the sharp metal or semiconductor edge.[21] This transmission efficiency meets requirement (A). Finally, the propagation length estimated above is longer than the incident light wavelength. This meets requirement (C).

In conclusion, we proposed and fabricated a plasmon waveguide using a metal-coated silicon wedge structure. Propagation of the TM plasmon mode was observed directly using a near-field optical microscope. Illumination ($\lambda = 830$ nm) of the metal-coated silicon wedge ($W = 150$ nm) caused a TM plasmon mode with beam width and propagation length of 150 nm and 2.5 μm, respectively. These results confirm that with the use of a metal-coated wedge structure it will be possible to create the optical far/near-field conversion devices required by future systems.

[1] M. Ohtsu, Proc. SPIE 3749, 478 (1999).
[2] Optical and Electronic Process of Nanomatters, edited by M. Ohtsu (Kluwer Academic, Dordrecht, 2001), Chap. 8.
[3] Y. Yamamoto, M. Kourogi, M. Ohtsu, V. Polonski, and G. H. Lee, Appl. Phys. Lett. 76, 2173 (2000).
[4] G. H. Lee, Y. Yamamoto, M. Kourogi, and M. Ohtsu, Tech. Dig. QELS 56, 17 (2000).
[5] Y. Yamamoto, T. Kawazoe, G. H. Lee, T. Shimizu, M. Kourogi, and M. Ohtsu, Tech. Digest CLEO Pacific Rim 4, I-520 (2001).
[6] T. Matsumoto, M. Ohtsu, K. Matsuda, T. Saiki, H. Saito, and K. Nishi, Appl. Phys. Lett. 75, 3246 (1999).
[7] T. Kawazoe, K. Kobayashi, J. Lim, Y. Narita, and M. Ohtsu, Tech. Digest CLEO Pacific Rim 4, I-194 (2001).
[8] T. Yatsui, M. Kourogi, and M. Ohtsu, Appl. Phys. Lett. 71, 1756 (1997).
[9] U. C. Fischer, J. Koglin, and H. Fuchs, J. Microsc. 176, 281 (1994).
[10] Handbook of Optical Constants of Solids, edited by E. D. Palik (Academic, New York, 1985).
[11] L. Novotny and C. Hafner, Phys. Rev. E 50, 4094 (1994).
[12] J. Takahara, S. Yamagishi, H. Taki, A. Morimoto, and T. Kobayashi, Opt. Lett. 22, 475 (1997).
[13] D. Marcuse, Light Transmission Optics (Van Nostrand Reinhold, New York, 1972), Chap. IV.
[14] J. C. Weeber, J. R. Krenn, A. Dereux, B. Lamprecht, Y. Lacroute, and J. P. Goudonnet, Phys. Rev. B 64, 045411 (2001).
[15] A. Eguiluz and Maradudin, Phys. Rev. B 14, 5526 (1976).
[16] K. Tachibana, T. Someya, S. Ishida, and Y. Arakawa, Appl. Phys. Lett. 76, 3212 (2000).
[17] T. R. Anthony, J. Appl. Phys. 58, 1240 (1998).
[18] B. Puers and W. Sansen, Sens. Actuators A21-A23, 1036 (1990).
[19] T. Yatsui, M. Kourogi, and M. Ohtsu, Appl. Phys. Lett. 73, 2090 (1998).
[20] A. Sommerfeld, Optics (Academic, New York, 1954), Chap. 10.
[21] J. Gersten and A. Nitzan, J. Chem. Phys. 73, 3023 (1980); 75, 1139 (1981).

Mercury treatment of optical near-field fibre probes for smoother tips with reduced light leakage

H N Aiyer[1], T Kawazoe[1], J Lim[2], Y Echigo[2] and M Ohtsu[1,2]

[1] ERATO Localized Photon Project, Japan Science and Technology Corporation, 687-1-17/4F, Tsuruma, Machida-shi, Tokyo 194-0004, Japan
[2] Tokyo Institute of Technology, 4259, Nagatsuta, Midori-Ku, Yokohama 226-8502, Japan

E-mail: hemant@ohtsu.jst.go.jp

Abstract
A study was conducted to explore the effect of simple mercury treatment on the metal (gold) coating of an optical near-field fibre probe and its performance. The method involves physically contacting a mercury droplet with the fibre probe for a short time, ~10 s. It is shown that, on interaction with the mercury, the grain boundaries on the gold surface are occupied by mercury atoms, resulting in smoother metal coating and thus reducing the light leakage and enhancing the optical damage threshold level. Probe-to-probe experiments performed on the apertured probes revealed improved spatial distribution of near-field intensity on the mercury treated probes.

1. Introduction

A metal coated optical near-field fibre probe with a subwavelength aperture constitutes a critical component in important applications such as imaging, spectroscopy, nanofabrication and high density data storage [1–4]. The desired properties of the subwavelength light source are small, well defined circular aperture, good polarization characteristics, high brightness with high optical damage threshold and good transmission with minimum light leakage [1]. The most widely used subwavelength light source consists of a tapered fibre probe. The fibre probe usually consists of a single-mode optical fibre with the tapered structure [1, 5]. In the taper region of the probe, where the waveguide properties of the fibre break down, metal film is usually coated around the sides of the probe to confine the light so that it exits the aperture at the very end of the tip. The quality of the metal film evaporated onto fibre probes is a critical issue as the resolution in near-field microscopy is pushed towards its theoretical limit. It is very important to minimize the light leakage from the taper region and maximize the efficiency.

One major problem originates from the grainy structure of the evaporated metal coating [6]. This structure often leads to a porous region at the taper part, which causes a significant loss of light. Hitherto, various methods such as the use of the angled evaporation method, etching the quartz optical fibres through their acrylate jacket, use of an adhesion layer, a protection coating preventing corrosion during the aging, application of mixed metal coating, etc, have been reported to give considerable improvement in the fibre probe properties [7–9]. In this paper, we propose and demonstrate a simple approach of 'mercury treatment' to improve the smoothness of the metal coating, yielding higher quality fibre probes. This method is based on mercury treatment of the as-fabricated fibre probes. Gold is well known to be a strong absorber of mercury and that it forms a solid solution amalgam phase at ambient temperature [10]. We have used this feature of the gold–mercury system in the following work.

2. Experimental details

The double-tapered fibre probe tips were fabricated by a two-step selective chemical etching process [11]. Briefly, in the first step, using a buffered HF solution of $X = 1.7$ with an etching time of 80 min, a short tip with large cone angle is fabricated. In the second step, a long tapered region which delivers the light to the cutoff diameter is obtained using a solution with $X = 10$ with an etching time of 25 min. A gold film is then coated on this fibre by the dc sputtering method.
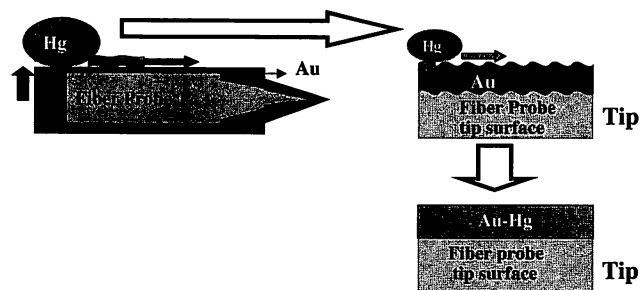
**Figure 1.** Schematic diagram of the mercury treatment applied to fibre probes in this work.

Typical deposition time and resultant gold thickness were 400 s and 70 nm, respectively. Typical gold coated length of the fibre probe was 1.5 cm from the tip apex. These fabricated fibre probes were then subjected to the mercury treatment (figure 1) by just physically contacting the metal coated fibre probe with a small mercury droplet fixed on a glass plate for ~10 s. An aperture was formed by focused ion beam slicing.

Various characterizations were carried out on the fibre probes to evaluate the effect of the mercury treatment. Scanning electron microscopy (SEM) was employed to examine the fibre probe structure and the morphology of the metal coating deposited onto the fibre probe. UV–visible measurements were performed on the mercury treated and bare gold coated glass substrates to study the optical changes upon mercury treatment. The ambient chemical stability of the mercury treated gold films has been investigated by identifying the nature of the surface species employing x-ray photoelectron spectroscopy with an incident x-ray energy of 1253.6 eV. XPS spectra were recorded for (a) untreated gold/glass film and (b) mercury treated gold/glass film (aged for 2 days) in the Au 4f and Hg 4f binding energy (BE) regions.

First, we tested the light leakage properties of mercury-treated apertureless fibre probes by conducting the damage threshold experiments. The light from an Ar laser (488 nm) was focused on a freshly cleaved fibre of the same type as that under study. This fibre was then coupled to the fibre probe using a fibre splicer. The fibre probe was carefully held against the photodiode of a power meter placed in proximity using a micropositioner. The light leakage from the tip of the apertureless fibre probe upon varying the power of the focused laser light was detected by a silicon photodiode. The effective optimum coupling efficiency of the fibre splicer in the present experiments was 15%. Second, the spatial distribution of the optical near-field intensity on apertured fibre probes prior to and after the mercury treatment was measured by carrying out 'probe-to-probe experiments', maintaining the 'probe-to-probe' distance within 20 nm using a shear force technique [12].

3. Results and discussion

Figures 2(a) and (b) show the SEM images of as-fabricated and mercury-treated apertureless fibre probes, respectively, revealing a smoother microstructure for Hg treated probes. This improvement is vividly seen in the magnified views of the two microstructures presented in the insets. This observation is explained as follows. The sticking coefficient
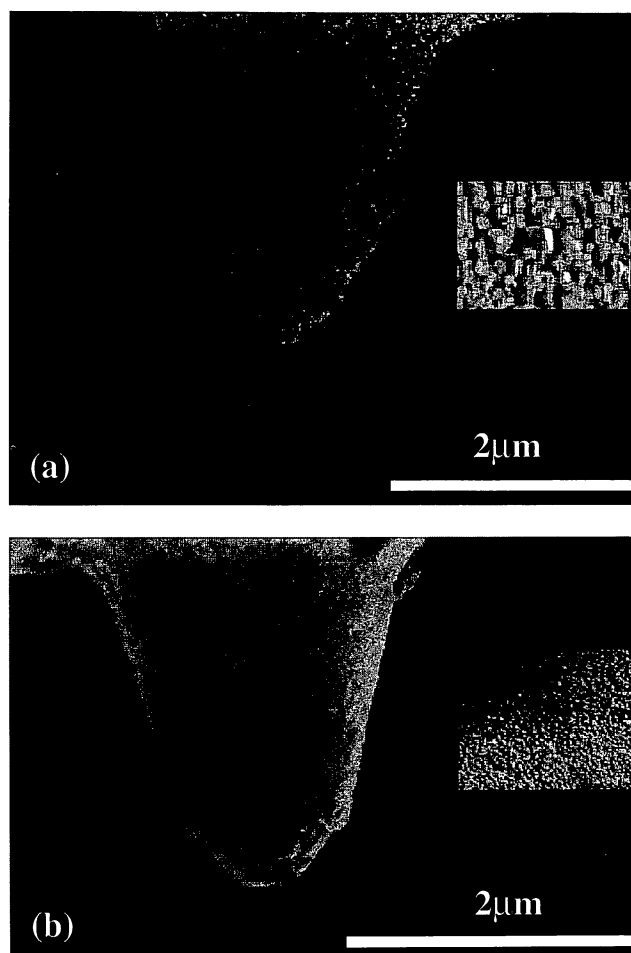
Figure 2. SEM images of double-tapered fibre probes (a) before and (b) after mercury treatment. The insets show the corresponding (×30) magnified views from the tapered region of the probes.

of mercury on gold is unity for coverages from less than one monolayer up to one monolayer. Thus the coverage up to one monolayer occurs rapidly, within 60 s. After one monolayer of coverage, the sticking coefficient of mercury on gold decreases. The diffusion coefficient for the Au–Hg system at room temperature is $\sim 1.14 \times 10^{-5}$ cm^2 s^{-1}. Mercury, being very mobile on the gold surface, diffuses rapidly into the grain boundaries giving a smoother microstructure. The sticking coefficient of mercury to mercury is 0.2. Coverages in excess of a monolayer lead to amalgamation at the mercury–gold interface, since mercury is soluble in gold and forms both a solid solution and an amalgam at room temperature. It may be noted here that, in our study, it was difficult to estimate the concentration of dosed mercury. However, the amalgam phase formation was confirmed from the EDAX measurements on mercury treated fibre probes which revealed the presence of both Hg and Au. Too long a mercury treatment is not desired as mercury–mercury attractive interactions lead to island formation with increased roughness after mercury adsorption.

The experimentally recorded absorption spectra for the 70 nm thick gold film showed an improved optical response on mercury treatment with ~9% decrease in the optical transmittance for the 300–900 nm wavelength range. The oxide formation, if any, on Hg treatment is detrimental. The oxide formation is generally accompanied by a decrease in
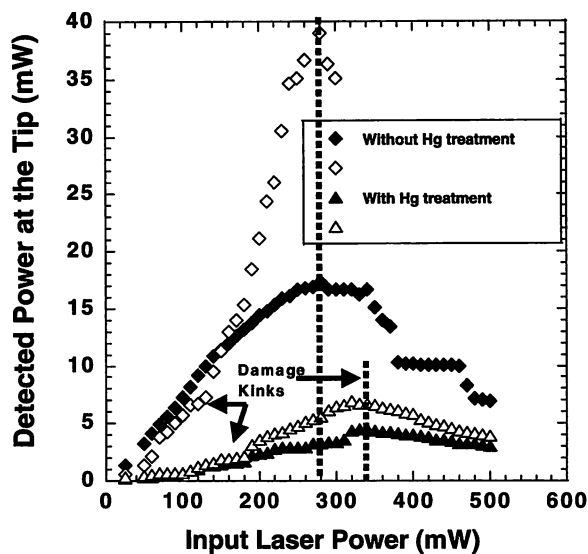
Figure 3. Variation of the detected power at the fibre probe tip with respect to applied input laser power (coupling efficiency = 15%).

the film reflectivity and an increase in the film roughness, both of which dramatically affect the performance of the fibre probes. This aspect was investigated by XPS measurements on (gold/glass) and mercury treated (gold/glass) films. The bare gold film spectra showed only Au $4f_{7/2}$ and Au $4f_{5/2}$ peaks at the expected positions of 83.8 and 87.5 eV, respectively. On mercury treatment, Hg 4f peaks appeared and the Au $4f_{7/2}$ peak showed a BE shift of 0.3 eV towards lower BE range. We also observed some change and broadening of the peaks. This indicates the chemical change upon mercury treatment which is attributed to the formation of the amalgamation phase. However, we rule out oxidation effects, as the observed BE shift is seen towards the lower BE range. Thus, the XPS observations confirm the chemical stability of the mercury treated gold films, which essentially implies the chemical stability of the mercury-treated fibre probes.

Immediately after the mercury treatment, the optical leakage property of the tip was assessed. Light from a Ar laser (488 nm) was coupled into the apertureless fibre probes and the variation of the emerging light output with increasing Ar laser power was studied. Figure 3 compares the typical result of such an experiment performed on as-fabricated gold coated apertureless fibre probes and on those after mercury treatment. On application of increasing laser powers, the detected power from the fibre probe increases linearly and shows a kink in the signal at the damage point. The output 'leakage' power detected at the tip end starts to fall off beyond a point when the fibre probe is completely damaged. It is seen that the mercury treatment yields ~(1/6) times reduction in the optical leakage (at 280 mW input laser power) and 21% increase in the optical damage threshold. Improved damage threshold on mercury treatment allows higher maximum light output at the tip apex on coupling the laser power into the cleaved fibre. The data in figure 3 refers to different fibre probes (prepared in the same batch) before and after the mercury treatment. Good reproducibility of the results is clearly seen below the damage threshold. SEM observations showed the clear ripping of the metal coating on the fibre probe beyond the optical damage threshold.

We have also conducted mercury treatment on apertured fibre probes and investigated its effect on the spatial distribution
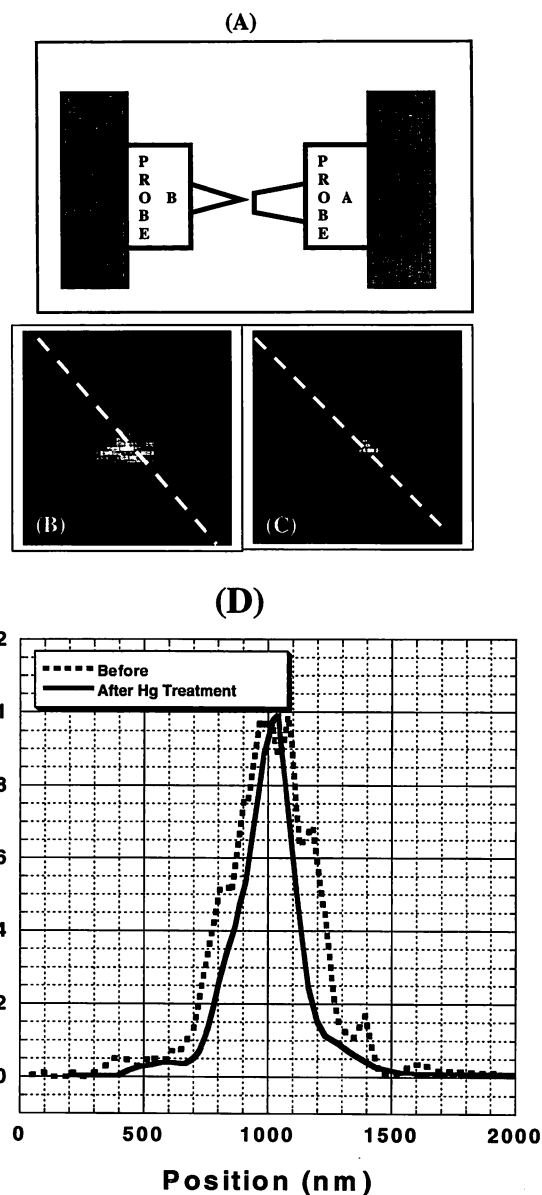
Figure 4. (*a*) Schematic of the 'probe-to-probe' experimental set-up, two-dimensional spatial distribution images (4 μm^2 × 4 μm^2) of the optical near-field on the apertured fibre probes (*b*) before and (*c*) after the mercury treatment. (*d*) Comparison of the cross sectional profiles for (*b*) and (*c*) along the lines indicated in (*b*) and (*c*), respectively.

of the optical near-field intensity by carrying out 'probe-to-probe experiments' (figure 4(*a*)). The optical near-field generated on 250 nm aperture diameter double-tapered fibre probes (probe A) was observed by scanning an apertureless single-tapered fibre probe (probe B, apex diameter ~100 nm) and detecting the scattered light with a photomultiplier while the separation between the two was maintained within 20 nm using a shear force technique. Figures 4(*b*) and (*c*) show the two-dimensional images of the observed spatial distribution of the optical near intensity on the 250 nm apertured fibre probe before and after the mercury treatment, respectively. The same fibre probe (probe B) was used for different scans. Without mercury treatment (figure 4(*b*)), the distribution is broad with full width at half maximum (FWHM) = 442 nm (see the dotted curve in figure 4(*d*) for its cross-sectional profile along the line in figure 4(*b*)) which is considered to be due to leakage through

the probe. Many distinct sharp features observed in this profile indeed indicate the presence of leakage points on the probe. On mercury treatment (figure 4(c)), the 250 nm apertured fibre probe showed an improved spatial distribution of the optical near-field with more focused near-field (FWHM = 282 nm) (see the full curve of figure 4(d)). The smooth cross-sectional profile observed for such a probe confirms the disappearance of the leakage points on these fibre probes. This aspect is particularly beneficial for the application of fibre probes for nanometric photochemical vapour deposition, where the leakage points can give rise to parallel, undesired secondary deposits [4]. Finally, it is noteworthy that appropriate care should be taken while handling mercury owing to its poisonous nature.

4. Conclusions

In conclusion, we have demonstrated a simple technique of mercury treatment for producing a smoother fibre probe surface coating. This resulted in $\sim 1/6$ times reduction in light leakage along the cone besides improving the fibre probe's optical damage threshold (by $\sim 21\%$). This approach also yielded significant improvement of the spatial distribution of near-field intensity on apertured fibre probes. Mercury treatment offers a simple technique to further improve the yield as well as the performance of fibre probes.

References

[1] Ohtsu M 1998 *Near Field Nano/Atom Optics and Technology* (Tokyo: Springer)

[2] Shchemelinin A, Rudman M, Liberman K and Lewis A 1993 A simple lateral force sensing technique for near field micropattern generation *Rev. Sci. Instrum.* **64** 3538–41

[3] Betzig E, Trautman J K, Wolfe R, Gyorgy E M and Finn P L 1992 Near field magnetooptics and high density data storage *Appl. Phys.Lett.* **61** 142–4

[4] Yamamoto Y, Kourogi M, Ohtsu M, Polonski V and Lee G H 2000 Fabrication of nanometric zinc pattern with photodissociated gas phase diethylzinc by optical near field *Appl. Phys. Lett.* **76** 2173–5

[5] Pangaribuan T, Yamada K, Jiang S, Ohsawa H and Ohtsu M 1992 Reproducible fabrication technique of nanometric tip diameter fiber probe for photon scanning microscope *Japan. J. Appl. Phys.* **31** L1302

[6] Pilevar S, Edinger K, Atia W, Smolyaninov I and Davis C 1998 Focussed ion beam fabrication of fiber probes with well defined apertures for use in near field scanning optical microscopy *Appl. Phys. Lett.* **72** 3133–5

[7] Lambelet P, Sayah A, Pfeffer M, Phillipona C and Marquis-Weible F 1998 Chemically etched fiber tips for near field optical microscopy: a process for smoother tips *Appl. Opt.* **37** 7289–92

[8] Stockle R, Fokas C, Deckert V, Zenobi R, Sick B, Hecht B and Wild U P 1999 High quality near field optical probes by tube etching *Appl. Phys. Lett.* **75** 160–2

[9] Hoffmann P, Dutoit B and Salathe R P 1995 Comparison of mechanically drawn and protection layer chemically etched optical fiber tips *Ultramicroscopy* **61** 165–70

[10] Castleman A W Jr and Conti J J 1970 Consideration of the mass effect on diffusion in the liquid state *Phys. Rev.* A **2** 1975–83

[11] Saiki T, Mononobe S, Ohtsu M, Saito N and Kusano J 1996 Tailoring a high transmission fiber probe for photon scanning tunnelling microscope *Appl. Phys. Lett.* **68** 2612–4

[12] Yatsui T, Kourougi M and Ohtsu M 1997 Highly efficient excitation of optical near field on apertured fiber probe with an asymmetric structure *Appl. Phys. Lett.* **71** 1756–8

Second-harmonic generation in a near-field optical-fiber probe

Tadashi Kawazoe

Exploratory Research for Advanced Technology, Japan Science and Technology Corporation,
687-1 Tsuruma, Machida, Tokyo 194-0004, Japan

Takashi Shimizu

Tokyo Institute of Technology, 4259 Nagatsuta, Midori-ku, Yokohama 226-8502, Japan

Motoichi Ohtsu

Exploratory Research for Advanced Technology, Japan Science and Technology Corporation,
687-1 Tsuruma, Machida, Tokyo 194-0004, Japan, and
Tokyo Institute of Technology, 4259 Nagatsuta, Midori-ku, Yokohama 226-8502, Japan

Second-harmonic generation (SHG) in a near-field optical-fiber probe was observed. The tip of the probe consists of a triple-tapered fiber with an aluminum coating. For a fiber probe with an aperture size of 100 nm, the SHG conversion factor was 2.0×10^{11} cm^2/W, which is as large as that of a 5-mm KDP crystal. In a probe-to-probe experiment, we demonstrated that SHG took place at the aluminum coating on the fiber probe. © 2001 Optical Society of America
OCIS codes: 190.4370, 350.3950, 190.4350.

Near-field optics offers a unique technique for achieving high spatial resolution beyond the diffraction limit of light.[1] Various interesting kinds of study, such as spectroscopy of quantum dots[2] and polymers[3] and near-field (NF) optical chemical-vapor deposition,[4] have been carried out with this technique. Second-harmonic (SH) near-field optical imaging of a metal surface has also been reported.[5] Second-harmonic generation (SHG) is a useful phenomenon not only for far-field spectroscopy but also for NF spectroscopy, which one can use to investigate material properties and examine nonlinear optical devices. A SH signal is generated by nonlinear polarization involving the asymmetric property of the material. A fiber probe used for NF optics can satisfy this condition, because it has large asymmetric regions in the sharpened fiber core, coated metal, and air. In addition, the coated metal surface can enhance the SHG intensity as a result of the surface plasmon effect.[6] The SHG efficiency of an apertureless metallic tip has been reported, and it may not be so low as that of a nonlinear crystal.[7] For a metal-coated fiber probe with an aperture, the SHG efficiency may not be so low, because of the complicated profile of the boundary between glass and metal. However, we know of no investigation of SHG in a fiber probe, in spite of its potential application to frequency conversion, optical chemical-vapor deposition with UV light, and so on. Thus we believe that it is important to investigate the phenomenon of SHG in fiber probes. In this Letter we demonstrate SHG in a fiber probe and report several of its properties for the first time to our knowledge.

Figure 1(a) shows the cross-sectional profile and a scanning-electron microscope (SEM) image of the NF fiber probe employed for SHG. A triple-tapered fiber probe, configured for use in the UV region,[8] was used as the NF probe. The fiber had a double-core structure consisting of a 0.16-μm GeO$_2$-doped core and a 3.0-μm pure-silica sheath. In fabricating the probe we used two buffered hydrogen fluoride (BHF) solutions as etchants. The two solutions differed in their ratios of NH$_4$F solution (40 wt.%):HF acid (50 wt.%):H$_2$O, which were 1.7:1:1 (BHF$_A$) and 10:1:1 (BHF$_B$). First, we etched the fiber end with BHF$_A$ for 56 min to taper the fiber. Next, we etched the tapered fiber with BHF$_B$ for 30 min to sharpen the center of the fiber core. The general shape of the probe was that of a cone with an angle of 17°. The triple-tapered end was coated with a 500-nm-thick aluminum layer by vacuum deposition. Two probes were prepared. We prepared probe A by coating the
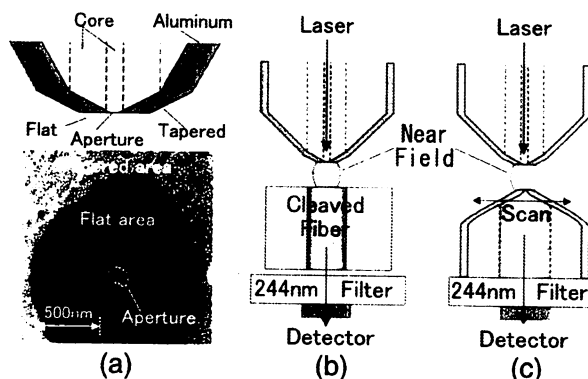

Fig. 1. Explanation of the experiments and the fiber probe. (a) Cross-sectional profile and a SEM image of the near-field probe for SHG. (b) Schematic drawing of the experimental configuration for measurement of SH intensity from the probe. (c) Schematic drawing of the probe-to-probe experiment.

aluminum from the top and probe B by coating it from the side. The probe apertures were created by use of the focused ion-beam technique. The roughness of the cut end was less than 5 nm, which was the spatial resolution of the SEM. The diameter of the aperture was found from the SEM image to be 100 nm.

Figure 1(b) is a schematic drawing of the experimental setup for measuring SH intensity. The SH intensity was measured with a cleaved fiber. The 10-μm core of the cleaved fiber was much larger than the apex diameter of the probe, and the distance between the cleaved fiber and the probe was less than 1 μm. Therefore, most of the fundamental and SH signals from the probe could be detected by the cleaved fiber. Figure 1(c) explains the method used for measuring the spatial distribution of the SH intensity in the probe-to-probe experiment.[9] The second probe used in the probe-to-probe scanning was a single tapered fiber probe that was fabricated by pulling and etching of a fiber with a pure silica core that was then coated with a 500-nm-thick layer of aluminum.[10] The diameter of its aperture was 100 nm. Separation between the two probes was regulated to several nanometers by use of a shear-force technique.[11] A 488-nm-wavelength Ar$^+$ laser was used as the light source for the experiments. We used a Hamamatsu Model R166UH photomultiplier tube, because it is sensitive in the wavelength range 160–320 nm, to detect the SH signal selectively. In addition, we used a bandpass filter with a bandwidth of 10 nm to reject the fundamental signal with an extinction ratio higher than 10^{-4} for the fundamental wavelength. The quantum efficiency of the photomultiplier tube was more than 30% for 244-nm light. A photon-counting technique was used for detection. For an accumulation time of 1000 s, the lowest observable SH power was 3.0×10^{-19} W.

Figure 2 shows the relationship between the fundamental and the SH powers when we used the fundamental signal passing through the probe as the reference for this measurement. The squares correspond to the experimental results for probe A. The SHG power is proportional to the square of the fundamental power in the low-power region and saturates at a fundamental power of ~20 nW. As the fiber probe can be thermally damaged by a fundamental output exceeding 100 nW, the observed saturation at 20 nW is reasonable. Thermal damage changes properties of the fiber probe such as aperture diameter and aluminum coating; then the SH signal intensity is saturated. The solid line in Fig. 2 fits the measured values in the unsaturated region. The conversion factor R is the ratio of the SH intensity to the square of the fundamental intensity. From the slope of the solid line, the value of R for probe A with an aperture of 100 nm is 2.0×10^{-11} cm^2/W. Because this value depends on the aluminum deposition technique, SHG was also evaluated for probe B, which was fabricated by the alternative approach of depositing aluminum from the side of the triple-tapered fiber. The results are shown by filled circles in Fig. 2, and the dashed line fits the data points for probe B in the unsaturated region. The slope of this line gives

the R value for probe B, which is estimated to be 2.1×10^{-12} cm^2/W, i.e., ten times smaller than the value for probe A. Such a large difference in the value of R supports the dependence of SHG on the deposition technique. Furthermore, it should be noted that the values of R for probes A and B are 5 orders of magnitude higher than that obtained for an aluminum surface coated upon a large flat piece of glass.[12] Such a large value corresponds to the value for a 5-mm-thick KDP crystal in the far-field configuration.[13] We believe that the highly efficient SHG localized at a small probe has immense potential for a wide range of applications.

Figure 3(a) shows the spatial distribution of the SH power on probe A obtained in the probe-to-probe experiment. The image size is 1.5 μm $\times$ 1.5 μm. The solid ellipse (X) shows the position of the aperture, and the dashed curve (Y) shows the boundary between the flat and the tapered areas. Strong SH light is emitted at the areas enclosed by the dotted dumbbell curve and about the boundary (Y). Figure 3(b) shows cross-sectional profiles of the SH power along the solid and
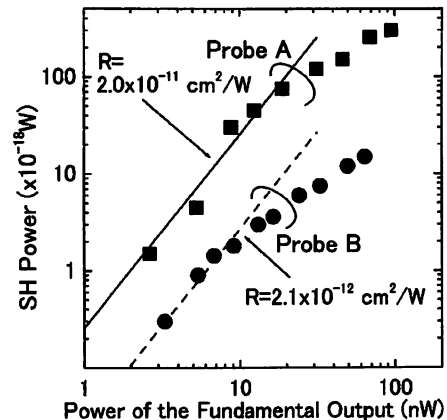

Fig. 2. Relation between the fundamental and the SH powers. Squares and circles represent the experimental results with probes A and B, respectively; the solid and dashed lines are fitted to them in the unsaturated region.
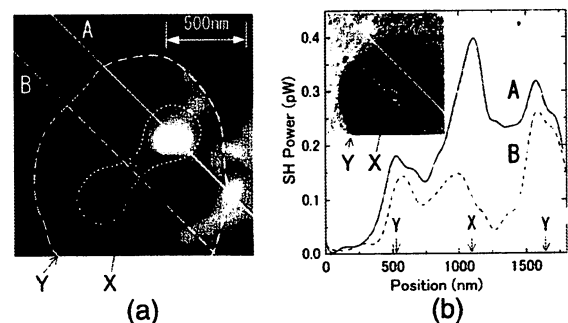

Fig. 3. Spatial distribution of the SH power on probe A measured by the probe-to-probe experiment. (a) Two-dimensional profile of SH distribution. Solid ellipse (X), position of the aperture. Dashed curve (Y), boundary between the flat and the tapered areas, as shown in Fig. 1(a). (b) Cross-sectional profiles of the distribution along A, the solid and B, the dashed lines marked in (a). Inset, SEM image of the probe corresponding to (a).

29

dashed lines in Fig. 3(a). The inset in Fig. 3(b) shows a top-view SEM image of the probe, and the image area corresponds to that of Fig. 3(a). The peak power of the SH signal was 0.4 pW. This observed power is much larger than the previous experimental result, shown in Fig. 2. We believe that this enhancement of SH signal comes from the resonant effect of two probes. In the area enclosed by the dotted dumbbell curve, a strong SH signal was recorded from both sides of the aperture. The SHG observations within the area enclosed by the dumbbell curve may be related to polarization of the SH light and correspond to the propagation mode of the fiber.[10] Near the boundary between the flat and the tapered areas (Y), nonlinear oscillation of the surface plasmon in the aluminum coating could easily emit SH light as a result of the edge effect. These results confirm that the SH signal was generated in the aluminum coating. Investigations of SHG in a bare-fiber probe without aluminum coating revealed no detectable SH signals despite a high fundamental intensity. This result also strongly indicates that the aluminum coating enhances SHG in the fiber probe. In a subwavelength-sized fiber probe, the optical NF becomes dominant and can excite the surface plasmon polariton on the coated metal, an effect that is well known in the case of flat metal surfaces.[6] Therefore we believe that the SHG enhancement with the fiber probe occurs as a result of the optical nonlinear response of the surface plasmon polaritons on the coated metal.

In conclusion, we have demonstrated SHG in a near-field optical-fiber probe for what we believe is the first time. A high SHG conversion factor in the range $2.1 \times 10^{-12} - 2.0 \times 10^{-11}$ cm^2/W was obtained for a 100-nm-aperture fiber probe. This highly efficient SHG promises several new applications in NF optics. The spatial distribution of SHG on the fiber probe was determined in a probe-to-probe experiment. The experimental results establish that the aluminum coating on the fiber probe and the shape of the fiber probe are important factors that govern this SHG phenomenon. Further studies to clarify the mechanism by which this SHG occurs would be useful.

T. Kawazoe's e-mail address is kawazoe@ohtsu.jst.go.jp.

References

1. D. W. Pohl and D. Courijon, eds., Near Field Optics (Kluwer Academic, Dordrecht, The Netherlands, 1993).
2. T. Matsumoto, M. Ohtsu, K. Matsuda, T. Saiki, H. Saito, and K. Nishi, Appl. Phys. Lett. 75, 3246 (1999).
3. R. Stevenson, M. Granstrom, and D. Richards, Appl. Phys. Lett. 75, 1574 (1999).
4. Y. Yamamoto, M. Kourogi, M. Ohtsu, V. Polonski, and G. H. Lee, Appl. Phys. Lett. 76, 2173 (2000).
5. I. I. Smolyaninov, A. V. Zayats, and C. C. Davis, Phys. Rev. B 56, 9290 (1997).
6. V. M. Agranovich and D. L. Mills, ed., Surface Polaritons: Electromagnetic Waves at Surfaces and Interfaces (North-Holland, Amsterdam, 1982).
7. I. I. Smolyaninov, H. Y. Liang, C. H. Lee, C. C. Davis, S. Aggarwal, and R. Ramesh, Opt. Lett. 25, 835 (2000).
8. S. Mononobe, T. Saiki, T. Suzuki, S. Koshihara, and M. Ohtsu, Opt. Commun. 146, 45 (1998).
9. T. Yatsui, M. Kourogi, and M. Ohtsu, Appl. Phys. Lett. 71, 1756 (1997).
10. M. Ohtsu, ed., Near-Field Nano/Atom Optics and Technology (Springer-Verlag, Berlin, 1998).
11. E. Betzig, P. L. Finn, and J. S. Weiner, Appl. Phys. Lett. 60, 2484 (1992).
12. R. Murphy, M. Yeganeh, K. J. Song, and E. W. Plummer, Phys. Rev. Lett. 63, 318 (1989).
13. A. Yariv, Introduction to Optical Electronics, 3rd ed. (Holt, Rinehart, & Winston, New York, 1985).

Near-field ultraviolet photoluminescence spectroscopy for evaluating the crystallinity of polycrystalline zinc oxide

T. Yatsui[a]

Japan Science and Technology Corporation, 687-1 Tsuruma, Machida, Tokyo, Japan 194-0004

T. Shimizu, Y. Yamamoto, M. Kourogi,[b] and M. Ohtsu[b]

Interdisciplinary Graduate School of Science and Engineering, Tokyo Institute of Technology, 4259 Nagatsuta, Midori-ku, Yokohama, Kanagawa, Japan 226-8502

G. H. Lee

Department of Advanced Materials Engineering, Dong-Eui University, Gaya-Dong 24, Pusanjin-Ku, Pusan, Korea, 614-714

By extending the optical near-field technique to the ultraviolet region, a two-dimensional evaluation of the optical properties and crystallinity of polycrystalline zinc oxide (ZnO) was carried out at room temperature. Using an ultraviolet fiber probe with an aperture diameter of 80 nm, we obtained spatially resolved photoluminescence spectra from individual ZnO nanocrystallites; the emission intensity depended on the topography and on crystal orientation. © 2001 American Institute of Physics. [DOI: 10.1063/1.1410357]

ZnO is a promising material for use in ultraviolet (UV) light-emitting devices at room temperature, due to its wide band gap of 3.37 eV and its exciton binding energy (60 meV), which is larger than its thermal energy at room temperature (26 meV). Recently, many different techniques, such as pulsed laser deposition,[1] molecular-beam epitaxy (MBE),[2] and the oxidation of metallic Zn,[3] have been used to fabricate high-quality ZnO nanocrystallites, which have realized room temperature UV lasing. Thus, ZnO nanocrystallites have been examined as a light-emitting source for advanced opto-electronic devices.

To apply single ZnO nanocrystallites in these devices requires lateral integration with nanometer-scale resolution. To meet this requirement, near-field optical chemical vapor deposition (NFO-CVD) is expected to become a key technology, because the size and positioning is controlled by scanning a fiber probe.[4] Recently, a ZnO dot with a size of 200 nm was fabricated by NFO-CVD.[5] However, to obtain high-quality ZnO, the substrate must be heated to 200 °C,[6] inducing thermal drift of the substrate and the probe. To deposit a smaller ZnO dot, this drift must be sufficiently reduced.

The optical properties and crystallinity of ZnO nanocrystallites have been evaluated by conventional techniques, such as far-field photoluminescence (PL) spectroscopy and Raman spectroscopy. Due to their low spatial resolution, however, these techniques measure an ensemble of nanocrystallites of differing size and shape. To apply single ZnO nanocrystallites to opto-electronic devices requires measuring the optical properties of nanometer-scale ZnO structures with nanometer-scale resolution.

This letter reports the observation of single ZnO nano crystallite spectroscopy using an optical near-field technique. Using a UV fiber probe with a subwavelength aperture, we measured the PL spectra and recorded images of single ZnO nanocrystallites, to evaluate their individual crystallinity.

Figure 1 shows the experimental setup, which used a collection-mode near-field optical microscope for spatially and spectrally resolved PL spectroscopy at room temperature. We used a UV fiber probe with aperture (D) and probe diameters of 80 nm and 1.1 μm, respectively. The probe consists of a pure silica core and fluorine-doped cladding. To fabricate this probe, the fiber was first sharpened, using a pulling/etching technique to realize a cone angle of 60° and an apex diameter of less than 10 nm.[7] Next, the sharpened core was coated with 500 nm thick aluminum film. Finally, the top of the core was removed with a focused ion beam to form an aperture. He–Cd laser light (λ=325 nm) was employed to excite the ZnO nanocrystallites. The PL signal was collected by the fiber probe and detected by a cooled charge coupled device through a monochromator [Fig. 1(a)]. Furthermore, for spatially and spectrally resolved imaging, the
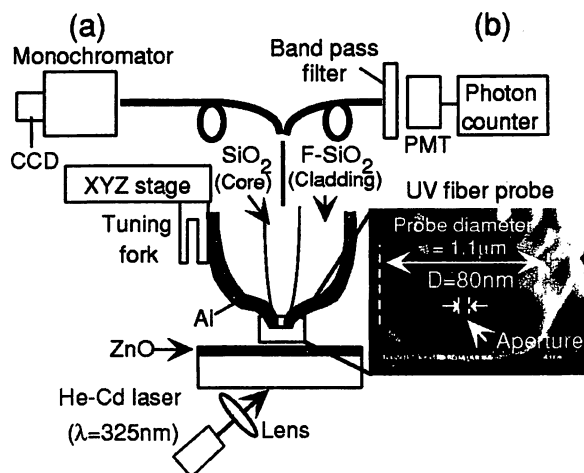

FIG. 1. Experimental setup for near-field spatially and spectrally resolved PL spectroscopy [(a) and (b)]. Inset: UV fiber probe with D=80 nm.

[a]Electronic mail: yatsui@ohtsu.jst.go.jp
[b]Also with: Japan Science and Technology Corporation, 687-1 Tsuruma, Machida, Tokyo, Japan 194-0004.
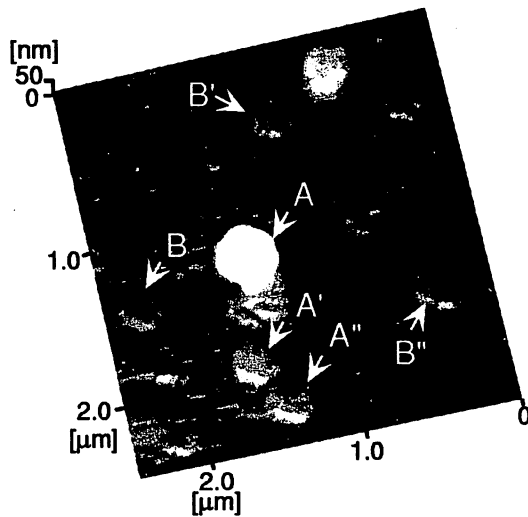
FIG. 2. Topographical image of polycrystalline ZnO.

FIG. 3. Near-field PL spectra of polycrystalline ZnO at room temperature [Fig. 1(a)].

signal collected through the fiber probe and band pass filter was focused on a photomultiplier tube (PMT) to count photons [Fig. 1(b)]. The fiber probe was kept in close proximity to the sample surface ($\sim$10 nm) by the shear-force feedback technique.

ZnO nanocrystallites were prepared by oxidizing Zn deposited by photochemical vapor deposition (PCVD). First, 200 nm thick Zn nanocrystallites were grown on a sapphire (0001) substrate at room temperature by PCVD. Gas-phase diethylzinc (DEZ) at a partial pressure of a few mTorr was used as a gas source. Since DEZ gas has a strong absorption at $\lambda<270$ nm, the second harmonic (SH) light of an Ar$^+$ laser ($\lambda=244$ nm) was used as the light source for the photodissociation of DEZ.[8] The power and spot size of the SH light were 10 mW and 600 μm, respectively. Since the Zn is deposited at room temperature, this method is applicable to NFO-CVD, as it avoids thermal drift of the substrate and the probe. Second, the deposited Zn nuclei were thermally oxidized in ambient oxygen at 1 atm and 750 °C for 30 min.

Figure 2 shows a shear-force image of oxidized Zn, obtained using a sharpened-fiber probe with an apex diameter of 100 nm. Hexagonal (indicated by arrows A, A', and A") and square nanocrystallites (indicated by arrows B, B', and B") can be seen, proving that oxidized Zn is composed of many nanocrystallites with various orientations. The grain sizes were in the range of 150–400 nm, which is comparable to the grain sizes evaluated by a commercial atomic force microscope.

Near-field PL spectra were measured, to investigate the optical properties of the oxidized Zn [see Fig. 1(a)]. Figure 3 shows the room temperature PL spectra, obtained using an apertured UV fiber probe with $D=80$ nm. The emission peak energy was close to the reported value of 3.26 eV ($\lambda=380$ nm), which corresponds to the spontaneous emission from the free exciton in high-quality ZnO nanocrystallites.[2] The full width at half maximum (FWHM) of the PL spectra was about 110 meV, which is comparable with the 117 meV of MBE-grown ZnO nanocrystallites at room temperature.[9] These results imply that the oxidized Zn was composed of high-quality ZnO nanocrystallites. Furthermore, since ZnO has a wurtzite structure, the hexagonal and square nanocrystallites shown in Fig. 2 represent nanocrystallites oriented
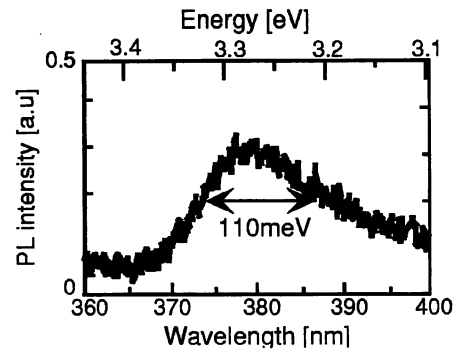
along the c axis[1] and in other directions, respectively. These results imply that fabricated ZnO nanocrystallites are polycrystalline.

Figures 4(a) and 4(b) show a monochromatic PL image and a shear-force image of polycrystalline ZnO, respectively, obtained using the setup in Fig. 1(b). We used an apertured UV fiber probe with $D=80$ nm. The detection wavelength was 380 nm with a spectral bandwidth of 5 nm. Curves A and B in Fig. 4(c) show the cross sectional profile along the dashed white lines in Figs. 4(a) and 4(b), respectively. The arrow in Fig. 4(a) indicates a bright emission spot. Since the 130 nm FWHM of curve A in Fig. 4(c) is comparable to the size of the ZnO nanocrystallites (see Fig. 2), the bright emission spot originated from a ZnO nanocrystallite. The intensity of the bright emission spot was 1.5 times that outside the white ellipse in Fig. 4(a). This indicates that the bright emission spot originated from a ZnO nanocrystallite that protruded from its surroundings. This occurs because the nuclei of Zn islands protruding in three dimensions have a larger total surface area than Zn film grown in two dimensions. Consequently, more oxygen diffuses into the Zn. Thus, the protruding ZnO formed by this diffusion was more crystal-
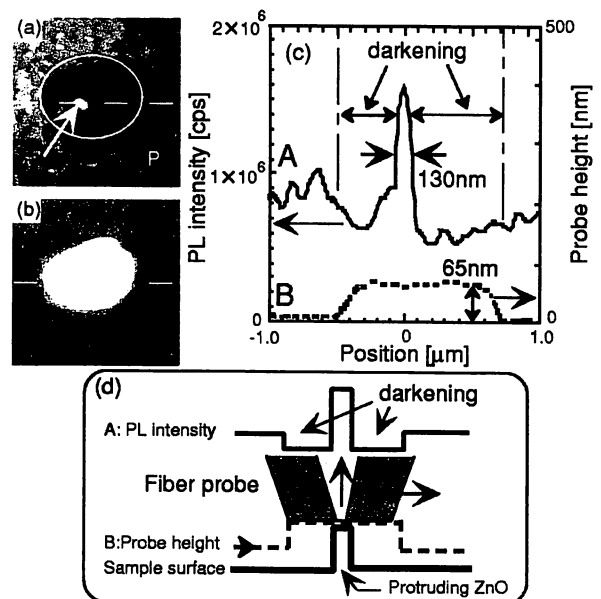

FIG. 4. Monochromatic PL (a) and shear-force (b) images of polycrystalline ZnO. The images are 2.0×2.0 μm. (c) Curves A and B show the cross sectional profile along the dashed white lines in (a) and (b), respectively. (d) A schematic of a scanning apertured fiber probe over a ZnO nanocrystallite that protruded from the surrounding area.
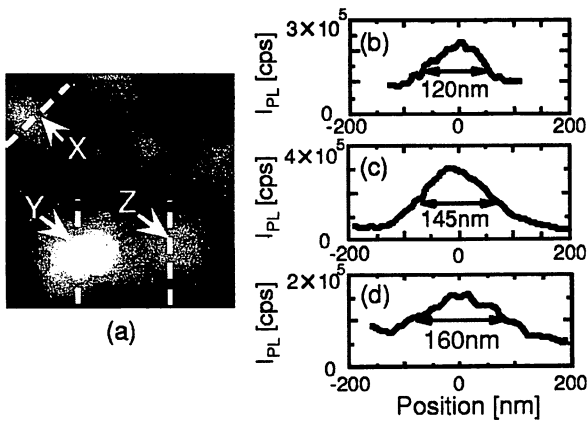
Appl. Phys. Lett., Vol. 79, No. 15, 8 October 2001

Yatsui *et al.*   2371

FIG. 5. (a) Monochromatic PL image of polycrystalline ZnO. The image is 750×750 nm. (b), (c), and (d) show the respective cross sectional profiles along the dashed white lines X, Y, and Z in (a). I_{PL}, PL intensity.

line than its surroundings, and exhibited a high emission capability. Note the dark area around the bright emission spot, which is indicated by the white ellipse in Fig. 4(a) and the white elliptical image in Fig. 4(b). Since the FWHM is comparable to the probe diameter (see Fig. 1) and the height of curve B equals the height of the single nanocrystallite (see Fig. 2), this dark area was a topographic artifact resulting from the protruding ZnO nanocrystallite [see Fig. 4(d)].

Figure 5(a) shows a monochromatic PL image of polycrystalline ZnO from the flat area indicated by P [see Fig. 4(a)], where the roughness was less than 5 nm, as estimated from the shear-force image. This indicates that oxygen diffused uniformly in area P. The detection wavelength was 380 nm with a spectral bandwidth of 5 nm. Figure 5 shows a number of spots with considerably higher emission intensities. Figures 5(b), 5(c), and 5(d) show the respective cross sectional profiles along the dashed white lines through spots X, Y, and Z in Fig. 5(a). Spots X, Y, and Z were 120 nm, 145 nm, and 160 nm in size, respectively, [the FWHM of the curves in Figs. 5(a), 5(b), and 5(c)], which is comparable to the grain size of ZnO nanocrystallites (see Fig. 2). This indicates that each emission spot originated from an individual ZnO nanocrystallite. Here, we roughly estimate the quantum yields (η) of the ZnO nanocrystallite as $\eta = (I_{PL}/E)/(da \exp[-\alpha t])/T=41\%$, where the maximum pick-up PL intensity is $I_{PL}=3.2\times10^5$ [counts per second (cps)], the quantum efficiency of the detector is $E=3.0 \times 10^5$ (cps/W), the density of incident light power is $d=2.6\times10^3$ (W/cm^2), the aperture size is $a=5.0 \times 10^{-11}$ (cm^2), the absorption coefficient is $\alpha=2.0 \times 10^5$ (cm^{-1}),[6] the thickness of ZnO is $t=2.0\times10^{-5}$ (cm), and the collection efficiency of the probe is $T=1.0\times10^{-3}$.[10]

Due to the flat surface of polycrystalline ZnO in area P, the difference in the PL intensity should not be attributed to a topographic artifact. Furthermore, since we did not observe any shift in the peak energy in the PL spectrum which can occur due to differences in crystallinity,[6] the crystallinity of polycrystalline ZnO in area P is considered uniform. Since a comparison of Figs. 5(b), 5(c), and 5(d) does not show a correlation between the PL intensity and spot size, the difference in the PL intensity between the emission spots is attributed to differences in the orientation of the ZnO crystallines. The low spatial resolution of the shear-force image does not establish the orientation of the ZnO crystallines. However, it is reasonable to consider that spot Y, which has the highest intensity and quantum yield[11,12] of the spots in Fig. 5(a), originated from a nanocrystallite oriented along the c axis. This conclusion is further supported by the fact that the exciton density with wave vector is greatest along the c axis.[13]

In summary, we carried out a two-dimensional evaluation of the optical properties and crystallinity of polycrystalline ZnO at room temperature. Using a UV fiber probe, we obtain spatially and spectrally resolved PL spectra from individual ZnO nanocrystallites. It was found that emission intensity depended on topography and on crystal orientation. Furthermore, since the ZnO deposition technique reported here is applicable to NFO-CVD, the high spatial resolution capability of the optical near-field technique could be used to fabricate size- and position-controlled nanometer-scale optoelectronic devices with high crystallinity.

[1] Z. K. Tang, G. K. L. Wong, P. Yu, M. Kawasaki, A. Ohtomo, H. Koinuma, and Y. Segawa, Appl. Phys. Lett. **72**, 3270 (1998).

[2] D. M. Bagnall, Y. F. Chen, Z. Zhu, T. Yao, M. Y. Shen, and T. Goto, Appl. Phys. Lett. **73**, 1038 (1998).

[3] S. Cho, J. Ma, Y. Kim, Y. Sun, G. Wong, and J. B. Ketterson, Appl. Phys. Lett. **75**, 2761 (1999).

[4] Y. Yamamoto, M. Kourogi, M. Ohtsu, V. Polonski, and G. H. Lee, Appl. Phys. Lett. **76**, 2173 (2000).

[5] G. H. Lee, Y. Yamamoto, M. Kourogi, and M. Ohtsu, Proc. SPIE **3791**, 132 (1999).

[6] G. H. Lee, Y. Yamamoto, M. Kourogi, and M. Ohtsu, Thin Solid Films **386**, 117 (2001).

[7] *Near-field Nano/atom Optics and Technology*, edited by M. Ohtsu (Springer, Berlin, 1999), Chap. 3.

[8] R. R. Krchnavek, H. H. Gilgenm, J. C. Chenm, P. S. Shaw, T. J. Licata, and R. M. Osgood, J. Vac. Sci. Technol. B **5**, 20 (1987).

[9] Y. Chen, D. M. Bagnall, H. J. Ko, K. T. Park, H. Hiraga, Z. Zhu, and T. Yao, J. Appl. Phys. **87**, 3912 (1998).

[10] T. Saiki and K. Matsuda, Appl. Phys. Lett. **74**, 2773 (2000).

[11] C. S. Sun, T.-L. Chiu, S. Keller, G. Wang, M. S. Minsky, S. P. DenBaars, and J. E. Bowers, Appl. Phys. Lett. **71**, 425 (1997).

[12] H. Ohta, M. Orita, M. Hirano, and H. Hosono, J. Appl. Phys. **89**, 5720 (2001).

[13] S. Bloom and I. Ortenburger, Phys. Status Solidi B **57**, 561 (1973).

化学エッチングに基づく石英系光ファイバの評価法

物部 秀二†a)　　　大津 元一††

Characterization of Silica Optical Fibers Based on Chemical Etching

Shuji MONONOBE†a) and Motoichi OHTSU††

あらまし　我々はサブミクロンサイズの分解能をもつ石英系光ファイバの評価法を提案する．本方法は光ファイバの緩衝フッ化水素水溶液中でのエッチングと電子顕微鏡観察に基づいて行われる．

キーワード　光ファイバ，エッチング，石英ガラス，緩衝フッ化水素水溶液，走査型電子顕微鏡

1. まえがき

新しい光ファイバの開発においては，その構造パラメータ（例えばコア径，比屈折率差など）を測定し，光ファイバの評価をする必要がある．これまで市販の多モードファイバと単一モードファイバを評価するためには，near field pattern [1] や side-view [2] と呼ばれる光学干渉法が使用されてきた．しかし，光の回折限界のために，これらの方法によってサブミクロン（< 10^{-6}m）サイズの構造や複雑な多段屈折率分布について調べることは困難である．本研究においては，サブミクロンあるいはそれ以下のサイズに相当する高分解能で石英系ファイバを評価するために，化学エッチングに基づく方法を提案する．

2. 方　　法

以下においては，二酸化ゲルマニウム添加石英製コアと純粋石英製クラッドをもつステップ状屈折率分布型ファイバの評価法について述べる．まず，光ファイバをへき開し，25°C に温度制御された40重量％フッ化アンモニウム水溶液：50重量％フッ化水素酸：水 = 10 : 1 : 1の混合体積比をもつ緩衝フッ化水素水溶液（BHF）中でエッチングする．このBHF中において，二酸化ゲルマニウム添加石英の溶解速度は純粋石英の溶解速度よりも小さく，コアとクラッドの溶解速
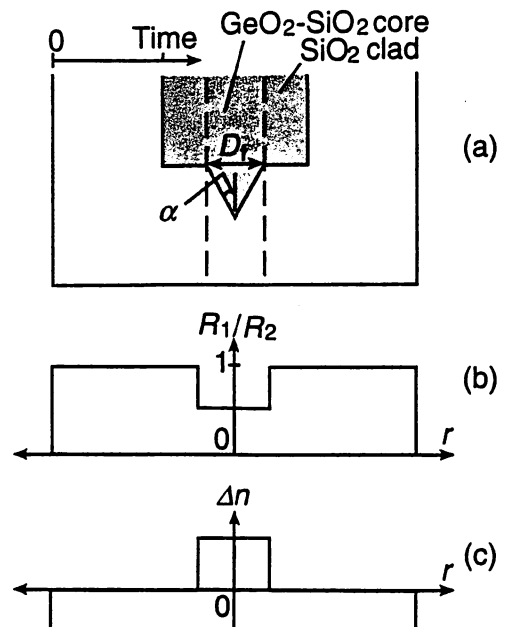
図1　(a) エッチングされたファイバ形状，(b) 溶解速度比 R_1/R_2，(c) 比屈折率差 Δn の断面プロファイル

Fig. 1　Cross-sectional profiles of (a) etched fiber, (b) dissolution rate ratio R_1/R_2, and (c) relative refractive index difference Δn.

度比をそれぞれ R_1 と R_2 で表すと，$R_1 < R_2$ である．このとき，コアは図1(a) に示されるようにテーパ角度 α でクラッドから突出し，テーパ角度 α は幾何学的関係から次式

$$\sin(\alpha) = R_1/R_2 \tag{1}$$

で表される [3],[4]．突出部の根元径 D_f はコア径に相当する．図1(b),(c) はそれぞれ光ファイバの溶解速度比と比屈折率差の断面プロファイルを示す．次に，ファイバをナノメータ（10^{-9}m）レベルの分解能をもつ走査型電子顕微鏡（SEM）によって観察し，テーパ角度 α とコア径を測定する．式(1) の右辺は二酸化ゲルマニウムの添加量を反映し，図2に示されるように比屈

† 神奈川科学技術アカデミー，川崎市
　Special Research Laboratory of Optical Science, Kanagawa Academy of Science and Technology, KSP East 408, 3-2-1 Sakado, Takatsu-ku, Kawasaki-shi, 213-0012 Japan
†† 東京工業大学大学院総合理工学研究科，横浜市
　Interdisciplinary Graduate School of Science and Engineering, Tokyo Institute of Technology, Yokohama-shi, 226-8502 Japan
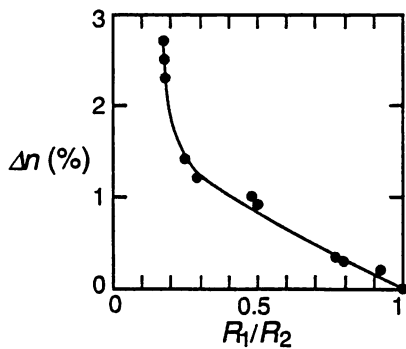a) E-mail: mononobe@net.ksp.or.jp

図 2 比屈折率差 Δn の溶解速度比 R_1/R_2 に対する依存性

Fig. 2 Dependence of the relative refractive index difference Δn on the dissolution rate ratio R_1/R_2.
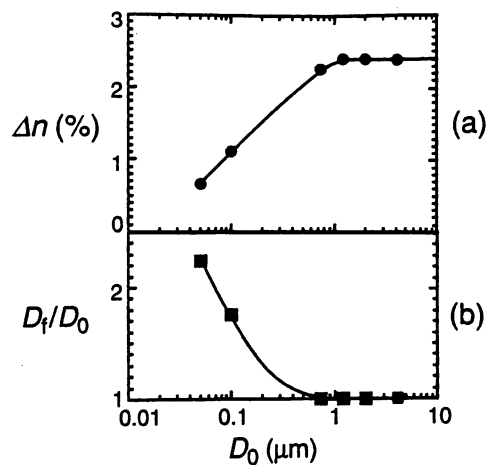

図 3 (a) 比屈折率差 Δn と (b) 測定値 D_f と式 (2) で与えられる比例減少計算値 D_0 のコア径比の D_0 に対する依存性

Fig. 3 Dependencies of (a) the relative refractive index difference Δn and of (b) the ratio of the core diameters D_f and the proportionally reduced diameter D_0 on D_0 given by Eq. (2).

折率差 Δn に依存するので，SEM によって測定されるテーパ角 α, 式 (1)，図 2 の依存性からナノメータの分解能で比屈折率差を見積もることができる．

3. 結果と考察

本方法のサブミクロンサイズの分解能を実証するために，クラッド径 $D_2 = 125\mu$m と $0.1\sim4\mu$m の範囲のコア径をもつ二酸化ゲルマニウム添加石英製ファイバを VAD 法 [5] により設計作製し，その比屈折率差を見積もった．作製において，これらのファイバは比屈折率差 $\Delta n_0 = 2.4\%$ の母材ロッドを加熱延伸することにより線引きされた．線引き時の張力値は $50\sim70$g であった．図 3(a),(b) はそれぞれ比屈折率差 Δn と SEM 測定コア径の比例縮小コア径に対する比 D_f/D_0 の D_0 に対する依存性を示す．光ファイバ線引き前の母材ロッドのコアとクラッドの直径をそれぞれ D_{P1} と D_{P2} とすると，D_0 は次式

$$D_0 = D_{P1} \cdot D_2/D_{P2} \tag{2}$$

によって定義される．

$D_0 < 1\mu$m の領域では，比屈折率差 Δn は母材における値の 2.4% より低下し，コア径が計算値 D_0 よりも拡大する．これらは線引き時におけるゲルマニウムの拡散の影響であると考えられる．0.1μm のコア径をもつファイバの比屈折率差を測定したのは我々の知る限りこれが初めてであり，本方法がサブミクロンサイズ

の構造をもつ光ファイバを評価するのに非常に効果的であることがわかる．

4. む す び

我々は選択エッチングと電子顕微鏡観察に基づく光ファイバ評価法を提案した．本方法により 0.1μm のコア径で設計された光ファイバの比屈折率差が線引き時に低下することを確認し，本方法がサブミクロンオーダの分解能をもつことを実証した．

文 献

[1] D. Gloge and E. A. J. Marcatili, "Multimode theory of graded core fibers," Bell Syst. Tech. J., vol.52, p.1563, 1973.

[2] Y. Hattori and A. Inoue, "Measurement of structural parameters of single-mode fiber by side-viewing method," OFC '88, 1998.

[3] 物部秀二, 学位論文, 東京工業大学, 1999, http://www.kast.or.jp/Mononobe.pdf/.

[4] 物部秀二, 大津元一, "光ファイバの選択エッチングとその応用," New Glass, vol.15, no.2, pp.47-50, 2000.

[5] T. Izawa and S. Sudo, Optical fibers: Materials and fabrication, KTK Scientific, Tokyo, 1987.

（平成 13 年 6 月 20 日受付）

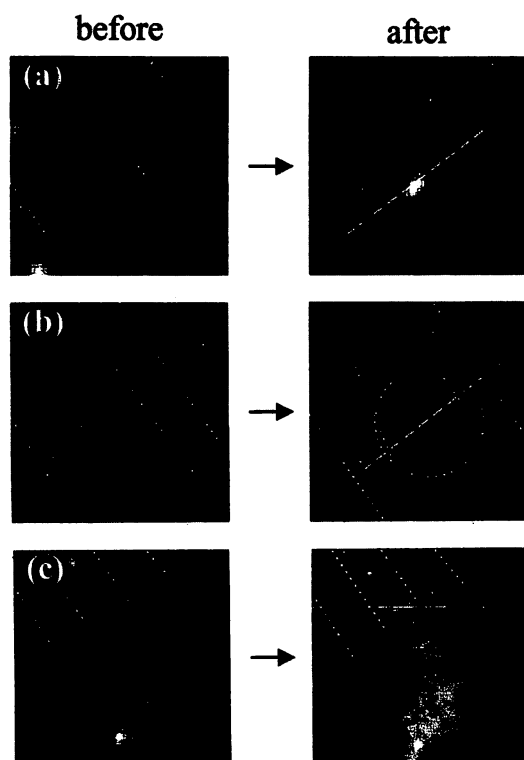# Fabrication of a nanometric Zn dot by nonresonant near-field optical chemical-vapor deposition

Tadashi Kawazoe[a]

Exploratory Research for Advanced Technology, Japan Science and Technology Corporation, 687-1 Tsuruma, Machida, Tokyo 194-0004, Japan

Yoh Yamamoto and Motoichi Ohtsu[b]

Interdisciplinary Graduate School of Science and Engineering, Tokyo Institute of Technology, 4259 Nagatsuta, Midori-ku, Yokohama 226-8502, Japan

We demonstrate a technique for the deposition of nanometric Zn dots by photodissociation of gas-phase diethylzinc using an optical near field under nonresonant conditions. The observed deposited Zn dot was less than 50 nm in size. The photodissociation mechanisms are based on the unique properties of optical near fields, i.e., enhanced two-photon absorption, induced near-field transition, and a direct excitation of the vibration-dissociation mode of diethylzinc. © 2001 American Institute of Physics. [DOI: 10.1063/1.1394955]

Optical near fields have been applied to high-resolution optical microscopy, high-density optical memory, atom manipulation, and so on.[1] Their application to nanostructure fabrication has the potential to make high-density nanometric-integrated photonic devices possible.[2] Recently, we demonstrated the feasibility of chemical-vapor deposition (CVD) of Zn dots using optical near-field techniques.[3–5] In our previous research, we utilized the high spatial resolution capability of the optical near field to deposit Zn wires with a width of 20 nm (Refs. 3 and 4) and Zn dots 60 nm in size.[5] The size of the objects deposited by conventional far-field optical CVD techniques was found to be diffraction limited. Conventional optical CVD utilizes a two-step process: photodissociation and adsorption. For photodissociation, the far-field light must resonate the reacting molecular gasses in order to excite molecules from the ground to the excited electronic state.[6,7] The Frank–Condon principle claims that this resonance is essential for excitation.[6] The excited molecules then relax to the dissociation channel, and the dissociated Zn atoms adsorb to the substrate surface. However, for near-field optical CVD (NFO CVD), photodissociation can take place even in nonresonant conditions, due to the inherent properties of the optical near field. In this letter, we examine the NFO CVD of nanometric Zn dots in nonresonant conditions. This technique makes it possible to use various light sources and gas sources for the deposition of a variety of nanometric materials.

Figure 1 shows the experimental setup for NFO CVD. Ultra-high-purity argon (Ar) was used as a buffer gas and diethylzinc (DEZn) as a reacting molecular gas source. The second harmonic ($\lambda = 244$ nm) of an $\mathrm{Ar^+}$ laser was used as a light source that resonates the absorption band of DEZn.[7] The fundamental frequencies of $\mathrm{Ar^+}(\lambda = 488$ nm) and He–Ne($\lambda = 633$ nm) lasers were used as nonresonant light

sources. The fiber probe used for NFO CVD was a high-throughput single tapered UV fiber probe, which was fabricated by pulling and etching a pure silica core fiber.[1] The cone angle of the fabricated fiber probe was 30° and its apex diameter was 30 nm. In order to investigate the deposition effect of nonresonant far-field light, a fiber probe without the usual metal coating, i.e., a bare fiber probe, was used for the deposition. Therefore, the optical far field was generated by light leaking through the circumference of the fiber probe, while the optical near field was generated at the apex, as shown in Fig. 1. The separation between the fiber probe and the sapphire substrate was controlled to within several nanometers by using a shear-force technique.[1] The laser output power from the fiber probe was measured with a photodiode placed behind the sapphire substrate. The sizes of the deposited Zn dots were measured using a shear-force microscope. During deposition, the partial pressure of DEZn was 100 mTorr and the total pressure in the chamber was 3 Torr. Details of the Zn deposition procedures have been reported in a previous work.[5] It should be noted that the deposition of Zn on the fiber probe and the resultant decrease in the efficiency of optical near-field generation are negligible because the deposition time is sufficiently short, as has been pointed out elsewhere.[5,8]

FIG. 1. Experimental setup for chemical-vapor deposition using an optical near field.

---

[a]Electric mail: kawazoe@ohtsu.jst.go.jp

[b]Also at: Exploratory Research for Advanced Technology, Japan Science and Technology Corporation, 687-1 Tsuruma, Machida, Tokyo 194-0004, Japan.

       1184

before   **after**

FIG. 2. Shear-force topographical images before and after NFO CVD at wavelengths of $\lambda = 244$ (a), 488 (b), and 633 (c) nm. The image sizes are 300×300 nm. The observed laser output power and the irradiation time for deposition were 1.6 μW and 60 s (a), 150 μW and 75 s (b), and 240 μW and 300 s (c).

Figure 2 shows the shear-force topographical images before and after NFO CVD on the sapphire substrate with atomic-level steps[9] for $\lambda = 244$ (a), 488 (b), and 633 (c) nm. For Fig. 2(a) ($\lambda = 244$ nm), the laser power was 1.6 μW and the irradiation time was 60 s. Atomic-level step structures 0.4 nm high on the sapphire substrate are clearly observed, as indicated by the dashed lines in the left-hand side of Fig. 2(a) (before the NFO CVD). However, after the NFO CVD (right-hand side), the atomic-level steps disappear and a deposited Zn dot less than 50 nm in diameter appears at the center of the image. This occurs because the optical near field deposited the Zn dot directly under the apex of the fiber probe. Furthermore, since the bare fiber probe also leaked strong far-field light, a Zn layer that covered the atomic-step structures was deposited.

For Fig. 2(b), the laser power was 150 μW and the irradiation time was 75 s. The photon energy at this wavelength ($\lambda = 488$ nm) is higher than the dissociation energy of DEZn, but it is still lower than the absorption edge of DEZn.[7,10] Therefore, it is not absorbed by the DEZn gas. A Zn dot less than 50 nm in diameter appears at the center of the broken circle on the right-hand side of Fig. 2(b). The atomic-level steps in Fig. 2(b) are still observed, despite the leakage of far-field light from the bare fiber probe.

In Fig. 2(c) ($\lambda = 633$ nm), the laser power was 240 μW and the irradiation time was 300 s. Despite the higher power and longer irradiation time, there was no Zn deposition. This shows that the thermal effect of laser irradiation is negligible for Zn deposition.

In Fig. 3, the solid curve is a cross-sectional profile of the Zn dot deposited at 488 nm across the dashed line in Fig.
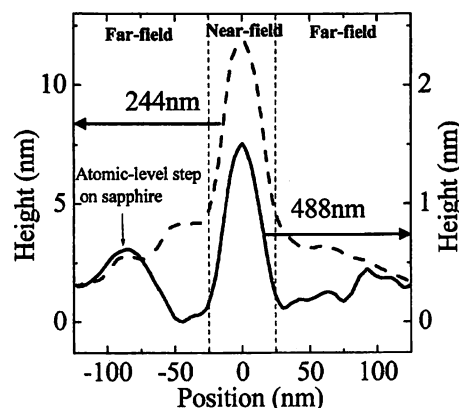
FIG. 3. Cross-sectional profiles of the deposited Zn patterns. Dashed and solid curves represent profiles along the dashed lines on the right-hand side of Figs. 2(a) and 2(b), respectively.

2(b). The dashed curve represents the cross-sectional profile of the Zn dot deposited at $\lambda = 244$ nm, taken across the dashed line in Fig. 2(a). These curves confirm that Zn dots with a full width at a half maximum of 30 nm were deposited in the region where the optical near field is dominant. The dashed curve has tails 4 nm high on both sides of the dot. These tails correspond to the deposition by the leaked far-field light. The solid curve has no tails; thus, it is clear that the leaked 488 nm far-field light did not deposit a Zn layer. This result agrees with previous work using conventional optical CVD for Zn deposition with a far-field light with $\lambda = 300$ nm.[11] It should be noted that the 30 nm Zn dot without tails was deposited under a nonresonant condition, despite the presence of leaked far-field light.

We now discuss the possible mechanisms of DEZn dissociation by the nonresonant optical near field. Figure 4 shows potential curves of an electron in the DEZn molecular orbital drawn as a function of the internuclear distance of a C–Zn bond, which is involved in photodissociation.[7] The relevant energy levels of the molecular vibration mode are also represented by horizontal lines in each potential curve. When using a conventional far-field light, photoabsorption (indicated by a white arrow in Fig. 4) dissociates DEZn.[12] In contrast, there are three possible mechanisms of photodissociation using a nonresonant optical near field. The first is the two-photon absorption process, as indicated by the two arrows ① in Fig. 4, due to the high-energy density of the
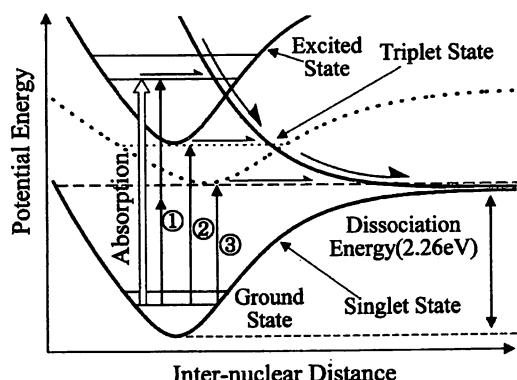
FIG. 4. Potential curves of an electron in DEZn molecular orbitals. The relevant energy levels of the molecular vibration modes are also represented by horizontal lines.

37

optical near field at the apex of the high-throughput fiber probe. The second is the transition, shown by arrow ②, to the intermediate-energy level (dotted curve) induced by the fiber probe and successive relaxation to the dissociative triplet state. Such an induced transition is due to energy transfer between two localized dipole oscillators, i.e., the near-field probe and the DEZn molecules. Similar energy transfer has been observed between optically forbidden levels in dye molecules.[13] The third mechanism involves the transition to an excited state of a molecular vibration mode whose energy is higher than the dissociation energy (2.26 eV), as indicated by the dashed line and arrow ③ in Fig. 4. Although this transition is prohibited by the wave-number conservation law for conventional far-field light,[14] it is allowed in the present case because of the large uncertainty in the wave number of the sub-wavelength-size optical near field. The three mechanisms mentioned above are not adopted when $\lambda = 633$ nm light is used, because its photon energy is lower than the dissociation energy of DEZn and its two-photon energy is also lower than the energy at the absorption edge. This is confirmed by Fig. 2(c).

The experimental results and the suggested mechanisms described above show numerous potential advantages, i.e., this technique not only increases spatial selectivity, but also makes it possible to use various light sources and gas sources not previously used in conventional far-field optical CVD. Thus, nonresonant NFO CVD is a very useful nanofabrication technique.

In conclusion, we demonstrated the deposition of a 30 nm Zn dot using NFO CVD with nonresonant light and discussed the possible mechanisms of deposition. Details of these mechanisms are under investigation, which involves evaluating the dependence of the deposition rate on the optical near-field energy density, the probe–substrate separation, photon energy, and so on.

[1] M. Ohtsu, Near-Field Nano/Atom Optics and Technology (Springer, Tokyo, 1998).
[2] M. Ohtsu, Tech. Dig. Ser.-Opt. Soc. Am. 3749, 478 (1999).
[3] V. V. Polonski, Y. Yamamoto, M. Kourogi, H. Fukuda, and M. Ohtsu, J. Microsc. 194, 545 (1999).
[4] V. V. Polonski, Y. Yamamoto, J. D. White, M. Kourogi, and M. Ohtsu, Jpn. J. Appl. Phys., Part 2 38, L826 (1999).
[5] Y. Yamamoto, M. Kourogi, M. Ohtsu, V. Polonski, and G. H. Lee, Appl. Phys. Lett. 76, 2173 (2000).
[6] J. G. Calvert and J. N. Patts, Jr., Photochemistry (Wiley, New York, 1966).
[7] R. L. Jackson, J. Chem. Phys. 96, 5938 (1992).
[8] M. Ohtsu, K. Kobayashi, H. Ito, and G. Lee, Proc. IEEE 88, 1499 (2000).
[9] M. Yoshimoto, T. Maeda, T. Ohnishi, H. Koinuma, O. Ishiyama, M. Shinohara, M. Kubo, R. Miura, and A. Miyamoto, Appl. Phys. Lett. 67, 2615 (1995).
[10] R. L. Jackson, Chem. Phys. Lett. 163, 315 (1989).
[11] M. Shimizu, H. Kamei, M. Tanizawa, T. Shiosaki, and A. Kawabata, J. Cryst. Growth 89, 365 (1988).
[12] H. Okabe, Photochemistry (Wiley, New York, 1978).
[13] H. Sumi, J. Phys. Chem. B 103, 252 (1999).
[14] M. Balkanski, Optical Properties in Solid, Handbook on Semiconductors (North-Holland, Amsterdam, 1980), Vol. 2.

Diagnostics of Semiconductor Devices beyond the Diffraction Limit of Light

Hiroaki Fukuda[1,2,*], Toshiharu Saiki[3,4] and Motoichi Ohtsu[1,5]

[1]Interdisciplinary Graduate School of Science and Engineering,
Tokyo Institute of Technology, 4259 Nagatsuda, Midori-ku, Yokohama 226–8502, Japan
[2]Research and Development Center, Richo Co., Ltd.,
16–1 Shineicho, Tsuzuki-ku, Yokohama 224–0035, Japan
[3]Kanagawa Academy of Science and Technology
3–2–1 Sakado, Takatsuku, Kawasaki 213–0012, Japan
[4]Depertment of Applied Physics, The University of Tokyo,
7–1 Hongo, Bunkyo-ku, Tokyo 113–8656, Japan
[5]Localized Photon Project, ERATO, Japan Science and Technology,
Tenko Building #17 687–1 Tsuruma, Machida-shi, Tokyo 194-0004, Japan

Near-field photocurrent measurements are applied to the diagnostics of the *p-n* junction of semiconductor devices beyond the diffraction limit of light. In order to probe the internal properties of these devices, modes of propagation into the sample are utilized, retaining high resolution as a result of the contribution of a penetration depth smaller than the aperture diameter of the probe. Near-field photocurrent measurements with multi-wavelength excitation are applied to investigate a lateral *p-n* junction grown on patterned GaAs(111)A. The slant angle of the *p-n* junction interface is determined to be $30\pm8°$. The minority carrier diffusion lengths of the electron L_n and the hole L_p of the Si *p-n* junction are estimated to be 0.47 ± 0.03 and 0.37 ± 0.02 μm, respectively. Near-field photocurrent measurements are also applied to the *p-n* junction on a Si substrate under the reverse-bias condition in order to estimate the dopant concentration of the *p-n* junction. The full-width at half maximum (FWHM) of the cross-sectional profile of the near-field photocurrent signal varied upon changing the applied reverse-bias voltage, according to the resulting change in the thickness of the depletion region. From the measured reverse-bias dependence of the FWHM of the cross-sectional profile, the local dopant concentration of the Si substrate was estimated to be $3.5\pm0.4\times10^{16}$ cm^{-3}. This result shows good agreement with the dopant concentration (3.1×10^{16} cm^{-3}) evaluated from the device specifications for device fabrication.

---

*Corresponding author, e-mail address: fukuda@rdc.ricoh.co.jp

1. Introduction

The recent miniaturization of semiconductor devices and circuits has made their diagnostics and analyses more difficult. Nondestructive and direct characterization of the microstructure of semiconductor devices has emerged as an important approach to understanding and improving the performance of these devices. Existing analytical tools yield the measured device parameter averaged over a large area. The electron-beam induced current method (EBIC)[1,2] and optical-beam induced current method (OBIC)[3] have been employed as useful analytical tools which measure the diffusion length of the minority carriers. However in these methods, the spatial resolution is limited to ~1 μm, and sample contamination and damage are serious problems. In the OBIC method, the diffraction of light limits the resolution. The dopant concentration is an important issue in semiconductor devices because it directly affects the device characteristics. Secondary ion mass spectroscopy (SIMS), which has been widely used to measure the dopant profile of semiconductor devices, can damage the sample and also lacks spatial resolution capabilities.

The near-field optical microscope (NOM) has been employed for the spatially resolved observation of subwavelength structures on the surface by overcoming the diffraction limit of conventional optical microscopes. Furthermore, NOM has been applied for imaging nanometric biological specimens, spectroscopy of semiconductor devices, high-density optical storage, atom manipulation, and nanostructure fabrication.[4-5] The near-field photocurrent measurements carried out with a near-field optical microscope have revealed useful information on semiconductor p-n junctions.[6-8]

In this paper, we review our results of near-field photocurrent measurements of semiconductor devices. After presenting the principle of the near-field photocurrent measurement system in section 2, the fabrication technologies of probes will be described in section 3. In section 4, the interaction between the optical near-field and high-refractive-index materials will be presented. Section 5 presents the experimental results of the near-field photocurrent measurements on a lateral p-n junction grown on patterned GaAs(111)A and a Si p-n junction. Section 6 gives the summary.

2. Principle of the Near-Field Photocurrent Measurement System

Figure 1 shows the experimental setup and sample structure. Operation of the near-field optical microscope in the illumination mode (I mode), where the optical near-field is generated from the subwavelength aperture at the fiber tip, is currently the most common method of selectively illuminating the sample. The electrode configuration for near-field photocurrent measurements of the p-n junction is also depicted in this figure. In order to maintain near-field excitation, the shear-force technique[9,10] was employed to maintain the separation between the fiber probe and the sample surface of 20 nm. All measurements were carried out under ambient conditions.

For excitation, light from an Ar⁺ laser (λ = 351, 458 and 515 nm), He-Ne laser (λ = 633 nm), and Ti:sapphire laser (λ = 780 and 830 nm) are coupled to the fiber probe. Using this light, the optical penetration depth of the semiconductor substrates can be tuned. When the
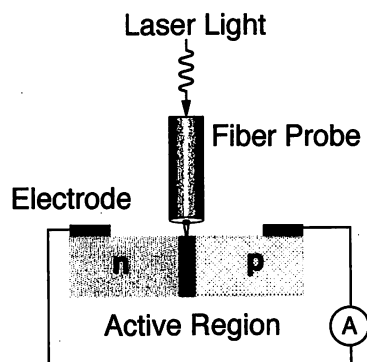
Fig. 1.   Experimental setup of the near-field photocurrent measurements.

optical near-field of the fiber probe tip generates electron-hole pairs in the sample, the respective minority carriers diffuse away over an average diffusion length before the recombination. The induced near-field photocurrent signal is thus proportional to the number of carriers. The signal is collected at the electrodes while scanning the probe across the *p-n* junction. Then the collected signal is amplified with a current injection preamplifier and synchronously detected with a lock-in amplifier as a function of the position of the fiber probe across the surface of the *p-n* junction.

3.   Fabrication of Probes

The fiber probe with the nanometer-scale aperture is the most essential device of the NOM. Several methods have been proposed for fabricating the probe.[4,5] A selective etching method using buffered hydrofluoric (HF) acid, which is widely employed in VLSI chip fabrication, is applied to sharpen an optical fiber. This method has achieved high reproducibility and realized a nanometer-scale tip diameter of the fiber probe. Section 3.1 describes the fabrication method of the high-sensitivity probe with a double-tapered structure. A novel fiber probe with a pure silica core is prepared for the ultraviolet (UV) near-field light source, which is described in section 3.2.

3.1   *Double-tapered fiber probe*

Figure 2(a) shows a scanning electron micrograph of the fiber probe used for the measurements. One of the advantages of a chemically etched probe is its extremely short light propagation length in a metal-cladding waveguide, which reduces the transmission efficiency of the probe.

An optical fiber with a germanium-dioxide (GeO_2)-doped core was used to fabricate the fiber probe. The core diameter of this fiber was 2 μm and the clad diameter was 125 μm. The fiber probe was fabricated by a two-step etching method.[4] The fiber was etched for 60 min in a buffered hydrogen fluoride (BHF) solution containing NH_4F (40 wt%), HF (50 wt%) and H_2O with the volume ratio of 1.7:1:1. Next, the fiber was etched for 40 min in
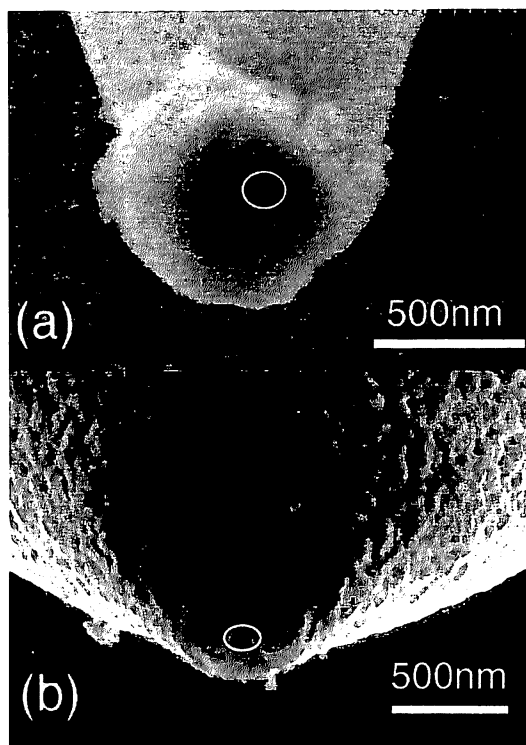
Fig. 2. Scanning electron microscope images of fiber probes. (a) Double-tapered fiber probe. (b) Fiber probe for UV region. White circle in these images represents the aperture. The diameters are 100 nm (a) and 150 nm (b).

NH_4F, HF and H_2O with the volume ratio of 10:1:1. The temperature of the BHF solution was maintained at 25 ± 0.1°C. The sharpened fiber probe was coated with 300-nm-thick Au. A subwavelength aperture was fabricated by pounding the metal-coated fiber probe on the Si substrate and squeezing the Au off to the side.[11] The diameter of the fabricated aperture was 150 nm.

The transmission efficiency was 5.0×10^{-3}, as estimated by collecting the far-field throughput with a 0.4-numerical-aperture objective lens.

3.2 Fiber probe for UV region

A novel fiber probe with a pure silica core is fabricated for the UV near-field light source. Because the conventional GeO_2-doped fiber exhibits strong optical absorption in the UV region, a single-mode fiber with a pure silica core and fluorine cladding is alternatively used to fabricate the fiber probe. The core diameter of this fiber is 10 μm and the clad diameter is 125 μm. After sharpening using a micropipette puller with a CO_2 laser as the heat source, the fiber probe is fabricated by selective chemical etching in BHF solution.[5,10]

Because of the pulling process, the diameter at the end of the tapered core is reduced to about 1 μm. The fiber is etched for 9 min in BHF containing NH_4F (40 wt%), HF (50 wt%) and H_2O with the volume ratio of 1.7:1:1. The temperature of BHF is 25 ± 0.1°C. This etching process is performed until the core is exposed from the cladding of fluoride-doped glass. To fabricate an aperture of subwavelength diameter (~100 nm), the sharpened fiber probe is coated with Al (300 nm thick).

The transmission efficiency is 1×10^{-5}, which is estimated by collecting the far-field throughput with a 0.4-numerical-aperture objective lens. Figure 2(b) shows a scanning electron micrograph of the fabricated fiber probe.

4. Interaction between Optical Near-Field and High-Refractive-Index Materials

The light emitted through the fiber probe has both optical near-field modes and propagating modes. The distribution of optical near-field modes in the tangential wave vector $k_{//}$ (component parallel to the surface) is determined by the aperture diameter d of the fiber probe. If d is less than half the wavelength $\lambda/2$ in free space, the optical near-field modes occupy the region $k_{//} > 2\pi/\lambda$. When the aperture of the probe is set close to an optically dense material, part of the optical near-field mode in the region $k_{//} < n(2\pi/\lambda)$ is converted to the propagating mode, where n is the refractive index of the material. Since Si is a much denser semiconductor material (refractive index of Si is ~5.44)[12] than the silica fiber probe (refractive index ~1.5) and surrounding air, almost all optical near-field modes from the fiber probe are coupled into propagating modes for the entire range of excitation wavelengths (λ = 351–515 nm). For the case of d = 150 nm and n = 4.58 (refractive index of Si at λ = 458 nm), almost all optical near-field modes from the fiber probe are coupled with propagating modes.

The propagating beam spread angle is determined by the aperture diameter. The cutoff wave vector of the optical near-field mode distribution lies at π/d.[7] The propagating beam spread angle is represented by $n(2\pi/\lambda) \sin \phi = \pi/d$. The dependence of the beam spread angle on the excitation wavelength is shown in Fig. 3 for d = 100, 150 and 200 nm. From these results, the beam spread angle of the light is found to be dependent on the excitation wavelength and the aperture diameter of the probe. The propagation modes are governed by the bulk absorption characteristics of the substrate material. Therefore, the resolution is limited by the aperture diameter, the penetration depth of the semiconductor material, and the diffusion length of photoexcited minority carriers.

5. Experimental Results

5.1 *Near-field photocurrent measurements of the lateral* p-n *junction of GaAs(111)A substrate*

Using the multiwavelength excitation light sources, near-field photocurrent measurements are applied to the lateral p-n junction on a patterned GaAs substrate.[13–15] A schematic of the sample structure is shown in Fig 4. After etching a semi-insulating
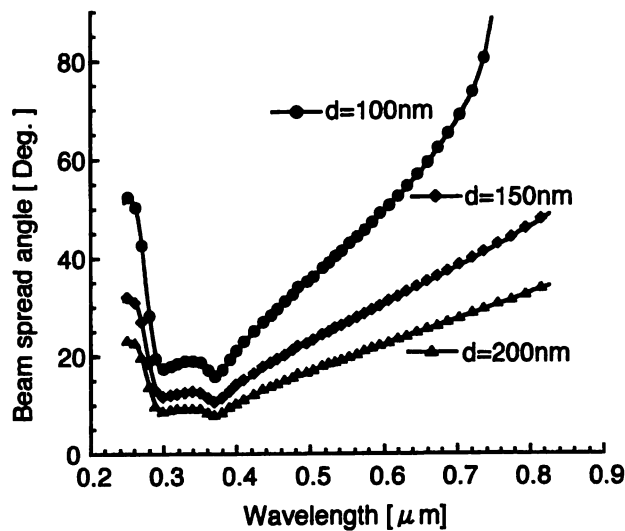
Fig. 3. Dependence of the beam spread angle of mode of propagation into Si on the excitation wavelength. d: aperture diameter.
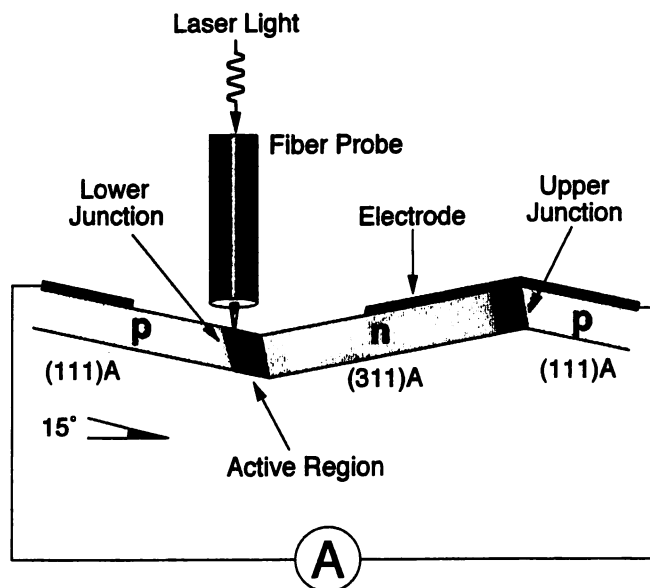
Fig. 4. Structure of lateral p-n junctions and experimental geometry. The lower junction was examined in this measurement. The sample was tilted by 15° in order to avoid contact with the cladding of the fiber probe.

GaAs(111)A substrate by the photolithography technique, 1-μm-thick Si-doped GaAs layers were grown by molecular beam epitaxy (MBE). The silicon concentration in the layer is 1 ×10^{-18} cm^{-3}. Due to the amphoteric nature of the Si dopant in GaAs, the lateral *p-n* junctions are formed at the upper and lower interfaces.[16,17]

A sharpened fiber probe was prepared by the two-step etching method described in section 3.1. After metallizing the exterior surface of the etched probe with 200-nm-thick

gold, a 200-nm-diameter aperture is fabricated by the resin coating method.[4] In order to realize high transmission efficiency, the shape of the tip is optimized by multistep chemical etching. The transmission efficiency is estimated as 1×10^{-3} with a 0.4-numerical-aperture objective lens. As multiwavelength light sources, the Ar^+ laser ($\lambda = 488$ nm), He-Ne laser ($\lambda = 633$ nm), and Ti:sapphire laser ($\lambda = 780, 830$ nm) are coupled into the fiber probe. Using these light sources, the optical penetration depths in GaAs can be tuned from 80 nm to 1.0 μm.

Near-field photocurrent images at the excitation wavelengths of 488 and 830 nm are shown as topographic images in Fig. 5. Uniformity of the photocurrent intensity is seen along the p-n active region. The full-widths at half maximum (FWHMs) of the photocurrent signal profiles are 0.6 and 1.7 μm at $\lambda = 488$ and 830 nm, respectively. The increase of penetration depth results in the decrease of the resolving power. Figure 6 shows the cross-sectional profiles of photocurrent intensities in logarithmic scale. Due to the shallow penetration depth of 80 nm at the excitation wavelength of 488 nm, the resolution is
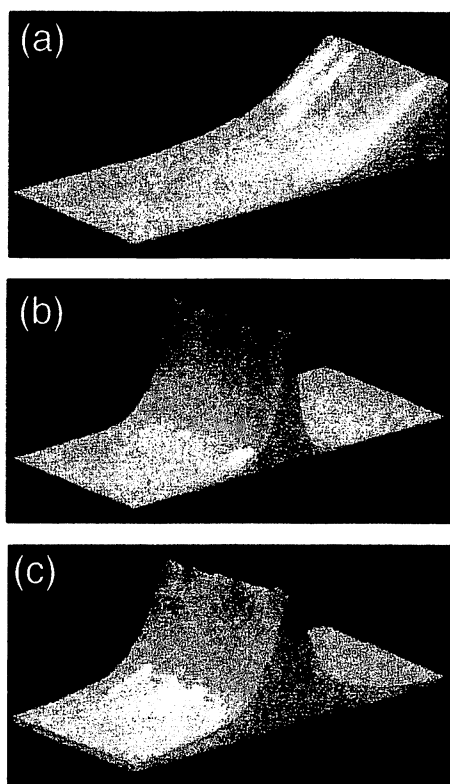
Fig. 5. Perspective views of the topographic image in the vicinity of lower junction (a), and the near-field photocurrent images at the excitation wavelength $\lambda = 488$ nm (b) and $\lambda = 830$ nm (c). The image size is 5×10 μm^2. The height of the slope in (a) is 1 μm.
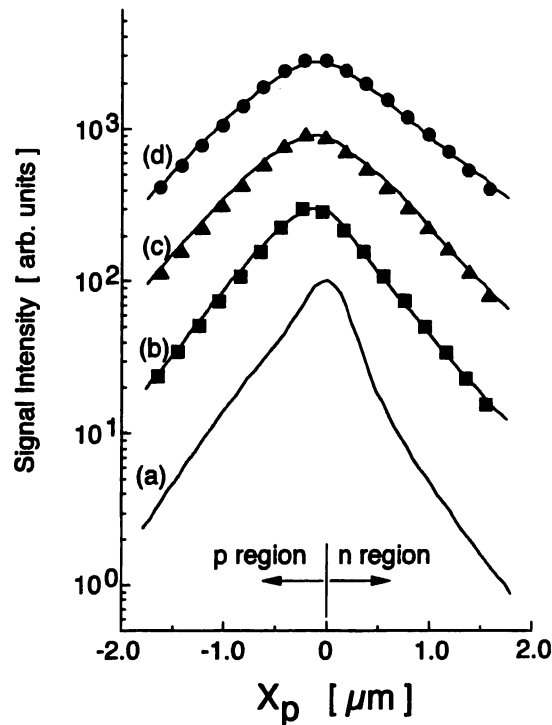
Fig. 6. Cross-sectional profiles of the near-field photocurrent signals at the excitation wavelengths $\lambda = 488$ nm (a), 633 nm (b), 780 nm (c), and 830 nm (d). Black circles, triangles, and squares represent the calculated results for $\phi = 40°$, $37°$ and $27°$, respectively, where $\theta = 15°$.

governed by the aperture diameter and the diffusion length of photogenerated minority carriers. Because of the difference in the diffusion length between electrons and holes, a large difference can be observed in the slower rise of the photocurrent signal in the p region than in the n region, which results in asymmetry of the signal profile. Moreover, with increasing penetration depth, the decay length increases and the asymmetric behavior reverses. The longer decay length in the n region than in the p region is due to the slant of the p-n interface.

The asymmetric signal behavior is analyzed using the one-dimensional model shown in Fig. 7. Here, the fitting parameters are the slant angle of the p-n junction interface θ and the beam spread angle ϕ. The application of this model to curves (b)–(d) in Fig. 6 is appropriate since, for the excitation wavelengths of 633, 780, and 830 nm, the respective penetration depths are much larger than those of the wavelengths in GaAs. With regard to the signal profile of $\lambda = 488$ nm, which is free from longer propagation into the sample, the characteristic decay length of the photocurrent signal due to the carrier diffusion effect is exactly imaged at least in the 200 nm region which is the aperture diameter of the fiber probe. Therefore, curve (a) in Fig. 6 depicts the spatial response profile of the p-n active region.

The spatial response profile of the p-n junction is described by the asymmetric form

$$F(x,z) = C \cdot \exp(x/L_n), \quad x < -z \cdot \tan \theta$$
$$C \cdot \exp(x/L_p), \quad x > -z \cdot \tan \theta, \tag{1}$$
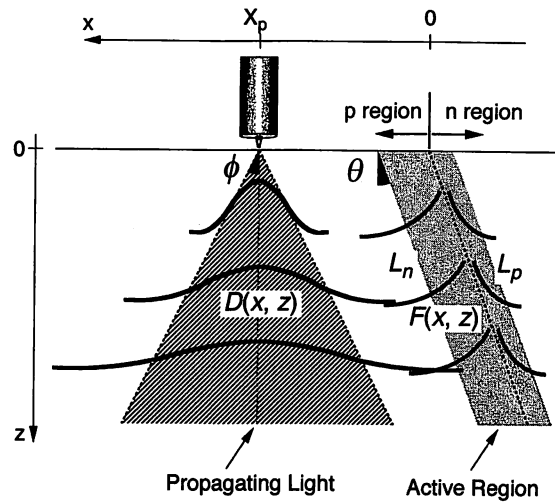
Fig. 7.   Schematic of the slant *p-n* junction interface and the light propagating into the sample.

where C is a normalized constant, and $L_p = 400$ nm and $L_n = 520$ nm are the minority carrier diffusion lengths of the hole and the electron of GaAs, respectively.

For the angular distribution of light propagating into GaAs, we assume the Gaussian profile given by

$$D(x,z) = \frac{\exp\left[\dfrac{-(x - X_p)^2}{(z \cdot \tan\phi)^2}\right]}{z}, \tag{2}$$

where X_p indicates the position of the fiber probe and ϕ is a function of the excitation wavelength. The spatial distribution of light propagating into the substrate is expressed as

$$A(x,z) = \exp\left[\frac{-(x^2 + z^2)^{1/2}}{L_{pd}}\right]. \tag{3}$$

The penetration depths L_{pd} for the excitation wavelengths of 633, 780, and 830 nm are 0.25, 0.65, and 1.0 μm, respectively. The intensity of the photocurrent signal is proportional to

$$I(X_p) = \int_0^d \int_{-\infty}^{\infty} D(x,z)A(x,z)F(x,z)dxdz, \tag{4}$$

where $d = 1.0$ μm is the depth of the *p-n* junction interface.

The experimental curves (b)–(d) in Fig. 6 are perfectly fitted by eq. (4). From this calculation, we obtain the slant angle of the p-n junction interface, $\theta = 15 \pm 8°$. The total slant angle of the p-n junction interface of $30 \pm 8°$ to the p side, which is the sum of the observed slant angle θ of $15 \pm 8°$ and intended tilt angle of $15°$ in the experimental setup, can be explained in terms of the nature of crystal orientation dependence of the growth.[18] The most significant reason is that the growth rate of GaAs on (311)A is faster than that on (111)A, which causes the shift of the n-type region to the p side on growth.

5.2 Near-field photocurrent measurements of Si p-n junction

Near-field photocurrent measurement using multiwavelength excitation sources is applied to evaluate the p-n junction of a Si bipolar transistor.[19] After removing the mold package of the bipolar transistor, the passivation layer and locally oxidized Si layer are etched by reactive ion etching. Furthermore, the surface of the p-n junction on the Si substrate is exposed by HF wet etching. The depth of the p-n junction interface is 0.6 μm. The slant angle of the Si p-n junction interface is $\theta = 0°$ (shown as θ in Fig. 7). When using UV light for excitation, the small penetration depth decreases the region in which photoexcited carriers are generated. The minority carrier diffusion length is determined from near-field photocurrent signals. As a multiwavelength excitation light source, the output light beam from an Ar$^+$ laser (wavelength $\lambda = 351, 458,$ and 515 nm) is coupled to the fiber probe. Using this light, the penetration depth in Si substrate can be tuned from 10 nm to 250 nm.[16] A novel fiber probe with a pure silica core, fabricated by the method described in section 3.2 (Fig. 2(a)), could be used as the UV near-field light source.

Figures 8(a), (b), and (c) show near-field photocurrent images for $\lambda = 351, 458,$ and 515 nm, respectively. The cross-sectional profiles of the near-field photocurrent signals taken along the two arrows in these figures are shown in Fig. 9. The FWHMs of the cross-sectional profiles are 0.6, 0.9, and 1.1 μm, respectively. This wavelength dependence of the FWHM is due to that of the penetration depth. At the excitation wavelength of 351 nm, the resolution is determined by the aperture size of the fiber probe and the diffusion length of photogenerated carriers, because the penetration depth is shallow. Therefore longer excitation wavelength deteriorates the resolution.

By fitting eqs. (1) – (4) to the experimental values in Fig. 9, the diffusion lengths of minority carriers L_n and L_p are estimated to be 0.47 ± 0.03 and 0.37 ± 0.02 μm, respectively. This difference in the diffusion lengths between electrons and holes can be seen in this figure as the slower rise of the photocurrent signal in the n region than in the p region.

5.3 Near-field photocurrent measurements of Si p-n junction under the reverse-bias condition

In this section, we review our results of near-field photocurrent measurements for the reverse-bias p-n junction on a Si substrate and estimate the local dopant concentration of the p-n junction.[20] Figure 10 shows the experimental setup and sample structure. The sample preparation of the Si p-n junction has been described in section 5.2. A fiber sharpened by two-step etching with a 100 nm aperture fabricated by the method described in section 3.1 is used as a probe (Fig. 2(b)). The electrode configuration for near-field photocurrent measurements of the Si p-n junction under the reverse-bias condition is also
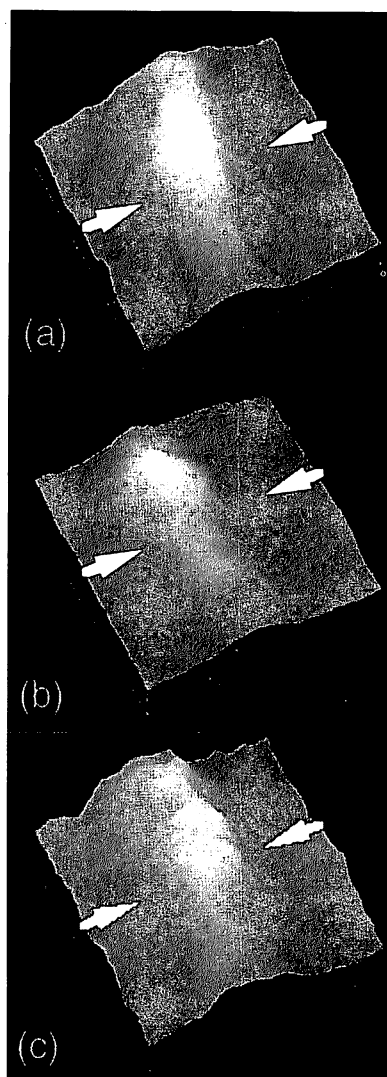
Fig. 8. Perspective views of the near-field photocurrent images at the excitation wavelengths λ = 351 nm (a), λ = 458 nm (b), and λ = 515 nm (c). The image size is 2.5 × 2.5 μm^2.

depicted in Fig. 10. The depth of the p-n junction in the substrate was 0.6 μm. The dopant concentration in the n-type region evaluated from the device fabrication condition is 3.1×10^{16} cm^{-3}.[21] For excitation, the light from an Ar$^+$ laser (λ = 458 nm) is coupled to the fiber probe. The penetration depth of this light into the Si substrate is estimated to be about 277 nm.

Figures 11(a), (b), and (c) show the near-field photocurrent images for the applied
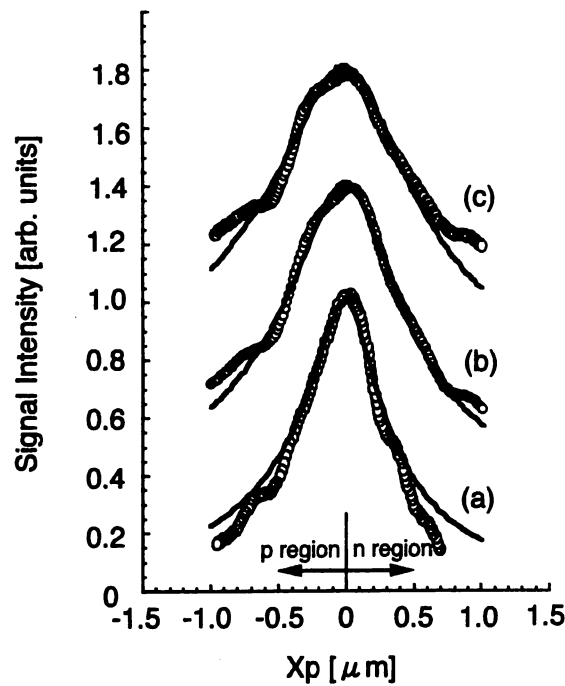
Fig. 9. Cross-sectional profiles of the near-field photocurrent signals at the excitation wavelengths λ = 351 nm (a), 458 nm (b), and 515 nm (c) taken along the two arrows in Figs. 8 (a), (b), and (c), respectively. The solid curves represent the results calculated from eq. (4).
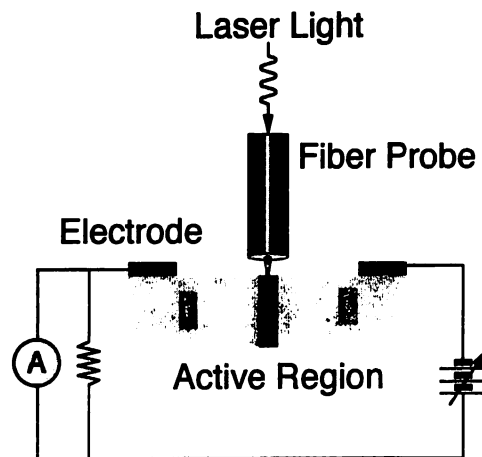
Fig. 10. Experimental setup and the cross-sectional structures of the sample.

reverse-bias voltages of 0 V, 3 V and 5 V, respectively. The uniformity of the decay length of the near-field photocurrent signals is clearly observed under the various reverse-bias conditions along the length of the p-n active region. Figure 12 shows the cross-sectional profiles of the near-field photocurrent intensities averaged over the measurement area. A clear peak of the cross-sectional profiles of the near-field photocurrent signals can be obtained by positioning the aperture above the depletion region. The FWHM of the cross-sectional profiles of the near-field photocurrent signal increases with increasing reverse-
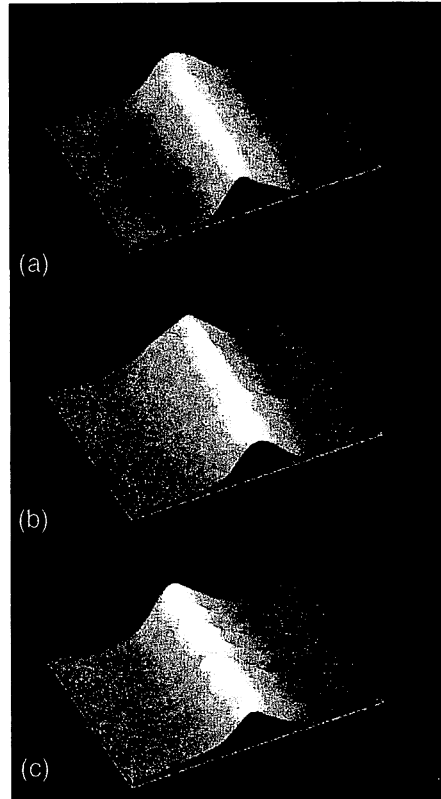
Fig. 11. Perspective views of the near-field photocurrent images under the reverse-biased voltages of 0 V (a), 3 V (b) and 5 V (c). The image size is $6 \times 4 \ \mu m^2$.

bias voltage.

The width of the cross-sectional profile of the near-field photocurrent signal increases according to the increase in the thickness of the depletion region with increasing reverse-bias voltage. Because the decay length of near-field photocurrent signals is constant regardless of the reverse-bias conditions, the relationship between the FWHM of the cross-sectional profile of the near-field photocurrent $W(V_R)$ and the thickness of the depletion region $D(V_R)$ under reverse-bias voltage V_R is described by

$$W(V_R) = D(V_R) + C, \tag{5}$$

where C is a constant. Because the depth of the junction is shallow, $D(V_R)$ is described by the one-side step junction approximation,[22] and is expressed as

$$D(V_R) = \sqrt{2\varepsilon \frac{(V_R + \phi_B)}{q \cdot N_D}}, \tag{6}$$
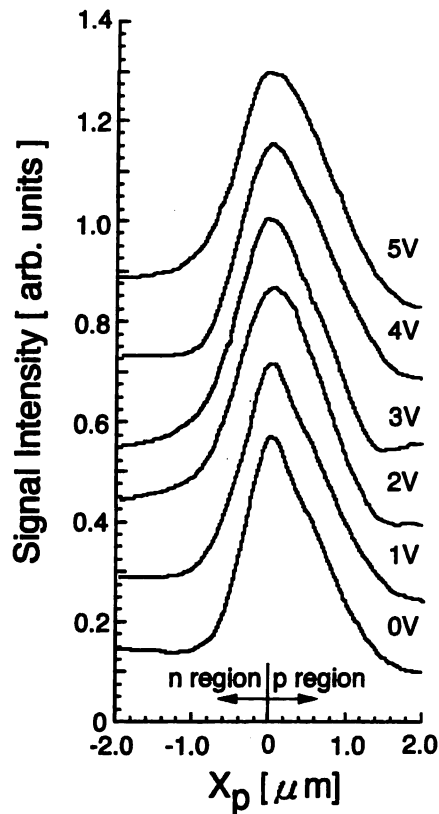
Fig. 12. Cross-sectional profiles of the near-field photocurrent signals under various reverse-biased voltages.

where N_D is the dopant density in the n-type sample, ε is the dielectric constant of Si, $\phi_B = 0.7$ V is the built-in voltage, and q is the electron charge. From eqs. (5) and (6), the difference in the FWHM of the cross-sectional profile of the near-field photocurrent between the reverse-bias V_R condition and no-bias condition is represented by

$$W(V_R) - W(0) = \sqrt{\frac{2\varepsilon}{q \cdot N_D}} \cdot \left(\sqrt{V_R + \phi_B} - \sqrt{\phi_B} \right). \tag{7}$$

From this equation, we obtain the dopant density N_D in the Si substrate.

Figure 13 shows the dependence of the FWHM of the cross-sectional profile of the near-field photocurrent signals under the reverse-bias condition obtained from Fig. 12. The reverse-bias voltage is varied from 0 V to 5 V. Upon increasing the reverse-bias voltage, the FWHM of the cross-sectional profiles of the near-field photocurrent signal increases. By substituting the slope of the line fitted to the measured values into eq. (7), the value of N_D in the n-type region is estimated to be $3.5 \pm 0.4 \times 10^{16}$ cm^{-3}. This is consistent with the dopant concentration (3.1×10^{16} cm^{-3}) evaluated from the design specifications of
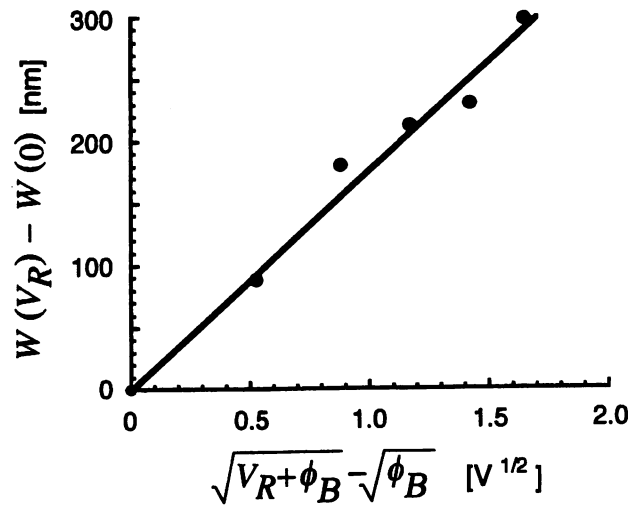
Fig. 13. Relationship between the reverse-biased voltage and the differential of the FWHM of the cross-sectional profile of the near-field photocurrent signals.

device fabrication. This result establishes a simple relationship between the FWHM of the cross-sectional profiles of the near-field photocurrent signal and the applied reverse-bias voltage. Thus, such measurement can be utilized as a simple nondestructive and local method for estimating the dopant concentration of semiconductor substrates and devices.

6. Summary

We have reviewed the application of near-field photocurrent measurements to the diagnostics of p-n junctions of semiconductor devices beyond the diffraction limit of light. Using multiwavelength excitation sources, we demonstrated that the near-field photocurrent measurement applied to the lateral p-n junctions of GaAs and Si is a powerful technique for investigating not only the surface properties but also the internal structure of bulk devices with high spatial resolution. When the aperture of the probe was close to an optically dense material, the optical near-field modes from the fiber probe were coupled to propagating ones. Since the propagation modes are governed by the bulk absorption characteristics of the substrate material, the resolution is limited by the size of the aperture diameter and the penetration depth of the semiconductor material.

The optical penetration depth into the semiconductor materials depends on the wavelength of the light sources. The increase of penetration depth results in the decrease of the resolution. The smallest penetration depth gives the spatial response profile of the active region, including the carrier transport properties, at the resolution of the aperture diameter.

Near-field photocurrent measurements with multiwavelength excitation were applied to investigate a lateral p-n junction grown on patterned GaAs(111)A. The slant angle of the p-n junction interface was determined to be $30 \pm 8°$. The minority carrier diffusion lengths for electrons L_n and holes L_p of the Si p-n junction were estimated to be 0.47 ± 0.03 and 0.37 ± 0.02 μm, respectively, from the near-field photocurrent signals. Near-field photocurrent

measurements were also applied to the p-n junction on a Si substrate under the reverse-bias condition in order to estimate the dopant concentration of the p-n junction. By increasing the reverse-bias voltage of the p-n junction, the FWHM of the cross-sectional profile of the near-field photocurrent signal increased according to the extent of the depletion region. From these results, the local dopant concentration N_D in the n-type region was estimated to be $3.5 \times 0.4 \times 10^{16}$ cm^{-3}. This result is consistent with the dopant concentration (3.1×10^{16} cm^{-3}) evaluated from the design specifications of device fabrication. From these results, tomographic diagnostics using the near-field photocurrent measurements method will provide new insight for understanding the characteristics of semiconductor devices and photonic devices, and enable reliability studies of industrial semiconductors and failure analysis of semiconductor devices.

References

1 H. J. Leamy: J. Appl. Phys. **53** (1982) R51.
2 W. H. Hackett, Jr.: J. Appl. Phys. **43** (1972) 1649.
3 H. Komoda and K. Shimizu: Jpn. J. Appl. Phys. **33** (1994) 3393.
4 M. Ohtsu: Near-Field Nano/Atom Optics & Technology (Springer-Verlag, Tokyo, 1998).
5 M. Ohtsu: J. Lightwave Technol. **13** (1995) 1200.
6 S. K. Buratto, J. W. P. Hsu, E. Betzig, J. K. Trautman, R. B. Bylsma, C. C. Bahr and M. J. Cardillo: Appl. Phys. Lett. **65** (1994) 2654.
7 M. S. Unlu, B. B. Goldberg, W. D. Hrzog, D. Sun and E. Towe: Appl. Phys. Lett. **67** (1995) 1862.
8 K. Karrai, G. Kolb, G. Abstreiter and A. Schmeller: Ultramicroscopy **61** (1995) 299.
9 E. Betzig, P. L. Finn and J. S. Weiner: Appl. Phys. Lett. **60** (1992) 2484.
10 R. Toledo-Crow, P. C. Yang, Y. Chen and M. Vaez-Iravani: Appl. Phys. Lett. **60** (1992) 2957.
11 T. Saiki and K. Matsuda: Appl. Phys. Lett. **64** (1999) 2773.
12 E. D. Palik: Handbook of Optical Constants of Solids (Academic Press, Orlando, 1985).
13 T. Saiki, N. Saito, J. Kusano and M. Ohtsu: Appl. Phys. Lett. **69** (1996) 644.
14 N. Saito, F. Sato, K. Takizawa, J. Kusano, H Okumura, T. Aida, T. Saiki and M. Ohtsu: Jpn. J. Appl. Phys. **36** (1997) L896.
15 T. Saiki, S. Mononobe, M. Ohtsu, N. Saito and J. Kusano: Appl. Phys. Lett. **67** (1995) 2191.
16 J. M. Ballingall and C. E. C. Wood: Appl. Phys. Lett. **41** (1982) 947.
17 W. I. Wang, E. E. Mendez, T. S. Kuan and L. Esaki: Appl. Phys. Lett. **47** (1985) 826.
18 T. Nishinaga, K. Mochizuki, H. Yoshinaga, C. Sasaoka and M. Washijima: J. Cryst. Growth **98** (1989) 98.
19 H. Fukuda, Y. Kadota and M. Ohtsu: Jpn. J. Appl. Phys. **38** (1999) L571.
20 H. Fukuda and M. Ohtsu: Jpn. J. Appl. Phys. **40** (2001) L286.
21 T. Hyodo, N. Yoshida and H. Watanabe: Ricoh Technical Report **23** (1997) 19.
22 A. S. Grove: Physics & Technology of Semiconductor Devices (John Wiley & Sons Inc., New York, 1967).

COHERENT DIPOLE OSCILLATION INDUCED BY LOCALIZED PHOTONS

K. Kobayashi [1], A. Shojiguchi [2], S. Sangu [1], K. Kitahara [2], and M. Ohtsu [1,3]

[1] Localized Photon Project, Japan Science and Technology, Tokyo, 194-0004, Japan

[2] Division of Natural Sciences, International Christian University, Tokyo, 181-8585, Japan

[3] Interdisciplinary Graduate School of Sciences and Engineering, Tokyo Institute of Technology, Kanagawa, 226-8502, Japan

Owing to rapid progress in nanotechnology, we have been able to explore the excitonic processes in a single semiconductor quantum dot or several coupled quantum dots (QDs). It will become possible to experimentally investigate the exciton dynamics by local excitation of a few QDs selected, with the help of the near-field optical techniques [1]. We then expect essentially different dynamics from what we obtain with optical far fields, which cannot selectively excite QDs arranged in a nanometer scale. The purpose of the study is to reveal new phenomena appeared in such an initially local-coupled QDs system via localized photons.

We consider a model system consisting of N two-level QDs closely configured in a ring and localized photons attached to each QD. Each exciton in QDs can only interact with localized photons in the same QD site while the localized photons can hop between the nearest neighbor sites. Note that equations of motion for the system become nonlinear because the exciton operators in the same site obey the fermionic commutation relation. In order to investigate the dynamics, we solve the equations perturbatively with respect to the exciton-photon interaction, and obtain expressions for the time evolution of the exciton and photon operators, respectively.

Numerical analysis, assuming the total number of QDs sites as eight, indicates that the incident dipole coherence of QD 1 can create a collective oscillation of all the other QDs when the population differences in QDs 4, 5, and 6 are set opposite to the others at time 0. This fact can be also applied to the more intriguing non-radiative case, where a local near-field probe initially sets the alternating dipole coherences. All the dipole coherences except QD 1 gradually oscillate collectively if the sign of the population difference in each QD is set opposite to that of the corresponding dipole coherence (see Fig. 1). According to our analysis on radiation property of the state, it is not exact, but close to the Dicke's superradiant state [2]. The origin and the mechanism of the collective oscillation will be discussed by using an effective Hamiltonian method. In addition, we will show that each state can be classified into four kinds of groups, some of which result in a "ferromagnetic" state or an "anti-ferromagnetic" state with respect to the dipole coherence of the system.

References

[1] M. Ohtsu, K. Kobayashi, T. Kawazoe, S. Sangu, and T. Yatsui, to appear in *IEEE J.*

[2] R. H. Dicke, Phys. Rev. **93**, 99 (1954).
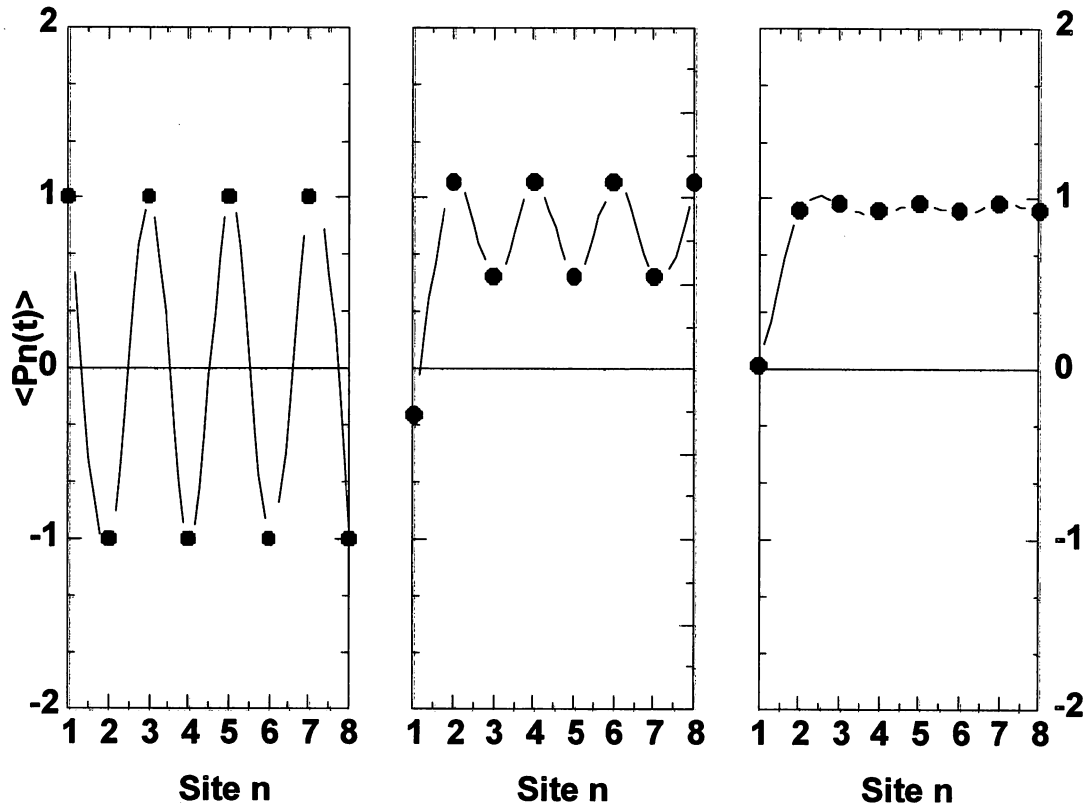
Fig. 1. Time evolution of the dipole coherence for the system. The vertical and horizontal axes represent the dipole coherence and the QDs site, respectively. From the left to the right, a collective oscillation due to the local manipulation of a non-radiative state is depicted as growing (the total number of the QDs sites is eight).

Nano- and atom-photonics: Beyond the fundamental limit of light

Motoichi Ohtsu*

Professor, Interdisciplinary Graduate School of Science and Technology
Tokyo Institute of Technology

This talk reviews recent progress in nano-photonics and atom-photonics which were proposed by myself several years ago in order to open a new field of optical science and technology beyond the diffraction limit of light. Nano-photonics is defined as a technology that utilizes local electromagnetic interactions between a few nanometric element and an optical near field. Since an optical near field is free from the diffraction of light due to its size-dependent localization and size-dependent resonance features, nano-photonics enables fabrication, operation, and integration of nanometric devices. Thus, this technology can solve the technical problems that are faced by the future optical industry. They are (1) increased integration of photonic devices if the data transmission rates of optical fiber transmission systems are to reach as high as 10Tb/s by the year 2015, (2) sub-100nm width pattern fabrication by photo-lithography for increasing the DRAM capacity by the year 2010, and (3) recording and readout of 25 nm pit pattern for realizing 1 Tb/in2 recording density of the optical memory systems by the year 2010.

The primary advantage of nano-photonics is its capacity to realize novel functions based on local electromagnetic interaction. It should be noted that some of the conventional concepts of wave-optics, such as interference, are no longer essential in nano-photonics. Instead, concepts of surface elementary excitation and nano-fabrication technology are essential.

Novel nano-photonic devices and their integration are proposed and theoretical/experimental studies on their functions are reviewed. Chemical vapor deposition by optical near field is also demonstrated to deposit a variety of nanometric materials on a substrate. A prototype of a high density, high speed optical near field memory system is demonstrated.

Finally, recent progress in our works on atom-photonics, manipulating neutral atoms by optical near field, is reviewed. It can open a new field of atom optics, and can be applied to atomic-scale deposition.

(*) also with ERATO Localized Photon Project, Japan Science and Technology Corporation, 687-1 Tsuruma, Machida-shi, Tokyo 194-0004, Japan

18
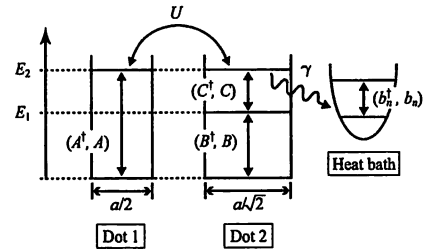
QMC3 Fig. 1. The system consisting of two quantum dots coupled with a heat bath.

QMC3   **8:30 am**

Characteristics of Relaxation Process in an Optically Coupled Quantum-Dots System

Suguru Sangu,[a] Kiyoshi Kobayashi,[a] Akira Shojiguchi,[b] and Motoichi Ohtsu,[a,c] [a]ERATO Localized Photon Project, Japan Science and Technology Corporation, 687-1 Tsuruma, Machida, Tokyo, 194-0004 Japan, Email: sangu@ohtsu.jst.go.jp; [b]Division of Natural Sciences, International Christian University, 10-2, Osawa 3-chome, Mitaka-shi, Tokyo, 181-8585 Japan; [c]Interdisciplinary Graduate School of Science and Engineering, Tokyo Institute of Technology, 4259 Nagatsuda-cho, Midori-ku, Yokohama, Kanagawa, 226-8502 Japan

Optical near-field techniques are considered promising as enabling technologies for fabrication and high-speed operation of novel optical devices in nanometric regime, because of the size-dependent localization far beyond the diffraction limit of light. We have regarded the optical near field as a coupled mode of photons and matter excitation, i.e., polaritons, and derived the interaction between nanometric objects mediated by such field.[1,2] In order to know dynamics of a nanometric device, it is very important to investigate how the signal transfers among quantum components. In this theoretical study, we discuss time evolution of exciton population in the system consisting of two quantum dots with optical near-field illumination.

Figure 1 shows an ideal quantum-dots system with discrete energy levels, which is coupled to a heat bath. The population transfer occurs through optical near-field interaction (coupling constant: U). Irreversibility of energy transfer that must be guaranteed for a functional device is

realized by considering the transition of population with the dissipation to heat bath. Equations of motion for such system can be described by using a density operator, where contribution from the heat bath is traced out and is related to the number of phonons.

As a first step, we use the Markov approximation[3] which may be somewhat rough approximation as described later, and examine the dynamics of population in each energy level, analytically. It follows that two important parameters determine the behavior of population: (1) the ratio of relaxation constant to the optical near-field coupling constant, $\hbar\gamma/2U$, and (2) temperature of the heat bath. In order to illustrate contribution from the first parameter, the time evolution of E_1-level population in the dot 2 is plotted in Fig. 2(a). Three curves correspond to *weak, medium,* and *strong couplings* with lattice vibration ($\hbar\gamma/2U = 0.1, 1,$ and 10). At first glance, the fastest transition to the E_1-level seems to be obtained for the strong coupling. However, it is achieved at $\hbar\gamma/2U \sim 1$. The reason why is that the energy level E_2 in the dot 2 looks blurred against that in the dot 1

QMC3 Fig. 2. (a) Time evolution of E_1-level population in the dot 2 at $T = 0$. The solid, dashed, and dotted curves represent in the cases of $\hbar\gamma/2U = 0.1, 1, 10$, respectively. (b) That of E_2 (solid) and E_1-levels (dashed) in the dot 2 at $T = 10$ K.

because of the strong coupling between the excitons and lattice vibration, that makes the population transfer from the dot 1 to 2 off-resonant. The fluctuation observed at $\hbar\gamma/2U = 0.1$ in Fig. 2(a) is caused by appearance of nutation between E_2-levels in the both dots.

Finite temperature is the origin of residual population in the E_2-levels. In the case of $T \neq 0$, the phonons in the energy level resonant to that in the dot 2 cannot be ignored, leading to energy back transfer from the heat bath to the dot 2. Figure 2(b) shows the E_1 and E_2-level populations in the dot 2, where the results are given from the first-order approximation about γ under the assumption of week coupling. The residual population at equilibrium state in the E_2-level is determined depending on the number of phonons or on the temperature of the heat bath.

The Markov approximation is known to be incorrect at low temperature, in which the time scales of the quantum-dots system and relaxation process are not distinguishable each other.[4] Moreover, a higher-speed operating device will go beyond a limit of the Markov approximation. Our preliminary work shows that any difference between the Markov and non-Markov treatment is not observed in weak coupling regime. The non-Markov behavior in the strong coupling regime is one of the problems to be solved, and now under investigation.

References

1. K. Kobayashi and M. Ohtsu, "Quantum theoretical approach to a near-field optical system," J. Microscopy **194**, 249–254 (1999).

2. K. Kobayashi, S. Sangu, H. Ito, and M. Ohtsu, "Near-field optical potential for a neutral atom," Phys. Rev. A **63**, 013806 (2001).

3. H.J. Carmichael, *Statistical Methods in Quantum Optics 1*, (Springer-Verlag, Berlin, 1999), Chap. 1.

4. K. Lindenberg and B.J. West, "Statistical properties of quantum systems: The linear oscillator," Phys. Rev. A **30**, 568–582 (1984).

native but equivalent approach explicitly expressing localized photonic degrees of freedom is still required for deep understanding of coherent excitation transfer between the QDs and its manipulation by localized photons attached to a so-called nanometric probe. In this paper we report a formulation and simulation based on such a localized photon picture to discuss coherent excitation dynamics of QDs driven by the optical near fields, resulting in an interesting possibility for a photonic switch and source on a nanometer scale.

A model Hamiltonian $\hat{H}$ given by Eq. (1) governs dynamics of an N-two-level-QD system ($\hat{H}_{ex}$) that is configured in a ring. Localized photons described by $\hat{H}_a$ are introduced so that the optical near field is expanded in terms of a basis whose functions are localized in each QD labeled by n, and the photons are allowed to hop only between the nearest neighbors. The usual dipole coupling ($\hat{H}_{int}$) between each QD and each localized photon is assumed as an intradot interaction. Note that the Hamiltonian $\hat{H}_a$ is analytically diagonalized to give a mixed photon basis.[5]

$$\hat{H} = \hat{H}_{ex} + \hat{H}_a + \hat{H}_{int},$$

$$\hat{H}_{ex} = E \sum_{n=1}^{N} \hat{B}_n^\dagger \hat{B}_n,$$

$$\hat{H}_a = \varepsilon \sum_{n=1}^{N} \hat{a}_n^\dagger \hat{a}_n + V \sum_{n=1}^{N} (\hat{a}_{n+1}^\dagger \hat{a}_n + \hat{a}_n^\dagger \hat{a}_{n+1}),$$

$$\hat{H}_{int} = U \sum_{n=1}^{N} (\hat{a}_n^\dagger \hat{B}_n + \hat{a}_n \hat{B}_n^\dagger). \qquad (1)$$

In order to investigate coherent excitation dynamics of the system, we examine time evolution of the expectation value of the dipole coherence at an arbitrary QD n, $\langle \hat{P}_n(t) \rangle = \langle \hat{B}_n(t) + \hat{B}_n^\dagger(t) \rangle$, under a variety of initial conditions. Noting that the exact expression for $\hat{P}_n(t)$ can be obtained if the exciton operator $\hat{B}_n$ is a boson, we first locally set the dipole coherence of QD 1 at time $t = 0$ as $\langle P_1(0) \rangle = 1$ by using a local probe, and then consider whether the dipole coherence is retained within QD 1, or transported to other QDs via localized photons. Figure 1 shows the coherence of QD 1 can be transferred to QD 5 when the total number $N = 8$ (even). This phenomenon depends on whether the total number N is even or odd, and it follows that QDs 4 and 5 are coherently excited in the case of $N = 7$. This kind of transportation of the local dipole coherence can be used for photonic signal switching, or for branching on a nanometer scale.

When the exciton operator $\hat{B}_n$ is a fermion, there is another locally controllable state parameter, the population difference $\langle \hat{W}_n \rangle = \langle \hat{B}_n^\dagger \hat{B}_n - \hat{B}_n \hat{B}_n^\dagger \rangle$, with sacrifice of exact expressions for $\hat{P}_n$ (t). Numerical analysis indicates that the incident dipole coherence of QD 1 can generate a collective oscillation of all the other QDs when the population difference in QDs 4, 5, and 6 are set opposite to the others at time $t = 0$. This fact can be applied to the more intriguing non-radiative case where the alternating dipole coherences are initially set by a local probe. As shown in Fig. 2, all dipole coherences except QD 1 gradually oscillate collectively if the sign of the population difference in each QD is set opposite to that of the corresponding dipole coherence as $\langle \hat{W}_n(0) \rangle = -\langle \hat{P}_n(0) \rangle$. One expects that this is applicable to a tiny photonic source of the order of the total number N.
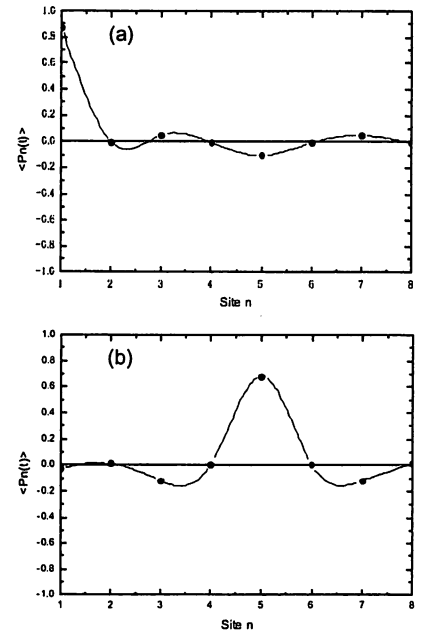
QTuI1   **Fig. 1.**   Time evolution of dipole coherence for the boson case. The vertical and horizontal axes represent the dipole coherence and the QD site, respectively. From (a) to (b), the coherence transfer from QD 1 to 5 is illustrated in the case of $N = 8$.
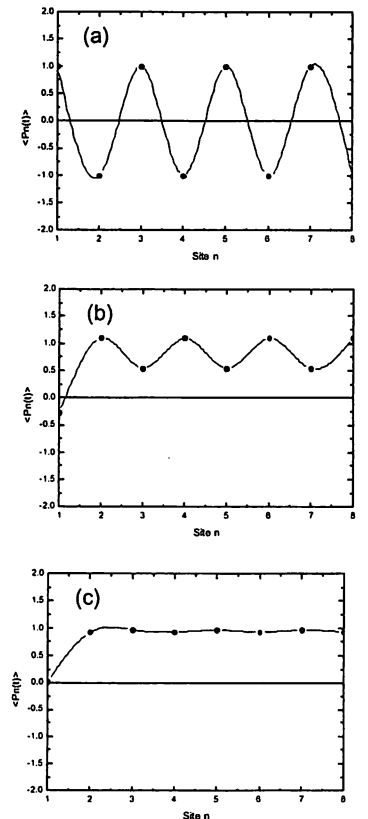
QTuI1   **Fig. 2.**   Time evolution of dipole coherence for the fermion case. The vertical and horizontal axes represent the dipole coherence and the QD site, respectively. From (a) to (c), a collective oscillation due to the local manipulation of a non-radiative state is depicted as growing in the case of $N = 8$.

QTuI   4:45 pm–6:30 pm
Room: 201

Semiconductor Quantum and Nonlinear Optics

Hui Cao, Northwestern Univ., USA, Presider

QTuI1   4:45 pm

Coherent Excitation Dynamics Controlled by Localized Photons

Kiyoshi Kobayashi,[1] Akira Shojiguchi,[2] Suguru Sangu,[1] Kazuo Kitahara,[2] and Motoichi Ohtsu,[1,3]
[1]ERATO Localized Photon Project, Japan Science and Technology, 687-1 Tsuruma, Machida, Tokyo 194-0004, Japan, Email: kkoba@ohtsu.jst.go.jp;
[2]Division of Natural Sciences, International Christian University, 10-2 Osawa 3-chome, Mitaka-shi, Tokyo 181-8585, Japan;
[3]Interdisciplinary Graduate School of Science and Engineering, Tokyo Institute of Technology, 4259 Nagatsuta-cho, Midori-ku, Yokohama, Kanagawa 226-8502, Japan

Much attention has been devoted to a photonic device using nanometric quantum dots (QDs) controlled by optical near fields because of its potential for ultra-high speed and miniaturization.[1-2] Owing to the unique property of localization (or non-propagation) of the field, QDs can interact only with the neighboring QDs without electronic overlapping. The dynamic behavior of the device has been analyzed considering the effective interaction, where the photonic degrees of freedom are effectively renormalized into the resonant interaction between the QDs.[3-4] An alter-

We have developed a novel formulation for a QDs system interacting with localized photons to discuss coherent dynamics of the system, and predicted some intriguing phenomena to be applicable to nanometric photonic devices. Higher order effects in the fermion case, as well as strong vibrational-electronic coupling effects remain as future areas for research.

References
1. See for example, *Optical and Electronic Process of Nano-matters,* M. Ohtsu ed. (Kluwer Academic, Dordrecht, 2001).
2. T. Kawazoe, K. Kobayashi, J. Lim, and M. Ohtsu, "Verification of principle for nanometer size optical near-field switch by using CuCl quantum cubes," CLEO/Pacific Rim 2001, MH2-4, 2001.
3. K. Kobayashi, T. Kawazoe, S. Sangu, J. Lim, and M. Ohtsu, "Theoretical and experimental study on a near-field optical nano-switch," IPR/PS 2001, PThB4, 2001.
4. K. Kobayashi, T. Kawazoe, S. Sangu, and M. Ohtsu, "Proposal for a near-field optical nano-switch," CLEO/Pacific Rim 2001, MH2-3, 2001.
5. See for example, *Resonance Energy Transfer,* D.L. Andrews and A.A. Demidov, ed. (John Wiley & Sons, Chichester, 1999).

Tuesday, May 21

QThB6   **9:15 am**

Dipole-forbidden Energy Transfer between CuCl Quantum Cubes via Optical Near-field

Tadashi Kawazoe,[1] Kiyoshi Kobayashi,[1] Jungshik Lim,[2] Yoshihito Narita,[3] and Motoichi Ohtsu,[1,2]
[1]*Exploratory Research for Advanced Technology (ERATO), Japan Science and Technology Corporation (JST), 687-1 Tsuruma, Machida, Tokyo 194-0004, Japan, Email: kawazoe@ohtsu.jst.go.jp;* [2]*Interdisciplinary Graduate School of Science and Engineering, Tokyo Institute of Technology, 4259 Nagatsuta, Midori-ku, Yokohama 226-8502, Japan;* [3]*JASCO Corporation, 2967-5, Ishikawa-cho, Hachioji, Tokyo, 192-8537, Japan*

The coupled quantum-dots system exhibits more unique properties in contrast with the single quantum-dot system.[1] The optical near-field interaction[2] is interesting, as it can govern the coupling strength among quantum dots. Recently, an ultra-fast energy transfer between bacteriochlorophyll molecules via the optical near field was theoretically shown.[3] This kind of the energy transfer is possible for the neighboring quantum dots system.

The quantized exciton energy levels of (1,1,1) in a CuCl quantum cube (QC) X (4.6 nm) and (2,1,1) in a QC Y (6.3 nm) resonate with each other.[4] For this type of resonant condition, the energy transfer time between QC via the optical near-field is estimated at 40 ps, assuming that the separation between two QCs is equal to 10 nm.[5] This energy transfer time is much shorter than the exciton lifetime and is longer than the inter-sub-level transition τ_{sub}. Therefore, most of the exciton in a 4.6-nm CuCl QC transfer to the neighboring 6.3-nm QC. Here, we note that this energy transfer is optically forbidden, but becomes allowed with the optical near field.[3]

Figure 1(b) shows a far-field luminescence spectrum at 15 K. It represents the luminescence intensity from large numbers of CuCl QCs, and is inhomogeneously broadened owing to the size distribution of the QCs. Figure 1(c) represents a near-field luminescence spectrum with many fine structures. The structures are due to the contribution of the QCs near the apex of the near-field probe with a 50-nm aperture. The peaks X and Y correspond to the confined Z_3-exciton energy levels of the QCs with side lengths of 4.6 nm and 6.3 nm, respectively.

Figures 2(a) and (b) show the near-field optical microscope images for peaks X and Y in Fig. 1 (c), respectively. These images clearly establish anti-correlation features in their intensity distributions, as manifested by the dark and bright regions surrounded by broken curves.

Figure 2(c) shows the values of the cross-correlation coefficient C between the spatial distributions of the luminescence intensity from a 6.3-nm QC and that from a different size QCs. The large negative value of C identified by an arrow (2,1,1) clearly shows the anti-correlation feature between Figs. 2(a) and (b). This anti-correlation feature can be understood by the energy transfer from X cubes to Y cubes. A 4.6-nm QC-, 'accidentally' located close to a 6.3-nm QC cannot emit light, but instead transfers the energy to the 6.3-nm QC. As a result, in the region containing embedded 6.3-nm QCs, the luminescence intensity from 4.6-nm QCs is low while it from 6.3-nm QCs is high. As explained in Fig. 1, it is reasonable to attribute the origin of the interaction to the near-field energy transfer.

For CuCl quantum cubes in a NaCl matrix, other possibility of energy transfer, such as carrier

X: L=4.6nm

Y: L=6.3nm
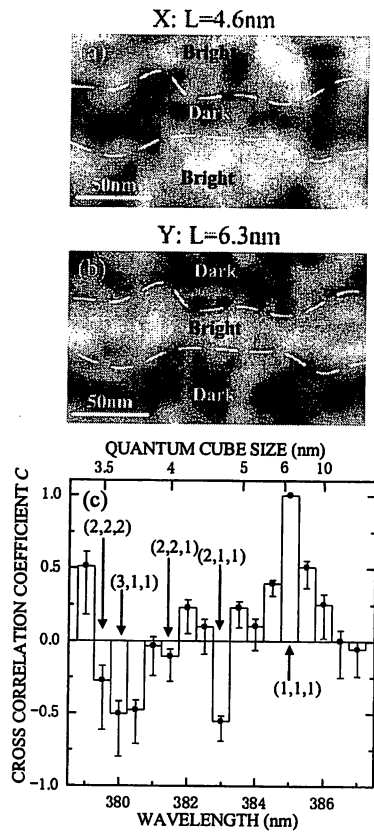
QThB6 **Fig. 2.** (a) and (b): Spatial distributions of the near-field luminescence intensity for peaks marked as X and Y in Fig. 1(c), respectively. (c): Values of the cross-correlation coefficient between the spatial distribution of the intensity of the luminescence emitted from a 6.3-nm QC and that from different size QCs. (1,1,1), (2,1,1), (2,21), (3,1,1), and (2,2,2) are the quantized exciton energy levels in a 6.3-nm QC.

tunneling, Coulomb coupling, and so on, can be neglected due to a deep potential depth and the small exciton Bohr radius. Therefore, we claim the first observation of the dipole-forbidden energy transfer QCs via the optical near field.

References

1. D. Goldhaber-Gordon, J. Göres, M.A. Kastner, H. Shtrikman, D. Mahalu, and U. Meirav, "From the Kondo Regime to the Mixed-Valence Regime in a single-Electron Transistor" Phys. Rev. Lett. 81, 5225 (1998).
2. M. Ohtsu, *Near-Field Nano/Atom Optics and Technology* (Springer, Tokyo, Berlin, Heidelberg, New York, 1998).
3. K. Mukai, S. Abe, and H. Sumi, "Theory of Rapid Excitation-Energy Transfer from B800 to Optically-Forbidden Exciton States of B850 in the Antenna System LH2 of Photosynthetic Purple Bacteria" J. Phys. Chem. B 103, 6096 (1999).
4. N. Sakakura and Y. Masumoto "Persistent spectral-hole-burning spectroscopy of CuCl quantum cubes" Phys. Rev. B 56, 4051 (1997).
5. K. Kobayashi, S. Sangu, H. Ito, and M. Ohtsu, "Near-field optical potential for a neutral atom" Phys. Rev. A 63, 013806 (2000).

Thursday, May 23

CMP5 Fig. 2. (a) and (b) Scanning electron microscope images of the metal-coated Si wedge. (c) Schematic of the experimental set-up used for the collection mode near-field microscope.

CMP5   **2:30 pm**

A Plasmon Waveguide for Optical Far/Near-Field Conversion

T. Yatsui,* T. Abe,** M. Kourogi,*** and
M. Ohtsu,**** *Ohtsu Project, ERATO, Japan Science and Technology Corporation, 687-1 Tsuruma, Machida, Tokyo, Japan 194-0004, Email: yatsui@ohtsu.jst.go.jp; **Interdisciplinary Graduate School of Science and Engineering, Tokyo Institute of Technology, 4259 Nagatsuta, Midori-ku, Yokohama, Japan 226-8502

To increase data transmission rates and capacity in future optical transmission systems, we proposed nanometer-scale photonic integrated circuits that are composed of sub-100-nm scale dots and wires.[1] Since coupling these devices with conventional external devices requires a nanometer-scale waveguide for far/near-field conversion, we propose a plasmon waveguide [see Fig. 1(a)]. The main part consists of a Si wedge and a metal core waveguide. Incoming light is first transformed into the two-dimensional (2-D) surface plasmon (SP) mode on the F1 side [see Fig. 1(c)]. The performance required for this type of waveguide includes: (A) high conversion efficiency, (B) a sub-100-nm beam width for efficient coupling of the converted optical near-field to sub-100-nm dots, (C) a wavelength-order propagation length to avoid direct coupling of the far-field light to the

nanometer-scale dots. Next, the scattering coupling converts the 2-D SP mode into the 1-D TM-plasmon mode at the edge between F1 and the plateau.[2] Third, the TM-plasmon mode propagates along the plateau. This propagation occurs because the metal film deposited on the plateau is thicker than that on the other faces due to the normal evaporation process. Consequently, the plateau acts as a metal core waveguide. Since this waveguide does not have a cutoff,[3] the beam width decreases with the core diameter, to as narrow as 1 nm. Finally, the TM-plasmon mode is converted to the optical near-field.

Using (100)-oriented Si with a thickness of 10 μm, the plasmon waveguide was fabricated by anisotropic etching [Figs. 2(a) and 2(b)]. Illuminating (λ = 830 nm) the F1 face of the waveguide (plateau width 150 nm), we measured the spatial distribution of the electric-field intensity throughout the plateau [Fig. 2(c)]. TE and TM polarization indicate that the incident light polarization is parallel to the x- and y-axis, respectively. A fiber probe P with aperture diameter D_a of 60 nm was used.

Figures 3(a) and 3(b) show the observed elec-
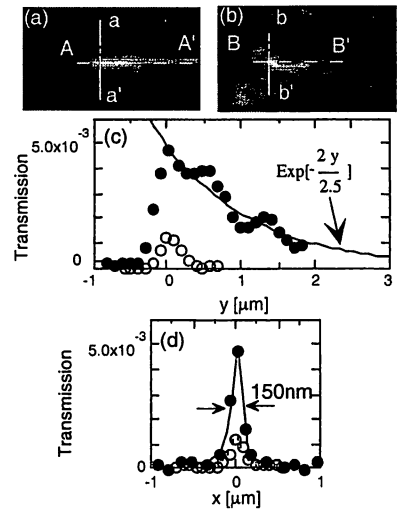
CMP5 Fig. 3. Electric-field distribution on the Si wedge plateau. (a) TM polarization. (b) TE polarization. The images are 5 × 3 μm. (c) Cross-sectional profiles along A-A' (closed circles) and B-B' (open circles) (c) Cross-sectional profiles along a-a' (closed circles) and b-b' (open circles). Transmission was defined as the ratio of the light power detected by the fiber probe to the input light power.

CMP5 Fig. 1. (a) A plasmon waveguide. The x- and y-axes are perpendicular and parallel to the plateau axis, respectively. (b) Cross-section along the xz-plane in (a). (c) Cross-section along the yz-plane in (a).

tric-field intensity distributions for TM and TE polarization, respectively. These results indicate that the propagating mode was excited efficiently only by TM-polarized incident light. From the dotted exponential curve in Fig. 3(c) fitted to the closed circles, the propagation length (the length after which the intensity decreases by a factor of e^{-2}) was estimated as 2.5 μm. This value is comparable to the theoretical value for the TM-plasmon mode in a cylindrical metal core waveguide consisting of a gold core ($D = 40$ nm) and air cladding at $\lambda = 830$ nm.[3] These results confirm that the observed excitation along the plateau was TM-plasmon mode. Figure 3(d) shows that the beam was 150 nm wide. Furthermore, note that the transmission was 5.0×10^{-3}, which is 10 times higher than that of a fiber probe with $D_a = 150$ nm.[4] This efficient excitation of the TM-plasmon mode is attributed to the scattering coupling at the edge between F1 and the plateau in Fig. 1(c). These results meet Requirements A, B, and C.

References

1. M. Ohtsu, "Near-field nano-optics toward nano/atom deposition," Proc. of SPIE, 3749, 478–479 (1999).
2. D. Marcuse, *Light transmission Optics* (Van Nostrand Reinhold Company, New York, 1972), Chap. 4.
3. J. Takahara, S. Yamagishi, H. Taki, A. Morimoto, and T. Kobayashi, "Guiding of a one-dimensional optical beam with nanometer diameter," Opt. Lett. 22, 475–477 (1997).
4. T. Yatsui, M. Kourogi, and M. Ohtsu, "Increasing throughput of a near-field optical fiber probe over 1000 times by the use of a triple-tapered structure," Appl. Physi. Lett. 73, 2090–2092 (1998).

CTuK67   **1:00 pm**

Near-field Components and Evaluation of the Photoluminescence in Si Nano-structure

*T. Yatsui,* T. Kawazoe,* and M. Ohtsu,*** *Ohtsu Project, ERATO, Japan Science and Technology Corporation, 687-1 Tsuruma, Machida, Tokyo, Japan 194-0004, Email: yatsui@ohtsu.jst.go.jp; **Interdisciplinary Graduate School of Science and Engineering, Tokyo Institute of Technology, 4259 Nagatsuta, Midori-ku, Yokohama, Japan 226-8502*

In order to increase the data transmission rates and capacity of optical transmission systems, the size of photonic devices must be decreased. Thus, we proposed nanometer-scale photonic integrated circuits (ICs) that are composed of sub-100-nm scale dots and wires.[1] Furthermore, we developed a far/near-field conversion device by introducing a metallized Si wedge.[2] The use of such a conversion device will realize the coupling of nanometer-scale photonic ICs with external conventional diffraction-limited photonic devices. Furthermore, since visible photoluminescence (PL) of the Si nanocrystals due to the confinement effect has reported,[3] Si nanocrystals are a promising candidate material for a visible light-emitting device. Due to the indirect-gap band structure of Si, however, the quantum efficiency is
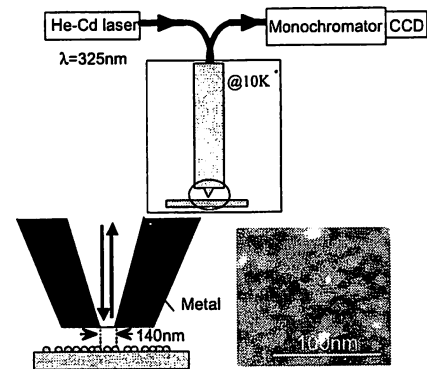
CTuK67   **Fig. 1.**   Schematic of the experimental setup used for illumination-collection mode near-field spectroscopy. Inset: Free-standing Si nanocrystals.

low. To overcome these difficulties, we propose using the optical near-field as a carrier for signal transmission, since it does not have to follow the wavevector conservation law. Consequently, an increase in the PL quantum efficiency is expected.

To evaluate the near-field components of the PL, we compared the PL spectrum using the conventional diffraction-limited optical method with that obtained using an illumination-collection mode near-field optical microscope (Fig. 1) at 10 K. For the near-field measurement, we used a fiber probe with an aperture diameter of 140 nm. Free-standing Si nanocrystals in the range of 5–10 nm were fabricated by wet etching (10 ml HF + 30 ml HNO_3 + 50 ml CH_3COOH).

As shown in Fig. 2, the emission peak energy for the far-field measurement was close to 1.53 eV (λ = 800 nm), which corresponds to the luminescence from the luminescence center. Furthermore, the emission peak energy for the near-field measurement was close to 2.1 eV (λ = 530 nm), which corresponds to the luminescence from the quantum-confinement state of Si nanocrystals with a diameter of 2.5 nm.[4]

Since visible PL in the near-field measurement was observed only when the fiber probe was in close proximity to the sample surface (~10 nm), the spectral shift is believed due to the near-field coupling of the probe and Si nanocrystals. Figure 3 illustrates the energy diagram of Si nanocrystals.[5] The PL from the quantum-confinement state of Si nanocrystals is subjected to both the charge transfer (denoted α) and recombination (denoted B) mechanisms. In the case of free-standing Si nanocrystals, the charge transfer rate of α is larger than the decay rate of B.[6] Consequently, we detect the PL from the luminescence center (denoted A) in the far-field measurement. However, the spectral shift of the PL in the near-field measurement implies that the charge transfer rate of β increases in comparison with that of α due to the near-field coupling of the Si nanocrystals and the probe.

Furthermore, considering the throughput of the fiber probe (~10^{-2}) and the respective peak PL intensities, the PL intensity for near-field measurement was 5 times larger than that for far-field measurement. This implies that the increase in the quantum efficiency is due to its wavevector non-conservation.

References

1. M. Ohtsu, "Near-field nano-optics toward nano/atom deposition," Proc. of SPIE, 3749, 478–479 (1999).
2. T. Yatsui, M. Kourogi, and M. Ohtsu, "A plasmon waveguide for optical far/near-field conversion," Appl. Phys. Lett. (in press).
3. H. Takagi, H. Ogawa, Y. Yamazaki, A. Ishizaki, and T. Nakagiri, "Quantum size effects on photoluminescence in ultrafine Si particles," Appl. Phys. Lett. 56, 2379–2381 (1990).
4. C. Delerie, G. Allan, and M. Lannoo, "Theoretical aspects of the luminescence of porous silicon," Phys. Rev. B, 48, 11024–11036 (1993).
5. T. Matsumoto, T. Futagi, H. Mimura, and Y. Kanemitsu, "Ultrafast decay dynamics of luminescence in porous silicon," Phys. Rev. B 47, 13876–13879 (1993).
6. Y. Kanemitsu, H. Uto, and Y. Masumoto, "Microstructure and optical properties of free-standing porous silicon films: Size dependence of absorption spectrum in Si nanometer-sized crystallites," Phys. Rev. B 48, 2827–2830 (1993).
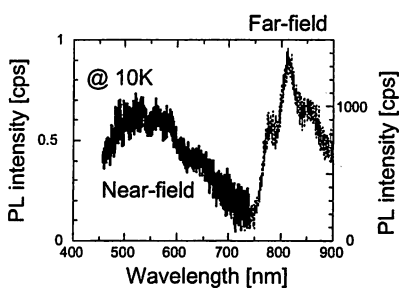
CTuK67 Fig. 2. PL spectrum of Si nanocrystals at 10 K.
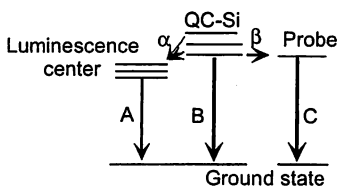
CTuK67 Fig. 3. Three-level-state model for free-standing Si nanocrystals.[4] QC-Si: quantum-confinement state of Si nanocrystals.
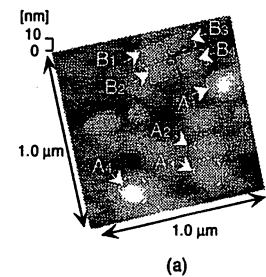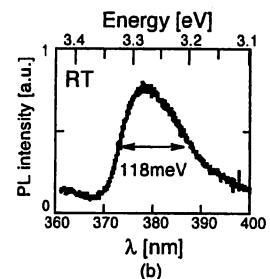
CFF7 **Fig. 1.** (a) Topographical image of polycrystalline ZnO. (b) Far-field PL spectra of polycrystalline ZnO.

free exciton in high-quality ZnO nanocrystallites.[2] The full width at half maximum (FWHM) of the PL spectra was about 118 meV, which is comparable with that of MBE-grown ZnO nanocrystallites.[4] These results imply that the oxidized Zn was composed of high-quality ZnO nanocrystallites. Furthermore, since ZnO has a wurtzite structure, the hexagonal (A_1, A_2, A_3, and A_4) and square (B_1, B_2, B_3, and B_4) nanocrystallites [see Fig. 1(a)] represent nanocrystallites oriented along the c-axis[1] and in other directions, respectively, indicating that fabricated ZnO nanocrystallites are polycrystalline.

Using a collection-mode near-field microscope, we obtained spatially and spectrally re-

CFF7   **11:45 am**

Observation of Size-dependent Features in the Photoluminescence of ZnO Nanocrystallites by Near-field UV Spectroscopy

T. Yatsui,* T. Kawazoe,* M. Ueda,**
M. Kourogi,*** M. Ohtsu,*** and G.H. Lee,***
*Ohtsu Project, ERATO, Japan Science and Technology Corporation, 687-1 Tsuruma, Machida, Tokyo, Japan 194-0004, Email: yatsui@ohtsu.jst.go.jp; **Interdisciplinary Graduate School of Science and Engineering, Tokyo Institute of Technology, 4259 Nagatsuta, Midori-ku, Yokohama, Japan 226-8502; ***Department of Advanced Materials Engineering, Dong-Eui University, Gaya-Dong 24, Pusanjin-Ku, Pusan, Korea, 614-714

ZnO is a promising material for room-temperature ultraviolet (UV) light-emitting devices due to its wide band gap (3.37 eV) and large exciton

binding energy (60 meV). Recently, several groups have reported room-temperature UV lasing from ZnO nanocrystallites.[1-3] To evaluate the optical properties and crystallinity of ZnO nanocrystallites, the optical properties must be measured with nanometer-scale resolution. Using a UV optical near-field technique, we observed size-dependent features of individual ZnO nanocrystallites.

ZnO nanocrystallites were prepared by oxidizing Zn deposited by photo-enhanced chemical vapor deposition (PE-CVD). First, 200-nm-thick Zn nanocrystallites were grown on a sapphire (0001) substrate at room temperature by PE-CVD. Second, the deposited Zn nuclei were oxidized in ambient oxygen at 1 atm and 750°C for 30 min.[3] The grain sizes were in the range of 30–160 nm [see Fig. 1(a)].

Figure 1(b) shows a far-field PL spectrum at room temperature. The emission peak energy corresponds to spontaneous emission from the
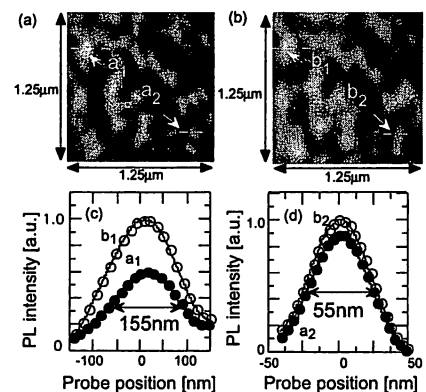
CFF7 **Fig. 2.** Monochromatic PL images of ZnO obtained at λ_d of (a) 370 and (b) 380 nm. (c) Closed and open circles represent cross-sectional profiles along the dashed lines through spots a_1 and b_1, respectively. (d) Closed and open circles represent cross-sectional profiles along the dashed lines through spots a_2 and b_2, respectively.
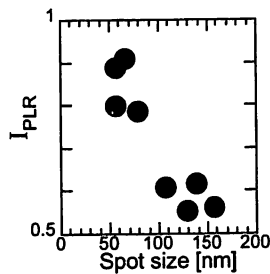
CFF7   Fig. 3. I_{PLR} [= $(I_{PL}$ at λ_d of 370 nm)/$(I_{PL}$ at λ_d of 380 nm)] of ZnO nanocrystallites as a function of spot size. The spot sizes were estimated from the FWHM in Fig. 2(a).

solved PL images. We used a UV fiber probe with an 80-nm aperture diameter. Figures 2(a) and 2(b) show monochromatic PL images at detection wavelengths (λ_d) of 370 ± 2.5 and 380 ± 2.5 nm, respectively. The closed and open circles in Fig. 2(c) represent cross-sectional profiles through spots a_1 [Fig. 2(a)] and b_1 [Fig. 2(b)], respectively. Those in Fig. 2(d) are for spots a_2 and b_2. Note that the FWHM of spots a_1 and a_2 was 155 and 55 nm, respectively, which is comparable to the grain sizes of ZnO nanocrystallites. This indicates that each emission spot originated from an individual ZnO nanocrystallite.

Furthermore, the PL intensity (I_{PL}) of spot b_1 for λ_d = 380 nm was twice that of a_1 at 370 nm, whereas that of spot b_2 for λ_d = 380 nm was comparable to that of a_2 at 370 nm. To examine such size-dependent features in the PL of individual ZnO nanocrystallites, we compared the I_{PL} value for several spots. Figure 3 shows the respective relative PL intensity I_{PLR} of ZnO nanocrystallites. Note that the I_{PLR} is larger for a smaller spot size. This originates from nanocrystallites with a higher PL peak energy due to the quantum size effect in ZnO nanocrystallites. Although this size-dependent feature of the PL intensity has been evaluated for an ensemble of nanocrystallites using a conventional diffraction-limited optical method,[3] our study is the first to evaluate individual nanocrystallites using an optical near-field method.

References

1. Z.K. Tang, G.K.L. Wong, P. Yu, M. Kawasaki, A. Ohtomo, H. Koinuma, and Y. Segawa, "Room-temperature ultraviolet laser emission from self-assembled ZnO microcrystallite thin films," Appl. Phys. Lett. 72, 3270–3272 (1998).

2. D.M. Bagnall, Y.F. Chen, Z. Zhu, T. Yao, M.Y. Shen, and T. Goto, "High temperature exitonic stimulated emission from ZnO epitaxial lasers," Appl. Phys. Lett. 73, 1038–1040 (1998).

3. S. Cho, J. Ma, Y. Kim, Y. Sun, G. Wong, and J.B. Ketterson, "Photoluminescence and ultraviolet lasing of polycrystalline ZnO thin films prepared by the oxidation of the metallic Zn," Appl. Phys. Lett. 75, 2761 (1999).

4. Y. Chen, D.M. Bagnall, H.J. Ko, K.T. Park, H. Hiraga, Z. Zhu, and T. Yao, "Plasma assisted molecular beam epitaxy of ZnO on c-plane sapphire: Growth and characterization," J. Appl. Phys. 87, 3912 (1998).

Owing to the unique property of optical near fields, considerable attention has been devoted to excitation energy transfer between nanometric quantum dots (QDs) triggered by the fields and its application to ultra-high speed and miniaturized photonic devices [1, 2]. Here it becomes essential to clarify the mechanisms of coherent excitation transfer and to investigate the possibility of its local manipulation with optical near fields. We report two alternative approaches to address these issues, and discuss the possibility of a coherent collective oscillation as well as transfer mechanisms. One is based on the effective interaction picture, where photonic degrees of freedom are effectively renormalized into the resonant interaction between QDs, with the help of the projection operator method. Equations of motion for 3- QD system can be shown with analytic and numerical results for coherent dynamics, where optical near-field coupling as the inter-dot interaction and phonon coupling as the intra- dot interaction are included (see Fig. 1). This kind of analysis predicts a typical time scale of phenomena. The other approach explicitly uses localized photonic degrees of freedom in order to discuss coherent excitation dynamics of QDs driven by optical near fields [3]. We consider a one-dimensional N-QD chain system that is expressed by either a set of bosons or fermions. The dynamics can be analytically solved in the boson case, and an initial dipole coherence of a QD can be transferred to another QD. When excitons of QDs are fermions, all dipole coherences except the initially excited QD gradually oscillate collectively if the sign of the population difference in each QD is set opposite to that of the corresponding dipole coherence. These phenomena suggest the possibility of a tiny photonic signal source and switch. Fig. 1 Two-exciton population dynamics in 3-QD system. Populations in QD 1 and 2, labeled by P6, are initially prepared, and final populations in QD 2 and 3, labeled by P8, are obtained.

S10.P.2.21

Coherent excitation dynamics of quantum dots systems controlled by optical near fields

K Kobayashi, S Sangu, T Kawazoe, A Shojiguchi*, K Kitahara*, M Ohtsu†

Japan Science and Technology Corporation, Japan
*International Christian University, Japan
†Tokyo Institute of Technology, Japan

[1] K. Kobayashi, T. Kawazoe, S. Sangu, J. Lim, and M. Ohtsu, Technical Digest in OSA IPR/PS 2001, PThB4, 2001

[2] T. Kawazoe, K. Kobayashi, J. Lim, Y. Narita, and M. Ohtsu, Phys. Rev. Lett. in press

[3] A. Shojiguchi, K. Kobayashi, K. Kitahara, S. Sangu, and M. Ohtsu, 3rd Asia-Pacific Workshop on Near Field Optics, 2001

Figure 1.

MpB1
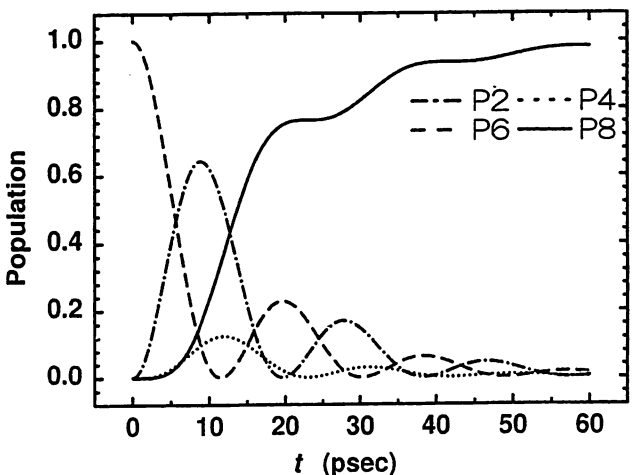
Near-Field Optical Microscopy and Application to

Nano-Photonics

T. Kawazoe[b] and M. Ohtsu[a,b,c]

[a] Interdisciplinary Graduate School of Science and Engineering, Tokyo Institute of Technology

[b] Localized Photon Project, ERATO, Japan Science and Technology Corporation

[c] Near-field Photonics Group, Kanagawa Academy of Science and Technology

Abstract

This paper reviews applications of near-field optical microscopy to depositing nanoscale materials, operating nano-photonic devices, and developing high-density optical storage systems. First, an UV near-field photochemical vapor deposition of nanometeric Zn, Al, and ZnO are demonstrated. Second, a concept of nano-photonic IC is proposed by utilizing the advanced potential of this deposition technology. The optical switching operation of a single InGaAs quantum dot is shown to be able to be used for nano-photonic devices. Nano-photonic switching operation utilizing optical near-field interaction is also proposed and related spectroscopy of CuCl quantum dots are demonstrated. Finally, high-density storage and read-out by optical near-field is demonstrated.

Room B   8 April, Monday

1:30 PM *S7.1
DEVELOPMENT OF NANO-PHOTONIC DEVICES AND THEIR
INTEGRATION BY OPTICAL NEAR FIELD. M. Ohtsu,
Interdisciplinary Graduate School of Science and Engineering, Tokyo
Institute of Technology, Nagatsuta-cho, Midori-ku, Yokohama,
JAPAN; Also with Localized Photon Project, ERATO, Japan Science
and Technology Corporation , and with Near-field Photonics Group,
Kanagawa Academy of Science and Technology, JAPAN.

72

Nano Photonic Device and Nano Optical Process using Optical Near-Field

Tadashi Kawazoe,[1] Takashi Yatsui,[1] and Motoichi Ohtsu[2]

[1]Japan Science and Technology Corporation, [2]Tokyo Institute of Technology

Abstract:

Performances of an optical device and an optical memory using existing technology are limited by the diffraction of light. We have been working on the studies for the nanometric optical near-field switch composed of several quantum dots, as an optical near field has a potential for a breakthrough in the limitation. For realization of the nanometric optical switch, new switching mechanisms, technologies of near-field signal waveguide, and process technologies of the nanometric optical device are necessary. We introduce these technologies for realization of the nanometric optical switch.

1. Introduction:

We have achieved the modern photo science and technology after the lapses of the particle and wave model in the 18th century, light quanta model in the beginning of the 20th century, the invention of lasers in the 1960s, and industrial technology of the informational communication and recording, i.e., photo-electronics and photonics. However, a technology and applied science for studies of concentrated light in the nanometer space that is less than the light wavelength is absent, so far. It is clear that the existing optical technology of information exchange and data storage will face a technological constraint due to diffraction limit and the existing technology will never respond to the social demand in the 21st century.

We have been working on the study of the optical near field for the breakthroughs of the limit of the opto-technology mentioned above. Realization of nanometric optical near-field device is the one of our goal. Figure 1 shows the schematic drawing of our proposed optical
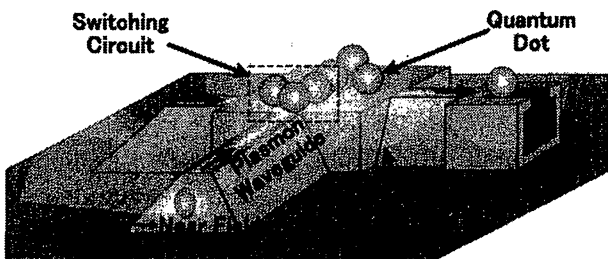
Fig.1. Near-field optical device.

near-field nano-photonic device. This device is composed of several quantum dots, and its in/out puts and signal propagation among devices are constructed with nanometric optical waveguide using plasemon propagation. In this paper, we introduce the proposal for the switching mechanism of nano-photonic device and the nanometric waveguide. Finally, we report the near-field optical chemical vapor deposition.

2-1. Near-Field Optical Nanometric Switch:
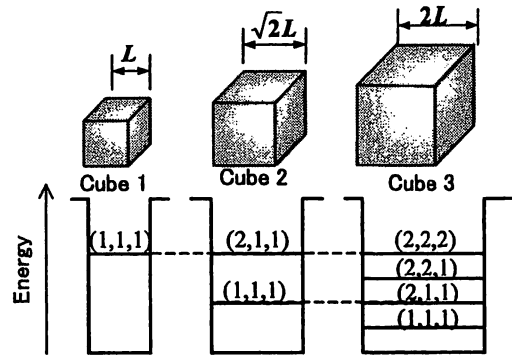
Fig.2. Quantum dots composing the near-field optical device and their carrier energy structure.

Figure 2 shows a schematic drawings of the three quantum dots and their enegy levels. In the cubic shape of the quantum dots, the energy eigenvalue for the quantized carrier energy level in a quantum cube with the side length of L are given by

$$E_{n_x,n_y,n_z} = E_B + \frac{\hbar^2\pi^2}{2ML^2}(n_x^2 + n_y^2 + n_z^2) \quad \cdots (1)$$

where E_B is the bulk carrier energy, M is the translational mass of carrier, (n_x, n_y, n_z) are quantum numbers (=1, 2, 3,...). The quantized energy sublevels (2,2,2) in cube 3, (2,1,1) in cube 2, and (1,1,1) in cube 1 resonates with each other. Under the resonant condition, the coupling energy of near-field interaction is given by the following Yukawa-type function;

$$V(r) = A\frac{\exp(-\mu \cdot r)}{r}. \quad \cdots (2)$$

Here, r is a separation between two quantum cubes, A is a coupling coefficient [1]. The values A and r should be determined from the experiment essentially, however, we estimated it

from the result of the previous work on the interaction between a Rb atom and the near-field probe. Assuming that the separation r between two quantum cubes is equal to 10 nm, the transition time is about 100 ps which is much shorter than the few ns carrier lifetime. In addition, inter sub-level transition is generally less than few ps and is much shorter than the transition time due to near-field coupling. Thus, almost all the energy of the excitation in the quantum cube 1 transfer to the lowest carrier energy level in the neighboring quantum cube 2, and finally, it transfers to the lowest energy level in the quantum cube 3. The cubes 1, 2, and 3 are regarded as input, output and control ports for the switch, respectively.

The schematic drawings of *ON* and *OFF* operations are shown in Fig.3. In the *OFF* operation, the input energy escapes to the control cube, and then the out put signal is obstructed. In the *ON* operation, the escape passes to the control cube are blocked by the excitation of the control cube, and then the input energy goes through this cube giving an out put signal.
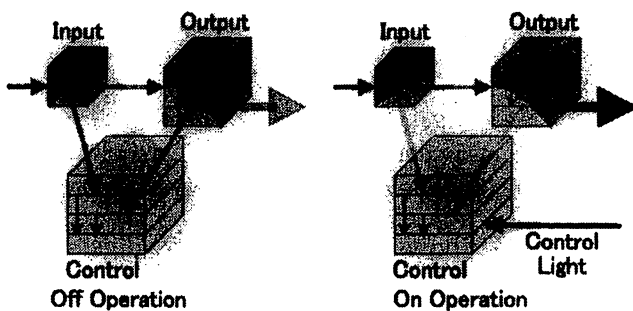
Fig.3. Off and on operation of near-field optical switch.

For realization of the near field optical switching operation, the energy transfer between quantum cubes via optical near field is most important phenomena, and it is also interesting physically. For verifying the energy transfer via optical near field, we observed the near-field luminescence of CuCl quantum cubes embedded in a NaCl matrix. The thickness of the sample and the average size of the quantum cubes are 100 μm and 4.3 nm, respectively. The sample was cleaved just before the experiment of the near-field spectroscopy in order to keep the sample surface clean. For the wavelength separation among the sub-levels, the sample temperature was set to be 15 K.

Figure 4 (a) shows the experimental result of the optical near-field luminescence spectroscopy. He-Cd laser (λ=325nm) was used as a light source. The luminescence spectrum is broadened by the inhomogenous size distribution of the quantum cubes. Thus, we can select the quantum cube size by selecting the wavelength of the luminescence. The luminescence peaks X and Y correspond to the luminescence from the 4.6 nm and 6.3 nm quantum cubes, respectively. Their size ratio is close to $1:\sqrt{2}$. Then, their exciton sub-level $(1,1,1)$ in a 4.6nm quantum cube and $(2,1,1)$ in a 6.3 nm quantum cube resonate to each other.
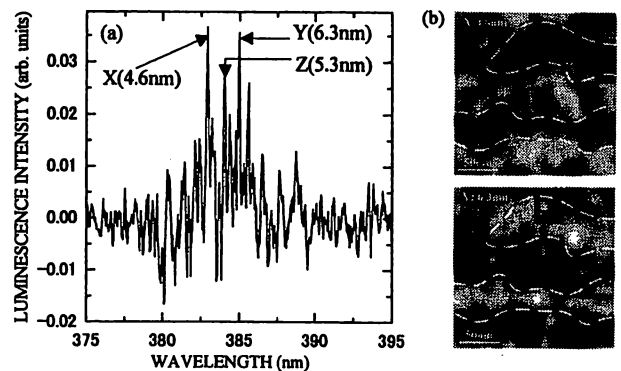
Fig.4. Experimental results of optical near-field luminescence measurement.

Figures 4 (b) shows the spatial distributions of the luminescence intensity, i.e. near-field optical microscope images, for the peaks X and Y in Fig.4 (a), respectively. These images clearly establish anti-correlation features in their intensity distributions, as manifested by the dark and bright regions surrounded by broken curves. The average quantum cube size of the sample was 4.3 nm, and the density of 4.6 nm quantum cube is much higher than that of 6.3 nm quantum cube. Thus, it is interpreted that a 4.6-nm quantum cube, 'accidentally' located close to the 6.3-nm quantum cube, can not emit light but transfers the energy to the 6.3-nm quantum cube. As a result, in the region where 6.3-nm quantum cubes are embedded, luminescence intensity from 4.6-nm quantum cubes becomes low, while that having no embedded 6.3-nm quantum cubes the luminescence intensity is high. Thus, we can claim the first observation of the energy transfer between quantum cubes via optical near-field [2].

2-2. Plasmon Waveguide:

Coupling the photonic devices with external conventional diffraction-limited photonic devices require a nanometer-scale optical waveguide for far/near -field conversion and vise versa. It is possible for a tapered fiber probe to act as a converter for conventional near-field optical

microscopy. The performance required for this type of waveguide includes:

A. High conversion efficiency.

B. The guide beam width should be less than 100 nm for efficient coupling of the converted optical near-field to sub-100 nm dots.

C. The guide propagation length should be on the order of the optical wavelength to avoid direct coupling of the propagating far-field light to the nanometer-scale dots.
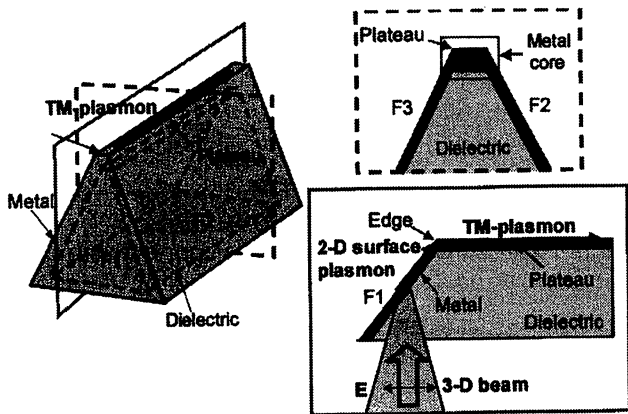
Fig.5. A plasmon waveguide structure.

Figure 5 shows our plasmon waveguide scheme. The main part consists of a silicon dielectric wedge, coated with a thin metal film. Incoming far-field light, which is polarized parallel to the y-axis, is first transformed into the two-dimensional (2-D) surface plasmon mode on the F1 side. Next, the 2-D surface plasmon mode is converted into the 1-D TM-plasmon mode at the edge between F1 and the plateau. This conversion occurs because of the scattering coupling at the edge. Third, the TM-plasmon mode propagates along the plateau in a manner similar to surface plasmon modes using metal stripes or edge modes using metal wedges. This propagation occurs because the metal film deposited on the plateau is thicker than on the other faces (F1, F2, and F3) due to the normal evaporation process. Consequently, the plateau acts as a metal core waveguide. Finally, the TM-plasmon mode at the waveguide outlet is converted to the optical near-field so that it couples to the nanometer-scale dots, which are located in close proximity to the outlet.

Advantages of our waveguide are:

a. High conversion efficiency from the 2-D surface plasmon mode to the 1-D TM-plasmon mode, due to the scattering coupling at the edge.

b. The beam width decreases (as narrow as 1 nm) with the core diameter, since this waveguide does

not have a cutoff. This decrease satisfies Requirement B.

c. The propagation length of the TM-plasmon mode is sufficiently long as to meet Requirement C. For example, the propagation length is 2.5 μm (@ l = 830 nm) for a TM-plasmon with a gold core (diameter D = 40 nm) insulated by air.
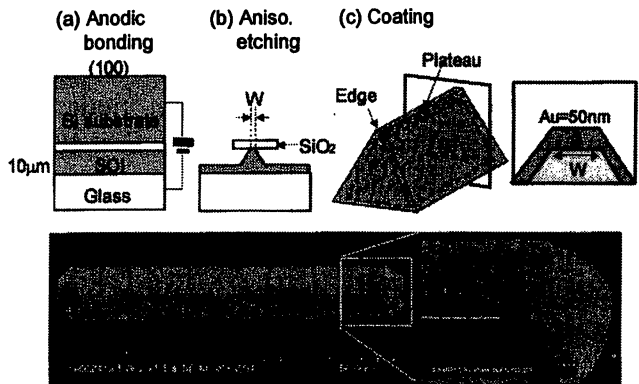
Fig.6. Fabrication steps for a plasmon waveguide and scanning electron microscopic images of the metal-coated silicon wedge.

The plasmon waveguide was fabricated by the following steps. A (100) oriented silicon on insulator (SOI) wafer was bonded to the glass substrate by anodic bonding [Fig.6(a)]. After removing the silicon substrate from the SOI wafer by wet etching, the SiO_2 layer was patterned using photolithography. In order to create specific shapes for the plateau, F1 face, and edge, the rectangular mask was tilted 30° with respect to the <110> crystal orientation of silicon. This avoids any deformation of the convex corners. The silicon wedge was fabricated by anisotropic etching [Fig.6(b)]. Maintaining the silicon wedge height at less than 10 μm also keep its propagation loss sufficiently low. The plateau width was accurately controlled using the etching time. After removing the SiO_2 layer, the silicon wedge was coated with a 50-nm-thick gold layer [Fig. 6(c)]. The plateau width, W, was 150 nm and its length, L, was 80 μm.

We examined the dependence of the mode propagation characteristics of the waveguide. For this measurement, a fiber probe with aperture diameter of 60 nm was used, and linearly polarized light from a laser diode (l = 830 nm, 0.1 mW) was focused onto the F1 face in order to generate the plasmon wave.

Figures 7(a) and (b) show the observed electric-field intensity distributions on the wedges with W = 1 μm and 150 nm for TM polarization. Figures 7(c) and (d) are for TE

4-29

75

polarization. The closed and open circles in Figs. 7(e) and (f) show the cross-sectional profiles along the dashed white lines in Figs. 7(a) (A-A' and a-a'), (b) (B-B' and b1-b1'). Here, transmission was defined as the ratio of the light power detected by the fiber probe to the input light power. From the dotted exponential curve in Fig. 4(e) fitted to the open circles, the propagation length was estimated as 2.5 μm for the 150-nm wedge. This value is comparable to the theoretical value for TM-plasmon mode in a cylindrical metal core waveguide with D = 40 nm and consists of a gold core and air cladding at a wavelength of 830 nm. From fitting the solid exponential curve in Fig. 7(e) to the closed circles, the propagation length for W = 1.0 μm was estimated as 4.0 μm, which is longer than that for W = 150 nm. This is because, as W increases, the effective refractive index approaches to that of surface plasmon at the planar boundary between gold and air. These experimental results confirm that the observed excitation along the plateau was TM-plasmon mode.
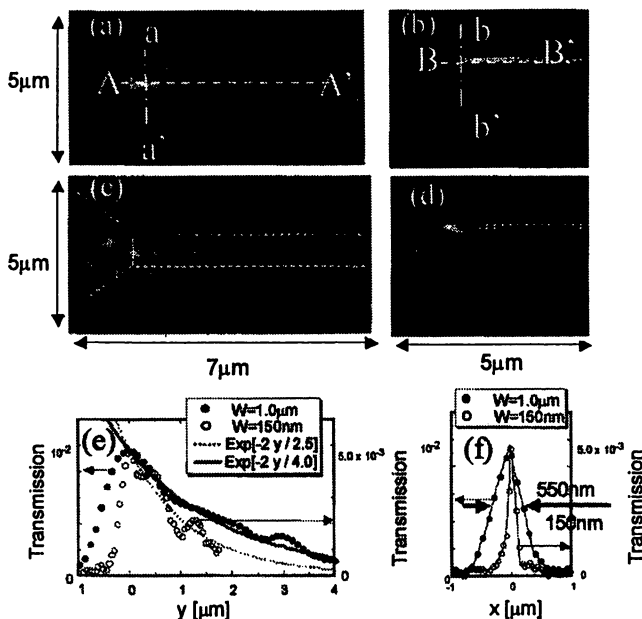
Fig.7. Experimental results of plasmon propagating along the waveguide.

Figure 7(f) shows that the full width at half maximum (FWHM) of the cross-sectional profiles was 550 nm and 150 nm for W = 1.0 μm and 150 nm, respectively. With minor improvements to the waveguide, this FWHM value of 150 nm for W = 150 nm should meet Requirement B. Furthermore, note that the transmission was $5.\times10^{-3}$ for W = 150 nm, which is 10 times higher than that of a fiber probe with Da = 150 nm. This efficient excitation of the

TM-plasmon mode can be attributed to the scattering coupling at the edge between F1 and the plateau. This transmission efficiency meets Requirement A. Finally, the propagation length estimated above is longer than the incident light wavelength. This meets Requirement C [3].

2-3. Near-Field Optical Chemical Vapor Deposition:
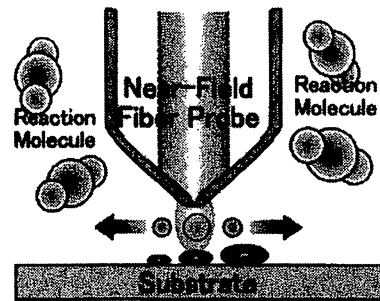
Fig.8. Near-field optical chemical vapor deposition
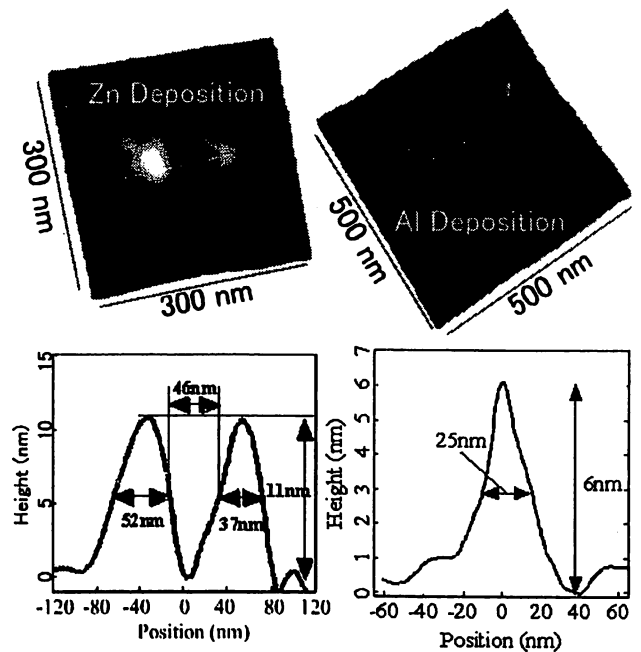
Fig.9. Zn dots and Al dots deposited by the near-field optical chemical vapor deposition.

For realization of our nanometric near-field optical switch, it is necessary to prepare the 10-nm size quantum dots with 10-nm accuracy. The technique of chemical vapor deposition (CVD) using optical near-field is able to satisfy this requirement. Figure 8 shows the principle of the near-field optical CVD. We utilize the high spatial resolution capability of the optical near-field to deposit nanometric Zn and Al dots as shown in Fig.9. The sizes of the deposited dots are less than 50 nm, and the accuracy of the deposition position corresponds to the accuracy of the instrument for the deposition (1nm) [4]. Recently, we found that for near-field optical CVD (NFO-CVD), the photodissociation can

take place even in nonresonant conditions, due to the inherent properties of the optical near-field [5]. Here, we introduce NFO-CVD of nanometric Zn dots in nonresonant conditions.
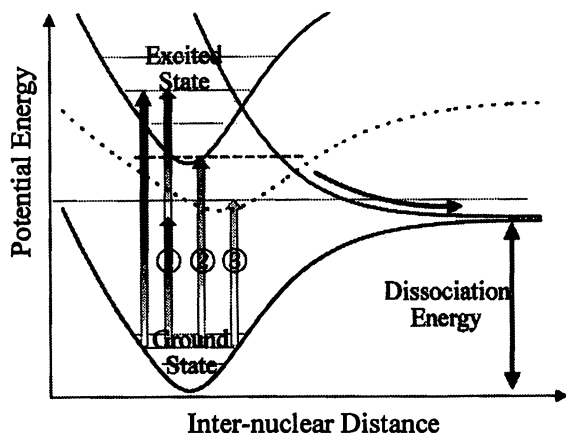
Fig.10. Potential curves of an electron in DEZn molecular orbitals.

We now discuss the possible mechanisms of diethylzinc (DEZn) dissociation by the nonresonant optical near-field. Figure 10 shows potential curves of an electron in the DEZn molecular orbital drawn as a function of the inter-nuclear distance of a C-Zn bond, which is involved in photodissociation. The relevant energy levels of the molecular vibration mode are also represented by horizontal lines in each potential curve. When using a conventional far-field light, photo-absorption (indicated by a white arrow in this figure) dissociates DEZn. In contrast, there are three possible mechanisms of photodissociation using a nonresonant optical near-field. The first is the two-photon absorption process, as indicated by the two arrows ① in Fig. 10, due to the high energy density of the optical near-field at the apex of the high throughput fiber probe. The second is the transition, shown by arrow ② , to the intermediate energy level (dotted curve) induced by the fiber probe and successive relaxation to the dissociative triplet state. Such an induced transition is due to energy transfer between two localized dipole oscillators, i.e., the near-field probe and the DEZn molecules. Similar energy transfer has been observed between optically forbidden levels in dye molecules. The third mechanism involves the transition to an excited state of a molecular vibration mode whose energy is higher than the dissociation energy (2.26 eV), as indicated by the dashed line and arrow ③ in Fig. 10. Although this transition is prohibited

by the wavenumber conservation law for conventional far-field light, it is allowed in the present case because of the large uncertainty in the wavenumber of the sub-wavelength-size optical near-field.
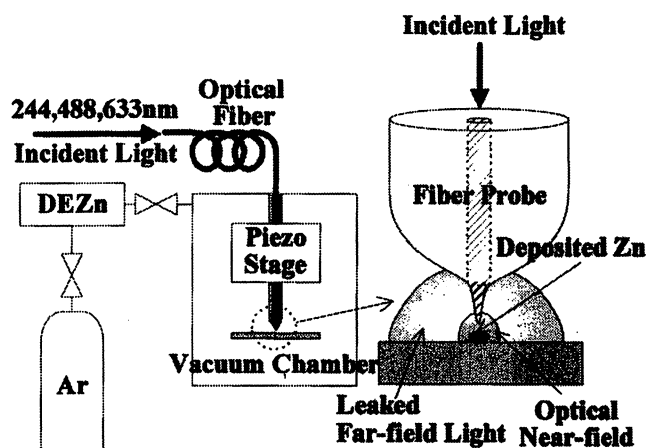
Fig.11. Experimental setup for chemical vapor deposition using an optical near-field.

Figure 11 shows the experimental setup for NFO-CVD. Ultra-high purity argon (Ar) was used as a buffer gas and (DEZn) as a reacting molecular gas source. The second harmonic (λ = 244 nm) of an Ar^+ laser was used as a light source that resonates the absorption band of DEZn. The fundamental frequencies of Ar^+ (λ= 488 nm) and He-Ne (λ= 633 nm) lasers were used as nonresonant light sources. In order to investigate the deposition effect of nonresonant far-field light, a fiber probe without the usual metal coating, i.e., a bare fiber probe, was used for the deposition. Therefore, the optical far-field was generated by light leaking through the circumference of the fiber probe, while the optical near-field was generated at the apex. During deposition, the partial pressure of DEZn was 100 mTorr and the total pressure in the chamber was 3 Torr.

Figure 12 shows the shear-force topographical images before and after NFO-CVD on the sapphire substrate with atomic-level steps for λ= 244 (a), 488 (b), and 633 (c) nm. For Fig. 12 (a) (λ=244 nm), the laser power was 1.6 μW and the irradiation time was 60 s. Since the bare fiber probe also leaked strong far-field light, a Zn layer that covered the atomic-step structures on a substrate was deposited. For Fig. 12 (b), the laser power was 150 μW and the irradiation time was 75 s. The photon energy at this wavelength (λ= 488 nm) is higher than the dissociation energy of DEZn, but it is still lower than the absorption edge of DEZn. A Zn dot less than 50

nm in diameter appears at the center of the broken circle on the right-hand side of this figure. In Fig. 12 (c) (λ= 633 nm), the laser power was 240 μW and the irradiation time was 300 s. Despite the higher power and longer irradiation time, there was no Zn deposition. This shows that the thermal effect of laser irradiation is negligible for Zn deposition.
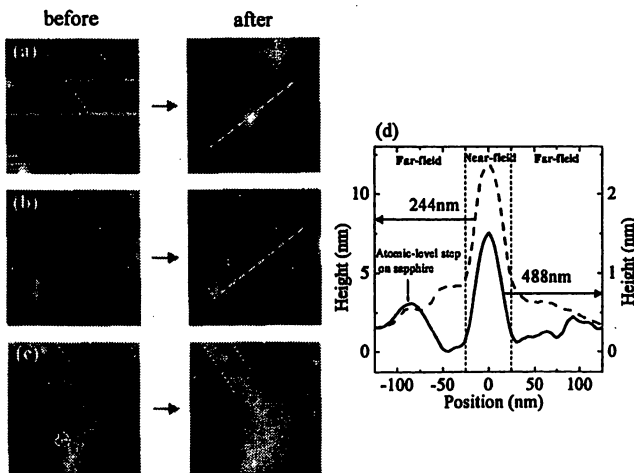
Fig.12. Wavelength dependence of Zn dots deposition. (a) 244 nm, (b) 488nm, (c) 633nm.

In Fig. 12 (d), the solid curve is a cross sectional profile of the Zn dot deposited at 488 nm across the dashed line in Fig. 12(a). The dashed curve represents the cross sectional profile of the Zn dot deposited at λ= 244 nm, taken across the dashed line in Fig. 12(b). These curves confirm that Zn dots with a full width at a half maximum of 30 nm were deposited in the region where the optical near-field is dominant. The dashed curve has side lobes 4-nm high on both sides of the dot. These side lobes correspond to the deposition by the leaked far-field light. The solid curve has no side lobes; thus, it is clear that the leaked 488-nm far-field light did not deposit a Zn layer. This result agrees with previous work using conventional optical CVD for Zn deposition with a far-field light with λ= 300 nm. It should be noted that the 30-nm Zn dot without side lobe broadening was deposited under a nonresonant condition, despite the presence of leaked far-field light.

The experimental results and the suggested mechanisms described above show numerous potential advantages, i.e., this technique not only increases spatial selectivity, but also makes it possible to use various light sources and gas sources not previously used in conventional far-field optical CVD. Thus, nonresonant NFO-CVD is a very useful nano-fabrication technique.

3. Conclusion:

In this paper, we introduced three parts of the research results for the realization of the nanometric near-field optical device. It is said that 1000x1000 matrix switch is necessary by 2015, and the size of the optical switch composing this device have to be less than few μm. We have been making efforts to overcome such difficulties for existing technology by the optical near field. Since there are not only the technical inversions but also new physical phenomena, we have to propel the study carefully.

References:

[1] K. Kobayashi, S. Sangu, H. Ito, and M. Ohtsu, Phys. Rev. A 63, 013806 (2000).
[2] T. Kawazoe, K. Kobayashi, J. Lim, Y. Narita, and M. Ohtsu, to appear in Phys. Rev. Lett..
[3] T. Yatsui, M. Kourogi, M. Ohtsu, to appear in Appl. Phys. Lett..
[4] Y. Yamamoto, M. Kourogi, M. Ohtsu, V. Polonski, and G. H. Lee, Appl. Phys. Lett. 76, 2173-2175 (2000).
[5] T. Kawazoe, Y. Yamammoto, M. Ohtsu, Appl. Phys. Lett. 79, 1184-1186 (2001).

Design, fabrication, and operation of nano-photonic devices by optical near-field

M. Ohtsu[123]

[1] Interdisciplinary Graduate School of Science and Engineering, Tokyo Institute of Technology

[2] Localized Photon Project, ERATO, Japan Science and Technology Corporation

[3] Near-field Photonics Group, Kanagawa Academy of Science and Technology

E-mail: ohtsu@ae.titech.ac.jp

This paper reviews the recent progress of application of interactions between optical near-fields and nanoscale materials[1][2][3]. Photochemical vapor deposition of nanometeric Zn and Al are realized by using an UV optical near-field. Deposition of nanoscale ZnO is also shown. Optical near-field technology offers the opportunity of modifying surfaces and developing new nanostructures that may exhibit a quantum effect due to their extremely small size. Utilizing the very advanced potential of this technology, the concept of nano-photonic IC is proposed. The optical switching operation of a single InGaAs quantum dot is shown to be able to be used for nano-photonic devices. Nano-photonic switching operation utilizing optical near-field interaction is also proposed and related spectroscopy of CuCl quantum dots are demonstrated. Sub-micron sized plasmon waveguide for converting far-field propagating light to optical near-field is propoposed in order for using as an input port of the nano-photonic IC. Its guiding characteristics are evaluated.

References

1. M. Ohtsu, Technical Digest of the 18th Congress of the International Commission for Optics, SPIE, 3749, 478 (1999)
2. M. Ohtsu, Proc. SPIE, vol.4416, Int. Conf. on Optical Engineering for Sensing and Nanotechnology, pp.1-13, 6-8 June 2001, Yokohama
3. M. Ohtsu, K. Kobayashi, H. Ito, and G.-H. Lee, Proc. IEEE, vol.88, no.9, 1499 (2000)

ACOLS 2001: Proceedings of the Australasian Conference on Optics, Lasers and Spectroscopy 2001. Brisbane, Australia. 27

79

Developing nano-photonic devices and their integration by optical near-field

M. Ohtsu[a,b,c]

[a] Interdisciplinary Graduate School of Science and Engineering, Tokyo Institute of Technology

[b] Localized Photon Project, ERATO, Japan Science and Technology Corporation

[c] Near-field Photonics Group, Kanagawa Academy of Science and Technology

E-mail: ohtsu@ae.titech.ac.jp

This paper reviews the recent progress of application of interactions between optical near-fields and nanoscale materials. Photochemical vapor deposition of nanometeric Zn and Al are realized by using an UV optical near-field. Deposition of nanoscale ZnO is also shown. Optical near-field technology offers the opportunity of modifying surfaces and developing new nanostructures that may exhibit a quantum effect due to their extremely small size. Utilizing the very advanced potential of this technology, the concept of nano-photonic IC is proposed. The optical switching operation of a single InGaAs quantum dot is shown to be able to be used for nano-photonic devices. Nano-photonic switching operation utilizing optical near-field interaction is also proposed and related spectroscopy of CuCl quantum dots are demonstrated. Sub-micron sized plasmon waveguide for converting far-field propagating light to optical near-field is prpoposed in order for using as an input port of the nano-photonic IC. Its guiding characteristics are evaluated.

REFERENCES

1. M. Ohtsu, *Technical Digest of the 18th Congress of the International Commission for Optics*, SPIE, **3749**, 478 (1999)

2. M. Ohtsu, Proc. SPIE, vol.4416, Int. Conf. on Optical Engineering for Sensing and Nanotechnology, pp.1-13, 6-8 June 2001, Yokohama

3. M. Ohtsu, K. Kobayashi, H. Ito, and G.-H. Lee, Proc. IEEE, vol.88, no.9, 1499 (2000)

29

NEW METHODS FOR IMPROVED OPTICAL NEAR FIELD FIBER PROBES

H.N. Aiyer, T. Kawazoe and M. Ohtsu
[1]ERATO Localized Photon Project
Japan Science and Technology Corporation
687-1-17/4F Tsuruma, Machida-shi, Tokyo, Japan
[2]Tokyo Institute of Technology
4259, Nagatsuta, Midori-Ku, Yokohama 226-8502, Japan
E-mail: hemant@ohtsu.jst.go.jp

The metal coated tapered optical near field fiber probes play a central role in the near field optics and its applications such as microscopy, nanofabrication, high density data storage and spectroscopy [1].

The important issues pertaining the probe performance are shape and size(diameter) of the aperture, optical throughput and the light leakage along the taper. We have devised and applied some new concepts to improve the characteristics of the optical near field fiber probes. These are described as follows:

(a) Mercury treatment of gold coated optical near field fiber probes to overcome the light leakage:

The quality of metal coating on probes directly governs the extent of light leakage through the pinhole defects. We have explored a novel approach of mercury treatment on near field fiber probes [2]. Mercury treatment is performed by

physically contacting the tip of Au coated chemically etched double tapered fiber probe onto a

mercury droplet for a short time. Mercury is soluble in gold and forms a solid solution at ambient temperature.

Fig.1

Mercury on the gold surface is very mobile and adsorbs fast migrating to different grain boundaries closing the detrimental porous structure. Different performance aspects like light leakage (Fig.1), chemical and optical stability, absorption characteristics and damage threshold of such mercury treated probes are investigated to reveal the beneficial effect of this approach.

(b) Thermal annealing approach for improved Al coated near field fiber probes:

We have studied the aperture formation by thermal annealing of Al coated heat-pulled UV fiber probes.1500 Å Al coating deposited on as fabricated tip completely blocked the laser light from exiting the tip end. Annealing the probes under ambient conditions at 180°C/12 hours forms Al_2O_3 on Al coated probe with only Al_2O_3 region at the tip apex as Al at the tip apex is thin in contrast with that on the lateral sides. On coupling He-Ne laser light (λ =633 nm), the annealed probe yields light output (Fig.2) from tip apex as oxide layer at the tip is transparent to this light. Probe throughput as high as 10^{-2} was recorded. Such Al_2O_3 coating on the probe could also improve mechanical toughness of the probe.

Fig.2
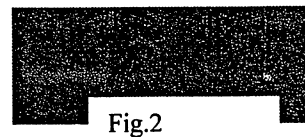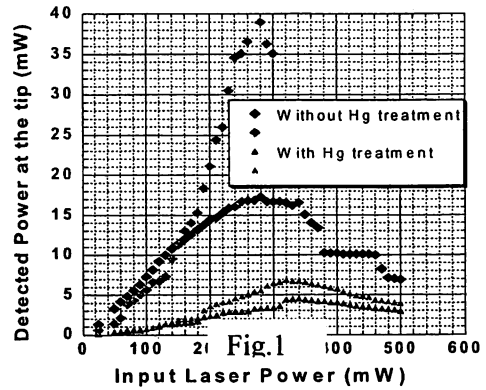
[1] Near field Nano/Atom Optics and Technology,
    edited by M. Ohtsu (Springer Verlag, Berlin, 1998).
[2] H.N. Aiyer, T. Kawazoe, J. Lim, Y. Echigo and M. Ohtsu,
    to appear in Nanotechnology.

51

A PLASMON WAVEGUIDE
FOR OPTICAL FAR/NEAR-FIELD CONVERSION

T. Yatsui,[a] T. Abe,[b] M. Kourogi,[a], [b] and M. Ohtsu[a], [b]

Japan Science and Technology Corporation, 687-1 Tsuruma, Machida, Tokyo, Japan 194-0004
Interdisciplinary Graduate School of Science and Engineering, Tokyo Institute of Technology, 4259
Nagatsuta, Midori-ku, Yokohama, Kanagawa, Japan 225-8502
Electronic mail: yatsui@ohtsu.jst.go.jp

To realize nanometer-scale photonic devices and integrated circuits [1], coupling them with external conventional diffraction-limited photonic devices requires a nanometer-scale optical waveguide for far/near -field conversion. To meet this requirement, a plasmon waveguide (Fig. 1) was designed and fabricated using a metal-coated silicon wedge structure that converts propagating far-field light to the optical near-field. Illumination (λ = 830 nm) of the waveguide (plateau width 150 nm) excited a transverse magnetic (TM) -plasmon mode. Use of a near-field optical microscope allowed us to determine its beam width and propagation length as 150 nm and 2.5 μm, respectively (Fig. 2).
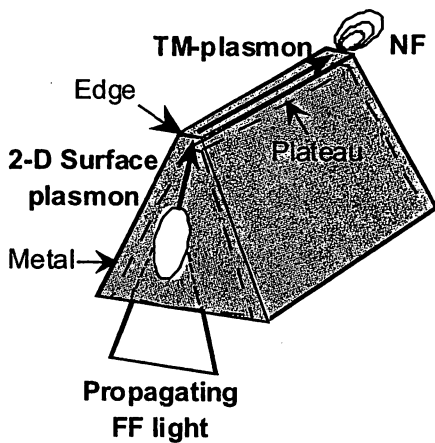
Fig. 1 A plasmon waveguide.
FF= far-field; NF= near-field.
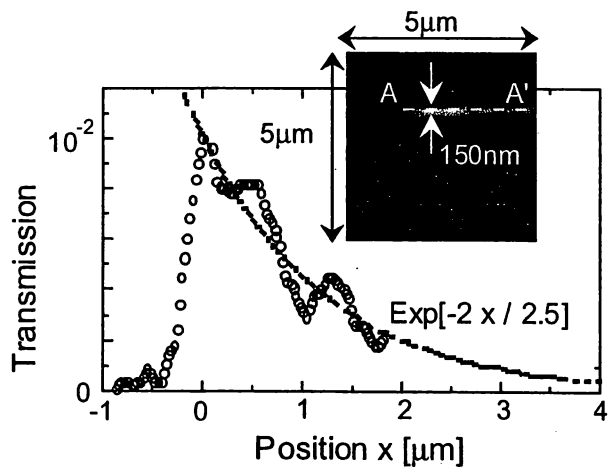
Fig. 2 Cross-sectional profile along A-A' in the inset. Dotted curves represent the exponential curves fitted to the experimental values.

REFERENCE
[1] M. Ohtsu, Proc. of SPIE, 3749, 478 (1999).

63

82

NEAR-FIELD COMPONENTS OF THE PHOTOLUMINESCENCE IN SILICON NANO-STRUCTURE AND ITS EVALUATION

T. Yatsui,[a] T. Kawazoe,[a] and M. Ohtsu[a], [b]

(a) Japan Science and Technology Corporation, 687-1 Tsuruma, Machida, Tokyo, Japan 194-0004

(b) Interdisciplinary Graduate School of Science and Engineering, Tokyo Institute of Technology, 4259 Nagatsuta, Midori-ku, Yokohama, Kanagawa, Japan 225-8502

Electronic mail: yatsui@ohtsu.jst.go.jp

For realization nanometer-scale photonic devices and integrated circuits (ICs) [1], a promising candidate material is a Si nanocrystal, from which visible photoluminescence (PL) due to the confinement effect has been reported [2]. However, due to the indirect-gap band structure of Si, the quantum efficiency is low. To overcome this difficulty, we propose the use of optical near-field as a carrier for signal transmission, which does not have to follow the wavevector conservation law,. Consequently, the increase in the PL quantum efficiency is expected.

As a Si nano-structure, a sharpened Si with an apex diameter of 10 nm was fabricated (Fig. 1). We evaluated near-field components of the PL from the apex. The PL signals were detected by the Illumination-Collection mode near-field optical microscope. The He-Cd laser light of 325 nm wavelength was employed to excite the Si.

As shown in Fig. 2, the PL spectra was obtained by the near-field detection. Note that the emission peak energy was close to the value of 2.1 eV, which corresponds to the luminescence from nanocrystal Si state with a diameter of 4 nm calculated from the effective mass approximation. This implies the increase in the quantum efficiency due to its the wavevector non-conservation.
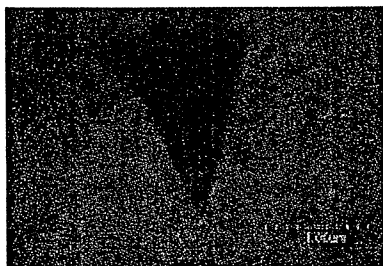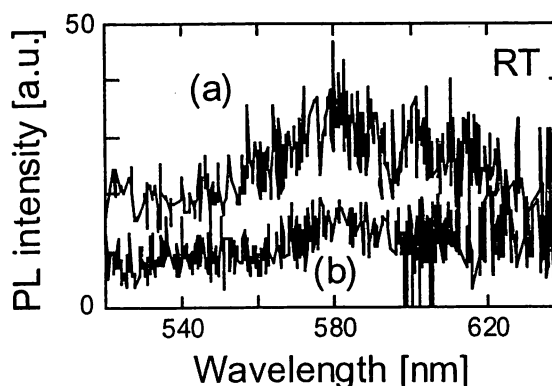
Fig. 1 Sharpened Si.   Fig. 2 PL spectrum from the sharpened Si.

Separation between fiber and Si of (a) 10 nm and (b) 30 μm

REFERENCE

[1] M. Ohtsu, Proc. of SPIE, 3749, 478 (1999).

[2] H. Takagi, et al, Appl. Phys. Lett. 56, 2379 (1990).

Optical near-field interaction and its application to a nano-device

K. Kobayashi [1)], S. Sangu [1)], T. Kawazoe [1)], A. Shojiguchi [2)], and M. Ohtsu [1), 3)]
1) ERATO/JST, 2) ICU, 3) Tokyo Inst. Technology; kkoba@ohtsu.jst.go.jp

We have proposed an optical nano-switch using quantum dots (QDs) and optical near fields, and estimated a typical switching time from phenomenological equations of motion as well as observation of excitation energy transfer (EET) between QDs[1-2]. Theory is now required so that coherence and dephasing, i.e., the essence of optical near-field problems, can be properly handled in order to consider higher speed and new frameworks of nano-devices. In this paper we report such a theoretical approach.

Three-QD system as shown in Fig. 1 is considered. It corresponds to a fundamental block of the nano-switch proposed [1]. Optical near-field coupling between resonant levels as the interdot interaction produces coherence of such levels. We assume it as the Yukawa coupling on the basis of our previous study. As the intradot interaction, phonon coupling is included, which is responsible for relaxation and dephasing of the levels. Equations of motion, for investigating dynamic properties of the system, can be written in the following form:

$$\sum_{\ell} \hat{M}(\ell)\frac{\partial W_{\ell}(t)}{\partial t} = \frac{1}{i\hbar}\left[\hat{H}, \sum_{\ell}\hat{M}(\ell)W_{\ell}(t)\right]. \tag{1}$$

Here $\hat{M}(\ell)$ is an operator describing coherence of the resonant states, or excited and ground states, and $W_{\ell}(t)$ denotes the probability corresponding to $\hat{M}(\ell)$. Total Hamiltonian of the system is designated as $\hat{H}$ that consists of the unperturbed part for each QD and phonon, the optical near-field coupling, and the phonon coupling. Using Eq. (1), we can discuss the differences in the results obtained from the previous study, especially the speeds of switching and EET that are shown to be proportional to the optical near-field coupling. In this context, thorough investigation including the coherence and dephasing processes should be conducted in future.

Fig. 1. Energy levels of the three-QD system
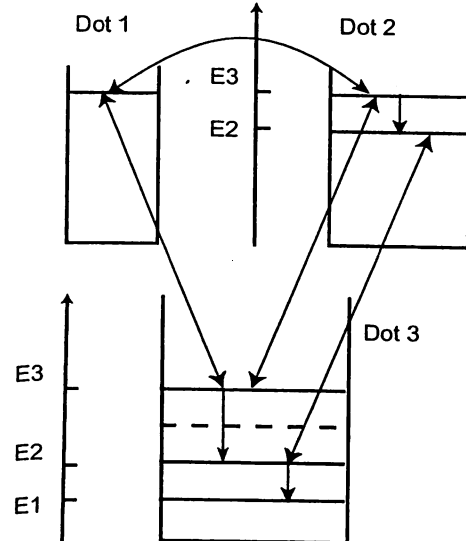
[1] K. Kobayashi et al., IPR/PS 2001, PThB4 –1 (2001).
[2] T. Kawazoe et al., CLEO/PR 2001, I-194 (2001); K. Kobayashi et al., ibid, I-192 (2001).

84

INTER-QUANTUM DOT ENERGY TRANSFER VIA
OPTICAL NEAR-FIELD INTERACTION

S. Sangu [1], K. Kobayashi [1], T. Kawazoe [1], and M. Ohtsu [1,2]

[1] ERATO Localized Photon Project, Japan Science and Technology Corporation

[2] Interdisciplinary Graduate School of Science and Engineering,
Tokyo Institute of Technology
E-mail: sangu@ohtsu.jst.go.jp

Optical near fields provide us a promising technique to realize miniaturization and higher speed of photonic devices, overcoming the diffraction limit of light. So far, we have proposed an optical nano-switch using quantum dots in which resonant energy transfer occurs via optical near-field interaction[3]. Irreversibility of signal has been guaranteed by non-radiative transition due to coupling between an exciton in a quantum dot and lattice vibration of each quantum dot. In this paper we analyze the energy transfer between quantum dots by means of quantum mechanical treatment instead of phenomenological one, in which the coupling of a quantum dot to heat bath is included.

Figure 1 shows a model of two-quantum dot system. Under the Born-Markov approximation[4], density matrix of the system can be derived where the ratio of relaxation constant γ (average contribution of coupling of all vibrational level g_n) to optical near-field potential U is an important factor determining dynamical properties for such a system. In Fig. 2, state-filling time is plotted as a function of the ratio $\gamma/2U$, which is the time constant for filling an exciton to the E_1 level in the Dot 2. The shortest state-filling time can be achieved when the near-field potential is comparable to the strength of coupling to heat bath, i.e., $\gamma/2U \sim 1$. According to our estimation, the potential U is on the order of 10 μeV, thus, the actual state-filling time is expected to be about 100 psec. The result shows that quite high-speed device could be achieved by using quantum dots and optical near-filed interaction.
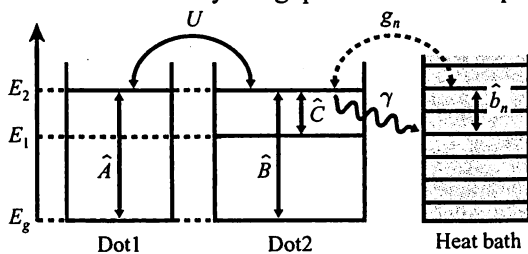
Fig. 1: Model of two-quantum dot system with coupling to heat bath.
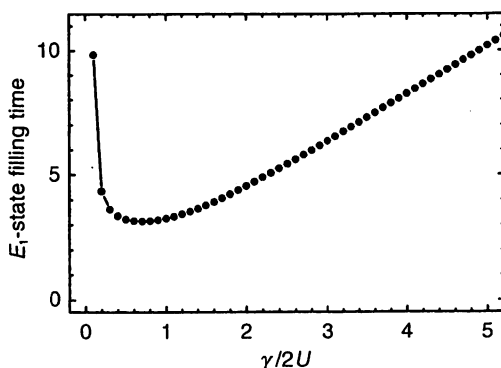
Fig. 2: State-filling time of exciton population at E_1 level in the Dot 2.

---

[3] K. Kobayashi, et al., CLEO/PR2001 Tech. Dig. (2001) I-192.

[4] H. J. Carmichael, *Statistical Methods in Quantum Optics 1* (Springer-Verlag, Berlin, 1999).

Excitation transfer by optical near-field interaction:
localized photon picture

A. Shojiguchi [*A], K. Kobayashi [B], K. Kitahara [A], S. Sangu [B], M. Ohtsu [B, C]

International Christian University [A], ERATO/JST [B], Tokyo Institute of Technology [C]

e-mail address of the contact author(who indicated by *):mxa01563@nifty.com

From the effective interaction viewpoint, optical near-field interaction among quantum dots (QDs) has been discussed and applied to a nanometric photonic device [1]. An alternative but equivalent localized photon picture, however, is still adequate for deep understanding of a variety of optical near-field phenomena and new insights, as well as in comparison with conventional electromagnetic field approaches. In this paper we report a formulation based on such a localized photon picture to discuss time evolution of dipole correlation in a QDs system: whether one can retain a dipole excitation in a QD localized or transport it to another QDs via localized photons.

We consider a system consisting of N two-level QDs closely configured in a ring and interacting with optical near field. Localized photons are introduced so that the optical near field is expanded in terms of a basis, whose functions are localized in QDs and can allow hopping only between the nearest neighbors. In addition usual dipole coupling is assumed as intradot interaction.

Figure 1 shows one of the results, where we investigate the correlation function between the dipole moment of the site n at time t and the one at the site 1 at $t = 0$. It predicts that one can keep the excitation at the site 1 as shown in Fig. 1(a), while one can transfer it to an arbitrary site as shown in Fig. 1(b), controlling the initial conditions. The hopping strength is found to be one of the key variables.
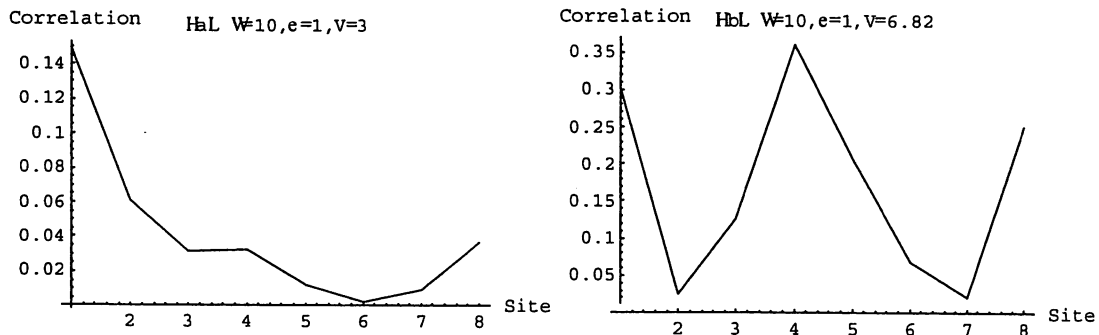
Fig. 1. Time evolution of dipole correlation. (a) localized case and (b) delocalized case.

From the results we expect a new equilibrium state that cannot be achieved in a propagating photon-matter system. Moreover the control of the excitation transfer discussed above may open the way to a novel functional device on a nanometer scale.

[1] K. Kobayashi et al., Technical Digest in OSA IPR/PS 2001, PThB4 (2001).

DIPOLE FORBIDDEN ENERGY TRANSFER VIA OPTICAL NEAR-FIELD INTERACTION BETWEEN CUPROUS CHLORIDE QUANTM CUBES

Tadashi Kawazoe[1], Kiyoshi Kobayashi[1], Suguru Sangu[1], Jungshik Lim[2], Yoshihito Narita[3] and Motoichi Ohtsu[1,2]

[1]Exploratory Research for Advanced Technology (ERATO), Japan Science and Technology Corporation (JST), 687-1 Tsuruma, Machida, Tokyo 194-0004, Japan
e-mail: kawazoe@ohtsu.jst.go.jp

[2]Interdisciplinary Graduate School of Science and Engineering, Tokyo Institute of Technology, 4259 Nagatsuta, Midori-ku, Yokohama 226-8502, Japan

[3]JASCO Corporation, 2967-5, Ishikawa-cho, Hachioji, Tokyo, 192-8537, Japan

We report, for the first time, the evidence of optical near-field energy transfer among CuCl quantum cubes (QCs) using an ultra high-resolution near-field optical spectroscopic microscope whose spatial resolution is less than 50 nm in near UV region at 15 K.

The sample was high-density CuCl QCs embedded in a NaCl matrix.[1] Quantized exciton energy levels (1,1,1) in 4.6-nm QCs and (2,1,1) in 6.3-nm QCs are resonant to each other. Since the energy level (2,1,1) is the dipole forbidden level, the possibility of energy transfer via optical far field is negligible. The carrier tunneling between QCs is also negligible due to the deep potential depth of 4 eV in this system. However, the energy transfer becomes possible by a resonant optical near-field interaction[2] in close proximity region, because the point transition dipole approximation is not effective due to the size effect of QCs, as shown in Fig.1.

The (2,1,1) excitons transferring via optical near field from 4.6-nm QCs relax to the lowest energy level (1,1,1) in the 6.3-nm QCs. Therefore, spatial distributions of the luminescence intensities from 4.6-nm and 6.3-nm QCs can be observed selectively by their wavelength difference. The measured optical near-field images clearly established anti-correlation features, as shown in Fig.2. On the other hand, the spatial distributions of luminescence intensities form the other sized QCs did not show any correlation features. Thus, we regarded the anti-correlation features as the evidence of the energy transfer via optical near field. While the possibilities of such dipole forbidden energy transfer have been pointed out,[3] our results is the first direct observation of the dipole forbidden energy transfer via optical near-field.

1) N. Sakakura and Y. Masumoto, Phys. Rev. B **56**, 4051 (1997).
2) K. Kobayashi, S. Sangu, H. Ito, and M. Ohtsu, Phys. Rev. A **63**, 013806 (2000).
2) K. Mukai, S. Abe, and H. Sumi, J. Phys. Chem. B **103**, 6096 (1999).
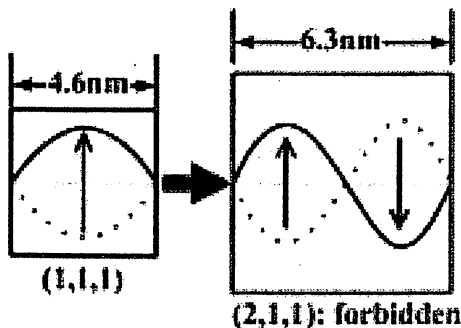
Fig.1. Quantized energy levels in QCs.
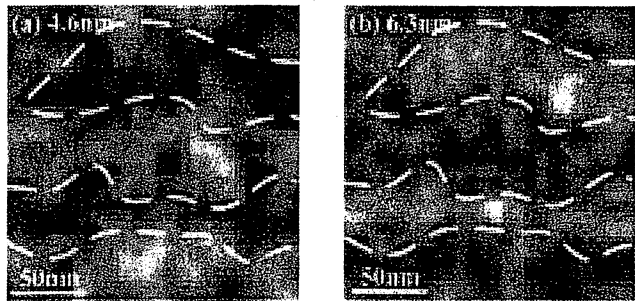
Fig.2. Near-Field luminescence images of QCs.

84
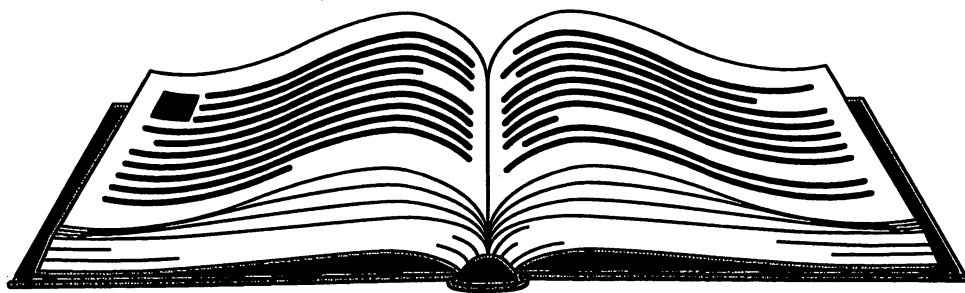
[I-3] REVIEW PAPERS

ナノフォトニクス

1 トップダウン型の要求に応（こた）えるナノフォトニクス

西暦1960年にレーザが発明され，1980年代には光通信，光メモリなどの産業が成長し現在に至っている．社会は今後の高度情報化・高度福祉化を支えるために光技術をいっそう進歩させることを要求しているが，これに応えるには光による計測，加工，デバイスなどの寸法を微小化し，高集積化，高速化，省電力化することが必要である．しかし既存の光技術は後述の回折限界のためにナノメートル寸法に至る微小化が不可能である．ナノフォトニクスとは，近接場光と呼ばれる寸法の小さな光を用いて回折限界を超え上記の要求に応えるために提案された技術である[1][2]．

ナノテクノロジーはナノ寸法物質を積み上げ，組み合わせてデバイスなどを構成するのでボトムアップの技術とも呼ばれている．一方，従来技術では大きな物質を削って小型化するのでトップダウンである．さてナノフォトニクスには，「社会的要求→それを満たす光システム→そのための光デバイス→そのためのナノ寸法材料と近接場光」という明確な階層構造があり，社会や応用システムからのトップダウン型の具体的な要求に応えるために進展している．筆者の知る限り，一般のナノテクノロジーにはこのように社会からのトップダウン要求はまだ明確でなく，ナノ寸法のテクノロジーとして成長するために必要なシステム的思考は必ずしも十分ではない．

これに対しナノフォトニクスはトップダウン要求を満たす必要上，システム的思考のもとに進展している．本稿の目的はこの点を理解していただくことである．

2 近接場光とは何か

既存の光技術では光を波として扱うが，光波は微小な穴を通り抜けた後に発散する．光波を絞って光ファイバの中を伝送させても出射後は発散する．この発散性は回折と呼ばれている．従って凸レンズで集光しても，焦点面上では光の波長程度の寸法のスポット径までしか絞れない．このピントのぼけのために光を使った計測，加工，デバイス動作は光波長程度以下の寸法を扱うことができない．これは
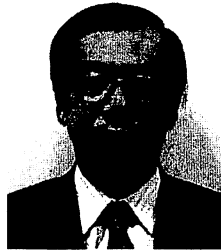
大津　元一
Motoichi OHTSU
◎1950年10月5日生まれ
1978年東京工業大学大学院博士課程修了，1978年同大学精密工学研究所助手，1982年同大学理工学国際交流センター助教授，1985年同大学大学院総合理工学研究科助教授，1991年より現職．1998年より科学技術振興事業団創造科学技術推進事業大津局在フォトンプロジェクト総括責任者を兼任
◎研究・専門テーマはナノフォトニクス
◎東京工業大学大学院　総合理工学研究科教授
（〒226-8502　横浜市緑区長津田町4259/
E-mail:ohtsu@ae.titech.ac.jp）

回折限界と呼ばれている．

ところで図1（a）に示すように光ファイバを先鋭化して根本に不透明な金属膜を塗り，先端部をわずかに突出させる（これはファイバプローブと呼ばれている）．すると光波が先端まで届かず，これでは従来の光技術の使用に耐えないが，金属膜から突出した先端部には光の薄い膜が発生している．その膜の厚さはファイバプローブの先端の直径程度であり，これが近接場光である[3]．さらに説明すると，近接場光とは図1（b）に示すように振動する電気双極子から発生する2種類の光のうちの近接場成分である．他方は遠隔場成分であり，その電場の電気力線は電気双極子から分離し，閉曲線となって遠方に伝搬する．従来の光技術ではこの伝搬光を使っており，これは回折する．これに対し近接場成分の電気力線は電気双極子に局在し，非伝搬である．

ナノフォトニクスはナノ寸法物質を扱うが，これに光を照射すると多数の原子に電気双極子が誘起され，おのおのが図1（c）に示すように図1（b）と同じ光を発生する．ここですべての電気双極子から発生する近接場光のエネルギーの総和をとると，それはナノ寸法物質表面から遠ざかるにつれて急激に減衰する．表面からの距離をr，ナノ寸法物質の大きさをaとすると，その減衰の様子は$\exp(-r/a)/r$なる湯川関数で表される[4]．すなわち近接場光の膜の厚みはナ

図1　近接場光の発生と利用の説明

(a) ファイバプローブの構造

(b) 振動する電気双極子から発生する光
x，yは直交座標．kは入射光の波数で，波長λとは
k＝2π/λの関係がある．

(c) ナノ寸法物質から発生する光

(d) 第一のナノ寸法物質表面の近接場光を第二のナノ寸法物質に照射している様子
これらのナノ系が巨視系に囲まれている様子も示す．
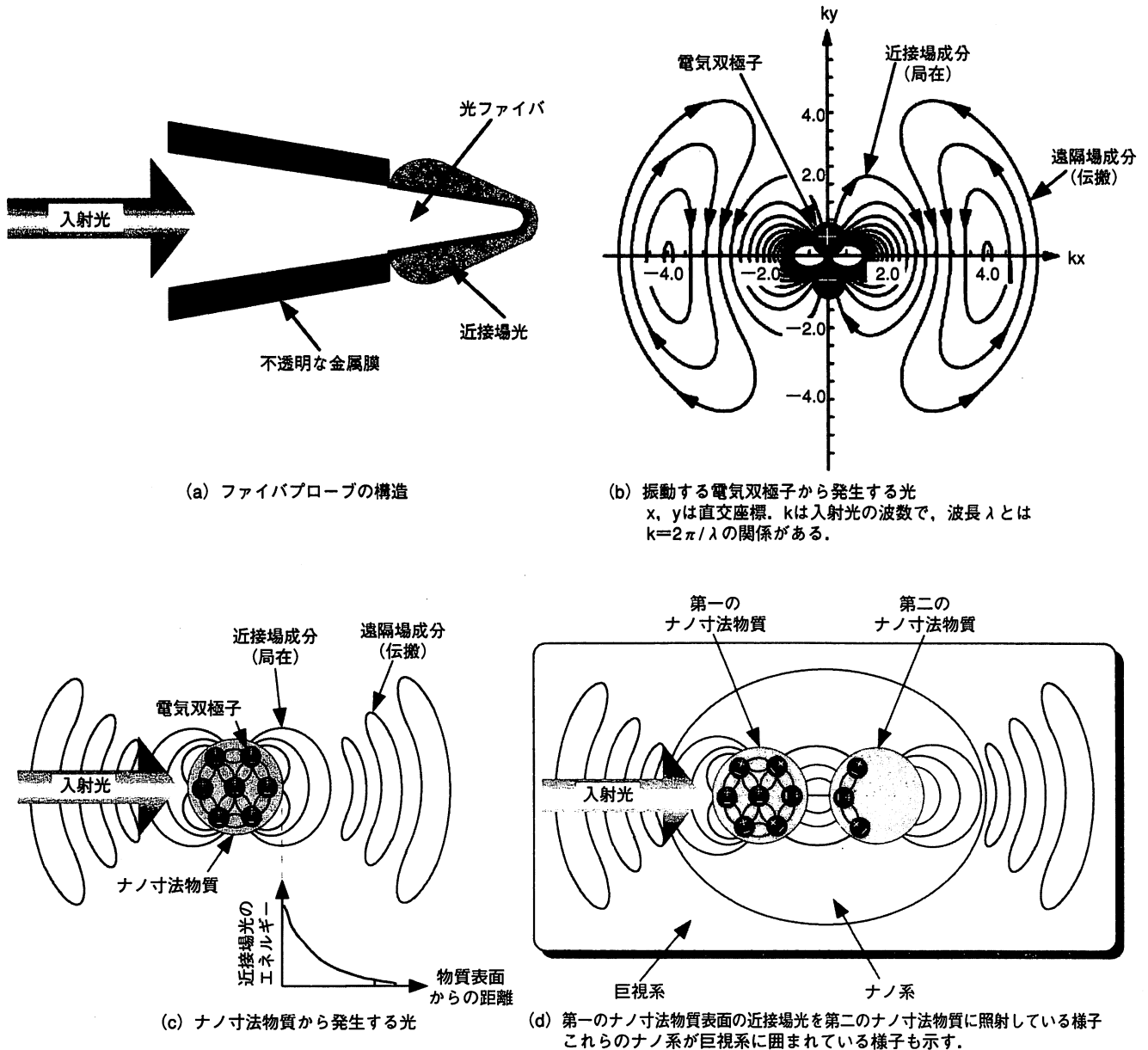
ノ寸法物質程度である．

　図1（d）のように第一のナノ寸法物質表面の近接場光を微小光源と見なすと，その寸法は入射光の波長にはよらず，第一のナノ寸法物質の大きさ程度なので第二のナノ寸法物質に近づけて照明しその像を観察したり，また加工することにより回折限界を超えた微小な光技術が可能となる．第二のナノ寸法物質が近づくと近接場光の電気力線はその表面に向かって伸び，第二のナノ寸法物質中に電気双極子を励振する．このとき重要なのは次の二点である．

　（1）二つのナノ寸法物質が近接場光を媒介として結合した状態になっている．

　（2）このように結合した微小な系（ナノ系と呼ばれている）が，それよりずっと寸法の大きな巨視系（ファイバプローブの根本，試料用基板，入射光，光検出器等から成る）

に囲まれている．

　この状態を詳細に記述するには量子力学の手法が必要であるが，それによると伝搬光を使う場合にはほとんど見られないエネルギーの移動（非共鳴エネルギー移動と呼ばれている）が二物質間で起こることが指摘されている[4]．すなわちナノ系のみに注目するとエネルギー保存則からのずれが生じる．そのエネルギーの過不足分は上記（2）の巨視系からまかなわれるので，ナノ系と巨視系とを合わせた全体ではエネルギー保存則は成り立つ．ナノフォトニクスの本質はこのように巨視系の中から適当なナノ系を抽出し，従来の光技術では困難なエネルギー移動の形態を利用することである．このほか，運動量，角運動量についても同様のことがいえる．ナノ寸法の光技術が実現することは副産物にすぎない．

③ どのように使われるか？

本章ではナノフォトニクスのカバーする分野について紹介し，特にトップダウン要求とそれに応えるシステム技術として発展させるための注意点を指摘する．

3-1 基本デバイスを作る

社会からのトップダウン要求に応える近接場光を発生するための基本デバイスを開発するにあたり，次の2点に注意が払われている．

（1）インピーダンス整合　　穴の空いた板や微小球に光を照射すれば近接場光が発生するが，そのエネルギー密度は低く使用に耐えない．高エネルギー密度の近接場光を発生させるには照射する伝搬光のエネルギーを効率よく近接場光エネルギーに変換する必要がある．これが「インピーダンス整合」であり，その条件は電磁気学の手法に求めることができる．これを実現したのが図1（a）のファイバプローブにほかならない．インピーダンス整合とはファイバプローブの傾斜部の形状，寸法を最適化することであり，その結果最近では近接場光の発生効率として数％に達するファイバプローブが開発されている[5]．この結果「近接場

光の発生効率は低い」という通説はもはや遠い過去のものとなった．なお，インピーダンス整合は2章で述べたナノ系と巨視系とのエネルギーの授受を効率よく行う方法ともいえる．

（2）歩留まり　　上記（1）のファイバプローブを高い歩留まり，再現性で作製することが最も重要である．ふっ酸系溶液による選択エッチングがその解を与え，これにより希望する性能が実現し，さらに優れたファイバプローブを設計するための基礎データが蓄積されている[6]．これをもとに，最近ではファイバではなくシリコン結晶基板を用いた高効率プローブも開発されており，量産性の高い技術として期待が高まっている．

3-2 情報を記録する

光メモリ技術ロードマップによると2010年には記録密度 $1Tb/in^2$，再生速度$1Gb/s$が必要とされている[7]．これが高度情報化社会を支えるためのトップダウン要求である．しかし既存のDVD技術では回折限界のために実現不可能であり，技術のパラダイムシフトが必要である．そのためには近接場光を用いた光記録再生法が有望であり，そのシステムの一例を図2に示す[8]．ここではシリコン結晶基板を用い，3-1の（1）に示したインピーダンス整合を実現し，（2）の

図2　光記録再生システムの例
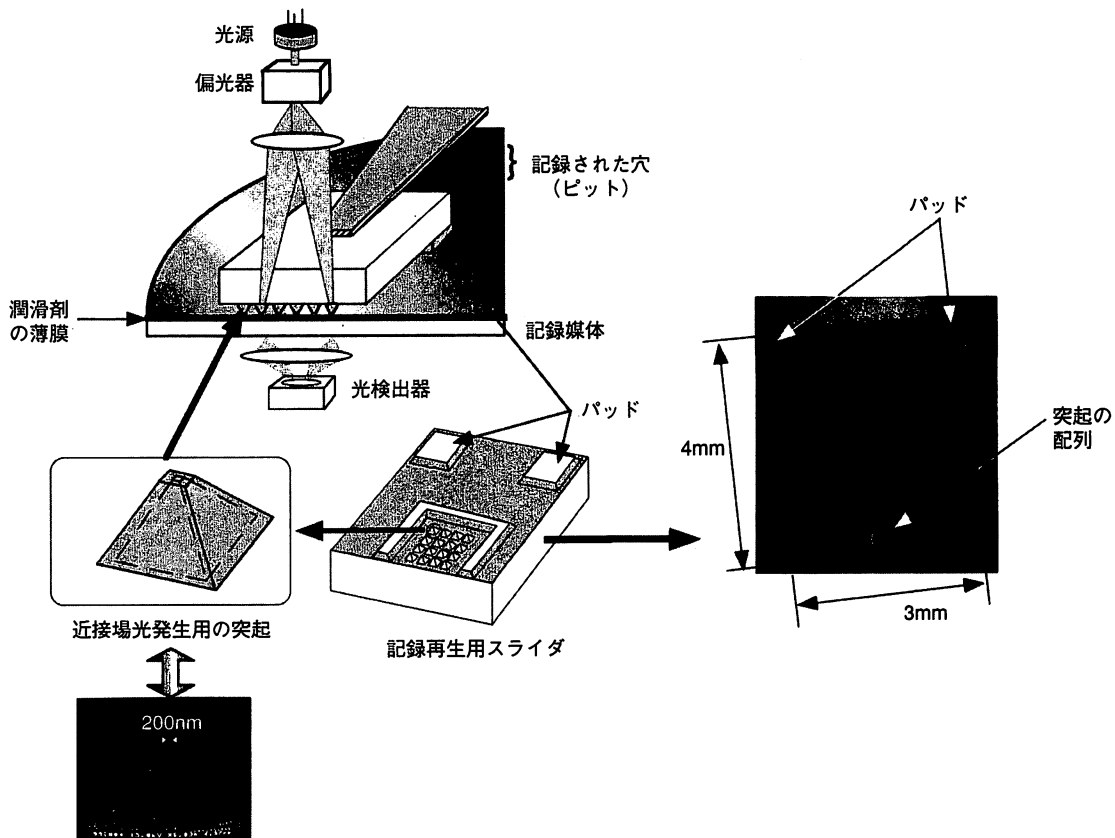
図3 ナノ光デバイスの集積化システムの構成例
3-4節の方法を使って作製されたナノ寸法物質などの例も示す.
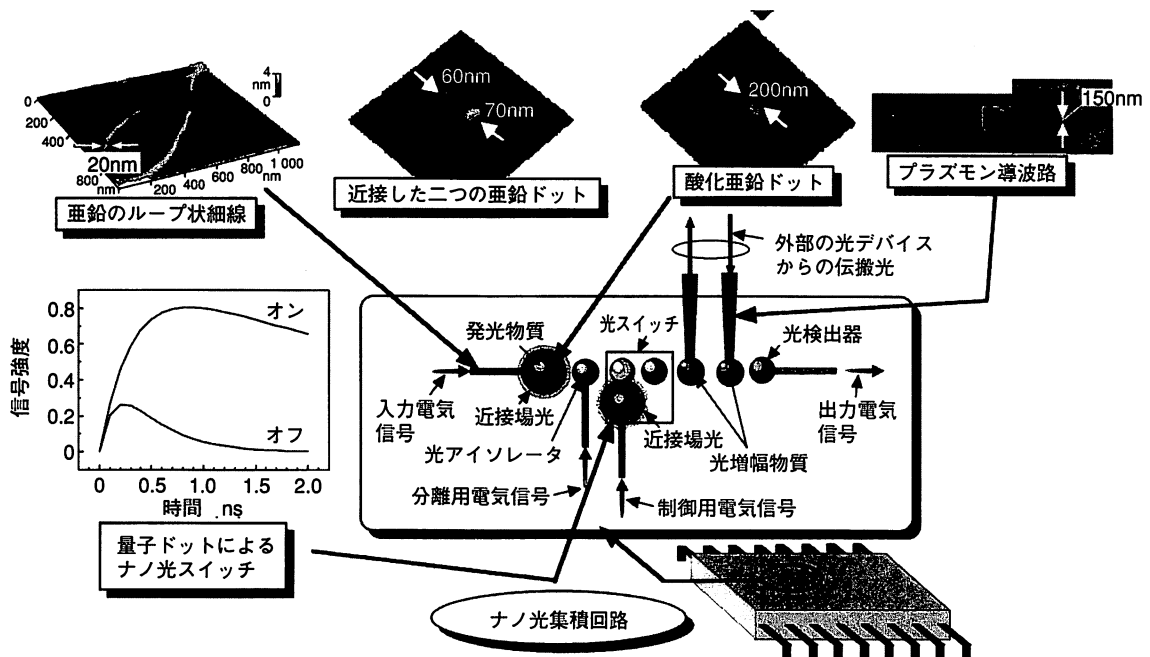
歩留まりを高めるために異方性エッチングにより作製した二次元プローブ配列を搭載した記録再生スライダが開発されている.その結果,相変化記録用光ディスクに密度約60Gb/in²で光記録され,それを速度0.4m/sで走査されたスライダで再生している.これは二次元配列中のプローブ数が100個の場合,400Mb/sの再生速度に相当する.今後はデバイス(スライダ),材料(記録媒体保護膜,潤滑剤),評価方法(光ディスク計測)などの要素技術を相互連携してさらに性能向上させるべく,システム開発が始まっている.

なお,ここで注意すべきはトップダウン要求に応えるために,ナノテクノロジーの基本的な計測技術である走査プローブ顕微鏡とは逸脱した形態をとっていることである.その代表例はスライダの著しい高速走査である.

3-3 情報を伝送する

光ファイバ通信の技術ロードマップによると,2015年には高度情報化社会を支えるために10Tb/sのデータ転送速度が必要,光交換機用の光スイッチ配列中の入出力端子数はおのおの1 000またはそれ以上必要と推定されている[9].これらのトップダウン要求を満たすには,回折限界を越え光スイッチ配列中の各光デバイスを微小化しなければならず,光デバイス技術のパラダイムシフトが必要である.そのために近接場光を用いたナノ光デバイスとその集積化が有望

である[6].集積化システムの構成原理を図3に示す[10].ここではナノ寸法物質と近接場光との相互作用を利用し,個々のナノ寸法物質に近接場光の発生,スイッチング,検出機能を発現させ,情報を担う近接場光をナノ寸法物質間で転送する.すでに酸化亜鉛の青色発光や三つの量子ドットを組み合わせた光スイッチングなどの実験及び理論的研究が行われている[11].トップダウン要求に応えるためにこのシステムは次の特徴を持つ.

(1)高い信頼性を確保するため図2の記録再生スライダのような可動部を排除し,平面埋込み型のシステムとなっている.すなわち,走査トンネル顕微鏡で採用されているプローブ走査,および試料と接近させる点接触の二つの概念を排除している.

(2)上記の光スイッチングはナノ寸法物質と近接場光との局所的相互作用(すなわち2章末尾の非共鳴エネルギー移動)を利用している.従ってこれは通常の伝搬光を用いたのでは実現不可能であり,光デバイスのパラダイムシフトの典型である.

(3)外部の大寸法の光デバイス(たとえば光ファイバなど)と接続して一般ユーザの使用に供するためのインターコネクションを配備している.これは図3の中の近接場光を伝搬光に変換して外部に伝送すること,またはその逆の働きをするものである.半導体と金属細線から構成されたプ

ラズモン導波路がこの機能を担っている[12]. これは3-1節のインピーダンス整合にほかならない.

３-４ 微細な加工をする

たとえば図3の集積回路を作るにはナノ寸法物質の寸法, 位置, 間隔に関する精度が高い加工技術が必要である. この精度はナノ寸法物質間で近接場光を転送するために不可欠である. さらに共通基板の上に多様な物質を堆積(たいせき)できることも重要であるが, 既存の加工技術はこれらの要求を満たさない. たとえば自己組織化などの微小物質堆積法は熱平衡と化学反応とを利用した集団的方法なので, 個々のナノ寸法物質の寸法, 位置, 間隔の制御性は高くない. 従って加工技術に関してパラダイムシフトが必要である.

そのために近接場光を使った化学気相堆積法が有望である. これは気体中の有機金属分子に近接場光を照射し, 分子中の電子を基底準位から励起準位へと励起し, 分子に含まれている金属原子などを解離して基板の上に堆積するものである. 近接場光発生用デバイスの寸法, 位置を制御することにより上記の精度を満たす. また近接場光発生用の光の種類を変えると多様な分子を解離, 堆積できる. 図3にも示したように亜鉛, アルミニウムなどの金属, 酸化亜鉛などの酸化物(半導体のエネルギー構造を有する)の微小パターンなどが形成されている. このほかGaAsなどの化合物半導体の堆積も可能である.

さて, 一例としてジエチル亜鉛分子を堆積する場合, 伝搬光で解離しようとすると電子を励起するために紫外線が必要であったが, 近接場光の場合はそれよりも光子エネルギーの低い青色光を用いても可能であることが確認されている[13]. これは2章末尾の非共鳴エネルギー移動の結果であり, このことは近接場光を用いれば伝搬光では不可能であった新物質が堆積できることを意味している.

４ 展望とまとめ

3章では近接場光を発生させ使うという新しい(従ってクレージーな)方法により光技術のハードウェアに関するパラダイムシフトを実現させる例を述べた. しかしこれを使うためのソフトウェアに関するパラダイムシフトは未発達といえる. 光メモリを例に取るとどのようなアプリケーションソフトウェアをユーザに供給するかという議論は従来技術の延長上で連続的, 帰納的になされているのみである. むしろ芸術家, ゲームソフト設計者などの不連続な発想(これは技術者から見てクレージーな発想といえるかもしれない)が必要である. また, 脱着可能型光メモリの規格の国際標準化も重要であり, これに関して我が国が主導権を握ることが光メモリの国内産業を進展させるのに必須(ひ

っす)である. しかしそのためには国際的な調整作業(ネゴシエーション)が必要である.

ただし誠実と奥ゆかしさとを美徳とする国民である日本人にとってクレージーな発想は国内で(むしろ本人の直近の周辺から)の道徳的批判を受ける可能性があるし, 国際的なネゴシエーション(もちろん英語で)も得意とはいえない. このことは国民性のパラダイムシフトを実現し, 正当な主張をスマートに行うことこそが今後のナノフォトニクス, さらにはナノテクノロジーの発展のために重要であることを意味している.

なお, ナノフォトニクスはナノ寸法物質のみでなく, さらに先の技術として中性原子を一つずつ操作するアトムフォトニクスへと展開されていることを指摘して筆を置きたい[14].

●文　献
(1) 大津元一, ナノフォトニクスとその展望, 電子情報通信学会誌, 84-1 (2001), 26-32.
(2) 大津元一, ナノ・フォトニクス, (1999), 12-26, 米田出版.
(3) 大津元一, 光の小さな粒, (2001), 19-35, 裳華房.
(4) Kobayashi, K.and Ohtsu,M., Quantum Theoretical Approach to a Near-field Optical System, *J. Microscopy,* 194-2 (1999), 249-254.
(5) Ohtsu, M., *Near-Field Nano/Atom Optics and Technology,* (1998), 71-87, Springer-Verlag.
(6) Ohtsu, M., *Near-Field Nano/Atom Optics and Technology,* (1998), 31-69, Springer-Verlag.
(7) 光テクノロジーロードマップ策定専門委員会, 光テクノロジーロードマップ報告書(情報記録分野), オプトニューズ, 105 (1998), 24-25.
(8) Yatsui, T., Kourogi, M., Tsutsui, K., Takahashi, J. and Ohtsu., M., High Density/speed Optical Near Field Recording/Reading with a Pyramidal Silicon Probe on a Contact Slider, *Opt. Lett.,* 25-17 (2000), 1279-1281.
(9) 光テクノロジーロードマップ策定専門委員会, 光テクノロジーロードマップ報告書(情報通信分野)改訂版, オプトニューズ, 116 (2000), 7-10.
(10) Ohtsu, M., Near-field Nano-optics Toward Nano/atom Deposition, *Technical Digest of the 18th Congress of the International Comission for Optics,* (1999), 478-479, SPIE Press.
(11) Kawazoe, T., Kobayashi, K., Lim, J., Narita, Y. and Ohtsu, M., Direct Observation of Optically-Forbidden Energy Transfer between CuCl Quantum Cubes by Optical Near-Field Spectroscopy, *Phys. Rev.Lett.,* 88-6 (2002), 067404 (1) - 067404 (4).
(12) Yatsui, T., Kourogi, M. and Ohtsu, M., Plasmon Waveguide for Optical Far/near-field Conversion, *Appl. Phys. Lett.,* 79-27 (2001), 4583-4585.
(13) Kawazoe, T., Yamamoto, Y. and Ohtsu, M., Fabrication of Nanometric Zn Dots by Nonresonant Near-field Optical Chemical Vapor Deposition, *Appl. Phys. Lett.,* 79-8 (2001), 1184-1186.
(14) 伊藤治彦・大津元一, 近接場光を用いた原子の制御, 光学, 28-11 (1999), 610-615.

3 High-Resolution and High-Throughput Probes

M. Ohtsu and K. Sawada

The basis of the near-field optical microscope (NOM) is short-range electromagnetism between two antennas, a probe antenna and a sample antenna, which are much smaller than the wavelength of the driving field [1,2]. It is apparent that fabricating and manipulating small antennas are the most important factors in the successful development of NOM. One of the most realistic and commonly used methods for preparating a small antenna is sharpening an optical fiber to a very small apex. By employing the scanning technique already established in a scanning tunneling microscope (STM) and an atomic force microscope (AFM), the antenna at the apex of a sharpened fiber works as a probe on a sample surface under precise distance control.

A conventional optical fiber is sharpened by chemical etching in buffered hydrofluoric acid. An apex (diameter $d = 2a$), which is the antenna of the fiber probe, can easily be made small, and a minimum apex size of only a few nanometers has already been achieved. In NOM, only the apex works as an antenna, which interacts electromagnetically with the sample. The tapered part has a simple conical shape, and the cone angle θ is clearly defined. The apex radius and the cone angle can be varied by controlling the etching conditions. The exterior surface of the probe is coated with opaque metal, such as aluminum or gold, to avoid the illumination of excitatory light or the detection of the background signal through the sidewall of the tapered part. The very end of the metal coating is removed to allow the sharpened glass part, including the apex, to protrude. The small aperture with a diameter of d_f (also called the foot diameter) makes an important contribution, as will be discussed later. We call the protruded glass part and the metal-coated part the tapered core and the metallized tapered core, respectively.

The metallized tapered core is regarded as a metal-clad (metallic) waveguide through which excitation or signal light passes. Since the metallic waveguide has a complex loss mechanism, e.g., the existence of a cutoff diameter and absorption by the metal cladding, optimization of the structure of the waveguide is essential.

The important components for optimizing of the probe are summarized as follows:
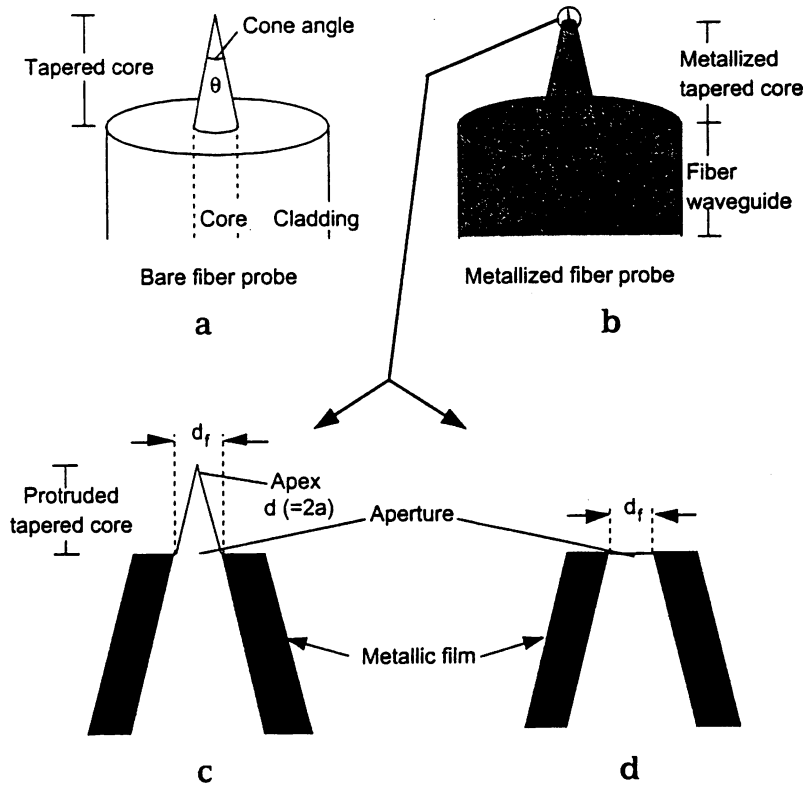
Fig. 3.1. Schematics of typical fiber probes

1. The apex size should be the same as the characteristic size of the sample to be investigated.
2. The smaller the cone angle, the smaller the undesirable background signal due to the dipole coupling between the sample and the tapered part.
3. The coupling can also be eliminated more efficiently by combining a metal aperture with a glass tapered part.
4. By proper metallization of the apex, the signal intensity is much enhanced compared with that from a bare glass apex.

Following these optimization criteria, high-quality fiber probes have been fabricated [1,2]. Using them, a near-field optical image of a single string of deoxyribonucleic acid (DNA) has been obtained by a collection mode operated under a constant-distance mode with the optical near-field intensity as the feedback signal [3]. As shown by Fig. 3.2, the observed width of the narrowest string is around 4 nm, even though the pixel size is as large as 2×2 nm. To our knowledge, this is the first and only successful optical observation of a single string of DNA by purely optical means and with such high resolving capability. This high resolution is attributed to the special care taken during the preparation of the sample and probe. The probe efficiently picks up the high spatial Fourier frequency component of the scattered near-field and simultaneously rejects the lower components effectively. With further improvement in the system, including a scanner and other mechanical component, it will be possible to observe the double-stranded or double helix of DNA by purely op-
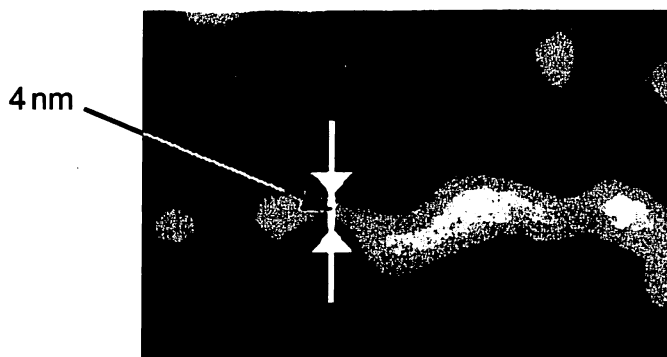
Fig. 3.2. Collection-mode optical near-field image obtained under a pixel size of 2 × 2 nm

tical means. Because the control is optical, it is easier to extend the operation into liquid or fluid environments which opens up the possibility of directly manipulating the DNA structure or investigating individual segments of the double helix structure itself [4].

The improvement of the sensitivity by a metal probe is frequently employed in a near-field plasmon microscope since it can easily be realized by using metal or metal-coated glass fiber probes for STM. In collection-mode NOM, however, when the protrusion part is completely metallized, the transmission intensity of the signal light into the fiber is generally decreased. Therefore, the thickness of the metal film, which also influences the resonant behavior of the plasmon probe, is an important design factor.

A serious problem of the fiber probe is its low throughput. The essential cause of low throughput is the guiding loss along (or inside) the metallized tapered core. To study this loss mechanism and to realize high throughput probes, we focus our discussion on the characteristics of the tapered core. Since the nanometric protruded part at the top of the fiber probe does not contribute to this loss, this section treats only the fiber probe without a protruded part, i.e., a flat apertured probe. Its cross-sectional profile is shown in Fig. 3.1d, for which the foot diameter d_f of the protruded probe in Fig. 3.1c can be called an aperture diameter.

As an example, the throughput of the probe of Fig. 3.1d decreases rapidly with decreasing probe size [1,2]. To increase the throughput, i.e., to generate a strong optical near-field under illumination-mode operation and to realize high collection efficiency in collection-mode operation, this section describes the possible excitation of the plasmon mode in the metallized tapered core. We also demonstrate highly efficient excitation of the optical near-field on a probe. Further, we demonstrate double- and triple-tapered probes fabricated to increase the throughput by shortening the tapered core.

3.1 Excitation of a HE-Plasmon Mode

3.1.1 Mode Analysis

Mode analysis has been carried out by approximating a tapered core as a cylindrical core with a metal cladding. The result shows that this core can guide the light, even if its diameter is smaller than half the wavelength. It also shows that the cutoff core diameter of the HE_{11} mode is as small as 30 nm, whereas that of the EH_{11} mode is 450 nm [5]. It means that only the HE_{11} mode can excite the optical near field efficiently when the apex size of the probe is in the sub-100 nm range. It is also found that the equivalent refractive index of the HE_{11} mode approaches that of a surface plasmon which is between those of glass and gold. This means that the origin of the HE_{11} mode in a metallized core is the surface plasmon. Thus, we call the HE_{11} mode the *HE-plasmon mode* from now on. However, the HE-plasmon mode is not easily excited in a conventional core because its coupling efficiency with the lowest order optical fiber guided mode is very low due to mode mismatching between the HE_{11} and HE-plasmon modes at the foot of the tapered core.

3.1.2 Edged Probes for Exciting a HE-Plasmon Mode

An effective way of exciting the HE-plasmon mode is to use the coupling of the plasmon by scattering at the edge of the metal [5]. If the tapered core has a sharp edge at its foot, part of the guided light inside the single-mode fiber can be scattered at this edge and converted to the HE-plasmon mode [6]. We call the probe with such a core *an edged probe.*

Figure 3.3 shows scanning electron micrographs of a fabricated edged probe with a flat aperture at the top (the aperture diameter d_f is 500 nm). An arrow R in Fig. 3.3a represents the direction parallel to the surface from which a part of the core was removed. The x and y axes are the directions normal and parallel to the arrow R, respectively. Figure 3.3b,c represents the profile of the tapered core buried in a gold metallic film. Part of the foot of the core was removed to form a sharp edge; the height of the removed part was 1.5 μm. This probe was fabricated by selective chemical etching [7] and by using a focused ion beam (FIB).

Probes with an aperture diameter d_f as small as 30 nm have been realized by these steps. Figure 3.4 shows the throughput of these probes. This figure confirms the realization of high throughput by the edged probe. We compared the output light power of the edged and the conventional fiber probes. Figure 3.5a,b shows the measured spatial distributions of the EH_{11} and HE-plasmon mode powers for an edged probe with $d_f = 500$ nm, respectively. They agree with the calculated results. As a reference, the spatial distribution for an axially symmetrical fiber probe with $d_f = 500$ nm was also measured. It had a double-peaked profile corresponding to the EH_{11} mode,
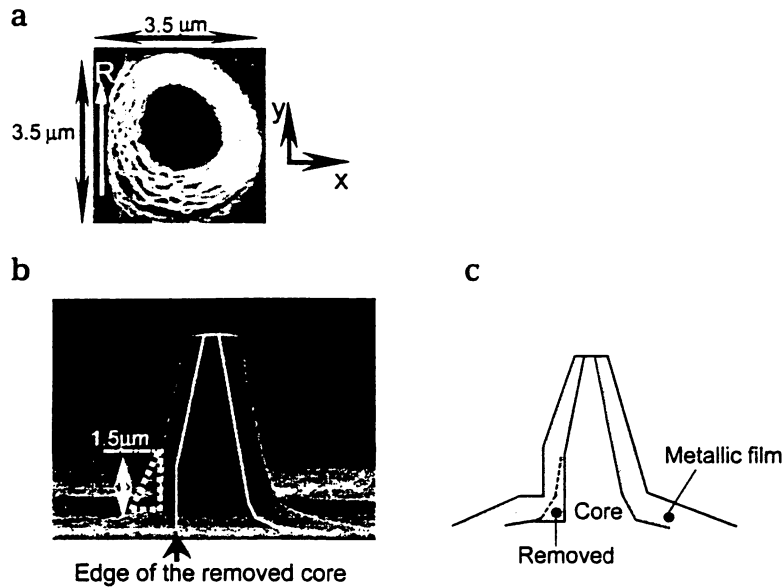
Fig. 3.3. Scanning electron micrographs of an edged probe with a flat aperture at the top. a Top view. b Side view. An arrow R in a represents the direction parallel to the surface from which a part of the core was removed. The x and y axes are the directions normal and parallel to the arrow R, respectively
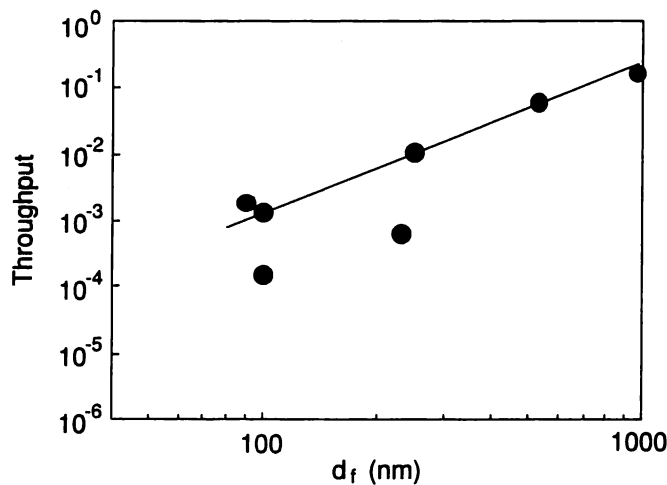
Fig. 3.4. Measured relation between the aperture diameter d_f and the throughput of the edged probe

and the positions of the peaks moved when the direction of the incident light polarization was varied. These results indicate that the edge at the foot of the tapered core successfully excites the HE-plasmon mode and the excitatory efficiency depends on the direction of the incident light polarization.

To check whether the output light power on the aperture was enhanced due to the edged structure, its spatial distributions on the probes with and without the edge were compared for $d_f = 100$ nm. Note that the EH_{11} mode is not guided inside the probe with $d_f = 100$ nm because it is smaller than its cutoff diameter (450 nm). The cross-sectional profiles of the measured

a   b

750 nm   750 nm

750 nm   750 nm
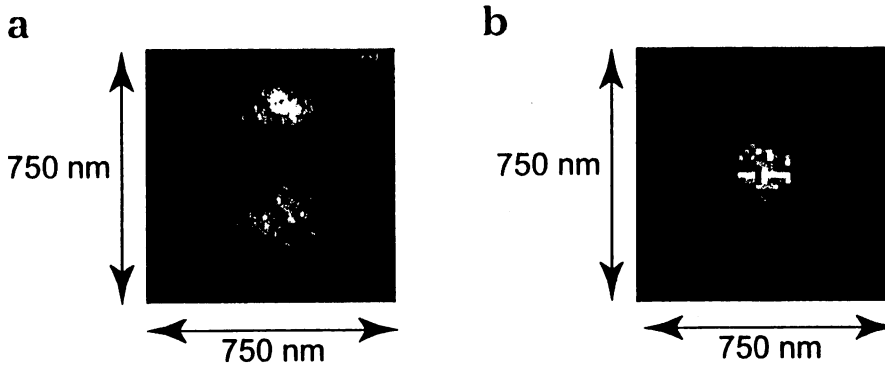
Fig. 3.5. Spatial distribution of the output light power on top of an edged probe with $d_f = 500$ nm. **a** The EH_{11} mode. **b** The HE-plasmon mode

light power distributions for edged probes are ten times larger than those of probes without an edge. The full width at half maximum is 150 nm, which is comparable to that of the HE-plasmon mode ($= 120$ nm) for $d_f = 100$ nm estimated by mode analysis. These results indicate effective excitation of the HE-plasmon mode by the edge at the foot of the tapered core.

3.2   Multiple-Tapered Probes

Note that an increase of throughput is possible by tailoring the probe structure. Since the guiding loss in the core is due to loss in the metal cladding, the easiest way to decrease the loss is to shorten the length of the tapered core.

3.2.1   Double-Tapered Probe

Chemical etching is a powerful technique for shortening the enormous absorption region because it enables reliable design and fabrication of an optimum structure for the tapered core. First, we demonstrate the strong dependence of throughput on the cone angle θ and hence the resultant length l of a tapered core. For probes with different cone angles, throughput is evaluated for a wide range of aperture diameters ($80 \leq d_f \leq 900$ nm). On the basis of these results, we optimize the shape of the probe taking into account the experimental utilities [8]; for example, by increasing the length of the tapered core, we can avoid contact between the cladding and the bumpy surface structure of the sample.

We briefly describe the fabrication technique of the probe by a selective etching process. The cone angle θ can be controlled by buffering the etching solution, which is adjusted by the volume ratio X of NH_4F maintaining that of HF to H_2O at $1 : 1$. Here, the composition of the solution is expressed as $X : 1 : 1$. To evaluate the dependence of throughput on the cone angle, two types of probes were prepared using a one-step etching technique with a
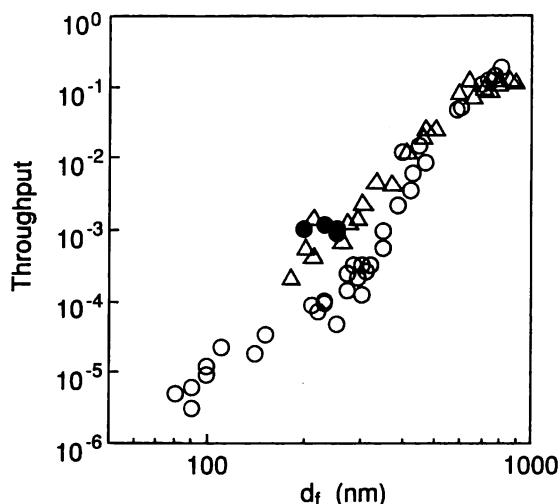
Fig. 3.6. Measured relations between the aperture diameter d_f and the throughput for probe A with a single tapered core whose cone angle is 20° (*open circles*), probe B with a single tapered core whose cone angle is 50° (*open triangles*), and a double-tapered probe (*closed circles*)

solution of $X = 10$ (probe A) and $X = 2.7$ (probe B). The cone angle θ and the length l of the tapered core of probe A were 20° and 6 μm, respectively, and those of probe B were 50° and 2.5 μm.

Using a sputter coating method, the exterior surface of the etched core was coated with a gold film 200 nm thick, which is seven times the skin depth at a wavelength of 633 nm. The selective resin coating (SRC) method is employed to fabricate a small aperture. Acrylic resin dissolved in an organic solvent is coated as a guard layer over the sides of the tapered part, leaving the top of the tapered core free of the acrylic resin. Here, the surface tension of the resin is used. On removing the gold film from the top of the core with the commonly used KI–I_2 etching solution, a small protruding type aperture (with the foot or aperture diameter d_f, c.f. Fig. 3.1) is fabricated. The aperture diameter d_f can be varied by controlling the etching time in the KI–I_2 etching solution and the coating condition which can be adjusted by changing the cladding diameter and the viscosity of the resin solution.

To estimate the throughput, the light from a He–Ne laser (633-nm wavelength) of 130 μW power is coupled into the fiber probe with a coupling efficiency of 60%. The far-field light ejected from the aperture is collected with a 0.4 NA objective. The output light power is measured with an optical power meter. The geometric size of the aperture is estimated with a scanning electron microscope after the throughput measurement.

Figure 3.6 shows the measured value of the throughput as a function of the aperture diameter d_f for probes A (open circles) and B (open triangles) of different cone angles. For the diameter d_f that is larger than the wavelength of He–Ne laser light in glass ($\lambda_c \sim 400$ nm), the throughput of probes A and B are almost the same when the aperture diameters are the same. This
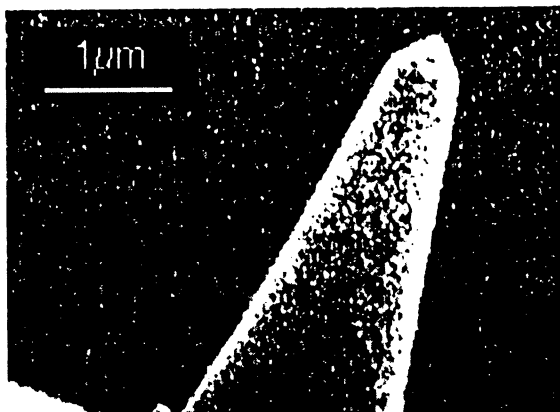
Fig. 3.7. Scanning electron micrograph of a double-tapered core prior to metal coating

means that the efficiency of delivering light into the region $d_f > \lambda_c$ is not so strongly dependent on the cone angle θ and the length l of the tapered core, which is 5 μm long at most. On the other hand, in the region $d_f < \lambda_c$ the difference between the two types of probes is remarkable due to the influence of the metal coating. For $d_f = 200$ nm, the throughput of probe A is ten times lower than that of probe B. Although the throughput depends on the spatial mode characteristics of the tapered core, the difference in the guiding lengths between probes A and B can also contribute considerably to the throughput. The guiding lengths of the core diameters of 400 nm ($= \lambda_c$) and 200 nm ($= d_f$) are 570 nm for probe A and 210 nm for probe B, respectively. It is theoretically estimated that, in the EH_{11} mode, the absorption of light by the coated metallic film is drastically influenced in the region where the core diameter is smaller than λ_c. In such a strong loss region, a difference in the guiding length of as much as 360 nm results in a decline of throughput by an order. We can conclude that, to increase throughput, it is reasonable to shorten the strong loss region in the tapered core by increasing the cone angle.

However, a short tapered core with a large cone angle leads to contact between its cladding and the bumpy surface of the sample during the actual scanning operation. To avoid this inconvenience, it is necessary to lengthen the tapered core while maintaining high throughput. For this purpose, we successfully developed a two-step etching process for fabricating a double-tapered probe with high reproducibility. As shown in the scanning electron micrograph of Fig. 3.7, the resultant cone angle is about 90°. The fabrication technique for the aperture is the same as that described above. Again, we measured the throughput of some of the fabricated double-tapered probes with $d_f = 200$ nm. The results are also plotted in Fig. 3.6 (closed circles). Throughput ten times higher than that of probe A (open circles) is achieved. This comparison implies that one of the most important factors in determining throughput is the length of the loss region in the narrow tapered core.
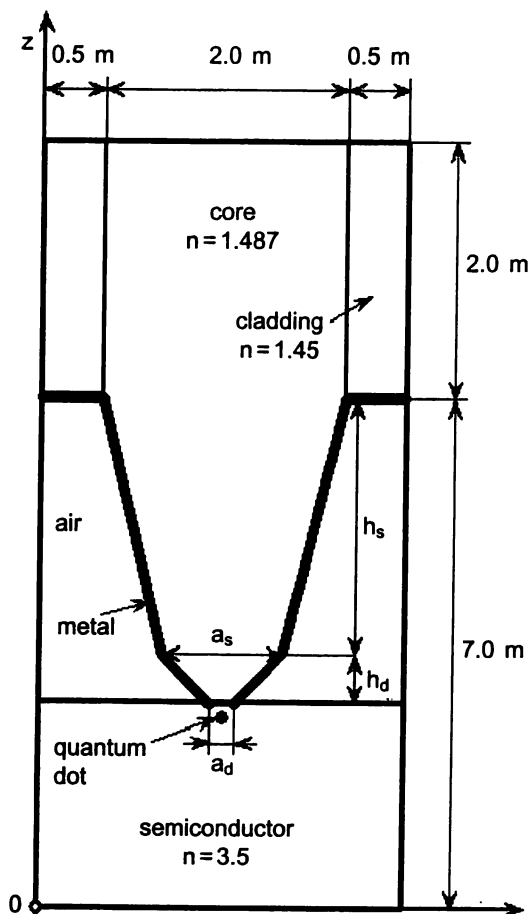
Fig. 3.8. Cross-sectional as diagram of the simulation model. Sample 1: $h_s =$ 3.6 μm, $a_s = 0.2$ μm. Sample 2: $h_s = 0.9$ μm, $a_s = 0.2$ μm. Sample 3: $h_s = 2.0$ μm, $a_s = 1.0$ μm, $h_d = 0.4$ μm, $a_d = 0.2$ μm

In double-tapered probes, realization of apertures smaller than 100 nm is not feasible due to its large cone angle. However, due to the limitations in measurement sensitivity, high throughput is more crucial than realizing a very small aperture for weak signal detection in the advanced spectroscopy of semiconductors.

Recently, with the progress of computational work, numerical analysis has come to be recognized as a powerful tool for deep understanding of the electromagnetic field in a tapered waveguide and in the vicinity of an aperture and for the systematic design of highly efficient probes. The finite-difference time-domain (FDTD) method [9–11] is one of the most promising methods for these purposes because it can be easily applied to actual three-dimensional problems. We have reported an FDTD simulation for the double-tapered structure in [12], in which spatial resolution beyond that of a conventional NOM is successfully reproduced by simulation.

Here, we show an FDTD simulation, which corresponds to the experimental configuration in [8]. Figure 3.8 illustrates the FDTD geometry of the probe model. A fiber probe with a double- or single-tapered structure collects

luminescence ($\lambda = 1$ μm) from a quantum dot (x-directed dipole radiation) buried $\lambda/40$ beneath the semiconductor surface. The radiation caught by the aperture with a diameter of $\lambda/5$ propagates in the tapered part clad with a perfectly conducting metal. The signal intensity is evaluated by calculating the light power finally coupled to the ordinary waveguide (optical fiber) region. The simulation box consists of a $120 \times 120 \times 360$ grid in the x, y, and z directions. The space step is $\lambda/40$. The calculation is done for three types of probes whose dimensions are summarized in the Fig. 3.8 caption. Sample 1 is a single-tapered probe. Sample 2 is a single-tapered probe which has a shorter tip length than that of sample 1. Sample 3 is a double-tapered probe whose cone angle at the tip is the same as that of sample 2. The calculation shows that the ratio of signal intensity for samples 1–3 is 1 : 32 : 100. It is clear that a large cone angle contributes to high collection ability since this structure minimizes the length of the cutoff region. In addition, the double-tapered probe makes the coupling of light into the normal waveguide more efficient than that of the single-tapered probe with the same cone angle. The collection efficiency and spatial resolution of the double-tapered probe in [13] are also reproduced by this FDTD simulation.

3.2.2 Triple-Tapered Probe

We have demonstrated above that by using a double-tapered structure in the probe, throughput can be increased more than ten times. However, a remaining problem of the double-tapered probe is the deterioration of resolution by the larger apex diameter of the double-tapered core due to its large cone angle. To solve this problem, the triple-tapered probe shown in Fig. 3.9 was proposed and fabricated [14]. The lowest right of this figure shows the
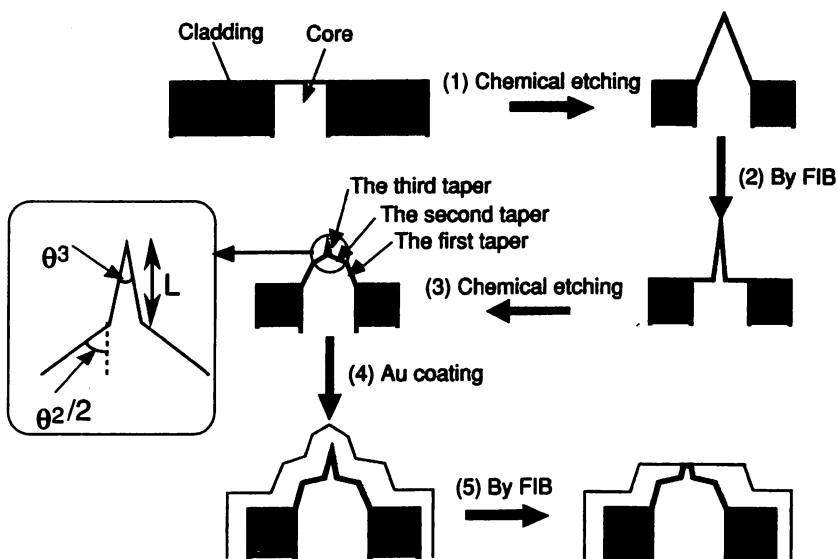
Fig. 3.9. Schematic of fabricating a triple-tapered probe with an aperature at a flat top

result of the fabrication which has a very sharp third taper at the top of the double-tapered core. Due to this sharp taper, generation and localization of a very high spatial Fourier frequency component of the optical near field are expected. Its fabrication consists of five steps.

1. chemical etching to sharpen the core and to reduce the cladding diameter;
2. irradiating the FIB to form a very sharp tapered core on a flat floor, which is used as the third taper;
3. chemical etching to form the first and second tapers at the foot of the third taper;
4. coating a gold film; and
5. removing a gold film from the top of the third taper to form an aperture.

Chemical etchings for steps 1 and 3 are the established techniques. Step 5 was used to form a flat aperture to compare the throughput with other apertured probes described in previous sections. However, it is also possible to maintain the top of the third taper after removing the gold film by using a KI–I$_2$ etching solution to produce a protruded triple-tapered probe, which can realize very high resolution while maintaining high throughput.

Figure 3.10 shows a scanning electron micrograph of the results of step 2 obtained by using a Ga+ ion beam of 30-nm diameter. Figure 3.10b shows a scanning electron micrograph of the triple-tapered core formed by step 3. A schematic of the triple-tapered core is given by the inset of Fig. 3.9, where θ_2 and θ_3 represent the cone angles of the second and third tapers, respectively. The length of the third taper is represented by L. Although Fig. 3.10b shows $\theta_2 = 150°$, the value of θ_3 realized by this step can be controlled within the range of 90–150° with an error of ±5°. Figure 3.10c is a magnified picture of the third taper of $\theta_2 = 30°$ and $L = 350$ nm with a fabrication error of 3° and 30 nm, respectively. It also shows the nanometric apex diameter of the third taper. Figure 3.10d,e shows the side and magnified top views of the probe, respectively, fabricated by steps 4 and 5. The value of d_f is 60 nm, and the gold film is 300 nm thick.

Figure 3.11 shows the measured results of the dependence of throughput on d_f. Closed circles, open circles, and open triangles represent the values for the conventional probe, the edged probe, and the triple-tapered probe, respectively. It is confirmed by this figure that the triple-tapered metallized fiber probe has a throughput 1000 times higher than that of the conventional probe for 60 nm $\leq d_f \leq$ 100 nm. In other words, a throughput as high as 1×10^{-4}–1×10^{-2} has been realized across the above range of values for d_f.

Realization of such an extremely high throughput can be attributed to several causes.

1. The overall profile of the first and the second tapers is similar to a convex lens, which enables focusing the guided light from the fiber at the foot of the third taper.
2. The third taper is much shorter than the total length of the conventional fiber probe, which reduces the guiding loss.

a

b   **c**

d   **e**
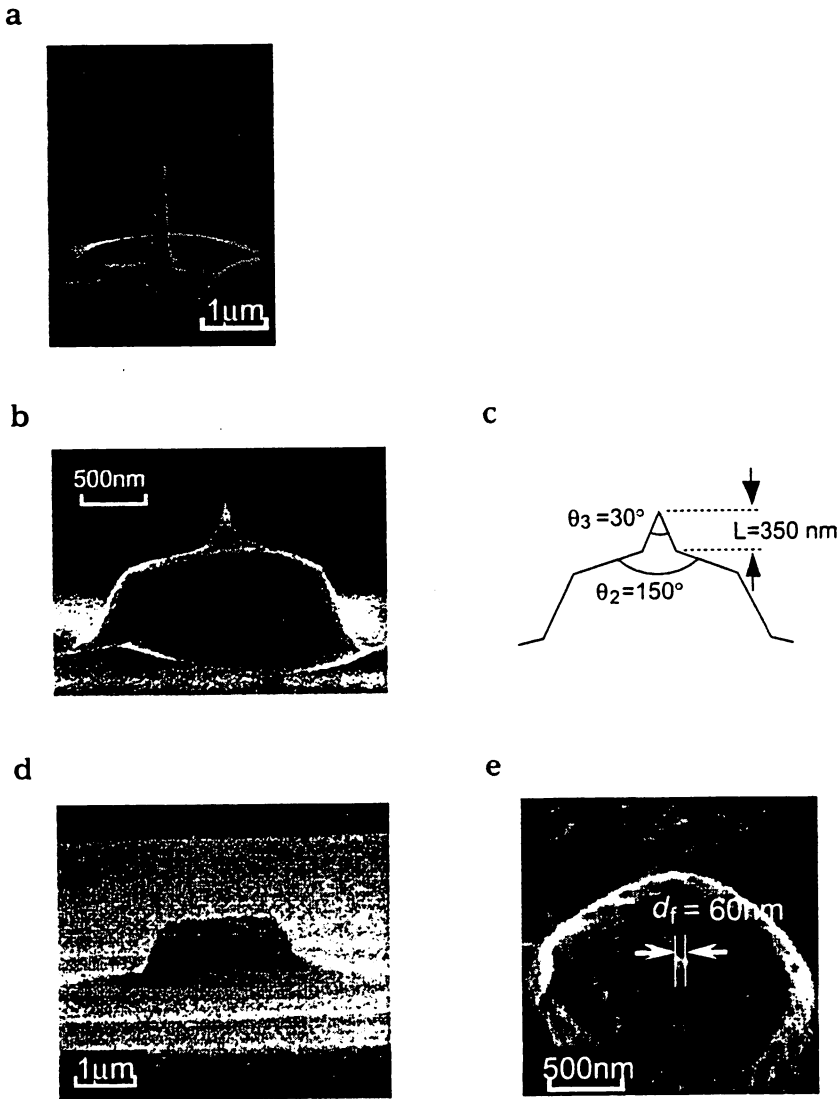
Fig. 3.10. Scanning electron micrographs of a triple-tapered probe. **a** Results of step 2 obtained by using a 30-nm diameter Ga+ ion beam. **b, c** Profile of the triple-tapered core formed by step 3 and a magnified image of the third-taper. **d, e** Side view and magnified top view of the probe produced by steps 4 and 5

3. Figure 3.10 also shows that the relation between d_f and the throughput of the triple-tapered probe is similar to that of the edged probe for 80 nm $\leq$ $d_f \leq$ 300 nm. This similarity reveals the possible excitation of the HE-plasmon mode, even in the triple-tapered probe. This is attributed to the edge formed between the second and third tapers due to the drastic change of the cone angle.

Figure 3.12 shows the measured cross-sectional profile of the spatial distribution of the output light power on the planar aperture (d_f = 60 nm) at the top of the triple-tapered probe. Its full width at half maximum is 160 nm which is the convolution between the aperture diameter (60 nm) and the size of the probe used for the measurement. A remarkably sharp peak at the center
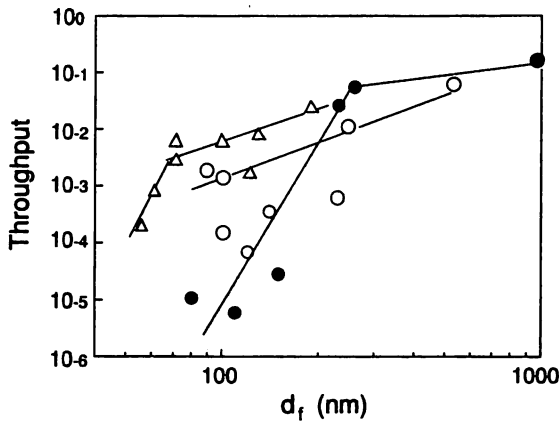
Fig. 3.11. Measured relations between the aperture diameter d_f and throughput. Closed circles, open circles, and open triangles represent the values for the conventional probe, the edged probe, and the triple-tapered probe, respectively
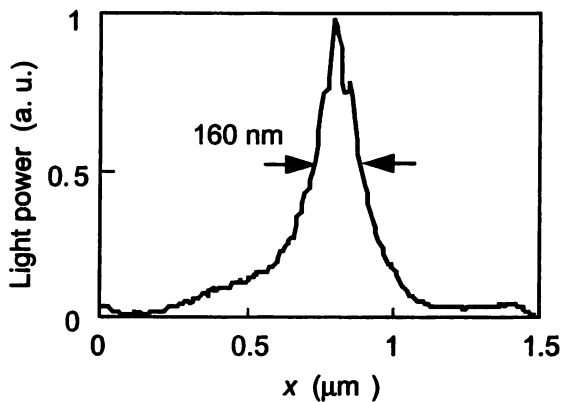
Fig. 3.12. Measured cross-sectional profile of the spatial distribution of the output light power on the planar aperture of the triple-tapered probe with $d_f = 60$ nm

of this curve is attributed to localization of the optical near-field due to the third taper on the top of the core.

References

1. M. Ohtsu: *Near-Field Nano/Atom Optics and Technology* (Springer-Verlag, Berlin, Tokyo, New York 1998)
2. M. Ohtsu and H. Hori: *Near-Field Nano-Optics* (Kluwer Academic/Plenum, New York 1999)
3. Uma Maheswari Rajagopalan, S. Mononobe, K. Yoshida, M. Yoshimoto, and M. Ohtsu: Jpn. J. Appl. Phys. **38**, 6713 (1999)
4. M. Naya, R. Micheletto, S. Mononobe, R. Uma Maheswari, and M. Ohtsu: Appl. Opt. **36**, 1681 (1997)
5. D. Marcuse: *Light Transmission Optics*, Chap. 10 (Van Nostrand Reinhold, New York 1972)
6. T. Yatsui, M. Kourogi, and M. Ohtsu: Appl. Phys. Lett. **71**, 1756 (1997)

7. T. Pangaribun, K. Yamada, S. Jiang, H. Ohsawa, and M. Ohtsu: Jpn. J. Appl. Phys. **31**, L1302 (1992)

8. T. Saiki, S. Mononobe, M. Ohtsu, N. Saito, and J. Kusano: Appl. Phys. Lett. **68**, 2612 (1996)

9. K. S. Yee: IEEE Trans. Antennas Propagat. **AP-14**, 302 (1966)

10. A. Taflove: in *The Finite-Difference Time-Domain Method* (Artech House, Norwood, MA 1995)

11. H. Furukawa and S. Kawata: Opt. Commun. **132**, 170 (1996)

12. H. Nakamura, K. Sawada, H. Kambe, T. Saiki, and T. Sato: Suppl. Prog. Theor. Phys. (in press)

13. T. Saiki and K. Matsuda: Appl. Phys. Lett. **74**, 2773 (1999)

14. T. Yatsui, M. Kourogi, and M. Ohtsu: Appl. Phys. Lett. **73**, 2090 (1998)

II 部・ナノマテリアルの基礎概念と基礎技術

5 近接場光を用いた ナノフォトニクス・システム

大津　元一（おおつ・もといち）
東京工業大学大学院総合理工学研究科

1950年　神奈川県生まれ．1978
年　東京工業大学大学院理工学
研究科博士課程修了．工学博士．
現在，東京工業大学大学院総合
理工学研究科教授．おもな研究
テーマは「ナノフォトニクス」．

回　折
光などの波が発散する性質．

回折限界
回折のために波のエネルギーを
空間的に集中できる寸法の下限．
またはこれによって制限される
計測，加工，などの限界．その
寸法は波の波長程度である．

近接場光
物質から発生する光のうちの非
伝搬成分．

1. は じ め に

　1960年にレーザーが発明されて以来，1980年代には光通信，光メモリなどの産業が成長し現在に至っている．社会は今後の高度情報化・高度福祉化を支えるために光技術をいっそう進歩させることを要求しているが，これに応えるには光による計測，加工，デバイスなどの寸法を微小化し，高集積化，高速化，省電力化することが必要である．しかし既存の光技術の代表例である光メモリー，光デバイス，光加工は次に示す問題を抱えている[1]．

　（1）光メモリー　光メモリー技術ロードマップによると2010年には記録密度 1 Tb/in^2，再生速度 1 Gb/s が必要とされている．しかし既存の DVD 技術では，後述の光の回折限界のために実現不可能である．

　（2）光デバイス　光ファイバー通信の技術ロードマップによると，2015年には高度情報化社会を支えるために10 Tb/s のデータ転送速度が必要，光交換機用の光スイッチ配列中の入出力端子数は，おのおの1000またはそれ以上が必要と推定されている．これらの要求を満たすには回折限界を超え，光スイッチ配列中の各光デバイスを微小化しなければならない．

　（3）光加工　DRAM の大容量化のために，半導体材料加工のいっそうの微小化が要求されている．光リソグラフィでは，光源を短波長化することによりこれに対応している．しかし，極端紫外光などの短波長光源などは実用的でなく，回折限界によって決まる微細化の限界に達しつつある．

　以上の様子を図1にまとめた．光技術は回折限界を超えるためのパラダイムシフトを必要としている．ナノフォトニクスとは，近接場光とよばれる寸法の小さな光を用いてこれを実現するために，筆者が考案した技術である[2]．本章では，社会の要求に応えるためのナノフォトニクス・システムについて説明する．さらに14章では各論について説明し，そのための材料とデバイスについて展望する．

図1　光メモリ，光デバイス，光加工の技術の進展と回折限界

2. トップダウン型の要求に応える

　一般のナノテクノロジーはナノ寸法物質を積み上げ，組み合わせてデバイスなどを構成するので，ボトムアップの技術ともよばれている．一方，従来の技術は大きな物質を削って小型化するので，トップダウンである．さてナノフォトニクスには「社会的要求→それを満たす光システム→そのための光デバイス→そのためのナノ寸法材料と近接場光」という明確な階層構造があり，社会や応用システムからのトップダウン型の具体的な要求に応えるために進展している．

　筆者の知る限り，一般のナノテクノロジーには，このような社会からのトップダウン要求がまだ明確でなく，ナノ寸法のテクノロジーとして成長するために必要な，システム的思考は必ずしも十分ではない．したがって現状はナノマテリアル，ナノサイエンスの段階にとどまっている感がある．これに対し，ナノフォトニクスはトップダウン要求を満たす必要上，システム的思考のもとに進展している点が際だった特徴である．

　ところで最近は図2に示すように，ナノメートル寸法の材料を多数用いた量子ドットレーザー，微小共振器レーザー，フォトニック結晶などが研究されている．これらは旧来の光デバイスとは異なった性能を発揮するが，ナノフォトニクスとは無縁である．なぜならば，これらは伝搬光を情報キャリヤーとして使っている

量子ドット
物質寸法がその中の電子のボーア半径程度まで小さく，電子のエネルギー値が離散的になり量子力学的な特性を表すような微小物質．

109
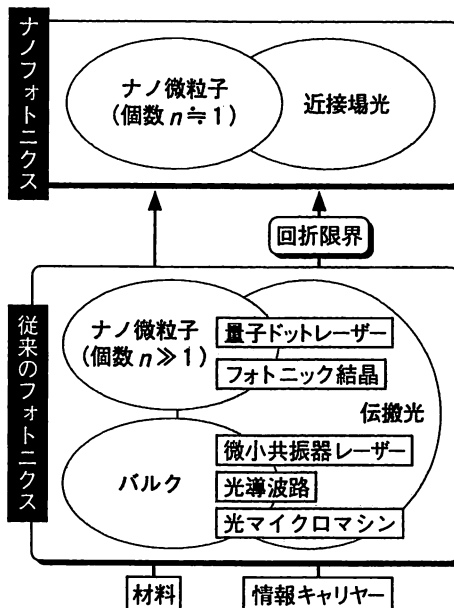
図2 従来の光技術(フォトニクス)と
ナノフォトニクスとの対比

からである. 伝搬光は波動の基本的な性質, すなわち回折のためにそのエネルギーは波長の寸法程度以下の領域に集中しない. すなわちこれらの技術では, 光の波長の寸法以下の微小光デバイスを実現することはできない.

ナノフォトニクスの実現には, 情報キャリヤーとしての光のエネルギーが集中する領域の寸法がナノメートルでなければならない. さらに, そのような「微小な光」を発生し使用するためには, 1個～数個のナノメートル寸法材料で光デバイスを構成する必要がある. これらを実現するのが近接場光である.

3. 近接場光とは何か

既存の光技術では光を波として扱うが, 光波は微小な穴を通り抜けたあとに発散する. 光波を絞って光ファイバーの中を伝送させても出射後は発散する. この発散性は回折とよばれている. したがって凸レンズで集光しても, 焦点面上では光の波長程度の寸法のスポット径までしか絞れない. このピントのぼけのために光を使った計測, 加工, デバイス動作は光波長程度以下の寸法を扱うことができない. これは回折限界とよばれている.

ところで図3(a)に示すように, 光ファイバーを先鋭化して根本に不透明な金属膜を塗り, 先端部をわずかに突出させる(これはファイバープローブとよばれている). すると光波が先端まで届かず, これでは従来の光技術の使用に耐えないが, 金属膜から突出した先端部には光の薄い膜が発生している. その膜の厚さはファイバープローブの先端の直径程度であり, これが近接場光である[3]. さらに説明すると, 近接場光とは図3(b)に示すように振動する, 電気双極子から発生する2種類の光のうちの近接場成分である. 他方は遠隔場成分であり, その電場の電気力線は電気双極子から分離し, 閉曲線となって遠方に伝搬する. 従来の光技術ではこの伝搬光を使っており, これは回折する. これに対し近接場成分の電気力線は電気双極子に局在し, 非伝搬である.

(a)

(b)

(c)

(d)
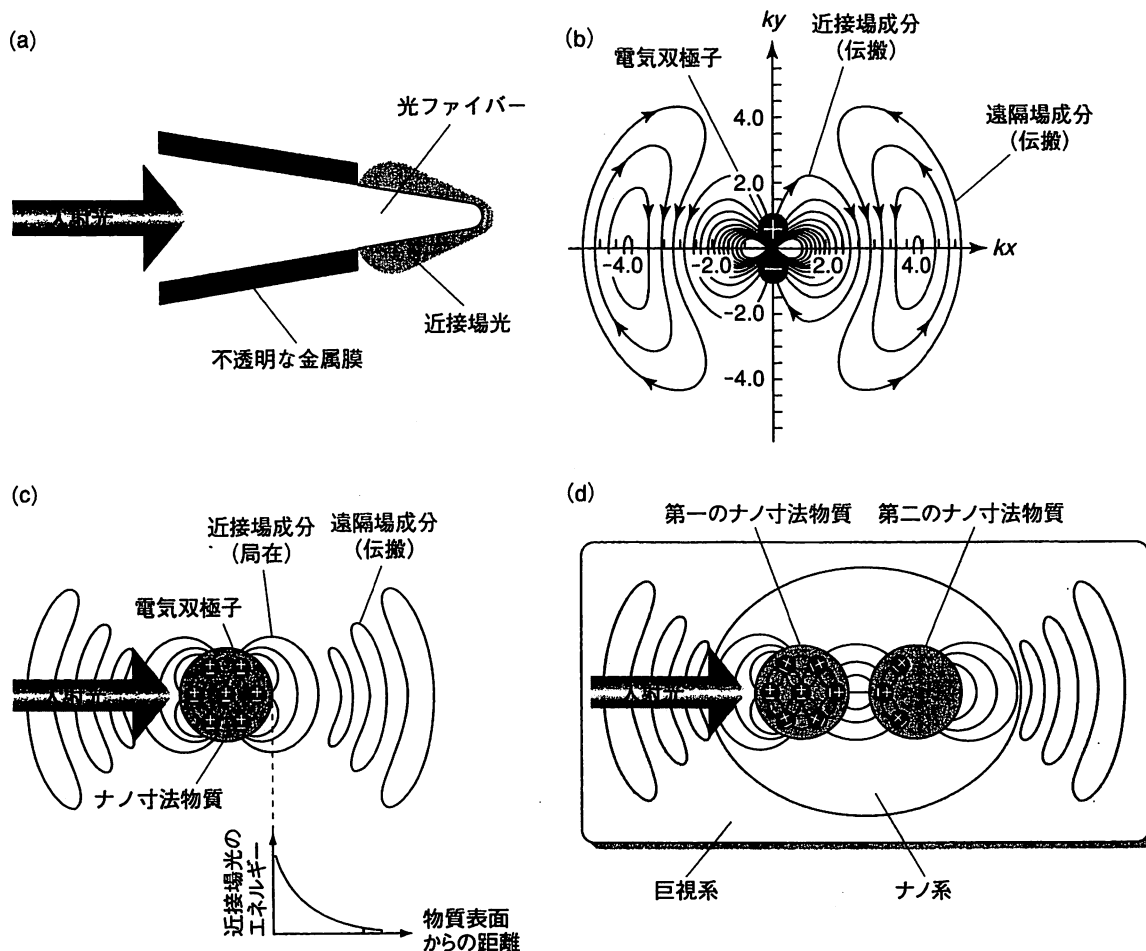
図3　近接場光の発生と利用の説明

(a) ファイバープローブの構造．(b) 振動する電気双極子から発生する光．x, y は直交座標．k は入射光の波数で，波長 λ とは $k = 2\pi/\lambda$ の関係がある．(c) ナノ寸法物質から発生する光．(d) 第一のナノ寸法物質表面の近接場光を第二のナノ寸法物質に照射している様子．これらのナノ系が巨視系に囲まれている様子も示す．

　ナノフォトニクスはナノ寸法物質を扱うが，これに光を照射すると多数の原子に電気双極子が誘起され，おのおのが図3(c)に示すように図3(b)と同じ光を発生する．ここですべての電気双極子から発生する近接場光のエネルギーの総和をとると，それはナノ寸法物質表面から遠ざかるにつれて急激に減衰する．表面からの距離を r，ナノ寸法物質の大きさを a とすると，その減衰の様子は $\exp(-r/a)/r$ なる湯川関数で表される[4]．すなわち近接場光の膜の厚みはナノ寸法物質程度である．

　図3(d)のように，第一のナノ寸法物質表面の近接場光を微小光源と見なすと，その寸法は入射光の波長にはよらず，第一のナノ寸法物質の大きさ程度なので第二のナノ寸法物質に近づけて照明しその像を観察したり，また加工することにより回折限界を超えた微小な光技術が可能となる．第二のナノ寸法物質が近づくと近接場光の電気力線はその表面に向かって伸び，第二のナノ寸法物質中に電気双極子を励振する．このとき重要なのは次の二点である．

　（a）二つのナノ寸法物質が近接場光を媒介として結合した状態になっている．

　（b）このように結合した微小な系（ナノ系とよばれている）が，それよりずっ

と寸法の大きな巨視系(ファイバープローブの根本，試料用基板，入射光，光検出器などからなる)に囲まれている．

この状態を詳細に記述するには量子力学の手法が必要であるが，それによると伝搬光を使う場合にはほとんど見られないエネルギーの移動(非共鳴エネルギー移動とよばれている)が二物質間で起こることが指摘されている[4]．すなわちナノ系のみに注目すると，エネルギー保存則からのずれが生じる．そのエネルギーの過不足分は上記(b)の巨視系からまかなわれるので，ナノ系と巨視系とを合わせた全体ではエネルギー保存則は成り立つ．ナノフォトニクスの本質はこのように巨視系の中から適当なナノ系を抽出し，従来の光技術では困難なエネルギー移動の形態を利用することである．このほか，運動量，角運動量についても同様のことがいえる．ナノ寸法の光技術が実現することは副産物にすぎない．

4. どのように進展しているか

近接場光を高分解能の光学顕微鏡として利用する提案は1928年にさかのぼるが[6]，この段階では旧来の光学の計測への応用の話題にすぎず，したがってそれ以降長年顧みられることはなかった．しかし近接場光の本質は，微小物質と電磁場のナノメートル寸法領域での局所的な相互作用である．1980年代以降はこの観点から理論的な枠組みを確立し，それを基礎として単なる計測技術ではなく情報通信，情報記録などを担うナノ光機能，デバイス，システムを実現し，ナノフォトニクスを構築する試みが始まった[5]．

そのためには実験と理論の両面からの革新的なアプローチが不可欠であったが，その一つは近接場光を検出，発生させる基本的なナノ寸法デバイス，すなわちファイバープローブの製作である．これについては筆者が1980年代初頭から開始した[6]．当初のファイバープローブの性能は必ずしも高くなく，筆者の周囲からは「近接場光などというものは存在しないので，そのことを証明してみせる」などの意見が出たこともあった．しかし最近ではその先端寸法が数nmに達する微小化，数％に達する高い発生検出効率などが実現している．この結果「ファイバープローブの効率が低い」という通説は遠い昔話となった感がある．このデバイス開発と歩をほぼ同じくし，欧米では1980年代に顕微鏡への応用が提案され，一方筆者はファイバープローブの基本技術を進展させてナノフォトニクスに至る研究開発を始めた．

この進展の過程でも高い性能のファイバープローブを作製する筆者らの技術が強みを発揮し，顕微鏡計測においてDNAの単一分子の形状を幅4nmで計測すること，また図4(a)，(b)のように半導体量子ドットの発光分光分析，単一色素分子からの発光計測などが最も高い分解能で実現している[2]．また，ナノフォトニクスよりもさらに微小寸法の極限的な科学技術として，真空中を飛行する中性原子を一つずつ操作するアトムフォトニクスを近接場光で実現する研究も，筆者が1990年代初期に開始し現在に至っている[4]．

このようなめざましい進歩の結果，最近では筆者に対し「実は私はあなたよりずっと昔に近接場光について考えたことがあった」との意見を寄せる人が増えて

発光分光分析
物質から発生する光のスペクトルを測定評価して，物質の構造を分析する方法．

(a)

(b)
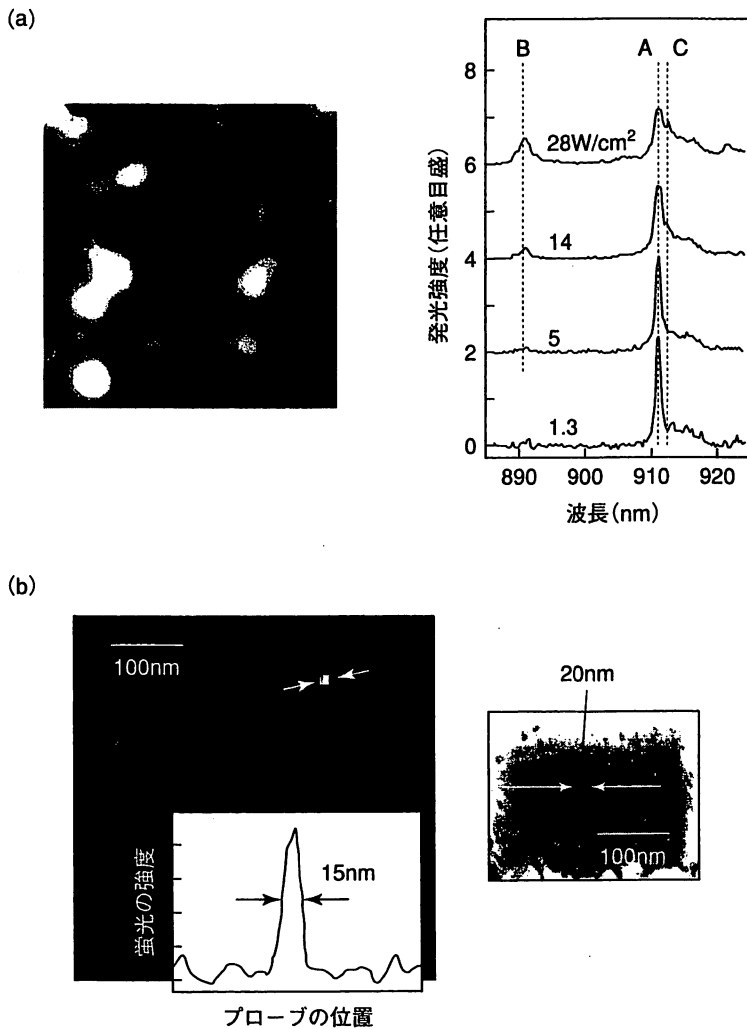
図4　計測の例
（a）InGaAs量子ドットの発光分光分析結果．左図は発光強度の空間分布．画像の寸法は3 μm × 3 μm．右図は発光スペクトル．パラメータは照射光パワー密度．A，B，C はおのおの基底準位，第一励起準位の励起子からの発光，結合した二励起子からの発光．
（b）単一色素分子からの発光．左図は発光強度の空間分布とその断面強度分布．右図は測定に使用したファイバプローブの先端の開口部の電子顕微鏡写真．開口直径は20 nm．

きた．一般に学問の世界においてこの種の回顧談が寄せられるようになるのは，その分野が真に成長した証であるといわれている．

5. お わ り に

　ナノフォトニクスは近接場光を使いこなす技術であるが，これは決して計測，分析技術ではない．近接場光の検出自身が，二つのナノ寸法物質間の近距離電磁相互作用を利用している以上，その本質的な利用技術は物質の加工，機能などである．これらは社会の要求，それを満たすシステムと密接に連携している．これらの詳細は14章で述べる．

参 考 文 献
（1）大津元一，「ナノ・フォトニクス」，米田出版(1999)，p. 1.
（2）大津元一，「光の小さな粒」，裳華房(2001)，p. 130.
（3）大津元一，光学，**31**，120(2002).
（4）M. Ohtsu, K. Kobayashi, H. Ito, G. H. Lee, *Proc. IEEE*, **88**, 1499(2000).
（5）M. Ohtsu, "Near-Field Nano/Atom Optics and Technology," Springer-Verlag(1998), p. 1.
（6）M. Ohtsu, "Near-Field Optics : Principles and Applications," ed. by X. Zhu, M. Ohtsu, World Scientific(2000), p. 1.

III 部・将来期待されるナノマテリアル

14
ナノフォトニクスの材料とデバイス

大津　元一（おおつ・もといち）
東京工業大学大学院総合理工学研究科

1. まえがき

本章の内容は5章と連携している．すなわち，5章で述べたナノフォトニクス，近接場光の原理に基づき，将来の社会からのトップダウン型の要求に応えるためのシステム，それを実現するためのデバイスと材料の技術について展望する．

2. 近接場光発生用デバイス

社会からのトップダウン要求に応える近接場光を発生するための基本デバイスを開発するにあたり，次の2点に注意が払われている．

（1）**インピーダンス整合**　穴のあいた板や微小球に光を照射すれば近接場光が発生するが，そのエネルギー密度は低く使用に耐えない．高エネルギー密度の
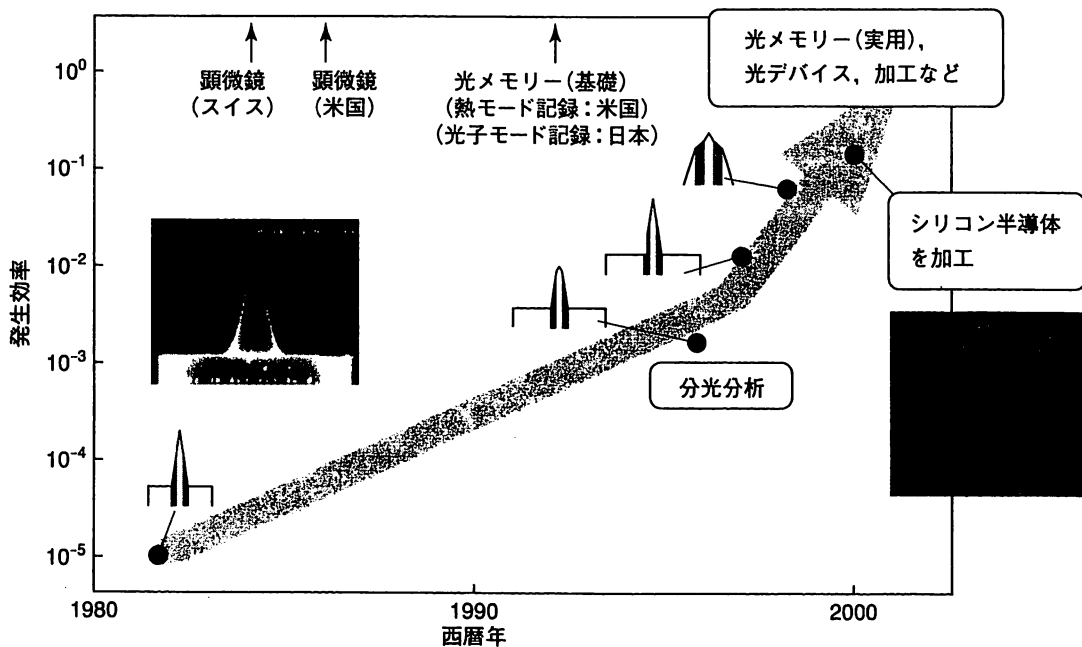
図1　ファイバープローブからの近接場光発生効率の進歩の様子

近接場光を発生させるには照射する伝搬光のエネルギーを効率よく近接場光エネルギーに変換する必要がある．これが「インピーダンス整合」であり，その条件は電磁気学の手法に求めることができる．これを実現したのが5章の図3(a)のファイバープローブにほかならない．インピーダンス整合とはファイバープローブの傾斜部の形状，寸法を最適化することであり，その結果，最近では近接場光の発生効率として図1に示すように，数%に達するファイバープローブが開発されている[1]．なお，インピーダンス整合は5章で述べたナノ系と巨視系とのエネルギーの授受を，効率よく行う方法ともいえる．

（2）**歩留まり**　上記(1)のファイバープローブを高い歩留まり，再現性で作製することが最も重要である．フッ酸系溶液による選択エッチングがその解を与え，これにより希望する性能が実現し，さらに優れたファイバープローブを設計するための基礎データが蓄積されている．これをもとに，最近ではファイバーではなくシリコン結晶基板を用いた高効率プローブも開発されており，量産性の高い技術として期待が高まっている．

3. 高密度光メモリー

記録密度1 Tb/in^{2}を実現するために，図2に示すように近接場光を用いた光記録再生システムが開発されている[2]．ここではシリコン結晶基板を用い，前節の(1)に示した「インピーダンス整合」を実現し，（2）の「歩留まり」を高めるために，異方性エッチングで作製した二次元プローブ配列を搭載した，記録再生スライダーが開発されている．その結果，相変化記録用光ディスクに密度約60 Gb/in^{2}で光
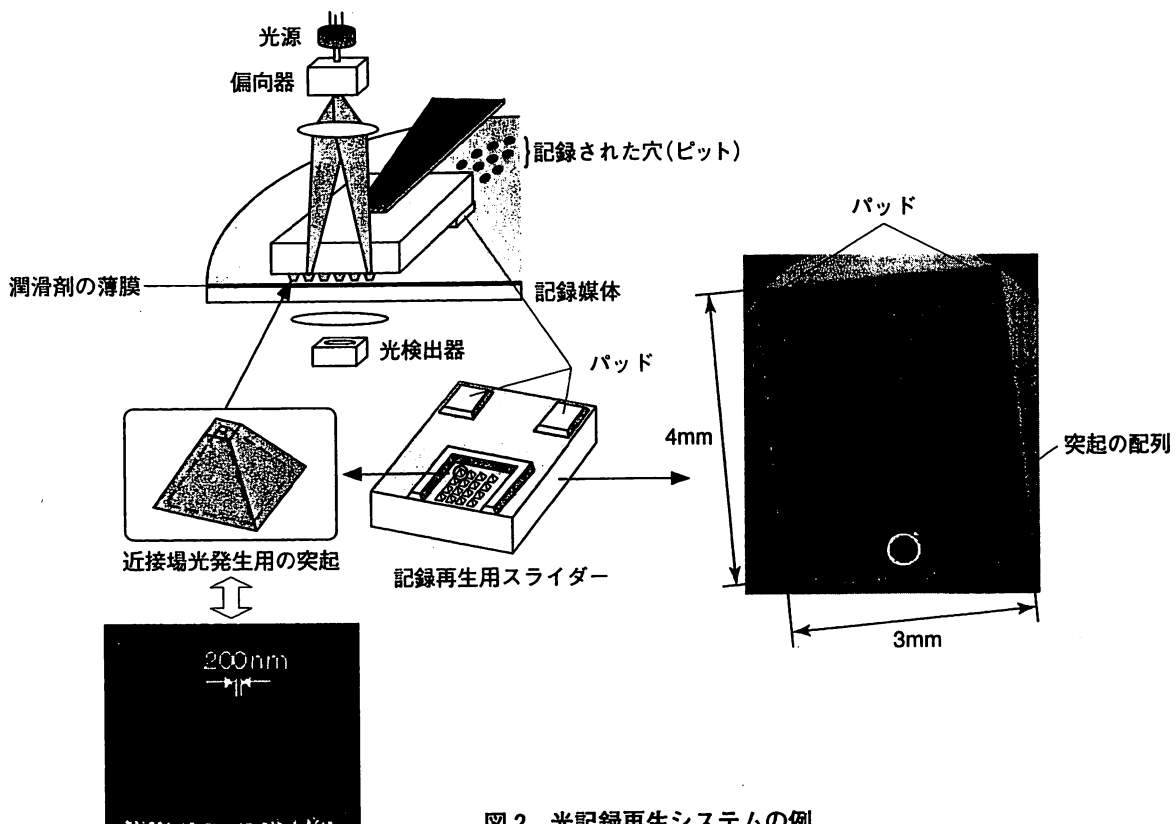
図2　光記録再生システムの例

記録され，それを速度0.4 m/s で走査されたスライダーで再生している．これは二次元配列中のプローブ数が100個の場合，400 Mb/s の再生速度に相当する．今後はデバイス（スライダー），材料（記録媒体保護膜，潤滑剤），評価方法（光ディスク計測）などの要素技術を相互連携してさらに性能向上させるべく，システム開発が始まっている．

なお，ここで注意すべきは，社会からのトップダウン型の要求に応えるために，ナノテクノロジーの基本的な計測技術である，走査プローブ顕微鏡とは逸脱した形態をとっていることである．その代表例はスライダーの著しい高速走査である．

4. 高速大容量光ファイバー通信用のナノフォトニクス集積回路

光ファイバー通信システムの要求に応えるために，近接場光を用いたナノ光デバイスとその集積化が開発されている[3]．集積化システムの構成原理を図3に示す．ここではナノ寸法物質と近接場光との相互作用を利用し，個々のナノ寸法物質に近接場光の発生，スイッチング，検出機能を発現させ，情報を担う近接場光をナノ寸法物質間で転送する．．すでに酸化亜鉛の青色発光や，三つの量子ドットを組み合わせた光スイッチングなどの実験，および理論的研究が行われている[4]．トップダウン要求に応えるために，このシステムは次の特徴をもつ．

（1）高い信頼性を確保するため，図1の記録再生スライダーのような可動部を排除し，平面埋め込み型のシステムとなっている．すなわち，走査トンネル顕微鏡で採用されているプローブ走査，および試料と接近させる点接触の二つの概念を排除している．

（2）上記の光スイッチングは，ナノ寸法物質と近接場光との局所的相互作用

走査プローブ顕微鏡
電子のトンネル効果，原子間力などの現象を利用し，それを発生測定するための針（プローブ）を走査して，試料形状などを観測する顕微鏡．
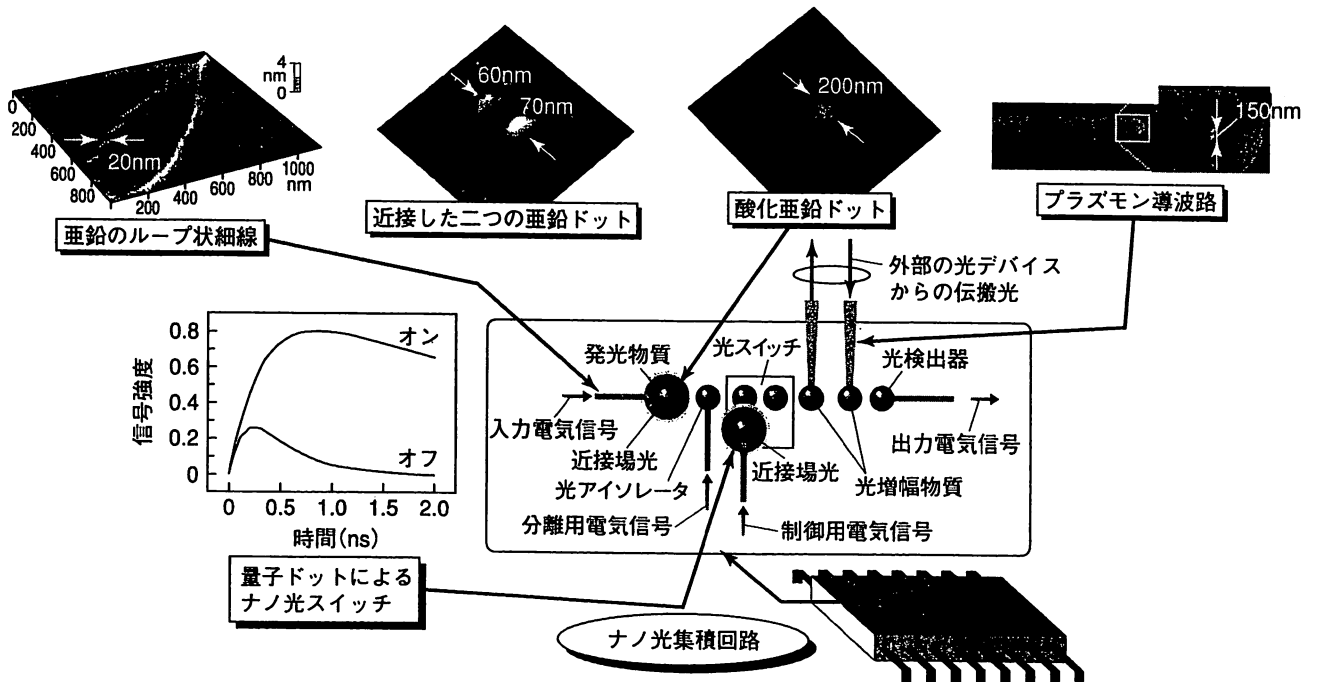
図3 ナノ光デバイスの集積化システムの構成例
本章5節の方法を使って作製されたナノ寸法物質の例も示す．

（すなわち5章3節末尾の非共鳴エネルギー移動）を利用している．したがって，これは通常の伝搬光を用いたのでは実現不可能であり，光デバイスのパラダイムシフトの典型である．

（3）外部の大寸法の光デバイス（たとえば光ファイバーなど）と接続して，一般ユーザーの使用に供するためのインターコネクションを配備している．これは図3の中の近接場光を伝搬光に変換して外部に伝送すること，またはその逆の働きをするものである．半導体と金属細線から構成されたプラズモン導波路が，この機能を担っている[5]．これは本章2節のインピーダンス整合にほかならない．

プラズモン
物質中での電子の振動に基づく量子力学的波動．

5. ナノ寸法の光加工

たとえば図2の集積回路をつくるには，ナノ寸法物質の寸法，位置，間隔に関する高い精度の加工技術が必要である．この精度は，ナノ寸法物質間で近接場光を転送するために不可欠である．さらに共通基板上に多様な物質を堆積できることも重要であるが，既存の加工技術はこれらの要求を満たさない．たとえば自己組織化などの微小物質堆積法は，熱平衡と化学反応とを利用した集団的方法なので，個々のナノ寸法物質の寸法，位置，間隔の制御性は高くない．もちろんDRAM用半導体材料などに用いられている，光リソグラフィーも使用不可である．したがって加工技術に関してパラダイムシフトが必要である．

そのために近接場光を使った化学気相堆積法が開発されている[6]．これは図4に示すように気体中の有機金属分子に近接場光を照射し，分子中の電子を基底準位から励起準位へと励起し，分子に含まれている金属原子などを解離して，基板上に堆積するものである．近接場光発生用デバイスの寸法，位置を制御することにより上記の精度を満たす．また近接場光発生用の光の種類を変えると，多様な分子を解離，堆積できる．図3にも示したように，亜鉛，アルミニウムなどの金属，酸化亜鉛などの酸化物（半導体のエネルギー構造をもつ）の微小パターンなどが形成されている．このほかGaAsなどの化合物半導体の堆積も可能である．

さて，一例としてジエチル亜鉛分子を堆積する場合，伝搬光で解離しようとす

化学気相堆積法
気体中での化学反応を用いて物質を基板の上に堆積する方法．
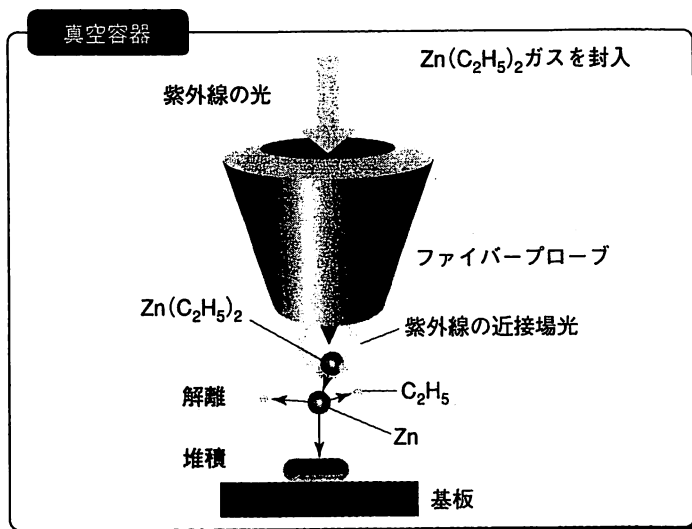
図4　近接場光による化学気相堆積の原理
気体状のジエチル亜鉛〔$Zn(C_2H_5)_2$〕分子を解離して，亜鉛（Zn）原子を堆積する例を示す．

ると電子を励起するために紫外線が必要であったが，近接場光の場合はそれよりも光子エネルギーの低い青色光を用いても可能であることが確認されている[7]．これは5章3節末尾の非共鳴エネルギー移動の結果であり，このことは，近接場光を用いれば伝搬光では不可能であった新物質が堆積できることを意味している．

6. 展望とまとめ

　本章では，近接場光を発生させ，使うという新しい（したがってクレイジーな）方法により，光技術のハードウエアに関するパラダイムシフトを実現させる例を述べた．しかし，これを使うためのソフトウエアに関するパラダイムシフトは，未発達といえる．光メモリーを例にとると，どのようなアプリケーションソフトウエアをユーザーに供給するかという議論は，従来技術の延長上で連続的，帰納的になされているのみである．むしろ芸術家，ゲームソフト設計者などの不連続な発想（これは技術者から見てクレイジーな発想といえるかもしれない）が必要である．また，脱着可能型光メモリーの規格の国際標準化も重要であり，これに関してわが国が主導権をにぎることが，光メモリーの国内産業を進展させるのに必須である．しかし，そのためには国際的な調整作業（ネゴシエーション）が必要である．

　ただし，誠実と奥ゆかしさとを美徳とする国民である日本人にとって，クレイジーな発想は国内で（むしろ本人の直近の周辺から）の道徳的批判を受ける可能性もあるし，国際的なネゴシエーション（もちろん英語で）も得意とはいえない．このことは国民性のパラダイムシフトを実現し，正当な主張をスマートに行うことこそが今後のナノフォトニクス，さらにはナノテクノロジーの発展のために重要であることを意味している．

参考文献

（1） M. Ohtsu, "Near-Field Nano/Atom Optics and Technology," Springer-Verlag (1998), p. 33.
（2） T. Yatsui, M. Kourogi, K. Tsutsui, J. Takahashi, M. Ohtsu, *Opt. Lett.*, **25**, 1279 (2000).
（3） 大津元一，電子情報通信学会誌, **18**, 26 (2001).
（4） T. Kawazoe, K. Kobayashi, J. Lim, Y. Narita, M. Ohtsu, *Phys. Rev. Lett.*, **88**, 067404 (2002).
（5） T. Yatsui, M. Kourogi, M. Ohtsu, *Appl. Phys. Lett.*, **879**, 4583 (2001).
（6） M. Ohtsu, K. Kobayashi, H. Ito, G. H. Lee, *Proc. IEEE*, **88**, 1499 (2000).
（7） T. Kawazoe, Y. Yamamoto, M. Ohtsu, *Appl. Phys. Lett.*, **79**, 1184 (2001).

Optical Data Recording in 2030s (2)

The Sub-Terabyte Optical Memory Committee of OITDA organized a workshop for discussing the future of data recording and the expected developments by 2030s, as a part of the Sub-Terabyte Optical Memory Symposium held in November last year. The purpose of the workshop was to consider and make projections on the memory market and technologies that will be available in 2030s; in other words, the market and the technologies that are a generation ahead of what is considered by the Sub-Terabyte Optical Memory Project currently undertaken by the committee. Since no projections on the development of either the industry or the technology had been previously carried out in earnest with regard to optical memory in 2030s, the discussions at the workshop were promoted by inviting experts in the field of memory as lecturers and encouraging the presenters to present bold and original predictions.

Contained in this issue is the presentation given by one of the lecturers, Professor Motoichi Ohtsu of Tokyo Institute of Technology, who is asked to summarize his presentation while also giving due consideration to the discussions that followed his presentation.

Optical Recording by Optical Near Field

By Motoichi Ohtsu

1. Introduction

This paper discusses the technological prospects of optical data recording in the year 2030 and is based on an assumption that there would be no drastic changes in the social and/or economic structures in the years to come. Since the subject matter is broad, full of uncertainties and beyond what the author can make substantiated predictions about, much of the discussions below are the author's subjective conjectures.

Fig. 1 shows two types of electromagnetic fields generated from an oscillating electric dipole. The fields are respectively indicated by electric lines of force. One forms a closed loop, representing a propagating wave extending to a far field. The other is what is called the near-field component, which is generated from the positive electric charge of the dipole and terminated at the negative electric charge. This component is localized around an electric dipole and does not propagate.   (Continued)

When a light is irradiated onto a nano-scale substance, a number of dipoles are induced within the substance and two types of lights, i.e., electromagnetic fields, are generated, as was illustrated in Fig. 1. Of the two, the optical near field is localized on the surface of the nano scale substance; and the thickness of its energy distribution is about the same as that of the nano scale substance. Therefore, by using this light instead of the conventional propagating light, it is possible to achieve nano technology. This is a technology of a scale less than wavelength of light (i.e., below diffraction limit), which is also called nano-photonics. In other words, this is a technology that surpasses the long-held principle of diffraction limit proposed by Newton.

Near field component
(Localized)

Far field component
(Propagate)
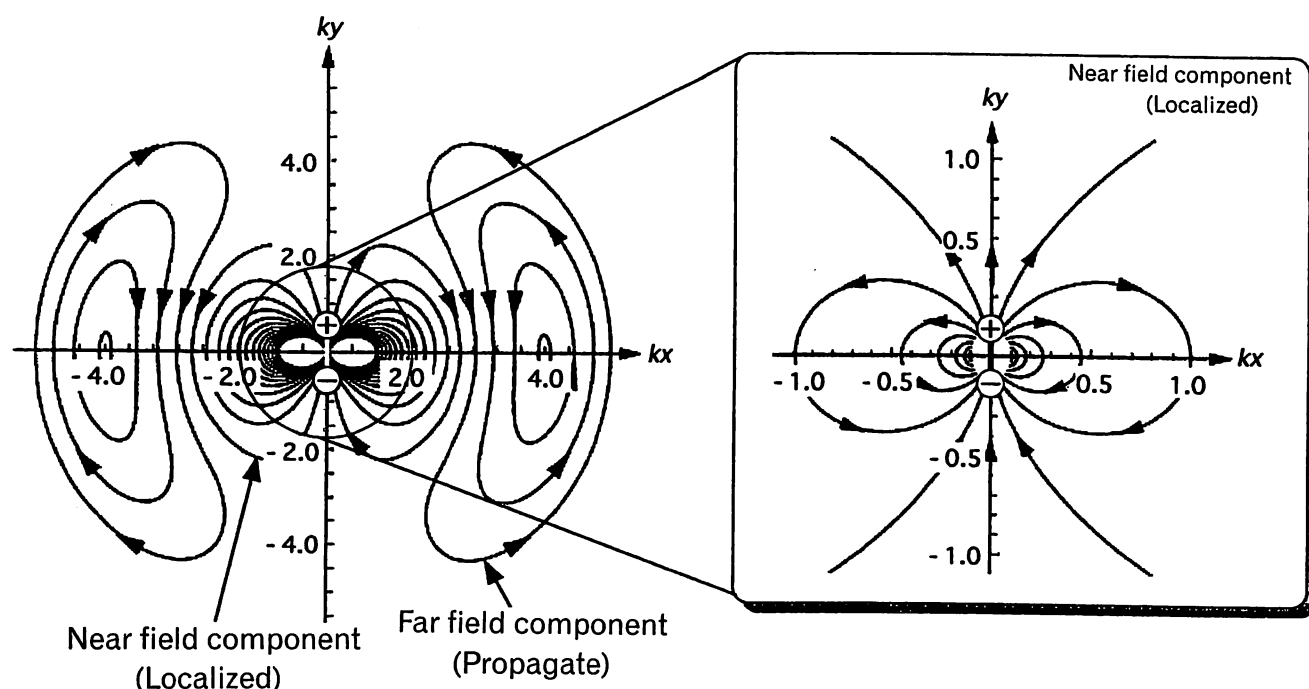
Fig. 1. Two Kinds of Electric Lines of Force of Electromagnetic Field
Generated by Oscillating Electric Dipole

As shown in Fig. 2, this technology is achieved by using the optical near field, which exhibits a totally different kind of spatial form from that of the conventional propagating light.
The discovery of optical near field is epochal enough to bring about a paradigm shift, just as the transition from ships to airplanes and from vacuum tubes to transistors had done in the past.

Conventionally, the trials to improve optical recording density have always struggled with the optical diffraction limit. Efforts have been made to shorten the wavelength of the light source since 1980s. Meanwhile, according to the technology roadmap depicting the future technological trends in optical recording, a recording density of 1 Tb/in^2 will become necessary by 2010. This required density, which is already several tens of times larger than the diffraction limit value of optical technology, is expected to increase additional several digits by 2030. Optical recording using optical near field is proved to be theoretically capable of achieving a recording density of 100 Tb/in^2, which is adequate for meeting the predicted requirements of the society in 2030.

- 2 -

Such a promising future of optical recording owes much to the improved performance of the probe used for generating the optical near field.   Nevertheless, the question still remains whether an optical disk memory with such a high recording density will be actually realized for consumer use.   In trying to answer this question, it is again important to re-member that the development of nano-photonics is substantial enough to eventually cause a paradigm shift as is mentioned in the previous paragraph.
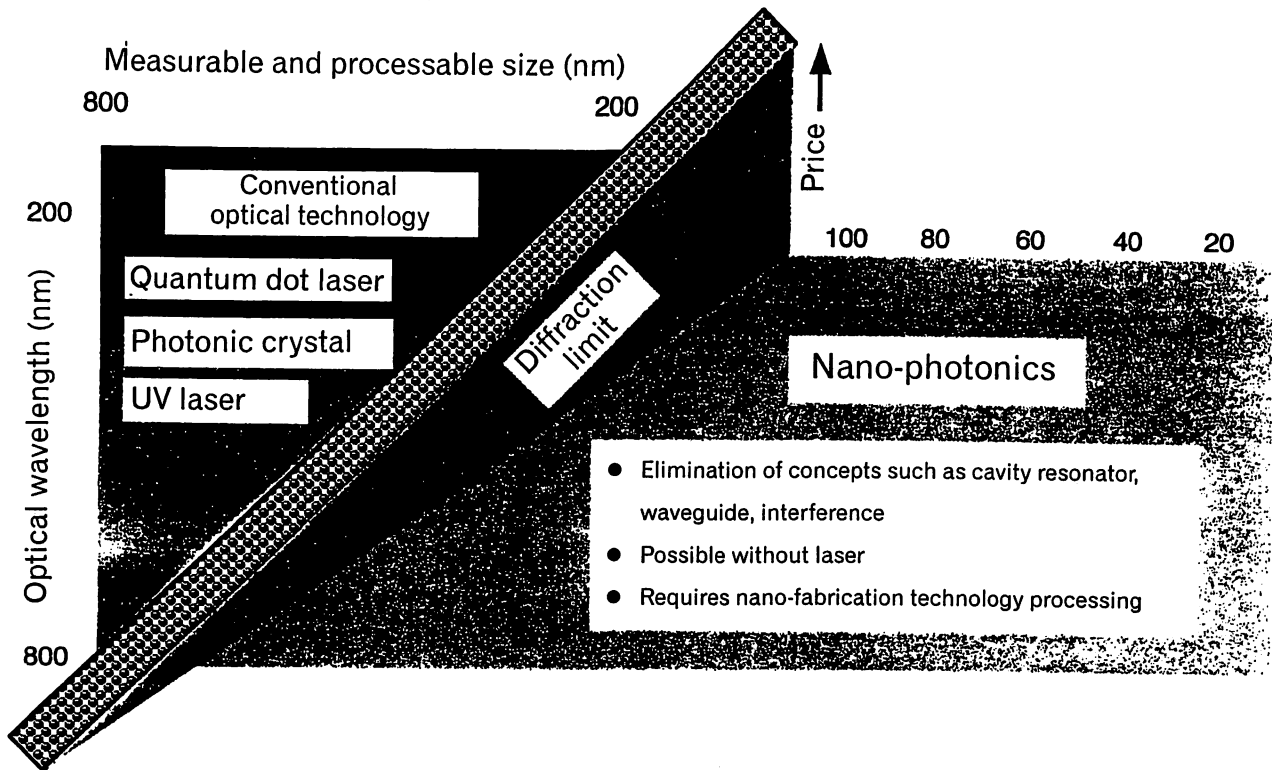
Fig. 2.   Paradigm Shift Provoked by Nano-photonics

2. Form of Optical Data Recording Using Optical Near Field

In an optical disk memory system using the optical near field, the data are recorded, read and deleted by the optical near field generated at the tip of a probe.   It is possible to achieve very high recording densities under this system, since the densities are determined by the size of the near-field optical energy distribution, or in other words, the size of the probe tip.   Since the beginning of 1980s, the R & D by the author has achieved a steady improvement in the efficiency of the probe, the key device for generating the optical near field, as shown in Fig. 3, particularly in the years since 1997.   This improved efficiency is a development that has made it possible to realistically envision the eventual development of practical technology for optical recording.

In order to construct a practical optical disk memory system, however, it is necessary to develop hardware for integrating the memory into the application to be provided to the users.   The development of such hardware involves the intricately related problems of the recording media and the recording/reading head device and its drive system.
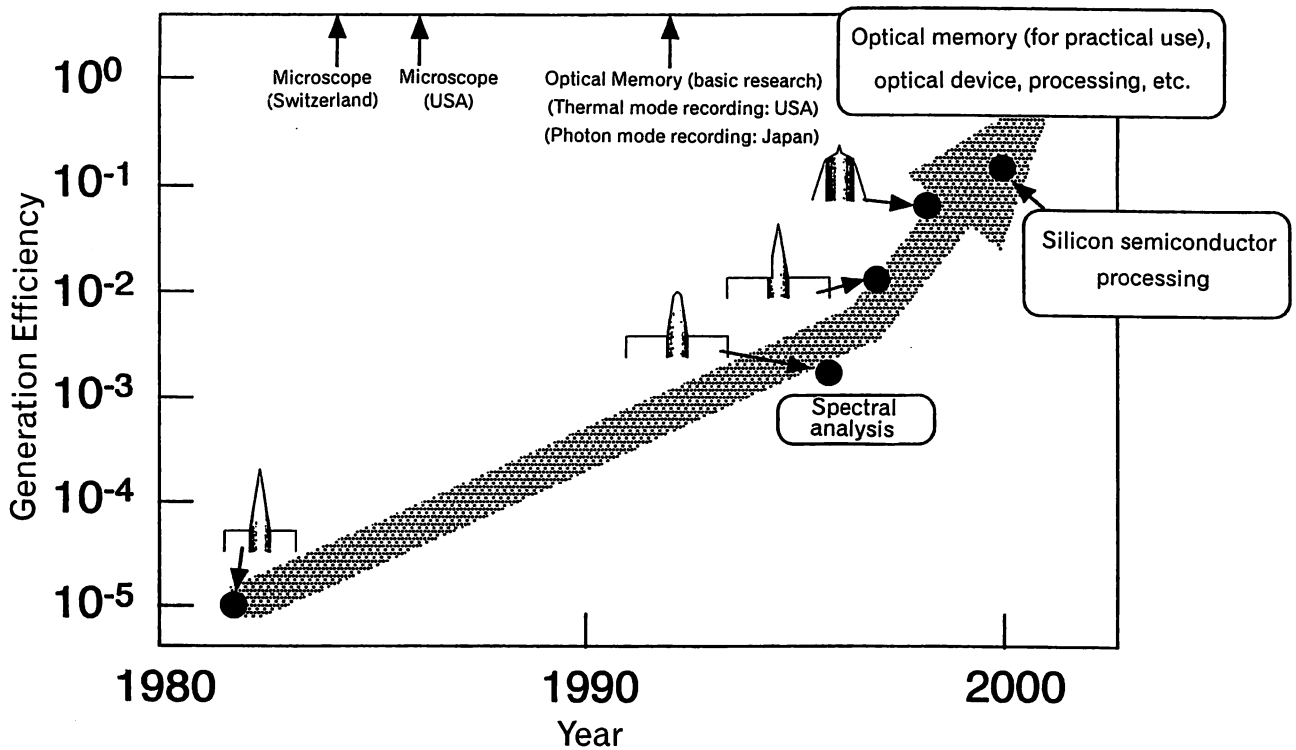
Fig. 3. Progress of Optical Near-Field Generation Efficiency of Fiber Probe (by M. Ohtsu)
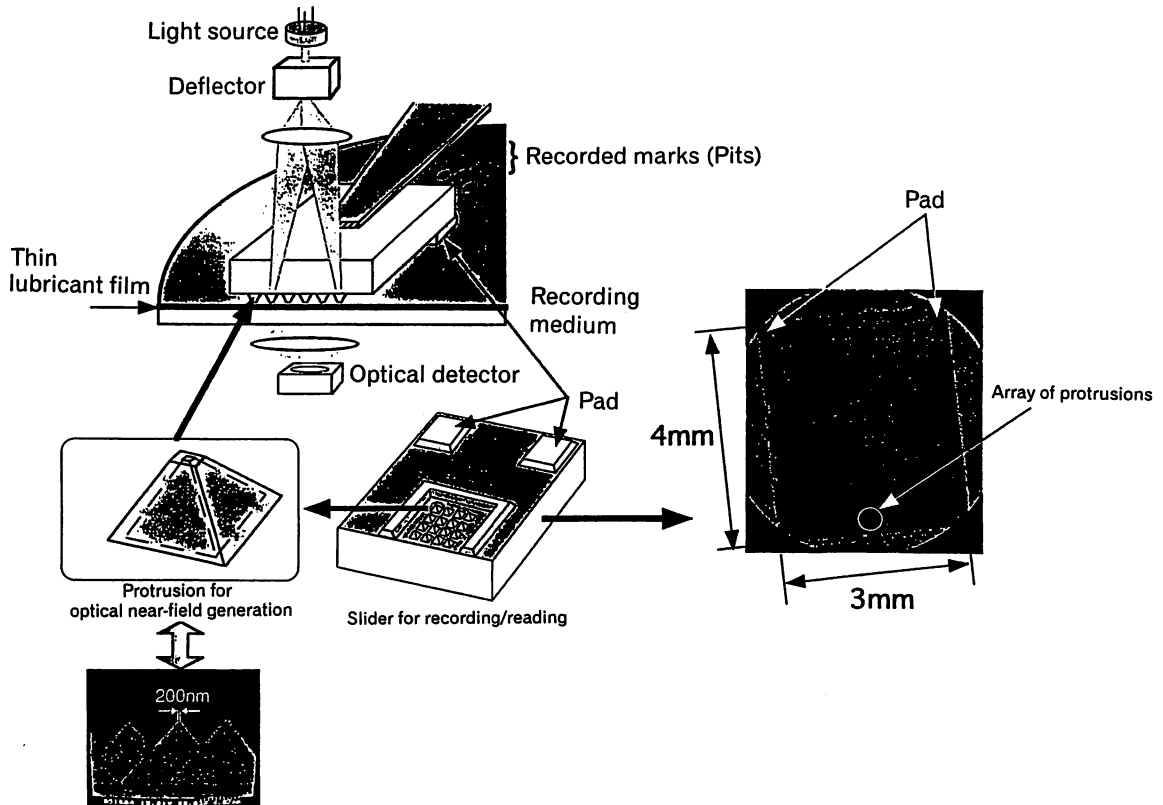
Fig. 4. A Method of Near-Field Optical Recording/Reading Using Silicon Protrusion

The Nano-photonics Technical Group of OITDA has been examining these problems for the past five years. One of the promising solutions is to employ a silicon protrusion for the optical near-field generation device, as shown in Fig. 4, and to incorporate this two-dimensional array into the contact-type recording/reading head. So far, recording and reading has been performed on the phase-change media; and a mark length of 110 nm was successfully recorded and read without any need for tracking or other adjustments. The development is presently continued with a focus on the improvement of detailed parts, in order to achieve successful recording of 25 nm mark length and reading on a CNR of 40 dB or more. The target density to be attained by 2010 is set at 1 Tb/in^2. The practical optical-disk memory system using the optical near field is expected to be either a sealed type or a removable package type. Both are to be eventually developed as ROM, WORM, and finally as RAM.

3. Towards 2030

Although it is very likely that 1 Tb/in^2 will be achieved by 2010, the recording density by 2030 remains uncertain. To be noted here is again the fact that the nano-photonics connotes a paradigm shift in optical technology. The past examples of scientific and technological developments indicate that a very long period is required between the occurrence of a paradigm shift and a full practical application of the developed performance. In the case of DRAM, for example, while the invention of the transistor, which was the element technology for DRAM, did undoubtedly bring about a paradigm shift, it took another 20 years before IBM finally succeeded in incorporating 1 kb DRAM into its large-scale computer. Since then, owing to the advancement in system technology, the DRAM capacity continued to increase to the present level, at a pace dubbed "4-fold in 3 years."

The same applies to optical technology. The invention of the laser in 1960 had provoked a paradigm shift. In the few months immediately after the invention, various proposals were made with regard to laser applications. However, it was not until 20 years later, or 1980s, that an optical-disk memory system for consumer use was finally introduced to the market. Likewise, while the proposal for the optical fiber amplifier had been originally made in 1960s, its introduction for practical use was not realized for another 30 years, until 1990s.

Given such large time lags, it can be safely said that the nano-photonics is sufficiently capable of offering a performance level that is adequate for meeting the needs of the society in 2030. Whether the nano-photonics will be actually developed for practical uses largely depends not so much on the course of technological development, but on the spirits of those involved-that is, on the determination on the part of researchers and technical experts. As was the case with airplanes and transistors, when a new concept or a technology is developed or discovered, it is inevitably exposed to various criticisms. This applied to the researches in the nano-photonics. Continuous effort and perseverance of the researchers however, has led to the progress illustrated in Fig. 3. The idea that "the fiber probes are inefficient" is considered highly outdated today. Presently, the main issue is on how to decrease the energy density of near-field optical energy at the tip of the fiber in order to prevent the nonlinear optical phenomenon.

It is therefore very important for those involved in the research to reject the criticisms and concentrate on the realization of practical application of the nano-photonics by 2030. It must be remembered that a number of new developments for practical application in the optical technology had been nothing but a result of the efforts of those who dared to work on what was considered "farfetched" at the time. The buried structure of semiconductor laser served as a starting point that led to the development of stable operation devices, while the development of long-wavelength semiconductor laser enabled practical application of long-distance optical-fiber communication. Moreover, it was the fiber production by VAD method that brought about the practical use of low-loss fibers.

Fig. 5 compares the progress of the nano-photonics with that of DRAM and optical technology. It is evident from the figure that the data recording technology using optical near field is still very new at this point. The very fact that this new technology is already regarded as a promising candidate for achieving 1 Tb/in^2 by 2010 suggests that this particular technology possesses superior qualities compared to others. Some of the researches conducted in relation to nano-photonics may seem "farfetched" at times. However, by advancing towards such "farfetched" goals and by developing various element technologies and combining them with software technology, the nano-photonics should be able to meet the needs of the society in 2030.
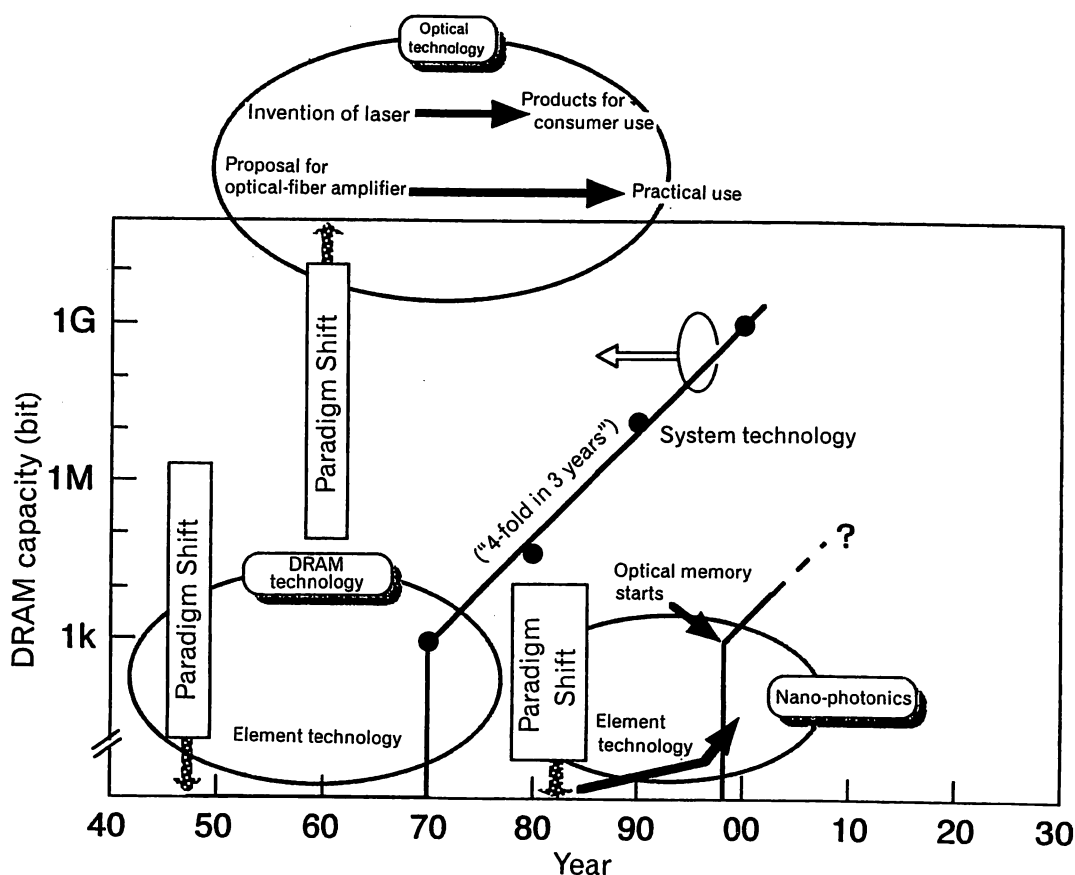
Fig. 5. Chronological Comparison of Nano-photonics, DRAM Technology, and Optical Technology

As shown in Fig. 4, the form of the optical near-field memory system resembles that of HDD. From this, it can be safely predicted that the new data recording technology to be developed in the future will be a combination of the HDD technology and/or the existing optical-disk memory technology with the nano-photonics. The very reason that the nano-photonics will provoke a paradigm shift in optical technology lies in the fact that this new technology is also applicable to a variety of fields other than optical data recording. Nano-photonics covers almost all fields of optical technology and encompasses the possibility of achieving nano optical technology. As is presented in Fig. 6, the rise of this possibility is exemplified by the ongoing development and attempts to integrate nano photonic devices to meet the needs of the optical communication system of 2015. These nano-photonic integrated circuits are applicable also to the conventional semiconductor memory, as well as to the solid memory such as optical memory cards. Finally, the nano-photonics has the potential of even transforming the memory devices into a totally new form that is totally different from the conventional ones that require disk rotation or tape winding.
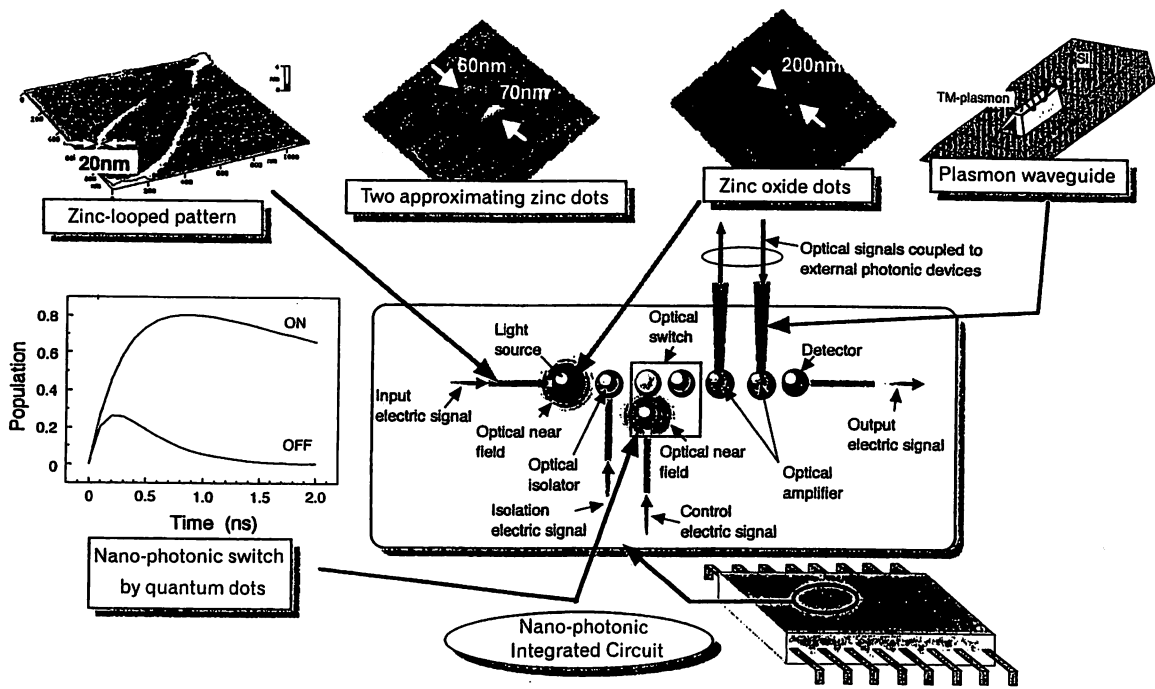
Fig. 6. Present Status of Nano-photonic Integrated Circuit Development

4. Conclusion

It is virtually impossible to discuss optical technology of 2030s. The discussions above are mostly the author's subjective conjectures, and the issue boils down to the strength of determination of those concerned in the development in the relevant fields. Assuming that it really is a matter of determination of the researchers, what is especially important is to eliminate all the obstacles that might get in the way of putting that determination into practice and to work on new developments. Since the R & D environment after a successful industrial application of an existing technology is apt to be influenced by the resulting industrial environment, it becomes necessary to establish anew an infrastructure

to promote R & D in yet another novel field. Moreover, new researchers must be welcome to replace the previous researchers. There are probably no senior engineers who have the experience of having taken a class on nano-photonics at college. Furthermore, it is additionally important to focus the researches between now and 2030 on the items in which Japan will be able to continue to maintain the lead over other countries. There is ample past evidence pointing to the likely possibility of other countries catching up with Japan in the case of relatively easy technologies.

From a scientific point of view, proposals have been made for nano technology applications such as STM and atom manipulation as possible future recording technologies. The author, however, is quite skeptical that these technologies would ever be realized in earnest. These proposals lack discussions on the efficiency and reliability of data recording as a system for consumer use. "Linearity," "room temperature," "atmospheric," "solid-state" are some of the key terms that must be addressed and satisfied by the technology that is entitled to survive and whose economic factors deserve consideration.

InterOpto '02

OITDA is presently preparing for the InterOpto (International Optoelectronics Exhibition) '02 to be held at Makuhari Messe (International Exhibition Hall, Nippon Convention Center, Chiba, Japan) from July 16 to 19 this year.

InterOpto, at which the latest optoelectonic industry and technology from throughout Japan and the world are exhibited, is the largest international optoelectronics trade fair and an excellent opportunity for exchanging technological developments, catching business chances, and having one's company known to the world. The products exhibited at InterOpto include: materials, optical devices and modules, optical equipment and instruments, industry-concerned equipment, as well as services and software. Exhibitors include corporate members representing optoelectronic R & D, technology, sales and other related departments, as well as the members of relevant public organizations.

The call for participation in InterOpto '02 was closed on March 8. OITDA is presently reviewing and confirming each of the received applications, which have exceeded the scheduled number of exhibitors (300 companies) and booths (700).

For more information, contact;

InterOpto SECRETARIAT, OITDA
1-20-10, Sekiguchi, Bunkyo-ku, Tokyo 112-0014, Japan
Tel: +81-3-5225-6431　　Fax: +81-3-5225-6431
http://www.oitda.or.jp

ナノフォトニクスのための近接場光学入門

大　津　元　一

Introduction to Near-Field Optics for Nano-Photonics

Motoichi OHTSU

Present and past of near field optics are reviewed. Electric dipole interaction model is presented to give a basic concept of optical near-field. For more general discussions, classical, semiclassical, and quantum theories are described.

Key words: optical near-field, dipole, probe, microscopy, nano-photonics

ナノテクノロジー（NT）の研究開発に象徴されるように，科学技術の重要な方向のひとつは材料を微小化して高度集積化デバイスを開発し，これによりシステムの大容量・高速化をめざすことである．ところで，光技術は以前より情報の通信，記録，表示などの情報技術（IT）を担ってきたので，NT を光技術に利用すれば IT の性能が飛躍的に向上する可能性がある．この観点に立てば，光による NT，すなわち筆者が「ナノフォトニクス」[1],[*1] と命名した光科学技術は将来への必然的な方向である．

ところで，最近はナノメートル寸法の材料を多数用いた量子ドットレーザー，微小共振器レーザー，フォトニック結晶などが研究されているが，これらはナノフォトニクスとは無縁である．なぜならば，これらは伝搬光を情報キャリヤーとして使っているからである．伝搬光は波動の基本的な性質，すなわち回折のためにそのエネルギーは波長の寸法程度以下の領域に集中しない．

ナノフォトニクスの実現には，情報キャリヤーとしての光のエネルギーが集中する領域の寸法がナノメートルでなければならない．さらに，そのような「微小な光」を発生し使用するためには，1個〜数個のナノメートル寸法材料で光デバイスを構成する必要がある．これらを実現するのが近接場光である．以上の状況を図1にまとめる．本稿では，ナノフォトニクスを支える基礎概念である近接場光について解説する．詳細は文献2-5）を参照されたい．

さて，本論に入る前に，近接場光学，ナノフォトニクスの歴史と現状について簡単に触れておこう．近接場光を高分解能の光学顕微鏡として利用する提案は 1928 年にさかのぼるが[6]，この段階では旧来の光学の計測への応用の話題にすぎず，したがってそれ以降長年顧みられることはなかった．しかし，近接場光の本質は微小物質と電磁場のナノメートル寸法領域での局所的な共鳴相互作用であるので，1980 年代以降はこの観点から理論的な枠組みを確立し，それを基礎として単なる計測技術ではなく情報通信，情報記録などを担うナノ光機能，デバイス，システムを実現し，ナノフォトニクスを構築する試みが始まった．そのためには，実験と理論の両面からの革新的なアプローチが不可欠であったが，そのひとつは近接場光を検出，発生させる基本的なナノ寸法デバイス，すなわちファイバープローブの製作である．これについては，わが国で 1980 年代初頭から開始され[7]，その先端寸法が数ナノメートルに達する微小化，10％に達する高い発生検出効率，などが実現している[3]．この結果，「ファイバープローブの効率が低い」という通説は遠い昔話となった感がある．このデバイス開発と歩をほぼ同じくし，欧米では 1980 年代に顕微鏡への応用が提案され[*2]，一方わが国では，ファイバープローブの基本技術を進展させてナノフォトニクスに至る研究開発が始まった．また，ナノフォトニクスよりもさらに微小寸法の極限的な科学技術としてのアトムフォトニクスを近接

東京工業大学大学院総合理工学研究科（〒226-8502 横浜市緑区長津田町 4259）　E-mail: ohtsu@ae.titech.ac.jp

*1 （財）光産業技術振興協会では筆者の提案により 1995 年に「ナノフォトニクス懇談会」が発足し，現在に至っている．
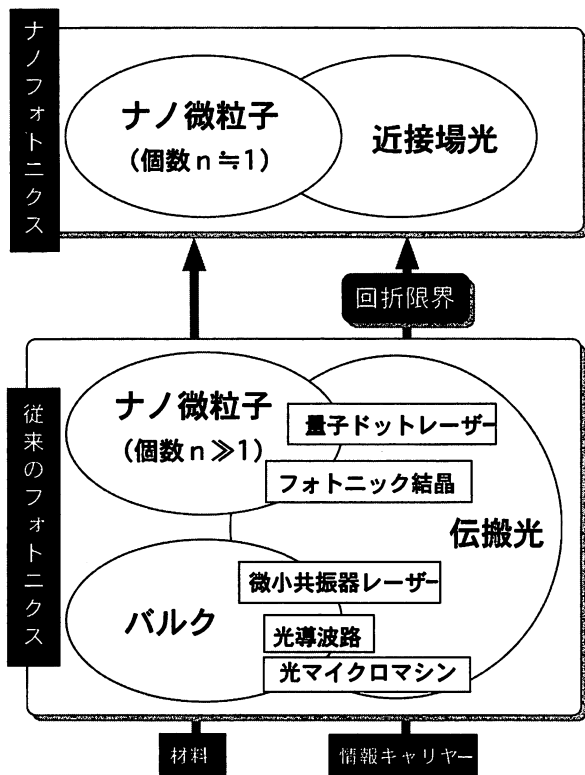
図1 従来のフォトニクスとナノフォトニクスとの違い.

(a)

(b)

図2 電気双極子モーメント p がその周囲の空間につくる全電場の電気力線. 横軸, 縦軸はおのおの kx, ky で示している. k は波数. (a) 中心部分, (b) 全体図.

場光で実現する研究も, わが国で1990年代初期に開始され現在に至っている[3].

1. 近接場光の考察の手がかり

近接場光とは, 光を物質に照射したときに, 物質表面から照射光の波長に比べ十分近い位置に発生する電気力線によって表される電磁場である. ナノフォトニクスでは, 特にこの物質の寸法が波長に比べはるかに小さい場合を扱う. ただし, この物質の寸法は, それを量子論で記述したときの状態関数の広がりの程度を表すドブロイ波長よりは大きいものとする. 近接場光は次の2つの主な性質をもつ. (a) 非伝搬である. いいかえると物質表面に局在している. (b) エネルギーは物質表面から遠ざかるにつれ減少する. その減少の度合いを表す「しみ出しの厚み」は物質の寸法程度である.

このような近接場光の発生, 検出の過程を直感的に把握するための最も単純なモデルは単一の電気双極子を用いる

ものである. 真空中で時間的に振動する電気双極子モーメント p から発生する電磁場の電気力線は, 図2(a), (b) のようになる. 図2(a) は図2(b) の中心部分 (すなわち $|kr|<1$ の領域, k は波数ベクトル, r は p を原点とする位置ベクトル) を拡大したもので, これが近接場光に対応する[*3]. これは p から発して p に終端しているので非伝搬光であることを表しており, 上記の性質 (a) に対応する. 一

[*2] これは近接場光学顕微鏡とよばれている. なお, その英文名としては, 初期の研究を行った機関での特許権の主張などにも関連して SNOM, NSOM, PSTM などの頭文字で表されるさまざまな英語の呼称が与えられていた. これらは近接場光学顕微鏡が走査プローブ顕微鏡(SPM)の一種であることを意識した呼称になっているが, 学術的に確固たる根拠に基づいたものではないのでいまだに統一的な呼称とはなっておらず, 正式な名前でもない. フルネーム near-field optical microscope を使うことが妥当であろう. 近接場光学顕微鏡はナノフォトニクスのうちの計測分野における装置のひとつに過ぎないので, 今後のナノフォトニクスの発展につれ上記の不統一な呼称は消滅するであろう.

[*3] 光を発生する物質の寸法を a とすると, $|k|a<|kr|\ll1$ は近接場条件とよばれている. 一方, $1\ll|kr|$ は遠隔場条件, さらに両者の中間の $|k|a\leq|kr|\leq1$ は準近接場条件とよばれている. また, これらの条件が成り立つ r の範囲はおのおの, 近接場領域, 遠隔場領域, 準近接場領域とよばれている.

128

走査方向

球T

球P

θ

球S

X

z

a_t

a_p

a_s

入射光

(a)

不透明膜

$2a_f$

先鋭化された
コア

θ
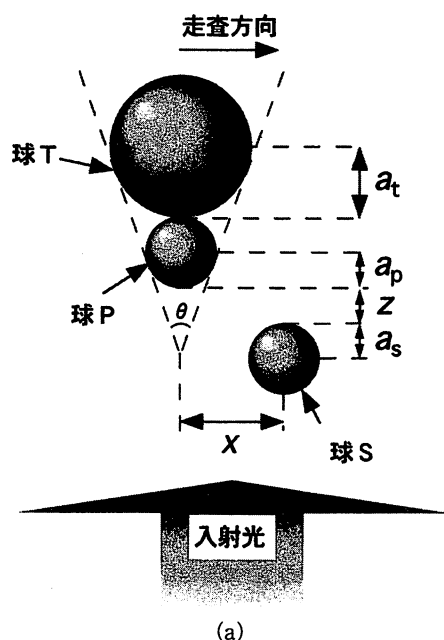
$2a$
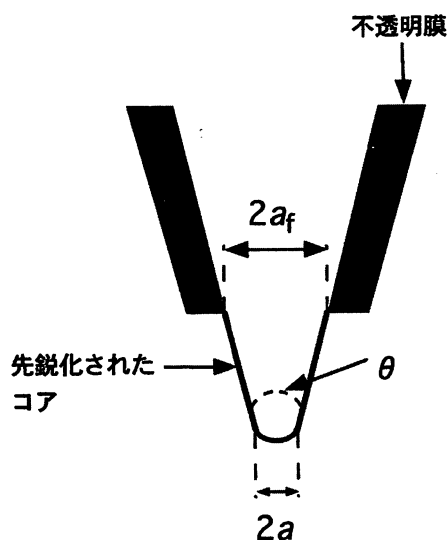
(b)

図3 近接場光の発生, 散乱, 検出の様子. (a) 球S, P, T の配置と走査方向. a_s, a_p, a_t はこれらの球の半径. θ は円錐角. x, z は球S, P 間の水平, 鉛直方向距離. (b) ファイバープローブの構造. a は先端曲率半径 (図(a) 中の a_p に対応), a_f は開口部の根元半径. θ は円錐角.

方, 図2(b) において, その外側にある閉曲線状の電気力線は遠隔場領域へと回折しながら伝搬する光を表している. 従来の光技術で使っているのはこの光である.

ここで, 近接場光学顕微鏡を例にとって考察しよう. この顕微鏡では, 図3(a) に示すように, 試料となる微小な球Sに入射光 (その電場は E_0) を照射し, その表面に近接場光を発生させる. 非伝搬光である近接場光を検出するためにプローブとして使われる微小な球Pを近づけて, これ

により近接場光を散乱させ, その散乱光強度を遠方で測定する[*4].

ここでは球Sにプローブとなる微小な球Pが近接しているので, 球Pにも入射光が同時に照射される. この状況では, 入射光の電場 E_0 により2つの球には電気双極子モーメントが発生する. これらの電気双極子モーメントが新たな電場を発生し, その電場が相手の球に電気双極子モーメントを変化させる. このような電磁的相互作用は双極子間相互作用とよばれる. この結果発生した電気双極子モーメントのすべてが源となって発生する電磁場のうちの散乱光成分の強度を遠方で測定する.

実際には, 球Pの代わりにファイバープローブを使う. それは図3(b) に示すように円錐形であるため, その先端部と試料との間の双極子間相互作用は円錐部と試料との間の双極子間相互作用に覆い隠される傾向をもつようになる. 簡単のために, ファイバープローブを, 図3(a) に示すように半径 a_p の球Pに, それよりも大きな半径 a_t をもつ球Tが接続したものと近似する. ここで, a_t の値は円錐角 θ と半径 a_p とによって決まる. このとき球S-P間の双極子間相互作用とともに球S-T間の双極子間相互作用も考えることにより, 近接場光の発生と検出に関する特性が明らかになっており, 次のように多様な実験結果と対応している: (1) 信号強度は a_p とともに増加する. (2) 分解能はほぼ a_p であり, 入射光の波長とは無関係である. (3) 試料のまわりの近接場光エネルギーの空間分布の厚みは試料の半径 a_s 程度である. (4) プローブと試料の鉛直方向距離 z が増加すると信号感度, 分解能は劣化する. (5) 背景光に対するコントラストは $a_p = a_s$ のときに最大となる (寸法依存の共鳴効果). (6) 集光モードの近接場光学顕微鏡において入射光がs偏光の場合, 試料形状の凹凸に対して画像の明暗が反転し, さらに走査方向に依存する端部効果がある[8]. p偏光の場合, 画像の明暗は反転しないが, 偏光に依存する端部効果がある. (7) θ の値の増加とともに, 球Pによる高い分解能での近接場光の散乱の効果が球Tによる散乱の効果に隠される傾向をもつ. 両者の効果の大きさの比をファイバープローブの明瞭度 V と定義すると, V の値は θ の増加とともに減少する. また, 試料とプローブとの鉛直方向距離の増加によっても減少する[9]. (8) ファイバープローブの根元の部分に不透明膜を塗布すれば, コントラストと明瞭度とを増加させることができる. (9) 屈折率の大きな材料をプローブとして用いると信号強度が増加する. そのためには, たとえば (a) 図4(a) に示すよう

[*4] この測定法は集光モードとよばれている. これとは反対に, 球Pに入射光を照射し, 発生した近接場光で球Sを照明し, 球Sで散乱された光強度を測定する方法は照明モードとよばれている. 本稿での議論は両モードに対して成り立つ.

に，シリコンを材料としてつくられたプローブを用いること[10]，(b) 図4(b) に示すように，先端部が金属で覆われたファイバープローブを金属のプラズマ振動数付近で使うこと[11],[*5]，が有効である．

2. 一般的な取り扱い

一般的には，試料やプローブの物質の形状，構造に起因して発生する多数の電気双極子の振る舞いを取り扱う必要がある．この場合に発生する近接場光もやはり1章冒頭に示した性質 (a)，(b) をもつが，これらに起因した各種現象を記述するために下記のいくつかの方法がある．

2.1 古典論と半古典論

2.1.1 自己無撞着法による古典論

巨視的な電磁現象を記述するマクスウェル方程式に基づき，ナノ寸法の領域の現象を記述する伝統的な方法は古典論とよばれている．この場合，試料，プローブなどの物質系の振る舞いは巨視的な屈折率または誘電率で表して電磁場を決定し，近接場光の空間分布を得る．古典論のひとつに，旧来のグリーン関数（伝搬関数）による自己無撞着法を流用したものがある[3]．この方法では，まず近接場条件下でマクスウェル方程式から位置 r における光の電場 $E(r)$ が満たす波動方程式を導く．この式中，波源として働く分極 $P(r)$ は光の電場 $E(r')$ によって物質中に生じるので，電気感受率 $\chi(r, r')$ と電場 $E(r')$ により与えられる．この分極を与える式と波動方程式とを連立して解を求める．この方法の利点は次の3点である．(a) 3次元の任意形状のプローブと試料からなる系を扱うことができる．(b) 電場のベクトル的な性質，すなわち偏光の効果を取り入れることができる．(c) 電場とプローブ，試料，基板の近接場領域での相互作用とその伝搬成分を考えることにより，理論値と実験データとの比較ができる．

ただし，具体的な結果を得るには長時間にわたる数値計算を使う必要があるので，物理的な直感に訴えるものではなく，見通しはよくない．この方法によりさまざまな数値計算が行われており，たとえば前章の (6) の特性が説明されている[3]．

2.1.2 表面電荷に基づく古典論

近接場光学の発展のためには，前項のような既存の方法を流用するのではなく，近接場光を含む系の特徴をうまく捉えて基礎となる方程式を見直して書き換え，物理的直感
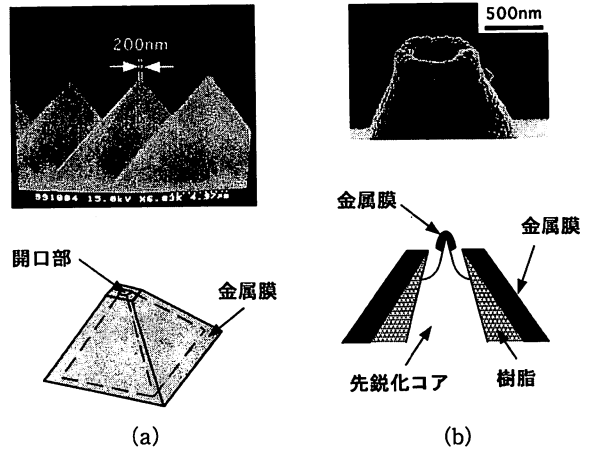
図4 高感度型のプローブの例．(a) シリコンを材料としたもの[10]．（上）アレイ状に作製されたものの電子顕微鏡写真．（下）構造説明図．(b) 先端が金属で覆われたファイバープローブ[11]．（上）電子顕微鏡写真．（下）構造説明図．

に訴えることができる見通しのよい理論モデルが必要である．本項では，このようなモデルのひとつについて概説する．このモデルの利点は，試料とプローブの寸法や試料・プローブ間距離が十分小さくて近接場条件が十分高精度に成り立つ場合，およびこれらの値が大きくなり準近接場条件を経て遠隔場条件に対応する場合の両方を統一的に扱えることである[12]．

入射光の波長より十分小さい寸法の誘電体の周囲に発生した光の電場を近接場条件下で観測する場合は，時間遅れの効果が無視できるので，静電的問題に帰着する．特にここでは真電荷がない場合を扱うので，この静電的問題はガウスの法則を表す式 $\nabla \cdot E = 0$ をもとに解くことができる．ここでは，ガウスの法則を誘電体中に拡張し，スカラーポテンシャル ϕ を用いると

$$-\Delta\phi(r) \cong \left(\frac{\varepsilon_1 - \varepsilon_0}{\varepsilon_0}\right) n_s E_0(r) \int_s \delta^3(r-s) \mathrm{d}^2 s \quad (1)$$

を得る．ただし，ε_1，ε_0 はおのおの試料内外の誘電率，n_s は表面の外向きの法線方向を表す単位ベクトル，δ はデルタ関数，s は物質表面の位置ベクトルである．式（1）はポアソン方程式に他ならないので，これより誘起される表面電荷がつくる電気力線を求めればよい．その電気力線の方向と本数が発生する電場ベクトル $\delta E(r)$ の大きさと方向とに比例した量である．

ここで検出される光の強度を

$$I(r) \equiv |E_0(r) + \delta E(r)|^2 - |E_0(r)|^2 =$$

[*5] 図4(b) のファイバープローブは球 P に対応する先端部分が金属で覆われている．根元は，近接場光に起因する光以外が光検出器に入射することを防ぐために不透明な金属膜で覆われている．このようなファイバープローブを作製する技術がない場合，その代わりに走査トンネル顕微鏡用のプローブである金属針を流用することも考えられるが，金属針は近接場光と伝搬光との間のインターフェイス機能（すなわちプローブ外部の伝搬光と先端の近接場光のエネルギーの変換機能），および近接場光以外に起因する光が光検出器に入射することを防ぐ機能の2機能を有しないことが致命的な欠点である．
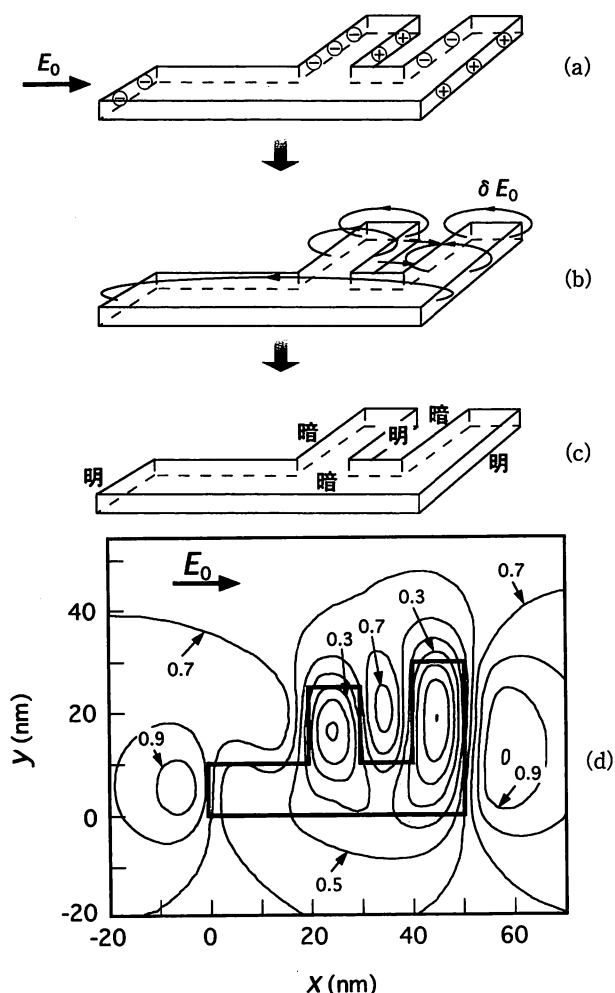
図5 アルファベットの大文字 F を裏返したような形の誘電体表面の光の強度 $I(r)$ の空間分布の図的な求め方. (a), (b), (c) はおのおの本文中の手順 (a), (b), (c) を表す. (d) 式(2) を用いた数値計算の結果[13]. 図中の等高線の高さを表す数値 η は文献 14) の図1(a) の値と比較するために記した. 式(2) の $I(r)$ はこの η と $I(r)=0.25\,\eta-0.17$ の関係がある.

$$2E_0(r)\delta E(r)+|\delta E(r)|^2 \qquad (2)$$

と定義する. 右辺第2行目の主要項は $E_0(r)\cdot\delta E(r)$, すなわち入射光と発生した光との干渉項である. 電場 $E_0(r)$, $\delta E(r)$ が互いに逆向きであれば干渉項 $E_0(r)\cdot\delta E(r)$ の値は負となり, 強度が背景強度よりも小さくなる.

以上の考察の適用例として, アルファベットの大文字 F を裏返したような形の誘電体表面の光の強度 $I(r)$ の空間分布を求める手順を以下の (a)〜(c), および図5に示す. すなわち, (a) (図5(a)) 表面誘起電荷の面密度の空間分布を求める (式(1) の $\{(\varepsilon_1-\varepsilon_0)/\varepsilon_0\}n_s\cdot E_0(r)$ より). (b) (図5(b)) 発生した光の電場 $\delta E(r)$ の空間分布を求め

る. (c) (図5(c)) $E_0(r)$ と $\delta E(r)$ の向きに注意して強度 $I(r)$ の空間分布を求め明るい箇所や暗い箇所を知る.

以上のようにして図的, 直感的に求めることができるが, この光強度の空間分布を定量的に求めたければ式(2) を用いて数値計算すればよい. その結果を図5(d) に示す[13]. これは前項の自己無撞着法によっても求められているが[14], 本方法の結果はこの方法による結果と一致しており, かつこの結果を得るための数値計算の時間は著しく短い*6.

以上の結果が集光モードの近接場光学顕微鏡の場合に適用され, 1章の (6) をはじめとする種々の特性が説明されている.

以上の議論は, 近接場条件から準近接場条件を経て遠隔場条件への移行の様子を記述する直感的描像も与えることができる. たとえば, 準近接場条件下での近接場光学顕微鏡像において試料の前面が暗くなり, あたかも影ができたようになることが説明されている. この現象は, 時間遅れの効果がもたらした結果である.

2.1.3 半古典論

物質の寸法が光の波長に比べ小さい場合, エネルギーなどの内部状態が近接場光の測定結果に反映する. これらを記述するためには, 電磁場はマクスウェル方程式に従う古典量として扱うが, 物質系の応答はシュレーディンガー方程式に基づく量子論で決定する方法が用いられる. この方法は半古典論とよばれている. すなわち, 線形応答理論に基づき, 外場としての光の電場が電子多体系に照射される場合を考える. この系を表す量子力学的ハミルトニアンを書き下し, 密度行列演算子のリュウヴィル方程式を解くことにより非局所的な電気感受率 $\chi(r, r', \omega)$ を導出し, その場所での局所的な電磁場との積から物質系に誘起される分極を求める. この誘起分極が源となって, 局所的な電磁場がマクスウェル方程式の解として求まる. 誘起分極と巨視的な電磁場との間に互いに矛盾がないものが最終的な解となる.

ここでは, 物質の電気感受率は非局所的であるので, ある場所での分極にはその場所以外での局所電磁場も影響してくる. 物質系の電子相関距離と, 微視的な電磁場を空間的に平均化して巨視的電磁場を得る際の空間平均距離に関して, 近接場光と物質とからなる系では特にこのような非局所性が重要になる場合がある[15,16].

---

*6 図5(d) を文献 14) の図1(a) と比較すれば, 両者は互いに一致していることがわかる. ところで, 図5(d) の等高線を求めるのに要した計算時間は学生用のパーソナルコンピューターを用いて1秒程度であった. これに対し, 文献 14) の図1(a) の等高線を求めるには IBM RISC system/6000 model 970 ワークステーションを用いて5分30秒かかっている.

2.2 量子論

原子, 分子, 量子ドットなどの物質とプローブとからなる系を考える場合, 光と物質励起を同時に考えることによって系の特徴を抽出できる場合がある. そのためには, 物質とともに電磁場も量子力学的に扱う. この方法は量子論とよばれている. 特に物質と近接場光からなるナノメートル寸法の系はその周囲の巨視的な系に囲まれているので, これら2つの系の結合系をうまく繰り込む必要がある.

近接場光学顕微鏡を例にとると, その2つの系はナノメートル寸法の物質系 (ファイバープローブ先端, 近接場光を介して相互作用する試料) と巨視的な物質系 (光源, ファイバー, 基板, 光検出器など) である. 原子の多体系が相互作用しているので厳密解を得ることはできないが, 近接場光の理論を構築する目的はそのような多体系の厳密解を求めるのではなく, ファイバープローブの先端と試料との相互作用, 相互作用の機構, 回折限界を超えた高分解能の原因などについて知ることである. さらに, 従来の光科学技術で研究されてきた伝搬光と物質との相互作用において暗黙のうちに仮定されている自由空間中の孤立系という枠を取り去ったとき, 従来の結果がどのように変更されるかということを知ることが重要である. このような要求に答えるために開発されている射影演算子と素励起モードの考え方を用いた定式化について, 以下で説明する[17,18].

上記のナノメートル寸法の系を副系 (n), これらを取り囲む上記の巨視的な系を副系 (M) とよぶ. 以後は副系 (n) のみを考え, 副系 (M) の影響は副系 (n) の中の試料とプローブとの電磁的相互作用の大きさを修正することにより取り込む. ここで副系 (n), (M) 中の各物質の状態を表す状態関数について考えよう. まず副系 (n) には試料, プローブがあるが, これらが単独に孤立して存在するときのエネルギー固有関数をおのおの $|s>$, $|p>$ と表す. さらに, これらの関数が基底状態か励起状態かを区別するときには添え字 g, e をつける. 一方, 副系 (M) は物質とその中の電磁場とからなる量子系である励起子-ポラリトンの状態関数 $|m_{(M)}>$ により表す ($m_{(M)}$ は量子数).

さて, 興味の対象は副系 (n) なので, 2つの状態関数 $|\phi_1> = |s_e>|p_g>|0_{(M)}>$, $|\phi_2> = |s_g>|p_e>|0_{(M)}>$ を取り上げ, これらが張る空間 (P 空間とよぶ) を考える. 以後は, 考察の対象となる系の状態を表す状態関数 $|\psi>$ をすべて P 空間の中で議論する. この方法は射影演算子法とよばれる. 試料, プローブの間での電磁的相互作用を量子力学的ハミルトニアン $\hat{V}$ で表し, この中で入射光は副系 (M) を経て副系 (n) 中の試料, プローブを照射するので励起子-ポラリトンの消滅演算子, 生成演算子で置き換える. こう

して得られた $\hat{V}$ に対し, 射影演算子の手法を用いて P 空間で有効な相互作用演算子 $\hat{V}_{eff}$ を書き下す. P 空間において始状態関数が $|\phi_1>$, 終状態関数が $|\phi_2>$ であるとすると, 相互作用の大きさは $V_{eff}(ps) = <\phi_2|\hat{V}_{eff}|\phi_1>$ となる. ここで試料, プローブおのおののエネルギー固有値として, 寸法がおのおの a_s, a_p の無限に深いポテンシャル井戸中の電子のエネルギー固有値を採用する. さらに励起子-ポラリトンのエネルギーと運動量との間の関係を表す分散関係中の励起子-ポラリトンの有効質量 m_p を用いると, $V_{eff}(ps)$ を書き下すことができる. 以上の議論と同様に今度は始状態関数が $|\phi_2>$, 終状態関数が $|\phi_1>$ であるとすると, 相互作用の大きさ $V_{eff}(sp)$ は添え字 p と s とを入れ替えたものとなる. そして, $V_{eff}(ps) + V_{eff}(sp)$ が相互作用の大きさ V_{eff} となり, それは

$$V_{eff} \propto \frac{\exp\left(\frac{-\pi\mu_p r}{a_p}\right)}{r} + \frac{\exp\left(\frac{i\pi\mu_s r}{a_s}\right)}{r}$$
$$+ \frac{\exp\left(\frac{-\pi\mu_s r}{a_s}\right)}{r} + \frac{\exp\left(\frac{i\pi\mu_p r}{a_p}\right)}{r} \quad (3)$$

と表される[7]. ただし r はプローブと試料との間の距離 $|r_p - r_s|$, m_{ep}, m_{es} はおのおのプローブ, 試料中の電子の有効質量, $\mu_p = \sqrt{3m_p/m_{ep}}$, $\mu_s = \sqrt{3m_p/m_{es}}$ である. 式(3)右辺の第1項は, プローブの大きさに応じた空間分布をもつ電磁場がプローブの近傍に存在することを意味する. これは湯川関数であり r の増加とともに急激に減少するので, 近接場光に対応している. また, この項は, 基底状態のプローブが励起子-ポラリトンのエネルギー量子を放出し, 励起状態の試料に吸収される非共鳴過程に対応する. 第2項は伝搬光を表し, 励起状態の試料が励起子-ポラリトンを放出し, 基底状態のプローブに吸収される共鳴過程に対応する. 第3項, 第4項はおのおの第1項, 第2項においてプローブと試料とを入れ替えたものである. 以上は, 微粒子に光を照射するとその周囲には伝搬光 (散乱光) とともに近接場光が発生することを意味している.

式(3)右辺の第1, 3項より, 一般に半径 a の球の中の各位置 r' に湯川関数で表される相互作用の源があると考えることができる. したがって, この球全体で源の総和をとることにより, 球の外部の任意の位置 r における電磁場を表すスカラーポテンシャル $\phi(r)$ は

$$\phi(r) = \left(\frac{2\pi}{\mu^3}\right)\left[(1+\mu a)\frac{\exp\{-\mu(r+a)\}}{r}\right.$$
$$\left. - (1-\mu a)\frac{\exp\{-\mu(r-a)\}}{r}\right] \quad (r > a)$$

$$(4)$$

となり, やはり湯川関数で表されることがわかる. ここで,

$\mu=\sqrt{3}\pi m_\mathrm{p}/m_\mathrm{e(a)}/a$，$m_\mathrm{e(a)}$ は球の中の電子の有効質量である．この式右辺の関数の中で，分子の指数関数の値が $r=0$ のときの e^{-1} になるときの r の値を近接場光のしみ出し厚みと定義すると，それは $1/\mu$，つまり球の大きさ程度であることがわかる．以上をまとめると，巨視的な副系（M）の効果を繰り込んだとき，微小な副系 (n) において仮想励起子ポラリトン（質量をもった仮想光子）を交換して働く相互作用の主要部は湯川ポテンシャルである．

以上で得られた仮想光子モデルでは，有限の相互作用範囲すなわち有限の有効質量をもつ仮想光子の媒介によって試料とプローブとの間に近接場光相互作用が生じ，それが湯川ポテンシャルで表されることを意味している．これは時間とエネルギーとに関するハイゼンベルクの不確定性原理から，観測にかかる時間に比べて十分短い時間の間ではエネルギー保存則を満たさないような過程が生じることに対応する．仮想光子とはこのような過程で発生する量子で，いわば物質励起の衣を着た光子である．

以上の結果を利用し，1章の (1)〜(9) の特性が説明されている[17-19]．さらに重要なことは，次に示すようにナノフォトニクスへの発展としてのナノ光スイッチング，アトムフォトニクスへの発展としての原子の捕獲と偏向の装置の設計指針などが得られていることである．

(1) ナノメートル寸法の光スイッチ：これは大きさの異なる複数個の半導体量子ドットがその寸法程度まで近接して置かれたとき，隣り合う量子ドット間で近接場光相互作用によるエネルギー移動を生じることを利用したナノメートル寸法の光スイッチ動作の可能性を示すものである．図6に示すように，スイッチング動作の時間的振る舞いなどが得られている[20]．
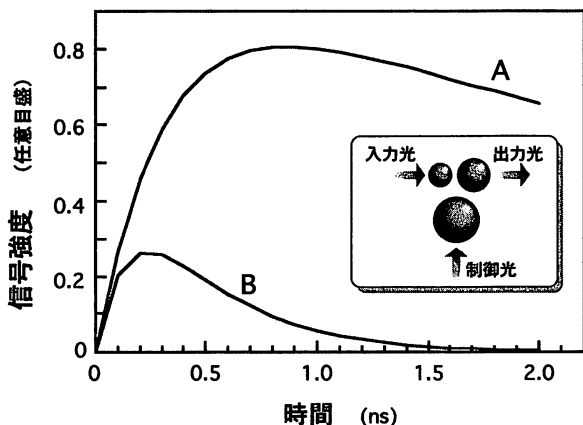
図6　ナノ光スイッチの出力信号強度の時間変化の計算結果．曲線 A，B はおのおののスイッチがオン，オフの状態に対応する[20]．内挿図は大きさの異なる 3 つの半導体量子ドットからなるナノ光スイッチの構造の概略．

(2) 近接場光による原子の捕獲と偏向：ファイバープローブ先端に発生した近接場光と真空中を飛行する中性原子との相互作用を利用し，原子を近接場光中に捕獲したり，または原子の飛行方向を偏向する可能性について，そのための原子に対する捕獲ポテンシャル形状，偏向の散乱断面積などが求められている[21]．

本節では微小な副系 (n) と巨視的な副系（M）とが結合しているという描像を示したが，そのような系での共振器内量子電気力学的効果の出現が期待される．Casimir-Polder 効果[22] は真空場のゆらぎと遅延に起因しているが，本節で展開した定式化では最初からこの 2 つを取り込んでいる．

本節で触れたように，微小な副系 (n) の構成要素間で交換される仮想光子の自由度に着目した P 空間を考え，それに射影を行うと物質励起の衣を着た光子という描像の定式化が可能となる．その取り扱いを発展させると伝搬する実光子との違い，仮想光子の位相，個数，相関といった問題，ひいては観測の問題と絡んで新しい知見が得られる可能性を含んでいる．

近接場光と相互作用する対象は原子，分子，さらにはナノメートル寸法の量子ドットのような低次元系である．このような系では，複数の熱浴との結合による競合が本質的となる．近接場光を光子と物質励起の混在するモードと捉えたとき，系のコヒーレンスを支配する基礎方程式，励起エネルギー移動の機構など，基本的な問題が未開拓のままである．このような基本的な問題を解明することにより，これまで回折限界によって制限されていた光科学技術に新しい展開が広がる．2章2節末尾の (1) で示したような新しい動作原理に基づくナノメートル寸法の光デバイスはその応用のひとつであり，これがナノフォトニクスを支援，発展させる．ただしその際，近接場光によってナノメートル寸法の物質，デバイスをつくるという「ナノの匠」の技術を極めることが不可欠である．

文　献

1) 大津元一：ナノ・フォトニクス（米田出版，1999）．
2) 大津元一：近接場光の基礎（裳華房，2002）．
3) M. Ohtsu: *Near-Field Nano/Atom Optics and Technology* (Springer-Verlag, Tokyo/Berlin, 1998).
4) M. Ohtsu and H. Hori: *Near-Field Nano-Optics* (Kluwar Academic/Plenum Publishers, New York, 1999).

5） 大津元一：光の小さな粒（裳華房，2001）.

6） E. A. Synge: "A suggested method for extending microscopic resolution into the ultra-microscopic region," Phil. Mag., **6** (1928) 356-362.

7） M. Ohtsu: "Overview," *Near-Field Optics: Principles and Applications*, eds. X. Zhu and M. Ohtsu (World Scientific, Singapore, 2000) pp. 1-8.

8） A. V. Zvyagin, J. D. White and M. Ohtsu: "Near-field optical microscope image formation: A theoretical and experimental study," Opt. Lett., **22** (1997) 955-957.

9） M. Naya, S. Mononobe, R. Uma Maheswari, T. Saiki and M. Ohtsu: "Imaging of biological samples by collection-mode photon scanning tunneling microscope with an apertured probe," Opt. Commun., **124** (1996) 9-15.

10） T. Yatsui, M. Kourogi, K. Tsutsui, J. Takahashi and M. Ohtsu: "High density-speed optical near field recording-reading with a pyramidal silicon probe on a contact slider," Opt. Lett., **25** (2000) 1279-1281.

11） T. Matsumoto, T. Ichimura, T. Yatsui, M. Kourogi, T. Saiki and M. Ohtsu: "Fabrication of a near-field optical fiber probe with a nanometric metallized protrusion," Opt. Rev., **5** (1998) 369-373.

12） 坂野　斎, 堀　裕和：" 光近接場の直感的描像"，電気学会論文誌 C，**119-C** (1999) 1094-1099.

13） 荻原　篤：" 微小誘電体試料における光の散乱"，山梨大学工学部電子情報工学科卒業論文，1997 年 3 月.

14） O. J. F. Martin, C. Girard and A. Dereux: "Generalized field propagator for electromagnetic scattering and light confinement," Phys. Rev. Lett., **74** (1995) 526-529.

15） H. Ishihara and K. Cho: "Nonlocal theory of the third-order nonlinear optical response of confined excitons," Phys. Rev., **B 48** (1993) 7960-7974.

16） Y. Ohfuti and K. Cho: "Nonlocal optical response of assemblies of semiconductor spheres," Phys. Rev., **B 51** (1995) 14379-14394.

17） K. Kobayashi and M. Ohtsu: "Quantum theoretical approach to near-field optical system," J. Microsc., **194** (1999) 249-254.

18） K. Kobayashi, S. Sangu, H. Ito and M. Ohtsu: "Near-field optical potential for a neutral atom," Phys. Rev. A, **63** (2001) 013806-1-9.

19） S. Sangu, K. Kobayashi and M. Ohtsu: "Optical near fields as photon-matter interacting systems," J. Microsc., **202** (2001) 279-285.

20） K. Kobayashi, T. Kawazoe, S. Sangu, J. Lim and M. Ohtsu: "Theoretical and experimental study on a near-field optical nano-switch," *Technical Digest of Photonics Switching, OSA/IEEE LEOS Meeting* (Opt. Soc. Am., Washington, D. C., 2001) pp. 27-29.

21） K. Kobayashi, S. Sangu, H. Ito and M. Ohtsu: "Effective probe-sample interaction: Toward atom deflection and manipulation," *Near-Field Optics: Principles and Applications*, eds. X. Zhu and M. Ohtsu (World Scientific, Singapore, 2000) pp. 82-88.

22） E. A. Hinds: "Perturbative cavity quantum electrodynamics," *Cavity Quantum Electrodynamics*, ed. P. R. Berman (Academic Press, Boston, 1994) pp. 1-56.

134

ナノフォトニクスと
ナノ光集積デバイス

東京工業大学大学院総合理工学研究科
科学技術振興事業団　創造科学技術推進事業　大津局在フォトンプロジェクト
㈶神奈川科学技術アカデミー　光科学重点研究室　大津・斉木グループ　**大津　元一**

1．まえがき

ナノテクノロジー（NT）の研究開発に象徴されるように科学技術の重要な方向の1つは材料を微小化して高度集積化デバイスを開発し，これによりシステムの大容量・高速化をめざすことである。ところで光技術は以前より情報の通信，記録，表示などの情報技術（IT）を担ってきたので，NTを光技術に利用すればITの性能が飛躍的に向上する可能性がある。この観点に立てば光によるNT，すなわち筆者が「ナノフォトニクス」[1]*と命名した光科学技術は将来への必然的な方向である。本稿ではナノフォトニクスとそのためのナノメートル寸法光集積デバイスの開発の状況について概説する。具体的には，なぜナノフォトニクスが必要？（Why?），ナノフォトニクスとは何？（What?），どのようにしてデバイスを開発？（How?），の順に記す。

2．Why?，What?

光技術の代表例として光メモリー，微細加工，光ファイバー通信がある。これらに対して2010〜2015年を目安とした将来の社会が要求する事柄とそれに関する問題が提起されているが，これらのうち前二者についてはすでに解説してある[2]。特に光メモリーについては筆者らがすでに高効率半導体プローブアレイを作製しこれを用いた記録再生実験を成功させており[3]，また，これと類似の研究の紹介記事が後藤により本号中に執筆されるので，ここでは光ファイバー通信システムとそれを支える光デバイスについて指摘する。

現在の光ファイバー通信システムを支える光デバイスは半導体レーザー，光導波路などであるが，これらの光デバイスを伝搬光の回折限界まで微小化しても1μm程度が限度である。一方，「光テクノロジーロードマップ」（情報通信分野）[4]によると，光通信システムでは2015年になると，急増するインターネット情報などの授受のためにナノメーター程度と小型で高効率の新しいデバイス（入出力チャンネル数1000×1000の光スイッチアレイ用デバイスなど）の開発が必要となる。そのためにはデバイスの寸法は100nmまたはそれ以下まで小さくする必要がある。しかしこの値は回折限界を超えており，現状の技術で実現することは不可能である。

図1に示すようにこの回折限界を打破する新技術がナノフォトニクスである。ところで最近は微小共振器レーザー，さらにはナノメートル寸法の材料を多数用いた量子ドットレーザーやフォトニック結晶などが研究されているが，これらはナノフォトニクスとは無縁である。なぜならばこれらは伝搬光を情報キャリアーとして使っているからである。ナノフォトニクスは**図2**に示すように
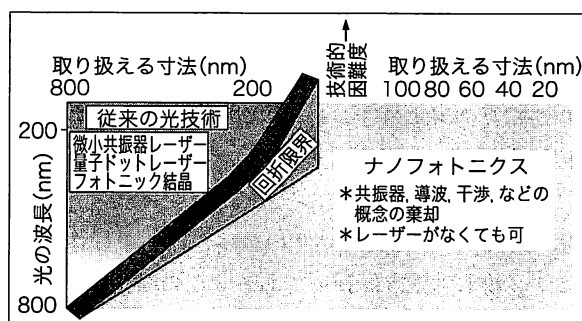
図1　従来の光技術とナノフォトニクスとの関係

おおつ　もといち

---

* ㈶光産業技術振興協会では筆者の提案により1995年に「ナノフォトニクス懇談会」が発足し，現在に至っている。
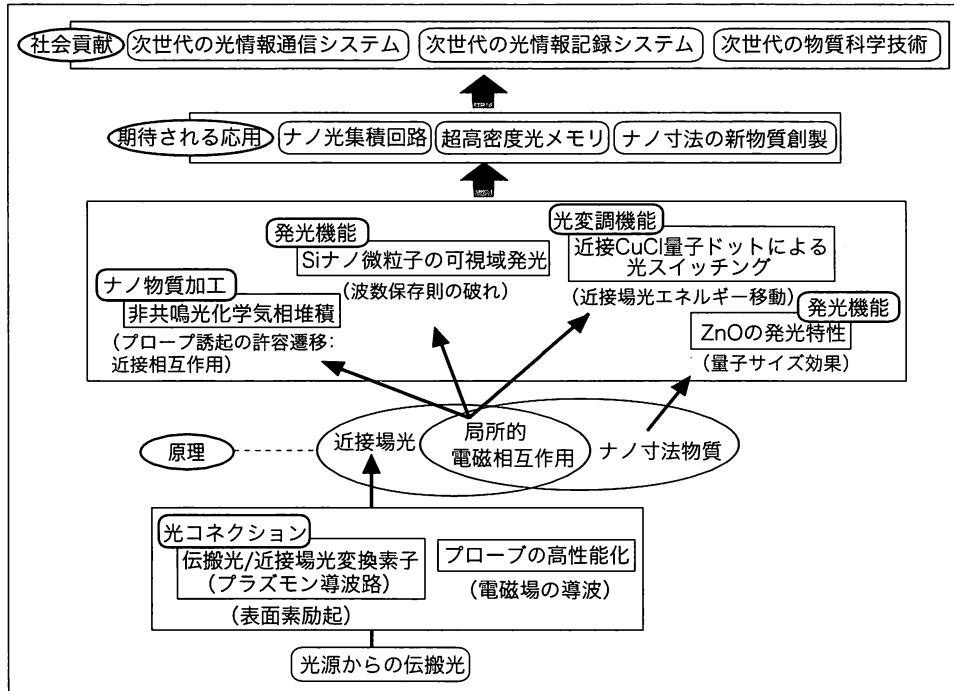
図2　ナノフォトニクスの原理と関連する技術，応用
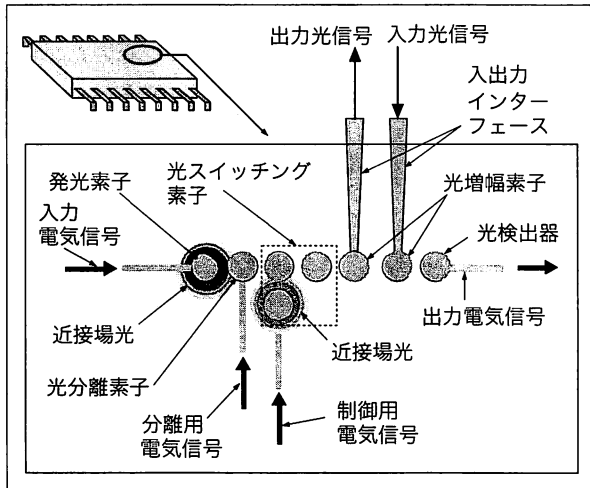
図3　ナノ光集積回路の構成

近接場光を介してナノメートル寸法の微小物質（ナノ物質）が相互作用することを利用した光技術である。なお近接場光とはナノ物質に光を照射したとき，散乱光と同時に発生する非伝搬光で，そのエネルギーはナノ物質表面に局在している[5)~8)]。そのエネルギーの局在する範囲はナノ物質寸法と同程度である。この局在の寸法は光波長とは無関係で，それよりずっと小さいので，従来のフォトニクスが抱えていた回折限界という本質的な問題を解決するパラダイムシフトとなる。

近接場光を使うと例えば2つのナノ物質が近接しているとき，

①第1のナノ物質表面に発生する近接場光を第2のナノ物質に照射して第2のナノ物質の形を計測したり構造を分析する。

②さらに近接場光のエネルギーを大きくして第2のナノ物質を加工する。

③近接場光のエネルギーを第2のナノ物質に移動させて情報伝送する。

といった応用が可能である。特に③は本稿で扱う光ファイバー通信システム用のナノ寸法の光デバイス，光集積回路の実現に有効である。

3. How?

近接場光を用いれば従来の光技術では不可能であったナノメートル寸法の新しい光デバイスの開発が可能となり，2節冒頭に記した要求に応えることができる。われわれが提案しているナノ光集積回路を図3に示す[9)]。この図ではレーザーなどの既存の光デバイスの概念は消失しており，ナノ物質から近接場光を発生させ，そのエネルギーを伝送，変復調することにより情報を送る。また外部の通常の光デバイス（ファイバー伝送路など）との
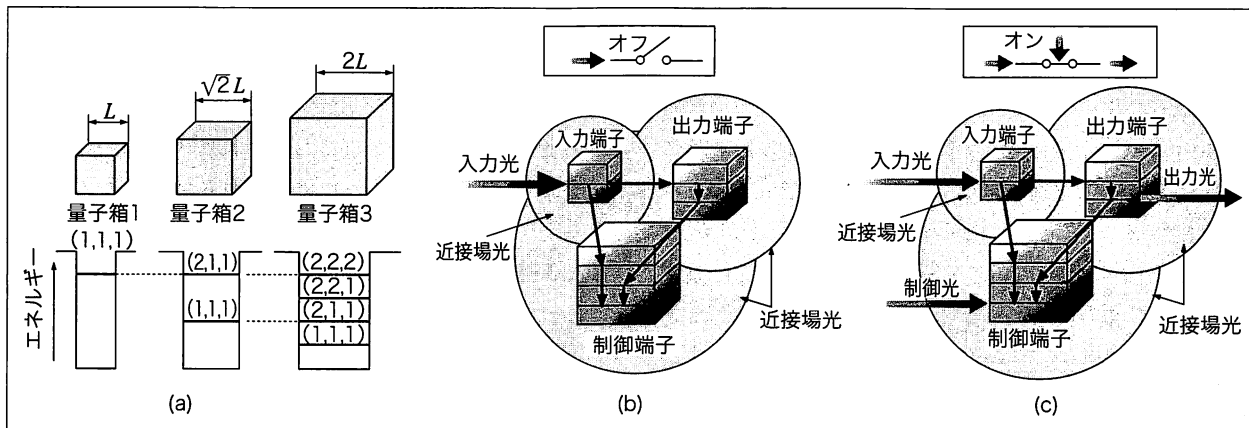
図4 ナノ光スイッチの原理。(a)構成する3つの半導体量子ドットとそのエネルギー準位。(b)オフ動作の説明。(c)オン動作の説明

光信号の授受にはプラズモン波動を伝送するナノ寸法光導波路を使用する。本節ではこれらの開発の現状を述べる。

3.1 ナノ光スイッチ

光スイッチの動作機構は光の発生，変調などにかかわるので基本的光デバイスであると考えられる。**図4**(a)にわれわれが提案しているナノ光スイッチの構成を示すが，それは寸法の異なる3つの半導体量子ドットからなる。その形状が一辺 L の立方体（量子箱）である場合，その中の励起子エネルギーは量子化され，$E_B+(h^2/8ML^2)(n_x^2+n_y^2+n_z^2)$ と表わされる。ここで E_B はバルク結晶における励起子エネルギー，M は励起子の有効質量，n_x, n_y, n_z（$=1,2,3,\cdots$）は主量子数である。この表式によると量子箱1，2，3の寸法がおのおの L，$\sqrt{2}L$，$2L$ の場合には量子箱1中の励起子閉じ込め準位 $E_{1,1,1}$ と量子箱2の励起子閉じ込め準位 $E_{2,1,1}$ と共鳴する。なお，この2つの準位間の遷移は通常の伝搬光による遷移では禁制であることに注意されたい。しかし空間的に局在している近接場光では許容される。すなわち，本スイッチは通常の伝搬光では動作せず，近接場光によってのみ動作するデバイスである。

共鳴する量子箱間に働く近接場相互作用ポテンシャルは $A\exp(-\mu r)/r$ なる湯川関数で表わされる[10]。ここで r は量子箱間距離である。A，μ は実験により求める係数である。この表式および注目するエネルギー準位の振動子強度等から近接場光エネルギーの移動時間が計算でき，$r=10\text{nm}$ の時それは約100ps と推定されている。この値は励起子寿命の数 ns に比べて十分早い。また量子箱中では ps 程度で副準位間緩和が起こると推定され

る。したがって近接場光が支配的となる領域に量子箱が近接している場合，量子箱1中に生成される励起子は近接場光を介して量子箱2へ移動する。そして最終的にはもっともエネルギー準位の低い量子箱3へ励起子が移動する。

これら量子箱1，2，3 をおのおの入力端子，出力端子，制御端子と見なし，図4(b),(c)にスイッチのオフ動作，オン動作の概略を示す。量子箱3のエネルギー準位が空いている場合，量子箱1に入力された励起子は量子箱2に移動後そこにとどまって発光することはできず量子箱3まで緩和する。これをスイッチのオフ状態とする。オン動作のためには量子箱3を制御用の光で励起することで量子箱3のエネルギー準位を埋める。この場合量子箱1に作られた励起子は近接場光を介して量子箱2までは移動できるが，そこからは量子箱3へは緩和できないため，量子箱2で発光し，オン動作が実現される[11]。

このスイッチ動作の基礎となる過程は量子箱間の近接場光エネルギーの移動である。これを観測するために NaCl 結晶中に成長させた CuCl 量子箱に対する近接場分光分析の実験が温度 15K にて行われた[12]。図5(a)に集光モードの近接場分光装置により測定された発光スペクトルを示す。励起光の波長は 325nm である。寸法の異なる CuCl 量子箱は発光の光子エネルギー（発光波長）が異なり，例えばこの図中のピーク X,Y はおのおの一辺 4.6nm，6.3nm の CuCl 量子箱からの発光に対応する。ところで両者の寸法比は 1:$\sqrt{2}$なので 4.6nm の CuCl 量子箱の励起子エネルギー準位 $E_{1,1,1}$ と寸法 6.3nm のそれ $E_{2,1,1}$ は共鳴しており，近接場光エネルギーの移動が観測される条件を満たすことがわかる。

図5(b)にピークX,Yの発光強度の空間分布の測定結果を示す。図中破線で囲まれた領域は発光強度分布が反転している。用いた試料の量子箱の一辺の寸法の平均値は4.3nmなので，4.6nmの量子箱は6.3nmの量子箱に比べ圧倒的に多数存在する。近接場光相互作用が起こりうる近接領域に6.3nmの量子箱が配備された4.6nmの量子箱はそのエネルギーを6.3nmの量子箱に受け渡すので，その結果発光できず，したがって暗い領域ができる。同時にその領域では6.3nmの量子箱の発光強度が強くなる。すなわちこの発光強度分布の反相関は4.6nmの量子箱のエネルギー準位$E_{1,1,1}$から6.3nmの量子箱のエネルギー準位$E_{2,1,1}$への近接場光エネルギーの移動が生じたことを示している。

以上により上記の光スイッチの動作の根拠となる現象が確認された。現在はこのデバイスの動作特性の温度依存性などについての理論的検討が行われ[13]，さらに近接場光による化学気相堆積法[14]~[17]などにより実際のデバイスを作製するための実験が進められている。
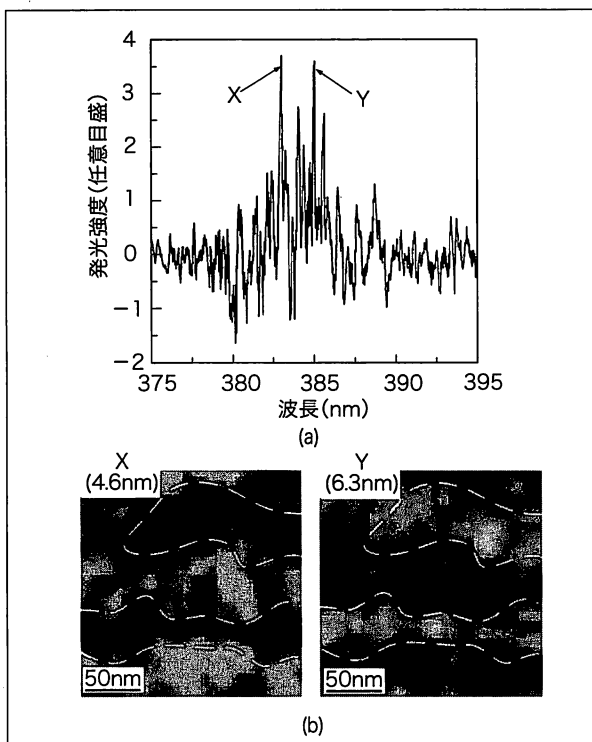

図5 CuCl量子箱に対する近接場分光分析の実験結果。(a)発光スペクトル。ピークX,Yはおのおの一辺4.6nm，6.3nmのCuCl量子箱からの発光。(b) 4.6nm，6.3nmのCuCl量子箱からの発光強度の空間分布の測定結果。

3.2 プラズモン導波路

ナノ寸法の光集積回路を外部の光デバイスにより駆動するためには伝搬光を近接場光に変換する必要がある。この変換用デバイスとしてわれわれはナノ寸法光導波路を提案しているが，これに要求される性能は次の3点である。

A.伝搬光から近接場光への変換効率が高いこと。

B.ナノ寸法の光集積回路中のナノ光デバイスに対し個別照射を可能とするために，導波光スポット径が100nm以下であること。

C.ナノ寸法の光集積回路中のナノ光デバイスが励起光である伝搬光と直接結合することを防ぐために，導波可能距離が伝搬の光波長（回折限界値）以上であること。

以上の性能を満たす伝搬光／近接場光変換用導波路としてわれわれは図6に示すデバイスを開発した[18]。これはくさび形のシリコン基板の上辺が細線状の平面（プラトー）になっており，それに金属膜を蒸着することにより，金属コア導波路を形成し，プラズモンを励起伝搬させるものである。まず入射する伝搬光が斜面において2次元の表面プラズモンに変換され，これがF_1面とくさび上辺のプラトーとの境界である角部において散乱し，この散乱光によってプラトーの金属コア導波路に1次元のTMプラズモンモードが励起される。

この導波路の特長は次のとおりである。

①斜面とプラトーとの境界の角部における散乱結合により2次元の表面プラズモンモードから1次元のTMプラズモンモードへの変換効率が高い。これは上記の要求Aを満たす。

②TMプラズモンモードは遮断径が存在しないので，導波光スポット径を1nmまで小さくすることが可能である。これは上記の要求Bを満たす。
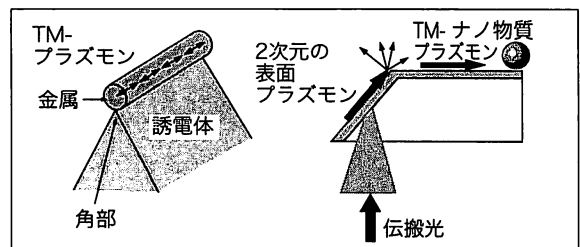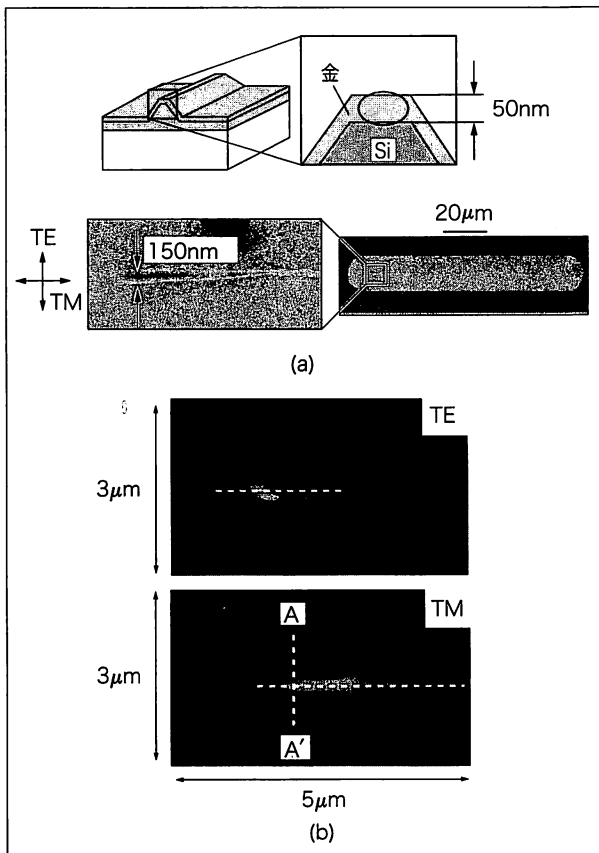
③TMプラズモンモードの導波可能距離は十分長い。

図6 伝搬光／近接場光変換用導波路の構成

図7 プラズモン導波路。(a)構成。(b)入射光がTE, TM偏光の場合のモード伝搬特性の測定結果。図中A, A'における光強度分布の断面形状の半値幅は110nm。

これは上記の要求Cを満たす。

以上のプラズモン導波路をSOI (Silicon on insulator)基板の異方性エッチングにより作製した。その形状を図7(a)に示す。プラトー幅は150nm，長さは80μmである。またプラトーの面には厚さ50nmの金を蒸着し，コアを形成している。このプラズモン導波路のモード伝搬特性を集光モードの近接場光学顕微鏡により測定評価した。入射光の波長は830nmである。実験結果を図7(b)に示す。これらは入射伝搬光がおのおのTM偏光（電場ベクトルの方向が導波路軸方向），TE偏光（電場ベクトルの方向が導波路軸と直角方向）の場合の結果である。両者を比較するとTM偏光時のみ伝搬モードが観測される。その光強度分布の断面形状の半値幅から導波光スポット径が110nmと推定された。一方導波可能距離は2.5μmであった。この値はコア径40nmの金（Au）製の円柱導波路に対する導波可能距離と一致している。また変換効率は0.5％であり，これは150nmの開口径

をもつファイバープローブの近接場光発生効率と比較すると約10倍大きな値であり，高効率が実現したことが分かる。以上によりここで作製したプラズモン導波路が伝搬光／近接場光変換デバイスとして十分な性能を満たしていることが確認された。今後の細線化などの改良により一層の性能向上が期待される。

4. まとめ

ナノ光集積回路実現のために，上記以外にも近接場光が関与するナノ物質の発光特性を利用して従来の光デバイスや光集積回路にはない機能と性能を発現させる試みが進展することが期待される。また，これらを作製するために近接場光を用いた微細加工も開発されており，2015年の光情報通信システムからの要求に応えるべく，ナノフォトニクスの新分野の今後の一層の発展が望まれる。

謝 辞

参考文献
1) 大津元一：「ナノ・フォトニクス」，米田出版，pp. 109～116 (1999)
2) 大津元一：「ナノフォトニクスとその展望」，電子情報通信学会誌，Vol. 84, No. 1, pp. 26～32 (2001)
3) T. Yatsui, M. Kourogi, K. Tsutsui, J. Takahashi, and M. Ohtsu: "High-density-speed optical near-field recording-reading with a pyramidal silicon probe on a contact sliter", Opt. Lett., Vol. 25, No. 17, pp. 1279～1281 (2000)
4) (財)光産業技術振興協会編：「光テクノロジーロードマップ報告書―情報通信分野―」，(財)光産業技術振興協会，p. 34 (1998)，およびその改訂として同協会編，「オプトニューズ」，Vol. 116, pp. 7～10 (2000)
5) M.Ohtsu: "Near-Field Nano/Atom Optics and Technology", Springer-Verlag, pp. 288～290 (1998)
6) M. Ohtsu and H. Hori: "Near-Field Nano-Optics", Kluwer Academic/Plenum Publishers, pp. 10～24 (1999)
7) 大津元一：「光の小さな粒」，裳華房，第2章 (2001)
8) 大津元一：「近接場光の基礎」，裳華房，第4章，第8章 (2002)

9) M.Ohtsu: "Near-fieled nano-optics toward nano/atom depotision", Technical Digest of the 18th Congress of the International Comission for Optics, SPIE Vol. 3749, pp. 478 ~ 479 (1999)

10) K. Kobayashi, S. Sangu, H. Ito, and M. Ohtsu: "Near-field optical potential for a neutral atom", Phys. Rev. A, Vol. 63, pp. 013806-1 ~ 013806-9 (2001)

11) K. Kobayashi, T. Kawazoe, S. Sangu, and M. Ohtsu: "Proposal for a near-field optical nano-switch", Technical Digest of the 4th Pacific Rim Conference on Lasers and Electro-Optics (CLEO/PR01), IEEE LEOS, pp. I1192 ~ I1193 (2001)

12) T. Kawazoe, K. Kobayashi, J. Lim, Y. Narita, and M. Ohtsu: "Verification of principle for nano-meter size optical near-field switch by using CuCl quantum cubes", Technical Digest of the 4th Pacific Rim Conference on Lasers and Electro-Optics (CLEO/PR01), IEEE LEOS, pp. I1194 ~ I1195 (2001)

13) S. Sangu, K. Kobayashi, and M. Ohtsu: "Optical near-field sample-probe Interaction depending on excitation energy of matter", Technical Digest of the 4th Pacific Rim Conference on Lasers and Electro-Optics(CLEO/PR01), IEEE LEOS, pp. I1352 ~ I1353 (2001)

14) Y. Yamamoto, M. Kourogi, M. Ohtsu, V. Polonski, G.H. Lee: "Fabrication of nanometric zinc pattern with photodissociated gas-phase diethylzinc by optical near field", Appl. Phys. Lett., Vol. 76, No. 16, pp. 2173 ~ 2175 (2000)

15) G. H. Lee, Y. Yamamoto, M. Kourogi, and M. Ohtsu: "Blue shift In room temperature photoluminescence from photo-chemical vapor deposited ZnO films", Thin Solid Films, Vol. 386, pp. 117 ~ 120 (2001)

16) M. Ohtsu, K. Kobayashi, H. Ito, and G.H. Lee: "Nanofabrication and Atom Manipulation by Optical Near-Field and Relevant Quantum Optical Theory", Proc. IEEE, Vol. 88, No. 9, pp. 1499 ~ 1518 (2000)

17) T. Kawazoe, Y. Yamamoto, and M. Ohtsu: "Fabrication of a nanometric Zn dot by nonresonant near-field optical chemical-vapor deposition", Appl. Phys. Lett., Vol. 79, No. 8, pp. 1184 ~ 1186 (2001)

18) T. Yatsui, M. Kourogi, and M. Ohtsu: "Plasmon waveguide for optical far/near-field conversion", Appl. Phys. Lett., Vol. 79, pp. 4583 ~ 4585 (2001)
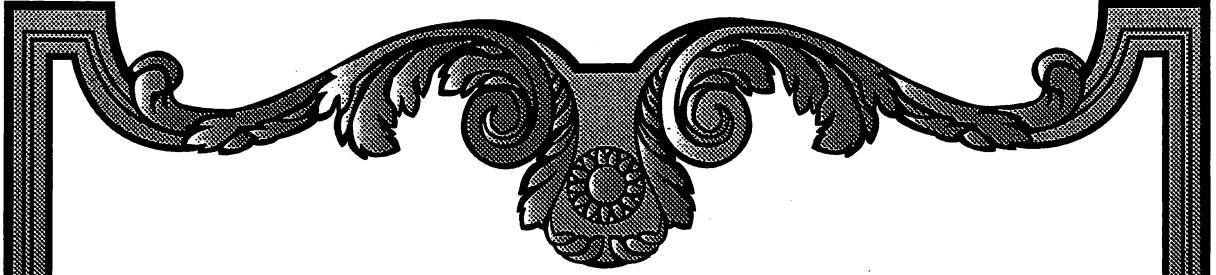
[II] PAPERS IN OTHER FIELDS

Ultrahigh Scanning Speed Optical Coherence Tomography Using Optical Frequency Comb Generators

Seok-Jeong LEE[1,*], Bambang WIDIYATMOKO[2], Motonobu KOUROGI[1,2] and Motoichi OHTSU[1]

[1]Interdisciplinary Graduate School of Science and Engineering, Tokyo Institute of Technology,
4259 Nagatsuta, Midori-ku, Yokohama, Kanagawa 226-8502, Japan
[2]Optical Comb Project, Japan Science and Technology Corporation, G-2 Building, Room 1106, Tokyo Institute of Technology,
4259 Nagatsuta, Midori-ku, Yokohama, Kanagawa 226-8502, Japan

A novel optical coherence tomography system without any moving parts for depth scanning was proposed and demonstrated. It was accomplished using two optical frequency comb generators, as broad-band spectrum generators, instead of moving parts for depth scanning. A high scanning speed of more than 12.5 km/s and also a high repetition rate of 500 kHz were achieved in a long scan range of 25 mm. The resolution was about 100 μm.

KEYWORDS: optical coherence tomography, optical frequency comb generator, phase modulator, sidebands, scan range, scanning speed, repetition rate

A high scanning speed and a high repetition rate were required in order to reduce the image blur due to the motion artifact of a living object[1] and to realize a high image acquisition rate.[2] To date, some mechanical methods have been used for depth scanning in conventional optical coherence tomography (OCT). The conventional stage methods have a scanning speed of 160 mm/s.[3–8] The method using a galvanometer with a reflector on a lever arm enabling small angular rotation has a repetition rate of 100 Hz and a scanning speed limited to 30 cm/s. The methods using a spinning mirror pair or a spinning glass cube have achieved a scanning speed of 20 m/s with a repetition rate of 400 Hz in the depth range of 3 mm.[9–11] The method using the fiber wrapped around a piezoelectric transducer (PZT) has a scanning speed of about 3 m/s and a repetition rate of 1200 Hz.[2,12,13] The method using a galvanometer with a reflector on a lever arm based on a grating, a successful method used in obtaining the first in vivo OCT images of an organic system based on the catheter-endoscope has a scanning speed of 6 m/s and a repetition rate of 2 kHz in the range of 3 mm.[14] However, these methods can be affected by the perturbation of the external environment and of the equipment itself because of the presence of moving parts. Maintenance of the mechanical parts is also required. The scan range of conventional systems is limited to only 3 mm in usual.

Our system has a high scanning speed of 12.5 km/s and a high repetition rate of 500 kHz in the scan range of 25 mm, which are several tens, to several hundreds times higher than those of the conventional system. Moreover, our system is mechanically stable because it contains no moving parts, and does not need any mechanical maintenance. It also provides flexibility for controlling the depth scanning speed and the repetition rate depending on the application by modification of the parameters such as modulation frequency and difference frequency. These advantages could be achieved by adopting two optical frequency comb generators (OFCGs).

The OFCG consists of an electro-optic (EO) phase modulator inside a Fabry-Perot (FP) cavity[15] as shown in Fig. 1. The basic concept to convert continuous light waves into subpicosecond optical pulses has been proposed in 1972 by T. Kobayashi.[16] We have improved the span of the comb since
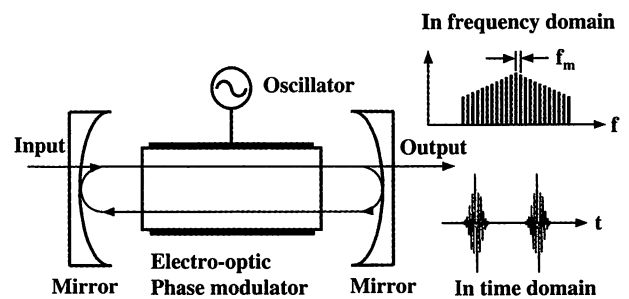

Fig. 1. Optical frequency comb generator, and its output in frequency domain and time domain.

1991.[15,17] The modulator is driven by the microwave signal, the modulation frequency of which is a harmonic of the free spectral range (FSR) of the FP cavity. The output of an OFCG is a broad-band ultrashort pulse train with frequency sidebands of wide span. The output waveform is a Lorenzian pulse train having a repetition rate twice the modulation frequency. The pulse width[16,17] $\Delta\tau$ is

$$\Delta\tau = \frac{1}{2Ff_m\beta}, \qquad (1)$$

where F is finesse of the FP cavity, β is the modulation index of the single-propagation (traveling) EO modulator, and f_m is the modulation frequency. In our case, $\Delta\tau \simeq 356$ fs was achieved when $F = 400$, $f_m = 6.2$ GHz, and $\beta = 0.18\pi$ rad.

The basic structures of a conventional OCT and an OCT using two OFCGs are shown in Figs. 2(a) and 2(b), respectively. The movement of the reference mirror shifts the frequency of the input beam by $\Delta\nu$ in the conventional OCT shown in Fig. 2(a). The frequency shift $\Delta\nu$ is

$$\Delta\nu = \frac{2v}{c}\nu, \qquad (2)$$

where ν is the optical frequency, v is the movement speed of the reference mirror, and c is the velocity of light.

However, in the OCT using two OFCGs shown in Fig. 2(b), OFCG1 in the object arm and OFCG2 in the reference arm, instead of the movement of the reference mirror, are modulated by the frequency of f_m and $f_m + \Delta f$, respectively. The
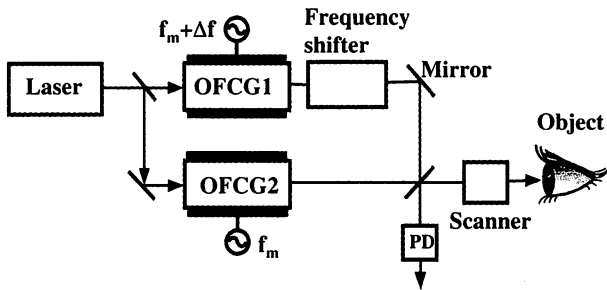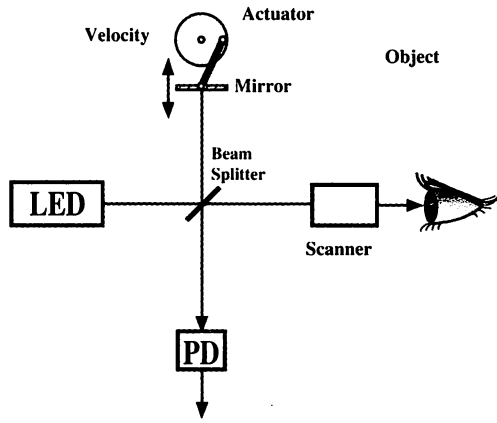
*E-mail address: lee@ae.titech.ac.jp

141

Fig. 2. Basic configuration of a conventional OCT and an OCT with two OFCGs. (a) Conventional OCT. (b) OCT with two OFCGs.

Fig. 3. Scanning speed proportional to frequency difference.

frequency shift Δv in OCT with two OFCGs is

$$\Delta v = \frac{\Delta f}{f_m} v + \text{Const.,} \qquad (3)$$

where Δf is the frequency difference between two OFCGs. OFCG1 and OFCG2 generate constant periodical pulse trains of different time durations, respectively. The time delay of the reference pulse train sweeps the path difference of two arms. The pulse trains in both arms interfere with each other when the delay is equal to the equivalent time interval corresponding to the path difference, or when their difference is smaller than the time coherence. In conventional OCTs, the movement distance and the repetition speed of the reference mirror limit the scan range and repetition rate, respectively. However, it is possible to achieve a very long scan range and fast repetition rate in our system because they depend on the modulation frequency and frequency difference between two OFCGs.

The scan range of depth scan in our system is defined as:

$$R = \frac{c}{2f_m}. \qquad (4)$$

The equivalent scanning speed for depth in our system v_s is

$$v_s = R\Delta f = \frac{c}{2f_m}\Delta f. \qquad (5)$$

The theoretical calculation of the equivalent scanning speed is shown in Fig. 3. In practice, there is a limit to the equivalent scanning speed due to overlap between neighboring sidebands in neighboring combs. Therefore, the maximum theoretical scanning speed $v_{s,\text{Max}}$ is

$$v_{s,\text{Max}} \leq \frac{c}{2N_s}, \qquad (6)$$

where N_s is the total number of sidebands included in one span of the comb. It is calculated as about 200 km/s when
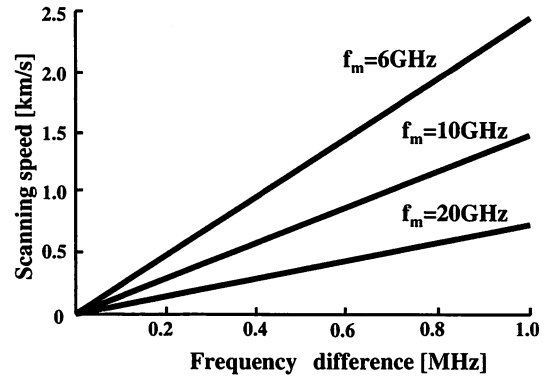
$N_s \simeq 800$ (from span of 5–6 THz and modulation frequency of 6.2 GHz in our case). The repetition rate v_R is

$$\Delta f = v_R \leq \frac{f_m}{N_s}. \qquad (7)$$

The theoretical maximum repetition rate is about 7.5 MHz when $N_s \simeq 800$.

The scan of a glass plate, as an object, in the depth direction was demonstrated using the setup shown in Fig. 2(b), but we did not use a frequency shifter and beam scanner because we were interested in demonstrating only the principle of our OCT this time. The light source was an Nd-YAG laser with a wavelength of 1319 nm, an output power of 100 mW, and a linewidth of < 10 kHz. The OFCG used in this experiment was the monolithic type consisting of a monolithic FP cavity[17] inside a microwave resonator. The monolithic cavity is a lithium niobate crystal $(1 \times 1.2 \times 22.4 \text{ mm}^3)$ with high-reflection coating mirrors, of a planar mirror (reflectivity $R = 99.6\%$) and a convex mirror (radius of curvature = 5 mm, reflectivity $R = 99.6\%$). The output of OFCG had a finesse of 400, modulation index of 0.18π rad, and span of 6 THz.

The output from OFCG1, an object beam, was reflected on a glass plate of an object and interfered with the reference beam for OFCG2. In the meantime, the modulated signals of OFCG1 and OFCG2 were mixed in a double balanced mixer (DBM) and supplied as a trigger signal to an oscilloscope. OFCG1 and OFCG2 were modulated by the frequencies of 6.20233 GHz and 6.202319 GHz, respectively. The frequency difference Δf was 11 kHz, corresponding to a 275 m/s-depth scanning speed.

In Fig. 4, the positive peak-to-peak signal is the scan range and is about 25 mm. The positive-peak-to-negative-peak signal is the optical path difference between the front and back reflection waves. It is about 1.32 mm and is determined by the thickness of the glass plate. Considering as an incidence angle of about 45° to the glass plate, the measured thickness of the plate was about 1 mm as shown in Fig. 4. This agreed with the result of direct measurement. Since this experiment is based on homodyne detection without a frequency shifter, the signal is very sensitive to the phase of light. Therefore, the signal shows positive and negative polarities as shown in Fig. 4, however the polarity is not important in our system. In our case, the depth resolution was equal to the pulse width and measured about 100 μm. It agreed well with the result calculated using eq. (1).

The corresponding equivalent scanning speeds by the vari-

ation of the frequency difference are shown in Fig. 5. As expected from the calculation using eq. (5), the scanning speed was proportional to the frequency difference. However, the resolution and signal-to-noise ratio were degraded for a frequency difference of more than 100 kHz because the detected beat signal was beyond the bandwidth of the photodetector used. The bandwidth of the photodetector in this experiment was about 3 MHz, while the condition of detection bandwidth B should be

$$B \geq \Delta f \frac{N_s}{2}, \qquad (8)$$
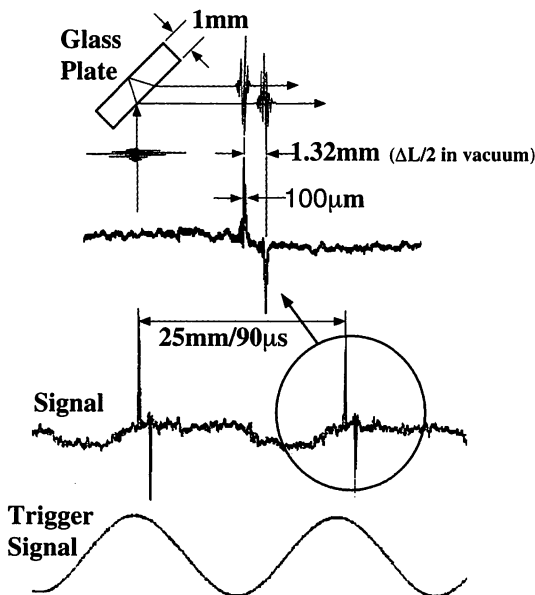
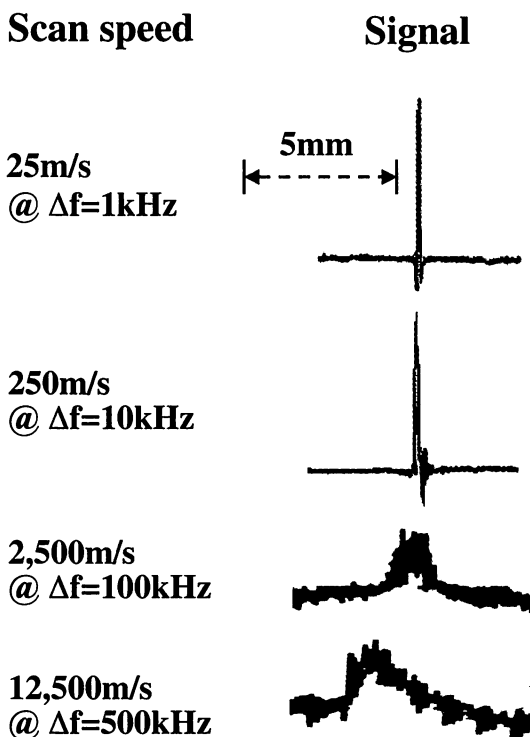Fig. 4. Measurement of the thickness of a glass plate; ΔL is the optical path difference.

Fig. 5. Measurement signal for different scanning speeds.

where Δf is the frequency difference, and N_s is the total number of sidebands in a comb span. In order to detect the beat signal when the frequency difference is higher than 100 kHz, a photodetector with a bandwidth higher than 50 MHz is necessary.

A high scanning speed of more than 12.5 km/s and also a high repetition rate of 500 kHz were achieved in a long scan range of 25 mm. The resolution was about 100 μm. In order to increase the scanning speed and improve the resolution, it is necessary to consider some improvements as follows: First, to increase the scanning speed, it is more important to increase the signal-to-noise ratio before using a detector of higher bandwidth. For increasing the S/N ratio, a higher-power laser and an optical amplifier can be used to increase the optical power. Another method is to use higher-efficiency OFCGs. The conversion efficiency of a conventional OFCG is less than 1%, but it can be increased to 30%.[18,19] Second, to improve the resolution, the signal can be processed using an optical filter and/or an electrical filter. On the other hand, the expanded-span-type OFCG[20] can be used. Thereby, the span of OFC can be increased to more than 30 THz, and the resolution can be improved to below 10 μm.

1) R. M. Steinman, G. M. Haddad, A. A. Skavenski and D. Wyman: Science **181** (1973) 810.
2) G. J. Tearney, B. E. Bouma, S. A. Boppart, B. Golubovic, E. A. Swanson and J. G. Fujimoto: Opt. Lett. **21** (1996) 1408.
3) X. Clivaz, F. Marqis-Weible, R. P. Salathe, R. P. Novak and H. H. Gilgen: Opt. Lett. **17** (1992) 4.
4) E. A. Swanson, J. A. Izatt, M. R. Hee, D. Huang, C. P. Lin, J. S. Schuman, C. P. Puliafito and J. G. Fujimoto: Opt. Lett. **18** (1993) 1864.
5) D. Huang, E. A. Swanson, C. P. Lin, J. S. Schuman, W. G. Stinson, W. Chang, M. R. Hee, T. Flotte, K. Gregory, C. A. Puliafito and J. G. Fujimoto: Opt. Lett. **18** (1993) 1864.
6) J. M. Schmitt: Opt. Lett. **20** (1995) 419.
7) M. R. Hee, E. A. Swanson and J. G. Fujimoto: J. Opt. Soc. Am. B**9** (1992) 903.
8) D. M. Baney and W. V. Sorin: IEEE Photon. Technol. Lett. **5** (1993) 1109.
9) J. Ballif, R. Gianotti, P. Chavanne, R. Walti and R. P. Salathe: Opt. Lett. **22** (1997) 757.
10) C. B. Su: Opt. Lett. **22** (1997) 665.
11) Z. A. Yasa and N. M. Amer: Opt. Commun. **36** (1981) 406.
12) J. P. Heritage, A. M. Weiner and R. N. Thurston: Opt. Lett. **10** (1985) 609.
13) R. N. Thurson, J. P. Heritage, A. M. Weiner and W. J. Tomlinson: IEEE J. Quantum Electron. QE-**22** (1986) 682.
14) G. J. Tearney, B. E. Bouma and J. G. Fujimoto: Opt. Lett. **22** (1997) 1811.
15) M. Kourogi, K. Nakagawa and M. Ohtsu: IEEE J. Quantum. Electron. **29** (1993) 2693.
16) T. Kobayashi, T. Sueta, Y. Cho and Y. Matsuo: Appl. Phys. Lett. **21** (1972) 341.
17) M. Kourogi, T. Enami and M. Ohtsu: IEEE Photon. Technol. Lett. **6** (1994) 214.
18) M. Kourogi, T. Enami and M. Ohtsu: IEEE Photon. Technol. Lett. **8** (1996) 1698.
19) A. Morimoto: *Proc. CLEO, Baltimore*, CThS84 (1993).
20) K. Imai, M. Kourogi and M. Ohtsu: IEEE J. Quantum Electron. **34** (1998) 54.

[III] Published Books
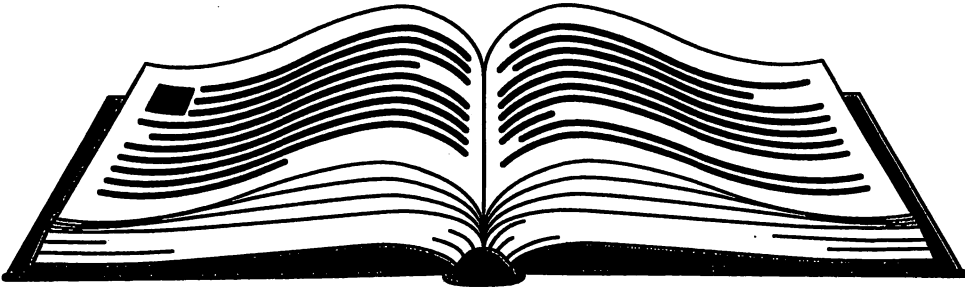
ポピュラー
サイエンス

光の小さな粒
――新世紀を照らす近接場光――

大津 元一 著

裳華房

ま　え　が　き

　常識で考えると，本書の題名の中にある"光"と"小さな粒"とは互いに矛盾していることに気がつくかもしれません．少なくとも，今までの光の常識では矛盾していると考えられてきました．なぜなら光は蛍光灯などの光源装置から出て空間を進むとき，どんどん広がってしまうからです．レーザーという"夢の"光源装置から出た光はまっすぐに進み，広がらないのではないかと考えるかもしれませんが，これでさえも実は広がっているのです．従って，凸レンズでこれらの光を集めて紙にあててみても，光は紙の上で点にはならず，1/1000 mm またはそれ以上の大きさの円になってしまいます．つまり，それよりも小さな"粒"を作ることはできません．また光が広がるために，蛍光灯のまわりで私達は本を読んだり，生活したりすることができるのです．もし光が広がらなければ蛍光灯の真下だけが明るく，そこから少しでもはずれると真っ暗な闇となり，蛍光灯は照明の役割を果たしません．光の学問は，科学の中でも最も長い歴史をもつものの１つと言われていますが，以上の話は，その長い歴史の中で基本的な原理，常識と見なされてきたことです．

　ところで光について，すでに一生懸命に勉強した人は"光子という光の粒があるよ"と思うかもしれません．ここで，光子とはフォトン（photon）という英語の和訳です．"こうし"と読みます．

"みつこ"と読むと，女性の名前のようになってしまい正しくありません．光についての教科書によると，たしかに"光子は光の粒である"と書かれていますが，これは，実は空間的に見て"小さな粒"であるということを意味しているのでは決してなく，そのエネルギーが，電子や原子などのような"小さな粒"と同じような性質をもつという意味なのです．つまり，光子も空間的に広がっているのです．

　以上では，いきなり難しい光子の話まで出てきてしまいました．しかし本書の本文では，光子を扱うわけではないので驚かないでください．その代わりに本書では，最初に述べた常識を覆す新しい光について説明します．それは本書の副題にある**"近接場光"**と言われる**"光の小さな粒"**なのです．この光を作り出すことは，私が1980年頃から約20年かけて挑戦してきたことで，ようやく約10年前から"光の小さな粒"がどんどん作れるようになりました．欧米でも，私と同時期にこのような研究を開始していますので，今ではこれを作ることができる人の数が増えています．

　"光の小さな粒"とは，鋭く尖らせたガラス製の光ファイバの先端にしみ出す光で，あたかも小さな懐中電燈のようなものです．本文中ではそれを"光ナノ粒子"とも呼んでいます．"ナノ"とは"ナノメートル"，つまり100万分の1 mmを表す単位ですが，光の小さな粒はそれほど小さいということを表す名前です．"何だ，懐中電燈を作る話か"と思われるかもしれませんが，このように光の小さな粒ができると，これがいろいろな新しい技術を生み出していくのです．たとえば読者の皆さんにおなじみのCD, MD,

DVD などの光メモリの性能を 100 倍以上向上させることができます．これは 21 世紀の高度情報化社会に大いに役立つことがわかっています．また，空中を飛んでいる原子を捕まえるというような極限的なことをはじめとし，今までの光を使ったのでは到底できないと考えられてきたことを，次々と可能にしつつあります．つまり，この光の粒は"小さい"けれど，話は革命的で"大きい"のです．

　今年から 21 世紀が始まりましたが，本書でその 21 世紀を明るく照らす"光の小さな粒"のお話を紹介することができることは私にとって大きな喜びです．さらに本書では，こぼれ話も紹介するために 話の小さな粒 の欄も設けましたので，ここにもお立ち寄りください．本書を読まれた後，さらに興味をもたれたのなら，巻末にあげた参考書をお読みになることをおすすめします．

　最後に，本書の執筆をお勧めくださり，出版に至るまで忍耐強いご協力と多大のご援助を頂いた裳華房編集部の亀井祐樹様をはじめとする皆様に感謝いたします．

　　2001 年 8 月

　　　　　　　　　　　　　　　　　大 津 元 一

目　　次

第1章　光は大きい

第2章　光の小さな粒を作る，使う

第3章　ファイバプローブを作る

第4章　測　　る

第5章　加工する

第6章　原子を操作する

第7章　将来の夢 ― あとがきにかえて ― ……128

┄┄┄ 話の小さな粒 ┄┄┄

光子の野球　4／文豪ゲーテと色彩　7／モデルの
階層性とアトム　29／魚の見る天空 ― 全反射と
エバネッセント光 ―　31／ファイバプローブを作
り始めた頃の苦労　49／近接場光学顕微鏡の名前
65／蓮の葉の上の水滴 ― 量子ドットの作り方 ―
70／地上すれすれに飛ぶジェット機　105／レン
ズは "RENS"？　111／ボスの居ない間に活躍
122／長さ300 m の管の中を通り抜ける　124

本文イラストレーション：つかもとえつこ